

“Solar 3D printing of Lunar Regolith”

Von der Fakultät für Georessourcen und Materialtechnik
der Rheinisch-Westfälischen Technischen Hochschule Aachen

zur Erlangung des akademischen Grades eines
Doktors der Ingenieurwissenschaften

genehmigte Dissertation

vorgelegt von **M.Sc.**

Alexandre René Jacques Meurisse

aus Tours, Frankreich

Berichter: Univ.-Prof. Dr. techn. Guillermo Carlos Requena
Univ.-Prof. Jochen M. Schneider, Ph.D.
Prof. Dr. Matthias Sperl

Tag der mündlichen Prüfung: 04. Mai 2018

Diese Dissertation ist auf den Internetseiten der Universitätsbibliothek online verfügbar

Abstract

The end-of-life of the International Space Station, not beyond 2030, opens the path to new potential international collaborations to perform research in space. One idea is to settle a research centre on the lunar surface. It would be the first Moon village. The construction of a Moon village could however not be feasible without the use of in-situ resources and advanced manufacturing technologies. Thereupon, this work developed the first solar 3D printer that solely works with lunar regolith and sunlight.

First, the research work focused on the sintering of glass beads and understanding the role played by the green body packing on the sintered material. Results showed that, during a sintering process, when the densest sample is targeted, the original packing fraction is a parameter quickly overtaken by a maximisation of the particles surface area. Then, traditional sintering of lunar regolith simulants exhibited the impact of each lunar mineral on the sintered product. Sintering five different simulants revealed the prominent role of plagioclase, active mineral affecting the sintering temperature. Ilmenite mineral, however, did not perturb the sintering process. Regarding the sintering atmosphere, vacuum had a positive impact on the sintering process, lowering the sintering temperature and increasing the material strength.

Secondly, after a complete characterisation of the existing lunar simulants and studying of their sintering, JSC-2A lunar simulant was chosen for carrying out the solar additive manufacturing experiments. The idea was to sinter lunar regolith simulant layer-by-layer at the focal point of concentrated sunlight. At the DLR-Cologne solar oven, fluctuation in the Earth atmosphere prevented any successful additive manufacturing of lunar regolith simulant with actual sunlight. The experimental set-up was therefore adapted to the Xenon-High-Flux Solar Simulator. Thus, the solar sintering process could run for several hours with steady light conditions. Adjusting the parameters, with a power density of 1.2 MW.m^{-2} focused on 20 mm diameter spot, it was possible to obtain the first solar 3D printed brick after 5 hours of sintering, layer-by-layer.

Finite elements method analysis of the heat transfer — inside loose and sintered regolith — highlighted the quick cooling of the surface happening between the sintering of two layers. Temperature inhomogeneities, which were responsible for thermal stresses within the sintered material and the warping of the edges, were also confirmed by the computer model.

Microscopic and tomography analysis of the sintered parts showed discontinuous layers which are non-homogeneously merged together, with open and closed pores up to $500 \text{ }\mu\text{m}$. The mechanical properties showed that the material has a similar strength to gypsum. Latest sintered parts that are smaller, appeared to have a higher strength due to the reduced cooling time between the layers. Sintering mechanisms, presented in different cases, detailed the necessity of obtaining a suitable melt fraction and a hot substrate for stimulating interlayer bonding. Finally, improving this new technology in the near future was proven

to be beneficial for saving significant costs and providing a reliable radiation shield to the astronauts stepping onto the Moon tomorrow.

Zusammenfassung

Das Ende der Lebenszeit der Internationalen Raumstation, nicht länger als 2030, öffnet Wege zu neuen potentiellen internationalen Kollaborationen, um im Weltraum zu forschen. Eine Idee ist, ein Forschungszentrum auf der Mondoberfläche zu errichten. Es wäre das erste Monddorf. Der Bau eines Monddorfs wäre jedoch ohne den Einsatz von Ressourcen vor Ort sowie fortgeschrittenen Fertigungstechnologien kaum möglich. Darauf aufbauend wird in dieser Arbeit der erste solare 3D-Drucker entwickelt, der ausschließlich mit Mondregolith und Sonnenlicht arbeitet.

Zunächst konzentriert sich die Forschungsarbeit auf das Sintern von Glasperlen und das Verständnis der Rolle, die die Grünkörperpackung auf dem gesinterten Material spielt. Die Ergebnisse zeigen, dass während eines Sinterprozesses als entscheidender Parameter bei dem eine möglichst dichte Probe hergestellt werden soll, die ursprüngliche Volumenfraktion schnell durch eine Maximierung der Partikeloberfläche ersetzt wird. Anschließend zeigte das herkömmliche Sintern von Mond-Regolith-Simulant den Einfluss jedes Mondminerals auf das gesinterte Produkt. Das Sintern von fünf verschiedenen Simulants zeigte die herausragende Rolle von Plagioklas, einem aktiven Mineral, das die Sintertemperatur beeinflusst. Ilmenitmineral störte jedoch den Sinterprozess nicht. Hinsichtlich der Sinteratmosphäre wirkte sich das Vakuum positiv auf den Sinterprozess aus, senkte die Sintertemperatur und erhöhte die Materialfestigkeit.

Dann wurde nach einer vollständigen Charakterisierung der existierenden Mond-Simulants und der Untersuchung ihres Sinterns JSC-2A Mond-Simulant ausgewählt, um die solare Additive Fertigungsexperimente durchzuführen. Die Idee bestand darin, Mond-Regolith-Simulant im Brennpunkt konzentrierten Sonnenlichts schichtweise zu sintern. Im Sonnenofen des DLR-Köln verhinderten Schwankungen in der Erdatmosphäre ein erfolgreiches generatives Fertigungsverfahren von Mondregolith-Simulant mit dem tatsächlichen Sonnenlicht. Der Versuchsaufbau wurde daher an den Xenon-High-Flux Solar Simulator angepasst. Somit konnte der Sonnensinterprozess für mehrere Stunden unter stabilen Lichtbedingungen ablaufen. Durch die Einstellung der Parameter mit einer Leistungsdichte von $1,2 \text{ MW/m}^2$, fokussiert auf einen Punkt mit 20 mm Durchmesser, war es möglich, den ersten solaren 3D-gedruckten Baustein nach 5 Stunden Sintern Schicht für Schicht herzustellen.

Eine Analyse der Wärmeausbreitung per Finite-Elemente-Methode — innerhalb von losen und gesinterten Regolith — hob die schnelle Abkühlung der Oberfläche zwischen dem Sintern von zwei Schichten hervor. Temperaturinhomogenitäten, die für thermische Spannungen innerhalb des gesinterten Materials und das Verziehen der Kanten verantwortlich waren, wurden ebenfalls durch das Computermodell bestätigt.

Die mikroskopische und tomographische Analyse der gesinterten Teile zeigte diskontinuierliche Schichten, die nicht homogen miteinander verschmolzen sind, mit offenen und geschlossenen Poren von bis zu 500 μm . Die mechanischen Eigenschaften zeigten, dass das Material eine ähnliche Festigkeit wie Gips aufweist. Jüngst hergestellte gesinterte Teile,

die kleiner sind, schienen eine höhere Festigkeit aufgrund der reduzierten Kühlzeit zwischen den Schichten zu haben. In verschiedenen Fällen nachgewiesene Sintermechanismen beschreiben die Notwendigkeit eines geeigneten Schmelzanteils und eines heißen Substrats zum Stimulieren der Zwischenschichtbindung. Schließlich hat sich die Verbesserung dieser neuen Technologie in der nahen Zukunft als vorteilhaft erwiesen, um erhebliche Kosten zu sparen und den Astronauten, die schon bald den Mond betreten, einen zuverlässigen Strahlungsschild zu bieten.

Résumé

La fin de vie de la station spatiale internationale, pas au-delà de 2030, ouvre la voie à de nouvelles potentielles collaborations internationales pour effectuer des recherches dans l'espace. Une idée est d'établir un centre de recherche sur la Lune. Ce serait alors le premier village lunaire. La construction d'un village lunaire pourra cependant difficilement être entreprise sans l'utilisation des ressources in-situ et de technologies avancées. Dans cette optique, ce travail a consisté à l'élaboration de la première imprimante 3D utilisant seulement du régolithe lunaire et la lumière du soleil.

Premièrement, le travail de recherche s'est concentré sur le frittage de billes de verres en comprenant le rôle joué par la densité du corps cru sur le matériau fritté. Les résultats ont montré que, pendant le procédé de frittage, si l'objectif est d'obtenir un matériau le plus dense, la compacité d'origine du matériau granulaire est un paramètre rapidement masqué par une maximisation de la superficie des particules. Ensuite, le frittage traditionnel de simulants de régolithe lunaire a exposé l'effet de chaque minéral lunaire sur le matériau fritté. Le frittage de cinq simulants différents a révélé le rôle important du plagioclase, un minéral affectant directement la température du procédé. L'ilménite, quant à lui, n'a perturbé d'aucune manière le procédé de frittage. Concernant l'environnement de frittage, le vide a montré avoir un impact positif sur le procédé, en diminuant la température de frittage et en augmentant les propriétés mécaniques du matériau.

Deuxièmement, après une caractérisation complète des simulants lunaires existants et l'étude de leur frittage, le simulant JSC-2A a été choisi pour effectuer des expériences de fabrications additives par énergie solaire. L'idée était de fritter du simulant de régolithe lunaire, couche par couche, au point focal d'un faisceau de lumière concentrée. Au four solaire du DLR-Cologne, les conditions atmosphériques n'ont pas permis la réussite de la fabrication additive de simulant de régolithe lunaire avec la lumière du soleil concentrée. L'expérience a donc été adaptée au simulateur solaire utilisant des lampes au xénon à haut flux. Ainsi, le procédé a pu fonctionner pendant plusieurs heures avec des conditions stables d'illumination. En ajustant les paramètres, avec une densité de puissance de $1,2 \text{ MW.m}^{-2}$ concentrée sur un disque de 20 mm de diamètre, il a été possible d'obtenir la première brique imprimée en 3D par énergie solaire en frittant, couche par couche, pendant cinq heures.

Une analyse par une méthode aux éléments finis du transfert de chaleur, dans le régolithe à l'état de poudre et fritté, a mis en valeur le refroidissement rapide de la surface frittée entre le frittage de deux couches. L'inhomogénéité des températures, responsable des contraintes thermiques à l'intérieur du matériau fritté et de la déformation des bords, a aussi été confirmée par le modèle numérique.

Les analyses au microscope et par tomographie des objets frittés ont montré des couches discontinues qui n'ont pas fusionnées de manière homogène, avec des pores ouverts et fermés pouvant mesurer jusqu'à 500 μm . Les propriétés mécaniques du matériau fritté étaient similaires à celle du plâtre. Les derniers objets frittés, plus petits, semblaient être plus

solides en raison d'un temps de refroidissement réduit entre les couches. Les procédés de frittage, présentés dans différents cas, ont montré la nécessité d'obtenir une concentration acceptable de matériau fondu et un substrat à haute température pour stimuler les liaisons inter-couches. Enfin, il a été prouvé qu'améliorer cette nouvelle technologie dans un futur proche serait bénéfique pour réduire les coûts et fournir une protection fiable contre les radiations, aux astronautes faisant demain un nouveau pas sur la lune.

Acknowledgement

This work could not have been carried out without the help and support of many people along these three years.

I first wish to thank my interns from Spaceship EAC Jean-Charles Beltzung, Marie Pedrazzani and Julie Gamer for the preparation and tests of an incommensurable number of regolith samples. Their extremely valuable work is an integral part of my thesis. I also should mention my RISE intern Maximilian Plavcan who performed a wonderful work sintering glass beads.

I, of course, thank DLR and RWTH professors Prof. Dr. Matthias Sperl, Prof. Dr. Guillermo Requena and Prof. Dr. Jochen Schneider for their supports, criticisms and leads for the past three years. Their trust in my work was very beneficial.

I am grateful to Dr. Advenit Makaya, Dr. Aidan Cowley, Dr. Laurent Pambaguian and Astronaut Dr. Matthias Maurer for the scientific discussions and help I got from ESA-ESTEC and ESA-EAC. This support greatly benefited my work.

I thank everyone from the Institute of Materials Physics in Space where I spent most of my time for the past three years. Especially my friends and physicist colleagues Dr. Sebastian Pitikaris, Jan Haerberle, Dr. Philip Born, Dr. Peidong Yu, Karsten Tell for teaching me how to properly program and answering my basic physics questions. From the engineering team, I am grateful to the help and discussions I got with Antoine Micallef, Olfa Lopez and Dr. Miranda Fateri. Thank you to Dr. Matthias Kolbe for his assistance in samples preparation and his deep knowledge in microscopy analysis. Also, I thank, Alberto, Alex, Ali, Celine, Jeremy, Koray, Lisa, Manel, Max, Nafiseh, Nishant, Romain, Till, Vibha and Ya Chun, they all played a role in making the granular matter group a nice working environment.

My research work was also scattered in different DLR institutes. I am appreciative to Christian Wilsch, Martin Thelen, Dr. Christian Raeder and Dr. Hans-Gerd Dibowski for the work carried out at the Solar Research institute. The numerous campaigns at the solar oven could not have been successful without their support. At the institute for Materials Research, I wish to thank Janine Wischek, Uwe Fuchs and Reinhard Sottong for the measurements which took part in the important characterisation procedure of the sintered lunar regolith.

Since no work can be done without funding, I am grateful to DAAD for the scholarship, and ESA and EU for funding the research work about solar sintering.

Last but not least, I give a big thank to my family for their steady support which, even from France, has always helped me moving forward.

Contents

Preface	v
List of Abbreviations	vii
List of Figures	ix
List of Tables	xv
Introduction	1
1 Additive Manufacturing of Lunar Regolith	3
1.1 Lunar soil	3
1.2 In-situ resource utilisation	6
1.3 Lunar soil simulants	7
2 Packing and sintering of simple and complex granular media	11
2.1 Basic principles	11
2.2 Bi-disperse granular media	13
2.3 Poly-disperse granular media	19
3 Simulants characterisation	23
3.1 Grain size distribution	23
3.2 Glass content	25
3.3 Mineral composition	27
3.3.1 As-received powder	27
3.3.2 Traditional sintering test plan	28
3.3.3 Ilmenite content variation	35
3.4 Grain shape	37
3.5 Simulant selection	42
4 Scope and design of the experimental set-up	43
4.1 Previous works on solar sintering	43
4.2 Scope of the experiment with respect to the lunar conditions	44
4.2.1 Vacuum conditions	44
4.2.2 Variations in mineralogical compositions	49
4.2.3 Electrical charging	49
4.2.4 Abrasiveness	49
4.2.5 Light intensity variations	49
4.2.6 Temperature variations	50
4.3 Requirements for solar sintering	52
4.3.1 Requirements for solar sintering on the Moon	52

4.3.2	Requirements for solar sintering on Earth	53
4.4	Design of the experimental set-up and process monitoring	54
4.4.1	Concentrated light source	54
4.4.2	Powder testbed	55
4.4.3	Powder feeder	56
4.4.4	3-axis tables	58
4.4.5	Cooled mirrors:	59
4.4.6	Extractor hood:	60
4.4.7	Light Shutter	61
4.4.8	Process monitoring	62
4.4.9	Complete set-up	63
5	Solar additive manufacturing experiments	65
5.1	Sintering strategy	65
5.1.1	Sets of parameters allowing 3D objects manufacturing	65
5.1.2	Sintering a line - 1D printing	66
5.1.3	Sintering a layer - 2D printing	67
5.1.4	Sintering a brick - 3D printing	67
5.2	Solar sintering campaigns	70
5.2.1	First experiments	70
5.2.2	Sintering on a solid substrate	76
5.2.3	Zig-zag sintering path	84
5.2.4	Sintering on melt	86
5.2.5	Convection shielding	91
5.2.6	Complex shape sintering	94
5.2.7	Summary of 3D printing experiments	95
6	Solar sintering modelling	97
6.1	Model definition	98
6.1.1	Solar Heat flux	98
6.1.2	Geometry	98
6.1.3	Boundary conditions	99
6.1.4	Simulation architecture	101
6.1.5	Model limitation	101
6.2	Model 1 - Loose regolith	102
6.3	Model 2 - Sintered regolith	105
7	Analysis and discussions on solar sintered lunar soil	111
7.1	Evaluation of the thermally induced deformations of the samples and the internal stresses in the material	111

7.2	Impact evaluation of the different contributors to the analogue lunar environment on the consolidation mechanisms	115
7.2.1	Xenon Lamps	115
7.2.2	Lunar regolith simulant	115
7.2.3	Environment	115
7.3	Mechanical characterisation of solar sintered samples	117
7.4	Compactness and homogeneity of the consolidated material on a line, a layer, a volume	119
7.4.1	Melt fraction between sintered layers	119
7.4.2	Sintered grain interfaces	124
7.5	Regolith sintering mechanisms	128
7.5.1	Planar mechanisms	128
7.5.2	Volume mechanisms	129
7.5.3	Melt/sintered regolith interaction	130
8	Outlook and Applications	135
8.1	Solar 3D printing of sand	135
8.2	Recommendation on process enhancement.	137
8.2.1	Strength enhancement	137
8.2.2	Sintering area	138
8.2.3	Substrate	138
8.2.4	Layer deposition system	139
8.2.5	Equipment robustness and dust mitigation	139
8.2.6	Vacuum environment	139
8.2.7	Close-loop sintering	139
8.3	Recommendation on potential process adaptation for lunar application.	140
8.3.1	Mobile concentrated solar beam	140
8.3.2	Shielding	140
8.4	Radiation shielding	140
8.5	Martian application	143
8.6	Cost estimate	143
8.6.1	First scenario - Thick shell	145
8.6.2	Second scenario - Thin shells	146
	Conclusion	147
	References	149
	Appendix	159

Preface

It is important to the author to mention that the doctoral work presented in this thesis was mainly project driven. The ESA carried out in 2010 a project European Space Agency (ESA)-General Studies Programme (GSP) “3D printing building blocks using lunar soil”, triggering the ESA activities combining lunar soil and additive manufacturing technologies. The project financing this work was the ESA-General Study Technology Programme (GSTP) “3D printing of a model building block for a lunar base outer shell”, a direct continuation of the mentioned ESA-GSP. Quoting the statement of work, the objective of this ESA-GSTP was to develop a “*3D-printing process for fusing/melting/sintering model lunar soil material with the use of concentrated solar energy.*”. The intended results were four brick-sized model building blocks from a model material. The project scientist had to “*study various parameters of the production process as well as of the model lunar soil in order to better understand and optimise the overall process also in view of application on the Moon.*”

Later on, additional funding came from European Union (EU) following a granted Horizon-2020 (H2020) proposal. The project, named “RegoLight”, aimed at developing further the solar 3D printing of lunar regolith. This work was performed in a consortium with partners from France, Belgium and Austria.

List of Abbreviations

1D	One dimensional
2D	Two dimensional
3D	Three dimensional
AM	Additive Manufacturing
BFO	Blood Forming Organs
CAD	Computer-Aided Design
CRaTER	Cosmic Ray Telescope for the Effects of Radiation
DAAD	Deutscher Akademischer Austauschdienst
DC	Direct Coupling
DIN	Deutsches Institut für Normung
DLR	Deutsches Zentrum für Luft- und Raumfahrt
DNI	Direct Normal Irradiance
DSC	Differential Scanning Calorimetry
EAC	European Astronaut Centre
EDX	Energy-dispersive X-ray spectroscopy
ESA	European Space Agency
ESTEC	European Space Research and Technology Centre
EU	European Union
FJS	Fuji Japanese Simulant
GB	Grain Boundary
GCR	Galactic Cosmic Rays
GSP	General Studies Programme
GSTP	General Study Technology Programme
H2020	Horizon-2020
IR	Infra-red

LIST OF ABBREVIATIONS

ISRU	In-Situ Resource Utilisation
ISS	International Space Station
JSC	Johnson Space Centre
LEO	Low Earth Orbit
LLO	Low Lunar Orbit
LPS	Liquid Phase Sintering
LRO	Lunar Reconnaissance Orbiter
MLS	Minnesota Lunar Simulant
NASA	National Aeronautics and Space Administration
NU-LHT	NASA/USGS-Lunar Highlands Type
PCB	Printed Circuit Boards
RADOM	Radiation Dose Monitor
RT	Room Temperature
RWTH	Rheinisch-Westfälische Technische Hochschule
SEM	Scanning Electron Microscopy
SLM	Selective Laser Melting
SLS	Space Launcher System
SPE	Solar Particle Events
TRL	Technology Readiness Level
XRD	X-Ray Diffraction
ZAP	Zybek Advanced Products

List of Figures

1.1	Two sides of the Moon taken from the LRO and titanium concentration from Clementine	3
1.2	3D printed lunar base, <i>credit: Foster + Partners</i>	7
1.3	Laser 3D printed lunar regolith simulant	7
2.1	Basic definition of the sintering driving force, $\Delta(\gamma A)$	11
2.2	Sintering steps of three modelled grains in contact.	12
2.3	Bi-disperse mixtures and their packing fraction φ	13
2.4	Experimental binary mixing apparatus	14
2.5	Optical microscopic image of monodisperse 615 μm beads sintered at 700°C for 90 minutes.	14
2.6	Optical images bidisperse granular matter with a size ratio of 0.15 sintered at 700°C for 55 minutes.	15
2.7	Micromeritics Geopyc 1360 envelope density analyser (a) and Accupyc 1360 skeletal density analyser (b).	17
2.8	Relative density of binary mixtures over sintering time.	18
2.9	Densification rate of glass beads sintered at 700 °C over the surface area of the beads for a same predefined volume.	19
2.10	Decumulative grain size distribution of lunar regolith.	19
2.11	Relative density of polydisperse glass beads sintered at 700°C over time. . . .	20
2.12	Relative density of JSC-2A lunar simulant sintered at 1110°C over time. . . .	21
2.13	Relative density of pressed and unpressed JSC-2A lunar simulant sintered at 1110°C for 45 minutes.	22
3.1	Grain size distribution of lunar simulants.	24
3.2	Grain size distribution of JSC-1A and JSC-2A obtained by particle size laser diffraction analysis.	24
3.3	DSC curves of as-received lunar simulants.	25
3.4	DSC curves of JSC-1A and JSC-2A after a 1-hour heat treatment at 900°C. Both lunar simulants do not show anymore an amorphous material feature: they are crystallised.	26
3.5	SEM images of as-received JSC-1A and DNA-1 lunar simulants at different magnifications.	28
3.6	Typical transformations for all simulants during the traditional sintering process	29
3.7	SEM images of JSC-1A after sintering in vacuum at 1100°C for 3 hours. . . .	31
3.8	SEM images of JSC-2A after sintering in vacuum. First Batch.	32
3.9	SEM images of JSC-2A after sintering in vacuum. Second batch.	32
3.10	SEM images of FJS-1 after sintering in vacuum at 1090°C for 3 hours. . . .	33
3.11	SEM images of NULHT after sintering in vacuum at 1200°C for 3 hours. . . .	33
3.12	SEM images of DNA-1 after sintering in vacuum at 1070°C for 3 hours. . . .	33

3.13	Plagioclase minerals in the lunar soil, JSC-1A, FJS-1 and DNA-1.	34
3.14	Plagioclase temperature-composition diagram, indicating solidus and liquidus temperatures at 1 bar pressure.	35
3.15	Young's Modulus and Compressive Strength of JSC-1A samples sintered in air with different ilmenite content	35
3.16	Mixture of JSC-1A lunar simulant and 20 wt.% of ilmenite (white grains) sintered under vacuum in a traditional oven at 1100°C for 3 hours.	36
3.17	Young's Modulus and Compressive Strength of DNA-1 samples sintered in air with 0 and 10 wt.% coarse ilmenite content.	37
3.18	Microscopic images of actual lunar soil from Apollo missions.	38
3.19	Table classifying grains according to their roundness and sphericity.	38
3.20	Microscopic images of lunar soil simulants.	40
3.21	Microscopic pictures of grains between 400 μm and 600 μm before and after milling.	41
3.22	SEM images of milled JSC-2A after sintering in vacuum. Powder taken from the second batch.	41
4.1	Sintered regolith simulant by concentrated solar light into an optical fibre. . .	43
4.2	Fresnel lens combined with a rover and a mirror and regolith testbed with solar sintered material.	43
4.3	Young's Modulus and Compressive Strength of lunar simulant sintered in air and in vacuum.	44
4.4	Young's Modulus and Compressive Strength of lunar simulant sintered in air and in vacuum related to the samples density.	45
4.5	SEM images of JSC-1A lunar simulant sintered in air and under vacuum. . .	45
4.6	Microscopic cross-sections of different lunar rocks.	46
4.7	Temperature x-ray diffraction analysis of JSC-1A lunar simulant in vacuum and in air.	48
4.8	Spectra of the sunlight (SOF) and Xenon light (HLS).	50
4.9	Thermal cycling illustration for two hot cycles and two cold cycles.	51
4.10	Temperature ramp after placing a sample in the oven at 150 °C.	51
4.11	Young's Modulus and Compressive Strength of sintered JSC-1A after various thermal cycling.	52
4.12	Sketch and pictures of the solar oven.	54
4.13	Xenon lamps from the Xenon High-Flux Solar Simulator	55
4.14	Testbed, 270 mm x 200 mm x 30 mm, filled with JSC-1A lunar simulant. . .	55
4.15	Automatic powder feeder	56
4.16	Sketch of electronic components used to automate the powder feeder	57
4.17	Testbed mounted on the 3-axis table in the solar oven (a) and the 3-axis table used in the solar simulator (b).	58
4.18	Mirrors reflecting the concentrated sunlight (a) and Xenon light (b).	59

4.19	Extractor hood in the solar simulator.	60
4.20	Solar oven shutter and solar simulator water-cooled wall.	61
4.21	Pyrometer and infra-red camera	62
4.22	CAD drawing of the set-up	63
4.23	Solar oven in operation.	63
4.24	Complete device set up in the solar oven.	64
4.25	Complete device set up in the solar simulator.	64
5.1	Modelled concentrated solar beam from the measured energy provided by two Xenon lamps.	65
5.2	Two lines sintered continuously.	66
5.3	Typical sintered regolith part after a too slow sweeping of the concentrated solar beam over the surface.	66
5.4	Acceptable planar sintering of JSC-2A lunar regolith simulant.	67
5.5	Typical sintered plane of JSC-2A lunar regolith simulant where sintered lines are too close to each other.	67
5.6	Algorithm for 3D printing building elements at the DLR solar simulator.	68
5.7	The slope angle of the powder feeder was fixed to 103°.	69
5.8	First sintered layers using Test 1 parameters.	70
5.9	Sintered object after a 30-minute process using Test 1 parameters.	71
5.10	Sintered object after a 30-minute process using Test 2 parameters.	72
5.11	Stops of several minutes in the process led to the formation of independent objects on top of the previous sintered one.	73
5.12	Bottom and middle sintered parts.	73
5.13	Delamination of successive groups of layers at the edges.	73
5.14	Sintered object after a process of 3 hours and 45 minutes using Test 3 parameters	75
5.15	Brick obtained using Test 3 parameters.	75
5.16	Brick obtained using Test 4 parameters.	76
5.17	Brick obtained using Test 4 parameters on its substrate.	77
5.18	Brick obtained using Test 4 parameters without the top layer.	77
5.19	During the sintering process (a) and after a 40-minute process (b).	78
5.20	Solar sintered part after a 5-hour process and Test 6 parameters.	79
5.21	Test 6 sintered part once the side porous ceramic bricks were removed.	80
5.22	Side view and top view of the Test 6 sintered part after polishing.	80
5.23	Substrate configuration for Test 7.	81
5.24	Part 3D printed after 30 minutes.	82
5.25	Solar sintered part after a 2-hour process and Test 8 parameters.	83
5.26	Solar sintered part using a zig-zag path for 2h30 and Test 9 parameters.	84
5.27	Solar sintered part using a zig-zag path for 2h30 and Test 10 parameters.	85
5.28	Crucible filled with lunar regolith simulant before and during melting.	86
5.29	Sintered regolith with Test 11 parameters at the end of the process.	87

5.30	Part sintered with Test 11 parameters.	87
5.31	Part sintered with Test 12 parameters.	88
5.32	Molten part detached from the sintered material.	89
5.33	Part sintered with Test 12 parameters.	89
5.34	Part sintered with Test 13 parameters	90
5.35	Part sintered with Test 13 parameters; side view	90
5.36	Part sintered with Test 14 parameters collected out the mould made of porous ceramic bricks.	91
5.37	Part sintered with Test 14 parameters collected out the mould made of porous ceramic bricks.	92
5.38	Part sintered with Test 14 parameters and collected on top of the porous ceramic bricks.	92
5.39	Part sintered with Test 14 parameters and collected on top of the porous ceramic bricks. Other views.	93
5.40	Location of the sintered regolith parts collected in the mould and on top of the surrounding porous ceramic bricks.	93
5.41	3D printed triangle.	94
6.1	Typical experimental IR picture during a solar 3D printing process.	97
6.2	Flux density provided by two xenon lamps.	98
6.3	Model 1 used for heat transfer simulation.	99
6.4	Model 2 used for heat transfer simulation.	99
6.5	Specific heat capacity of lunar regolith.	102
6.6	Thermal conductivity of lunar regolith.	103
6.7	Cross-section in the middle of the model brick.	104
6.8	Simulated temperature profile at the centre of the model 1.	104
6.9	Measured specific heat capacity of sintered JSC-2A.	105
6.10	Measured thermal conductivity of sintered JSC-2A.	106
6.11	Locations of the read temperature on the studied brick. The naming is used afterwards in this work.	106
6.12	Simulated temperature evolution at the centre of the brick.	107
6.13	Simulated temperature evolution at the centre of a small brick.	108
6.14	Temperature variation over 5 minutes for two brick sizes.	108
6.15	Temperature profile along the width and the length of the brick.	109
6.16	Surface temperatures for the brick 3D-printed without and with a preheated contour.	109
7.1	Thermally induced bending of the samples on their porous substrates after solar sintering JSC-2A using Test 4 parameters.	111
7.2	Porous ceramic brick.	112
7.3	Brick sintered on a porous ceramic substrate	112
7.4	Thermal stresses breaking the porous ceramic substrate.	113

7.5	Fibrous ceramic substrate.	113
7.6	Aluminium plate coated with high temperature resistance glue.	113
7.7	Zirconia base and alumina base ceramic filters.	114
7.8	3D printed triangle, half sphere, and S-shape parts.	114
7.9	JSC-1A traditionally sintered under vacuum at 1125°C for three hours.	116
7.10	Cut solar sintered samples after being coated.	117
7.11	Solar sintered sample broken after undergoing a compressive stress by an uniaxial testing machine PEZ 1595.	118
7.12	Young's Modulus and Compressive Strength of solar 3D printed regolith.	118
7.13	Cross section of solar sintered regolith simulant.	119
7.14	Cross section model of solar sintered regolith simulant.	120
7.15	Top view of a sintered part split along the XY plane.	120
7.16	Optical microscopic pictures of a cross-section of solar sintered regolith	121
7.17	Tomography of a solar sintered sample with Test 14 parameters.	122
7.18	Tomography of a solar sintered sample with Test 11 and 12 parameters.	123
7.19	Tomography of a solar and molten sintered samples.	124
7.20	Tomography of a solar sintered JSC-2A at 48 mm/s with a contour sintered at 38 mm/s (Test 3).	124
7.21	Embedded cut solar 3D printed sample.	125
7.22	SEM Secondary electron image of the cross section of a solar sintered sample.	125
7.23	Joined SEM back-scattered electron images of the cross section of a solar sintered sample.	126
7.24	High magnification of a back-scattered electron images of the cross section of a solar sintered sample.	127
7.25	Different scenarios of grain-to-surface bonding according to the delivered solar flux density.	129
7.26	Contact angle of wetting and non-wetting of the solid surface by a drop a liquid.	131
7.27	Back-scattered images of as-received and solar sintered JSC-2A.	132
8.1	Deposition and solar sintering of one layer of sand.	135
8.2	Solar sintered block of sand.	136
8.3	CAD drawing of the modified set-up, not using a mirror.	137
8.4	CAD drawing of the modified set-up, using infra-red lamps for keeping the sintered part at high temperature.	138
8.5	Average percent dose reduction per unit areal density (g.cm^{-2}) for various materials.	142
8.6	Dose estimate inside the lunar shelter as function of aluminum and regolith shield thickness	142
8.7	Scenario 1	145
8.8	Scenario 2	146

List of Tables

1.1	Regolith composition in wt.% of Apollo samples.	4
1.2	Principal lunar minerals.	5
1.3	Composition of Lunar Simulants in wt.%.	9
2.1	Monodisperse glass beads sintering trials. Rough description of the results is written for each time and temperature tested.	15
2.2	Bidisperse glass beads sintering trials at 700°C. Rough description of the results is written for each time and temperature tested.	16
2.3	Envelope density, skeletal density and relative density of three binary mixtures sintered at 700°C for 35 minutes. \hat{X}_B represents the small beads fraction.	17
2.4	Correlated equation to each sintered binary mixture	18
2.5	Polydisperse glass beads sintering trials at 700°C. Rough description of the results is written for each sintering time tested.	20
3.1	Skeletal density of lunar soil and simulants	27
3.2	Sintering temperature of each simulant and sample density after sintering.	30
3.3	New sintering parameters and density of sintered FJS-1. The first set of chosen parameters is shown as a reference. When more than one sample was sintered, the mean value of the density is shown.	30
3.4	Density and porosity of powders, sintered JSC-1A +10wt% ilmenite coarse powder and JSC-1A +10wt% ilmenite fine powder	36
3.5	Roundness and Sphericity of lunar regolith.	37
3.6	Roundness and Sphericity of lunar simulants.	39
3.7	Roundness and Sphericity of JSC-2A lunar simulant, before and after milling.	41
3.8	Table summarising the pros and cons of each lunar simulant.	42
5.1	Recap chart of sintering parameters of JSC-2A.	69
5.2	Recap table of performed solar sintering tests.	96

Introduction

A rediscovered passion for the Moon dawns little by little in the scientific and engineering community. The concept of a Moon village, supported by ESA Director General Johann Wörner, is currently motivating the young generations to work in this direction so that mankind could step on the lunar surface again. A return to the Moon will however not be for short duration missions, as the ones from the Apollo programme, but with the building of an international settlement where astronauts could work on one-year missions. They will perform various scientific experiments as it is currently the case in the International Space Station (ISS). Such lunar exploration programme is expensive and having habitats for the crew that stay safe over time remains an issue. It is now the role of space agencies and scientists to respond at their best to the technological challenges.

In-Situ Resource Utilisation (ISRU) has become in the last decade a prominent approach for the construction of a Moon village. The use of local resources to reduce up-mass, cost and risk of mission is now an essential consideration in future exploration scenarios. One aspect of ISRU is the oxygen production. The extraction of this vital element out the lunar soil could be used as rocket fuel or for creating a breathable atmosphere in the lunar habitats. Another aspect of ISRU is the use of lunar soil as a construction material for roads, launchpads or habitat shelters. The lunar environment is indeed hostile, the lack of magnetosphere and atmosphere makes the lunar surface a front line to space radiation and meteoritic bombardment. Hence, each habitat needs to be sheltered to protect the explorers. Shelters on the Moon will not be constructed as on Earth. Lunar constructions should be done by robots, before the arrival of astronauts, without scaffolds. Consequently, it is necessary to use a flexible technology that can fully be automated with robots.

Additive Manufacturing (AM), or 3D printing, is a good candidate to play a key role in the establishment of a lunar base. This technology builds parts layer-by-layer, allowing the manufacturing of complex shapes without post-processing. On Earth, this technology is used more and more in the automotive and aerospace industries. As for the Moon, several 3D printing technologies already exist to turn the sandy lunar material into a solid structure. The D-shape approach [1] mixes a binder with lunar simulant. The mixture is then distributed layer-by-layer by a printer head mounted on a XYZ stage. The contour crafting [2] uses the same principle replacing the binder by cement. Both technologies showed proof of concept but they are still relying on a terrestrial shipments to receive their respective binders. Other approaches only use lunar regolith. Combining additive manufacturing with a sintering or melting process, it is therefore possible to bond lunar soil grains together into a solid mass. Laser additive manufacturing [3, 4] showed prominent results but the μm -resolution of the machines is not suitable for 3D printing several cubic meters of lunar soil to protect an habitat. Several concepts use microwave for sintering large surfaces of regolith layer-by-layer. This technology has however never shown any significant proof of concept: the thermal runaway and the high sensitivity of the process to the lunar

composition remained, up to now, an issue [5].

In this project we develop a solar additive manufacturing process of lunar regolith. To begin with, the research work focused on understanding the sintering mechanisms using glass beads and existing lunar simulants for carrying out traditional sintering experiments in ovens. Then a simulant was picked to carry out a set of solar 3D printing experiments having in mind a potential direct application to the Moon. Developing such additive manufacturing technology could provide a solution for sintering the large quantities of lunar soil required for a road or the outer shell of an habitat. Some heat transfer simulations were carried out to understand further the process. Sintered materials were then characterised and ways of improving the process were described at micro- and macroscale. Finally, an assessment of the cost and possible other extraterrestrial applications were also treated at the end of this work.

1 Additive Manufacturing of Lunar Regolith

1.1 Lunar soil

The Moon was formed 4.51 billion years ago after a Mars-size planetary body collided with the Earth. 500 millions years after, the Moon underwent a heavy bombardment, activating volcanism that only ended 1 billion years ago: the basalt ejections stopped when the Moon started cooling down. Ever since, the continuous bombardment of meteoroids transformed the lunar soil into a sandy material with irregular shape grains. Today, the lunar surface is composed of broken rocks, soil and dust. Fine particles, within a range from 10 μm to a couple of millimetres, are commonly called regolith [6]. The regolith is composed of minerals, chemical compounds occurring naturally. The knowledge of these minerals comes from the different satellite missions (Clementine, Lunar Reconnaissance Orbiter (LRO)) and samples brought back to Earth from the Luna and Apollo missions. Looking at the Moon, two zones are visible to the naked eyes: the dark regions, called maria and the light-coloured, the highlands. This colour difference is mainly due to a variation in the regolith composition as shown in Figure 1.1. All the main minerals present in the lunar soil are listed in Table 1.1 in normative mineralogy (e.g., wt.% Ca is expressed as wt.% CaO). It can be noticed that the regolith composition varies according to the location on the Moon's surface even in a same zone.

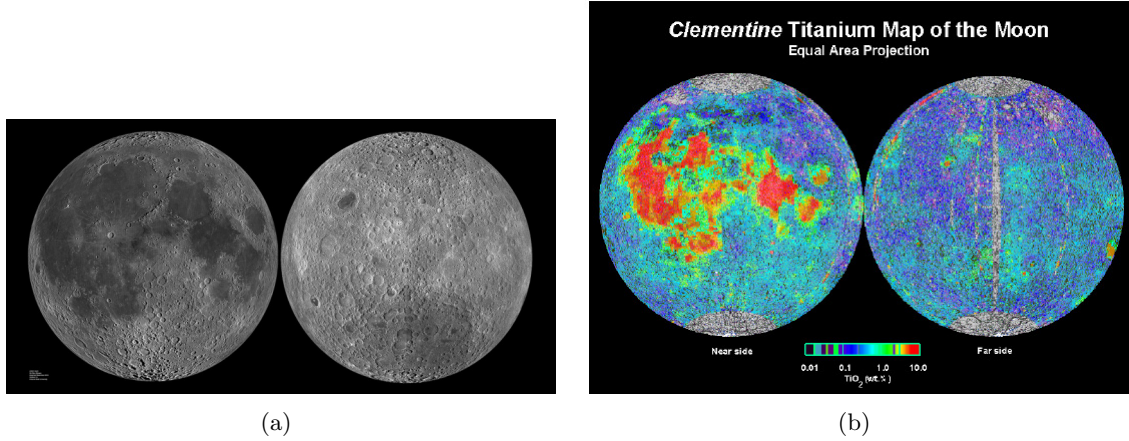


Figure 1.1: (a) The two sides of the Moon from the LRO (left: the near side, right: the far side); the darker areas are known as the Maria whereas the brighter ones are called Highlands. (b) Image derived from the Clementine global colour data showing the concentration of titanium on the lunar surface [7].

Table 1.1: Regolith composition in wt.% of Apollo samples (Average of all mission samples) [8].

Apollo Mission	Place	Type	SiO ₂	TiO ₂	Al ₂ O ₃	Cr ₂ O ₃	Fe ₂ O ₃	FeO	MnO	MgO	CaO	Na ₂ O	K ₂ O	P ₂ O ₅	S
A11	Mare Tranquillitatis	Mare	42.20	7.80	13.60	0.30	/	15.30	0.20	7.80	11.90	0.47	0.16	0.05	0.12
A12	Oceanus Procellarum	Low-Ti Mare	46.30	3.00	12.90	0.34	/	15.10	0.22	9.30	10.70	0.54	0.31	0.40	/
A14	Oceanus Procellarum	Low-Ti Mare	48.10	1.70	17.40	0.23	/	10.40	0.14	9.40	10.80	0.70	0.55	0.51	/
A15	Eratosthenes	Low-Ti Mare	46.80	1.40	14.60	0.36	/	14.30	0.19	11.50	10.80	0.39	0.21	0.18	0.06
A16	Ptolemaeus Border Mare	Highlands	45.00	0.54	27.30	0.33	/	5.10	0.30	5.70	15.70	0.46	0.17	0.11	0.07
A17	Serenitatis /Tranquillitatis	Low-Ti Mare	43,20	4,20	17.10	0.33	/	12.20	0.17	10.50	11.80	0.40	0.13	0.12	0.09

The normative mineralogy can however be misleading to people not familiar with the lunar minerals. Although the SiO_2 content is about 45 wt.% all over the lunar surface, it is likely that there is not a single quartz crystal on the Moon [6]. The lunar soil is indeed made of different complex minerals. Table 1.2 lists the lunar minerals with their group, chemical composition and relative abundance on the Moon. In practice, it is not always possible to identify a mineral from another one of the same group. When this case occurs, only the group of the mineral is mentioned.

Table 1.2: Principal lunar minerals [9]. Typical relative abundance, A-abundant, M-major, m-minor, t-trace.

Group	Mineral	Composition	Abundance
Plagioclase	Anorthite	$\text{CaAl}_2\text{Si}_2\text{O}_8$	A
	Bytownite	$(\text{Ca},\text{Na})(\text{Si},\text{Al})_4\text{O}_8$	M
	Labradorite	$(\text{Ca},\text{Na})(\text{Si},\text{Al})_4\text{O}_8$	M
Olivine	Fayalite	Fe_2SiO_4	m
	Forsterite	Mg_2SiO_4	M
Pyroxene	Clinoenstatite	$\text{Mg}_2[\text{Si}_2\text{O}_6]$	M
	Pigeonite	$(\text{Mg},\text{Fe},\text{Ca})_2[\text{Si}_2\text{O}_6]$	M
	Hedenbergite	$\text{CaFe}[\text{Si}_2\text{O}_6]$	m
	Augite	$(\text{Ca},\text{Na})(\text{Mg},\text{Fe},\text{Al},\text{Ti})[(\text{Si},\text{Al})_2\text{O}_6]$	M
	Enstatite	$\text{Mg}_2[\text{Si}_2\text{O}_6]$	A
/	Ilmenite	FeTiO_3	m
Spinel	Spinel	MgAl_2O_4	m
	Hercynite	FeAl_2O_4	m
	Ulvospinel	TiFe_2O_4	m
	Chromite	FeCr_2O_4	m
/	Troilite	FeS	t
Phosphate	Whitlockite	$\text{Ca}_9(\text{Mg},\text{Fe})(\text{PO}_4)_6(\text{PO}_3\text{OH})$	t
	Apatite	$\text{Ca}_5(\text{PO}_4)_3(\text{OH},\text{F},\text{Cl})$	t
/	Native Iron	Fe	t

1.2 In-situ resource utilisation

ISRU has a predominant role in any future exploration scenario. The use of local resources, such as the lunar regolith and the sunlight, reduces up-mass, cost and overall risk of mission. ISRU covers several aspects from the oxygen production to the construction of road and shelters for a lunar base.

The extraction of oxygen from lunar regolith is a crucial point. The regolith is composed of 43 wt.% oxygen that could be used as rocket propellant or to produce a breathable atmosphere for the crew in the habitats. Various studies exist, the main ones use hydrogen as a reducing agent which is then recycled [10, 11, 12, 13]. The hydrogen reduction process is however more efficient using pure ilmenite, an iron-titanium rich lunar mineral [14]. Other approaches have also been studied, such as the oxygen extraction by fluorination [15] or by pyrolysis [16, 17].

This project focuses on the construction aspect of ISRU. Several works have extensively covered the topic, all recent concepts of habitats and lunar bases using regolith as an essential construction material [18, 19, 20, 21, 2, 1]. Various ways exist to turn lunar regolith into a solid body: by melting [22, 23, 18, 24], by mixing it with a binder or a reactive compound [25, 26, 27, 28, 29, 30] or by sintering [31, 32, 33, 4, 34, 35, 36]. Applied to the regolith, a sintering process can create solid building elements without the use of any kind of glue or binder. The construction of a Moon village will most likely be done by robots, not by astronauts piling up bricks. New sintering approaches are therefore open for space applications.

Additive Manufacturing, or 3D-printing has been the most prominent approach for any lunar construction for the last 15 years. This manufacturing technique, building parts from the bottom up and layer-by-layer, gives a lot of flexibility, essential for facing potential issues in the harsh space environment. Several research works were carried out on this topic [1, 21, 2, 37, 38, 39]. In 2013, the ESA - European Space Research and Technology Centre (ESTEC) conducted a study about building a lunar base on the Moon, as shown in Figure 1.2, by means of the 3D-printing technology, mixing lunar regolith with a binder [1].

Research works on AM solely using lunar regolith proved the feasibility of Selective Laser Melting (SLM) [3, 4] for producing small sintered parts, as shown Figure 1.3. As for microwave sintering for additive manufacturing, it is often mentioned in publications [2] but no large scale proof of concept was ever made.

An issue working with processes using lunar regolith comes from a lack of true regolith (less than 400kg returned from Apollo missions). The scientific community is then obliged to use models of soil, or simulants, created from Earth basalt rocks in order to obtain results with a direct application to the Moon [34, 3, 33, 26].

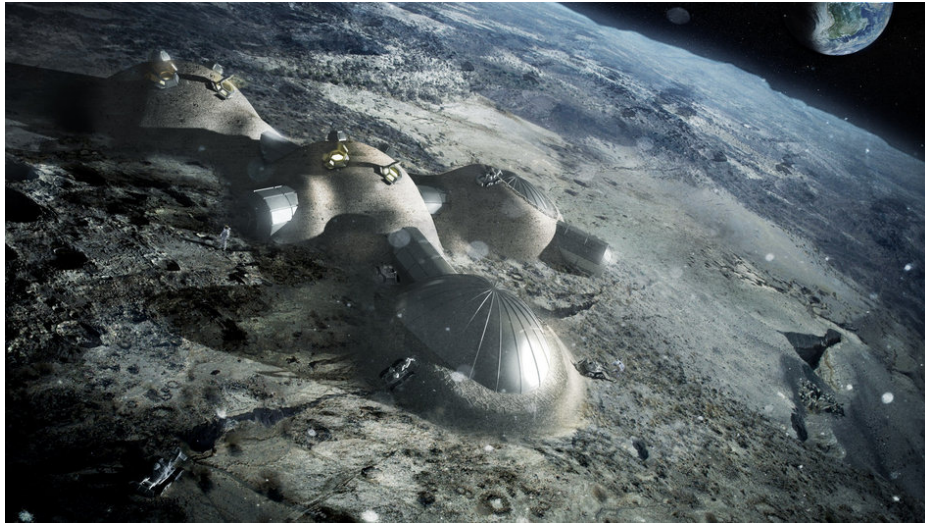


Figure 1.2: 3D printed lunar base, *credit: Foster + Partners*



Figure 1.3: Laser 3D printed lunar regolith simulant, [4]

1.3 Lunar soil simulants

Lunar simulants mimic several aspects of the lunar soil but not all of them, a simulant shall therefore be produced and used only for a defined purpose [40]. A list of existing lunar simulant is shown Table 1.3. Most of them are by-products of quarries, post-processed to get some extra features of the lunar regolith such as the grain size or shape. Other simulants, such as JSC-2A and NU-LHT-3M, are completely artificial: the required compounds are mixed and molten together before a machine creates the grains out of a glass stream. A control cooling of the melt allows them to get the different lunar minerals [41].

The main lunar simulants that have already been used in the literature are listed below:

JSC-1A: This is a low-Ti Mare lunar simulant with a glass content over 50 wt.%. The raw material, from a volcano in Arizona, is dried and milled in order to obtain a grain distribution close to Apollo samples. Originally produced and sold by Orbitech from a

NASA request after the scarcity of JSC-1 [42] in 2005, this simulant has been the major one used in the last 10 years. JSC-1A lunar simulant has been characterised multiple times extensively studied worldwide [43, 44, 45, 46, 47, 48, 49, 50]. It was replaced by JSC-2A in 2013, an artificial lunar simulant with the exact same composition as JSC-1A according to the material data sheet. It is produced by the American company Zybek Advanced Products (ZAP).

DNA-1: This low-Ti Mare simulant is the only European one available up to now. DNA simulant is a volcanic ash coming from a quarry situated nearby Bolsena lake, in Italy. This simulant was originally only used in the ESTEC study about 3D-printing on the Moon mentioned before [1].

FJS-1: FJS-1 is another low-Ti Mare simulant coming from mount Fuji in Japan. Shibaura company produces it on request.

NU-LHT-1: One of the few Highlands simulants produced by NASA. Few information is available about this simulant. It has been replaced artificially by NU-LHT-3M, also produced by ZAP.

MLS-1: This is the only High-Ti Mare simulant produced and commercially available in the 90s. It is one of the first simulant commercially available but its stock has been now depleted for years.

To compensate the scarcity of High-Ti Mare simulant, ilmenite (FeTiO_3), main source of titanium in the lunar soil, could be added to a low-Ti Mare JSC-1A-like simulant.

Table 1.3: Composition of Lunar Simulants in wt. %.

Regolith Simulants	Type	SiO ₂	TiO ₂	Al ₂ O ₃	Fe ₂ O ₃	FeO	MnO	MgO	CaO	Na ₂ O	K ₂ O	P ₂ O ₅	References
MLS-1	Mare	42.80	6.77	12.10	2.60	13.40	0.22	6.19	11.10	2.22	0.20	0.04	[51]
JSC-1	Low Ti Mare	47.71	1.59	15.02	3.44	7.35	0.18	9.01	10.42	2.70	0.82	0.66	[52]
JSC-1A	Low Ti Mare	46.67	1.71	15.79	3.41	7.57	0.19	9.39	9.90	2.83	0.78	0.71	[48]
JSC-2A	Low Ti Mare	46.67	1.71	15.79	3.41	7.57	0.19	9.39	9.90	2.83	0.78	0.71	[48]
DNA-1	Low Ti Mare	41.90	1.31	16.02	14.60	/	0.21	6.34	12.90	2.66	2.53	0.34	[1]
ALS	Low Ti Mare	42.36	2.73	13.48	12.55	/	0.18	10.23	8.61	3.29	1.49	0.53	/
ASL	Low Ti Mare	49.00	2.40	14.75	3.25	9.75	0.23	5.40	9.30	2.85	1.00	/	/
BP -1	Low Ti Mare	47.20	2.30	16.70	5.90	6.20	0.21	6.50	9.20	3.50	1.10	0.52	[53]
CAS-1	Low Ti Mare	49.24	1.91	15.80	11.47		0.14	8.72	7.25	3.08	1.03	0.30	[54]
FJS-1	Low Ti Mare	49.14	1.91	16.23	13.07		0.19	3.84	9.13	2.75	1.01	0.44	[54]
MKS-1	Low Ti Mare	52.69	1.01	15.91	12.28		0.22	5.41	9.36	1.90	0.58	0.14	[54]
MLS-2	Highlands	48.30	0.03	32.40	0.45		/	0.15	16.00	2.42	0.06	/	[55]
NU-LHT-1	Highlands	44.20	0.32	27.90	4.22		0.09	7.92	12.50	1.32	0.09	/	[55]
OB-1	Highlands	48.28	0.05	32.01	0.09	1.34	0.01	0.22	15.43	2.38	0.16	0.01	[56]
Claudia	High-Ca-plagioclase	62.00	21.50	0.40	1.20		/	8.0	5.70	0.40	/	/	[55]
Hap	High-Ca-plagioclase	48.80	30.10	2.30	0.40		/	14.90	2.60	0.20	/	/	[55]

2 Packing and sintering of simple and complex granular media

The sintering of powders has been widely studied over the last decades [57, 58, 59, 60, 61]. Lunar regolith is, however, a complex powder with irregular particle shapes and sizes. The preparation of samples with such powder could lead to different packing fraction. The role played by the starting packing fraction in the density level of the sintered end product needs therefore to be better quantified before sintering lunar regolith simulants. This chapter aims at understanding the packing role while sintering well-defined mono-, bi- and poly-dispersed glass beads.

2.1 Basic principles

Granular matter refers to any aggregation of macroscopic particles, large enough to show no thermodynamic motion. It includes a broad range of materials, from everyday-life products such as beach sand, corn grains or table salt, to more technical or unusual powders like selective laser melting (SLM) metallic powders or lunar soil. Physics problems related to granular media are numerous: the complex behaviour of the granular matter, similar to a flowing liquid in a dynamic environment or to a solid rock in a static system, are still not fully understood [62].

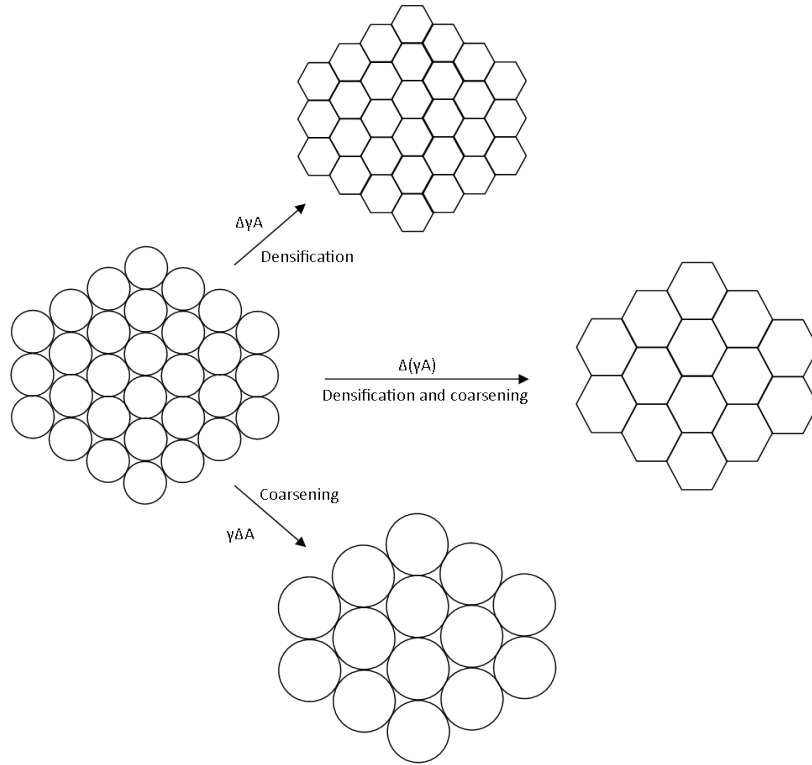


Figure 2.1: Basic definition of the sintering driving force, $\Delta(\gamma A)$. [63]

An aspect that one can study is the packing of a granular media. The packing of a sample, the arrangement of the grains, varies according to the sample preparation and have a clear impact on the granular matter behaviour. A same monodisperse media can be, for instance, loose or solid, with a maximal packing fraction of about 0.64, simply changing the sample preparation. Studying packing properties becomes crucial when granular matter is sintered together.

Sintering is a process for bonding grains until forming a solid mass, applying heat without reaching the liquefaction point of the material [63, 64, 57, 58]. For solid-state sintering, heated dense granular packing tends towards a reduction of the total interfacial energy. This driving force, noted $\Delta(\gamma A)$, is the sum of the change in total surface area ΔA , coming from the matter reorganisation and the increasing of the average grain size, also called coarsening, with the change in specific interfacial energy $\Delta(\gamma)$, where the atomic diffusion densifies the material, reducing the pore content [63]. Figure 2.1 shows the reduction of the total interfacial energy of a packing.

On a smaller scale the atomic diffusion processes, responsible for the interfacial energy reduction and the coarsening of the grains, drag along several matter transport mechanisms. The formation of a neck, between two particles in contact is the first step towards the merging of the particles. This neck is formed by diffusion from the surface, the volume, the grain boundaries and the displacement of dislocations. Some matter can also evaporate and condensate at the neck. Figure 2.2 presents the mentioned mechanisms.

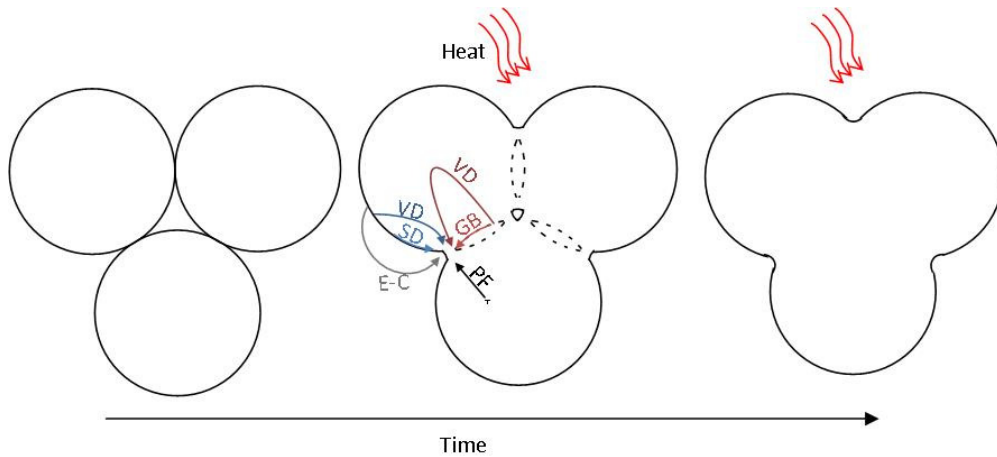


Figure 2.2: Sintering steps from left to right: Three modelled grains are in contact, then the atomic diffusion processes, starting from the grain boundary and the surface, create necks and a closed pore between the sintered grains. In the end, the pore can be removed and the sintered grains formed one solid body. Diffusion mechanisms: SD - Surface diffusion, VD - Volume diffusion, E-C - Evaporation-Condensation, GB - Grain boundary diffusion, PF - Plastic flow from dislocations.

Liquid Phase Sintering (LPS) is also possible for bonding different grain-shape materials together. This process uses the melt of the material with the lowest melting point for wetting and joining the other grains together.

2.2 Bi-disperse granular media

For bi-disperse granular media, the packing behaviour is even more dependent on the preparation and the homogeneity of the grains mixture. A previous work has investigated this topic [65], examining the correlation between mixture ratio and packing fraction in green body soda-lime glass bead granular mixtures. Figure 2.3 shows the packing fraction of bi-disperse mixtures with different proportions of beads A and beads B, and different size ratio between the bigger beads and the smaller beads.

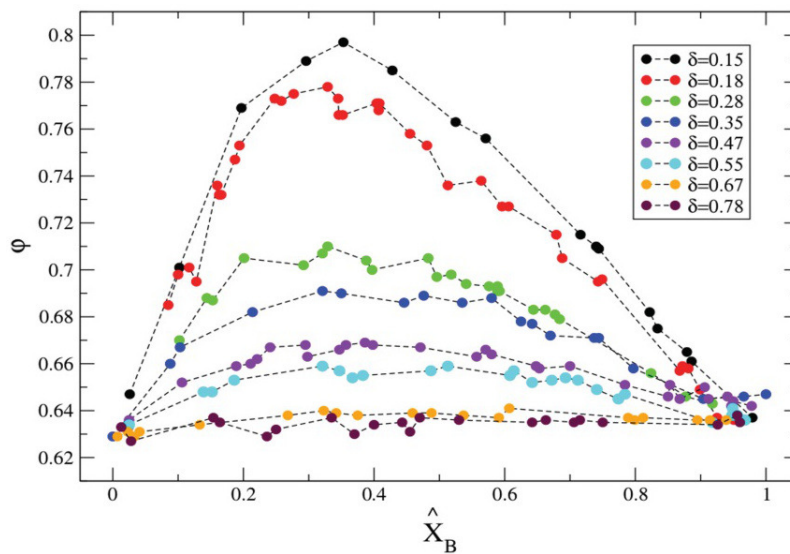


Figure 2.3: Bi-disperse mixtures and their packing fraction φ . \hat{X}_B represents the mass proportion of small beads B. δ is the size ratio between big and small beads. The glass bead mixture with a size ratio of 0.15 gives the highest packing fraction 0.80, with a mixture ratio of 0.35 [65].

Sintering similar granular packings becomes therefore interesting to assess the impact of the original packing on the sintering process efficiency. The first step was to reproduce a homogenised bi-dispersed mixtures. Using a mixing device, designed by Frank-Richter S. [65] and shown in Figure 2.4, granular binary mixtures were prepared inside alumina crucibles that can handle high temperature for directly sintering the soda-lime glass beads afterwards. Beads A and B were placed respectively in two different funnels on top of the device. The two flows of beads joined into a helicoidal funnel and a balanced mixture came out into the sample container. A power supply provided energy to a vibration motor which prevented the set-up from jamming. Tapping the samples was at the end required for densifying the packing.

The prepared binary mixtures were sintered with a size ratio of 0.15 and three different mixing ratio: 0.11, 0.35 and 0.72. These mixing ratio corresponds to three interesting points on the graph, Figure 2.3. The mixing ratio 0.35 leads indeed to the highest packing fraction, 0.8, and the excess of big beads and small beads, respectively for the ratio $\hat{X}_B = 0.11$ and

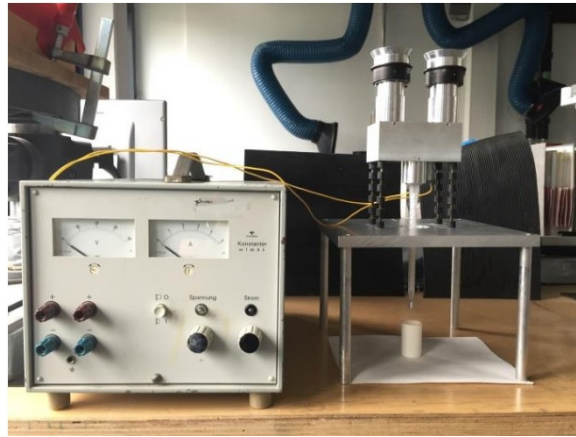


Figure 2.4: Experimental binary mixing apparatus setup and its power supply. Beads A and B are placed respectively in the two funnels on the top right corner.

$\hat{X}_B = 0.72$, gives both a similar packing fraction about 0.7. Soda-lime glass beads of 90 μm and 615 μm were used for respecting the size ratio of 0.15.

First sintering experiments were however performed with monodisperse granular samples, easier to prepare. Soda-lime glass beads of 615 μm were sintered at different times and temperatures in order to estimate the sintering parameters of the bidisperse mixtures. Table 2.1 summarises the trial parameters. The targeted end product was a sintered sample, without visible melting of the beads as shown Figure 2.5 by optical microscope.

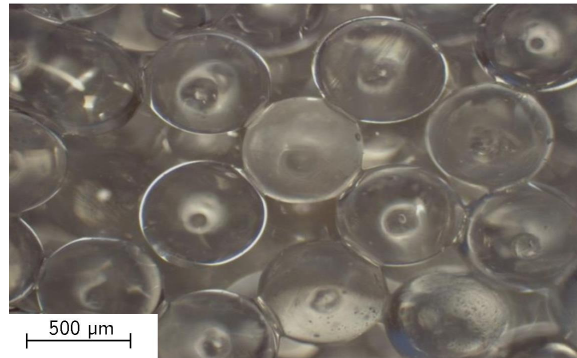


Figure 2.5: Optical microscopic image of monodisperse 615 μm beads sintered at 700°C for 90 minutes. The neck formation between the glass beads is clearly visible at the contact point.

From the table, it can be concluded that 700°C yields best results for glass bead sintering due to the large time range of successful sintering results. The 700°C temperature gives to the granular samples a longer period of time to sinter, thus leading to various densification levels that can be measured. Based on the observed results a sintering temperature of 700°C was therefore chosen for the bidisperse glass bead mixtures. New sintering trials at 700°C, listed in Table 2.2, were therefore performed with three binary mixtures in order to see the possible time range allowing the bonding of the beads. Figure 2.6 shows pictures taken at

the optical microscope of the sintered binary mixtures.

Table 2.1: Monodisperse glass beads sintering trials. Rough description of the results is written for each time and temperature tested.

Temperature (°C)	Time (min)	Result
700	5	Unsuccessful Sintering
700	10	Unsuccessful Sintering
700	15	Unsuccessful Sintering
700	30	Successful Sintering
700	45	Successful Sintering
700	50	Successful Sintering
700	55	Successful Sintering
700	60	Successful Sintering
700	75	Successful Sintering
700	90	Successful Sintering
800	5	Unsuccessful Sintering
800	10	Successful Sintering
800	15	Successful Sintering
800	30	Molten Sample
800	45	Molten Sample
800	60	Molten Sample
900	5	Successful Sintering
900	10	Molten Sample
900	15	Molten Sample
900	30	Molten Sample
900	45	Molten Sample
900	60	Molten Sample

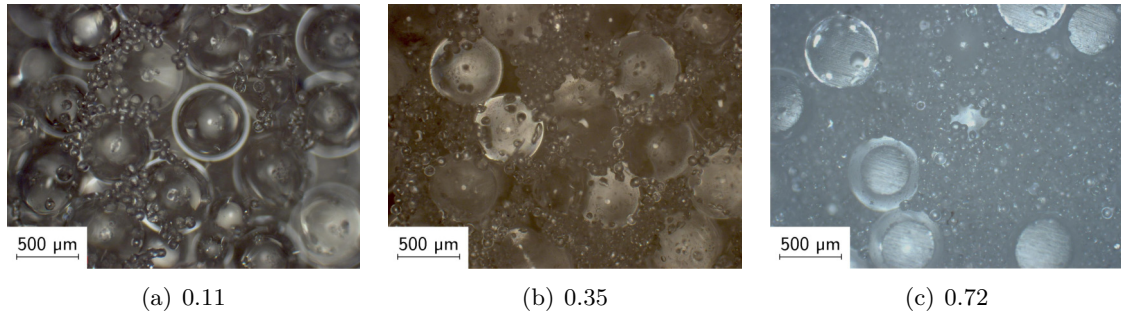


Figure 2.6: Optical images bidisperse granular matter with a size ratio of 0.15 sintered at 700°C for 55 minutes. The exposed mixing ratio are 0.11, 0.35 and 0.72. Even using the mixing apparatus, the binary mixtures are not perfect, the small beads not being present in all the pores formed between the big beads in contact.

For the 0.11 mixture, the small beads do not seem homogeneously distributed and form clusters. Even with the mixing device, a perfect homogeneous distribution was not achievable with a size ratio of 0.15. The quality of the sintered binary samples was however much lower without using the mixing device. Once the binary mixtures sintered, the envelope

Table 2.2: Bidisperse glass beads sintering trials at 700°C. Rough description of the results is written for each time and temperature tested.

Mixing ratio	Time (min)	Result
0.11	35	Successful Sintering
0.11	45	Successful Sintering
0.11	50	Successful Sintering
0.11	55	Successful Sintering
0.11	60	Sintered/Molten
0.11	75	Molten Sample
0.11	90	Molten Sample
0.35	35	Successful Sintering
0.35	45	Successful Sintering
0.35	50	Successful Sintering
0.35	55	Successful Sintering
0.35	60	Successful Sintering
0.35	75	Molten Sample
0.35	90	Molten Sample
0.72	35	Successful Sintering
0.72	45	Successful Sintering
0.72	50	Successful Sintering
0.72	55	Successful Sintering
0.72	60	Successful Sintering
0.72	75	Molten Sample
0.72	90	Molten Sample

density of the samples were measured using an envelope density analyser, Figure 2.7(a). This device measures first an operator-defined volume of a fine powder placed in a tube, compacting it with a piston. Then, the sample is placed in the same tube and surrounded by the powder which fits closely to the sample. The whole volume is measured again and the volume difference is the envelope of the sintered sample. Measuring precisely the mass of the sample beforehand, the envelope density is simply the mass over the volume.

Knowing the sample's envelope density is nonetheless not enough for determining the relative density of the sample, the skeletal density of the glass beads needs to be also measured. In a gas pycnometer, Figure 2.7(b), few milligrams of glass beads are placed in a chamber which has a volume well-defined by the machine. The crucible is then closed and some Helium fills the chamber up to certain pressure. Once there is equilibrium, the gas contained inside the chamber is released into a second chamber, with the same defined volume as the first one, but totally empty. At equilibrium, the pressure is measured again and linked to the volume of the sample which was inside the first chamber. With the mass and the volume, the density can be measured. This density corresponds to a packing fraction maximum of 1, assessing that no close pores are inside the raw beads before sintering and that no material is lost (sublimation) or gained (oxidation) during the sintering process. A skeletal density of $d_{1.00} = 2.48 \text{ g.cm}^{-3}$ was hence found for the raw soda-lime glass beads.

Using the measured envelope density for each sintered sample and the envelope density



Figure 2.7: Micromeritics Geopyc 1360 envelope density analyser (a) and Accupyc 1360 skeletal density analyser (b).

of the raw glass beads, a relative density of the sintered samples could be determined, by the relation (1).

$$d_{rel} = \frac{d_{env}}{d_{1.00}} \quad (1)$$

where

d_{rel} : Relative density

d_{env} : Envelope density

$d_{1.00}$: Skeletal density

The results from the shortest sintering process, at 700 °C for 35 minutes are listed in Table 2.3. The measured relative density d_{rel} were unexpectedly lower than the original packing fraction φ . After repeating the binary sample's preparation and the sintering process, similar values were found. No mass was also lost by sublimation during the sintering process. This difference was linked to the operator change between the experiments carried out in Frank-Richter's work [65] and the presented ones. The way of tapping the sample seemed to influence significantly the original packing fraction before sintering. Following results are therefore not directly compared with the packing fractions published in Frank-Richter's thesis.

Table 2.3: Envelope density, skeletal density and relative density of three binary mixtures sintered at 700°C for 35 minutes. \hat{X}_B represents the small beads fraction.

\hat{X}_B	d_{env}	$d_{1.00}$	d_{rel}
0.11	1.62	2.48	0.65
0.35	1.75	2.48	0.71
0.72	1.52	2.48	0.61

Binary mixtures were then sintered for longer times, ranging from 40 min to 65 min. Figure 2.8 shows the densification of the sintered binary mixtures. As each sintering process

progressed with time, transport mechanisms on grain surfaces as well as bulk transport between grain contact areas result in a net neck growth, shrinkage and densification. Surface area provides the driving force in sintering: the reduction of free surface energy resulting from a high surface area of initially packed particles [66]. Hence, the binary mixture with the highest small grains content densified faster due to the highest number of contact points between the grains. Table 2.4 shows the slope of the linear fits for the different binary mixtures. The steepest slope corresponds to the binary mixture with the highest small beads fraction.

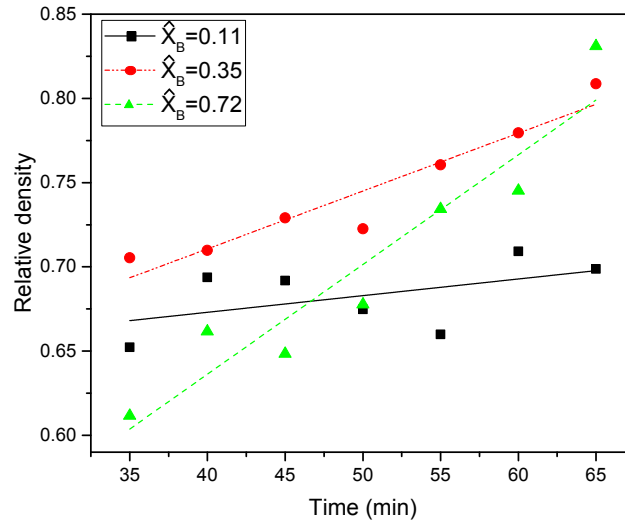


Figure 2.8: Relative density of binary mixtures over sintering time. \hat{X}_B represents the small beads fraction. The dots are the experimental values and the lines are the linear fits.

The surface area could be easily calculated from the number of glass beads and considering the beads as perfect spheres. Using the slope value of the fit curves as a sintering rate for a given binary mixture, it is possible to extrapolate and plot, Figure 2.9, the glass bead sintering rate over the surface area, considering a fix volume and a sintering temperature of 700 °C.

Table 2.4: Correlated equation to each sintered binary mixture

\hat{X}_B	Sintering Rate Equation	R2
0.11	$y = 0.0010x + 0.63$	0.26
0.35	$y = 0.0034x + 0.57$	0.91
0.72	$y = 0.0065x + 0.38$	0.90

The linear behaviour of plotted curve confirmed that the grain-to-grain contacts are a more important feature than the original packing fraction for enhancing the sintering process efficiency.

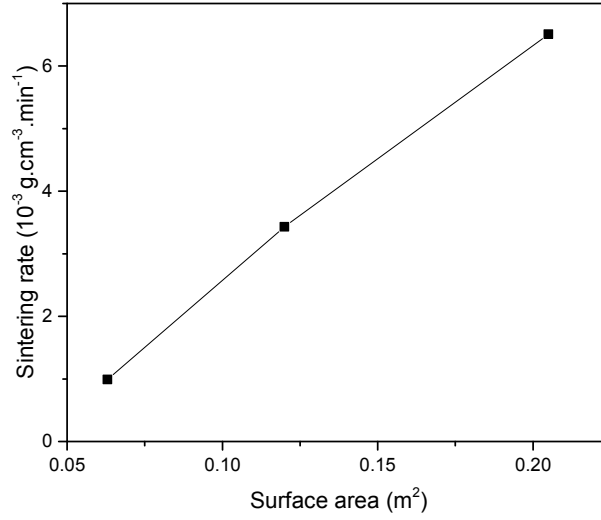


Figure 2.9: Densification rate of glass beads sintered at 700 °C over the surface area of the beads for a same predefined volume.

2.3 Poly-disperse granular media

A bi-disperse model reaches its limit when natural materials are used. On Earth, the erosion by weathering grinds particles and rock fragments, thus leading to the creation of poly-disperse granular media. On the Moon, the weathering does not come from the winds and water flows but from the constant bombardment of micrometeoroids. The result is however similar, the lunar soil being also a poly-disperse material.

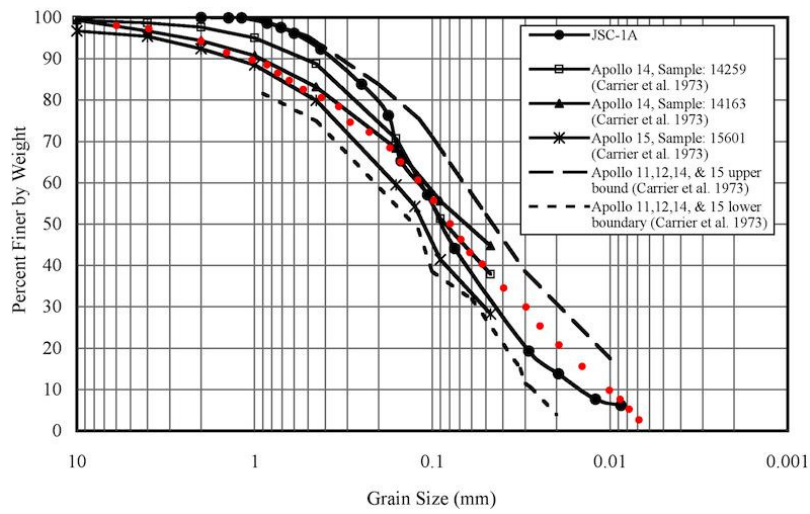


Figure 2.10: Decumulative grain size distribution of lunar regolith [49]. Red dots represent the referenced points for the preparation of the granular mixture by successive sieving.

Before using lunar simulants, a lunar grain size distribution was created out of different glass beads bags. The idea was to have the right mass of different glass bead sizes, following the lunar distribution as shown Figure 2.10. A successive dry sieving was therefore required, using a vibratory sieve shaker. Sieves of upper and lower bounds of a desired grain sizes were stacked on the vibration table and shaken. Each batch was allowed to sieve for five minutes. Once the sieving process was finished, the resulting grains between the upper and lower bound sieves were collected and the correct quantity was added to the lunar distribution. The container was then manually shaken to homogenise the mixture.

The polydisperse glass bead mixture had a noticeably higher sintering rate than the previous mono- and bi-disperse bead mixtures. With this increase in sintering rate, the polydisperse bead mixture was placed into the furnace for a shorter period of time to avoid melting. Results of the tests are shown Table 2.5. Related density measurements are shown in Figure 2.11.

Table 2.5: Polydisperse glass beads sintering trials at 700°C. Rough description of the results is written for each sintering time tested.

Sintering time (min)	Result
25	Successful Sintering
35	Successful Sintering
45	Sintered/Molten
55	Sintered/Molten

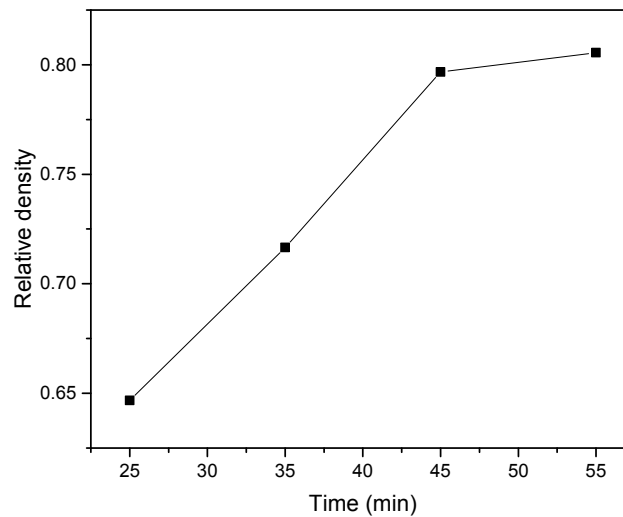


Figure 2.11: Relative density of polydisperse glass beads sintered at 700°C over time.

The relative density reaches a plateau at about 0.8 after sintering 45 minutes. This was due to the concurrent effects of sintering and melting (densification), and the potential

outgassing from the melt which creates new pores. Another hypothesis was the sintering rate reduction when only closed pores remained to be removed: this step was slower than the densification and coarsening happening at the beginning of the process.

Although a similar relative density as the binary mixture can be achieved with the polydisperse one, the sintering rate is faster due to the higher surface area. The small particles, μm -size, can get into the tiniest spaces between two grains and sinter very quickly. However, the smallest particles have the tendency to melt due to the temperature fluctuation in the oven and the trapped heat which could form inside the sample.

Using glass beads, the main features impacting the sintering process were highlighted: sintering is a matter of contact points between the particles constituting the green body. Nevertheless, this model was limited to the sintering of single compound materials and other processes, driven by the compounds chemistry, could happen if several elements, or minerals, were sintered together. Lunar soil is a multi-mineral polydisperse powder. Using JSC-2A lunar soil simulant, it was then possible to observe the effect of minerals on the sintering process. JSC-2A was sintered at 1110°C for a time ranging between 25 and 55 min. Due to the unexpected results of the first trial, two more sample sets were sintered. Figure 2.12 shows the relative density evolution over time. No trend could be noticed and each sample set had a different evolution over time, no linear function could fit as for the sintering of glass beads. The irregular density trend over time could be explained by the inter-mineral reactions and the oxidation of some elements, competing with the densification process. A close-scale study of lunar regolith sintering is developed in chapter 1.

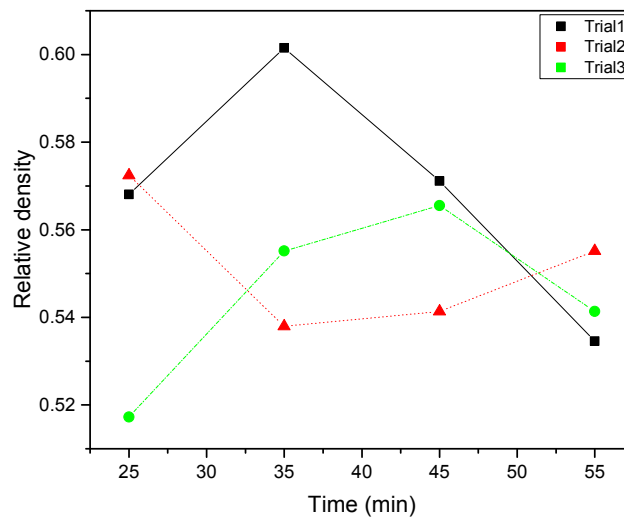


Figure 2.12: Relative density of JSC-2A lunar simulant sintered at 1110°C over time.

One way of limiting the uncontrolled densification is to apply pressure on the samples. Pressing particles together forces them to be in contact, thus improving the sintering, lim-

iting the open porosity to a minimum and starting with a packing fraction closer to 1. Applying 255 MPa on the sample, pressed polydispersed JSC-2A lunar simulant reached a relative density of 0.73 after being sintered for 45 minutes. Pressing also eliminates the original packing disparities as it is shown Figure 2.13 with binary mixtures of JSC-2A lunar simulants. After 45-minute sintering at 1110°C, all pressed samples reached a relative density of about 0.72. An experiment with pressed binary mixture of glass beads would have been more accurate but pressing glass beads was not possible due to the elasticity of the material. Repeating the experiment with pressed binary JSC-2A showed consistent results.

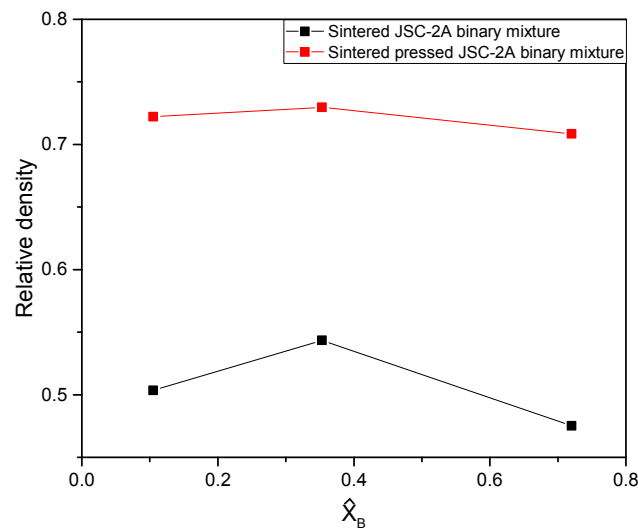


Figure 2.13: Relative density of pressed and unpressed JSC-2A lunar simulant sintered at 1110°C for 45 minutes. \hat{X}_B represents the small beads fraction.

3 Simulants characterisation

Since the beginning of research on ISRU, scientists working on sintering lunar soil chose simulants which mimic several aspects of the actual lunar soil [34, 26, 3, 33] in order to obtain results with a direct application to the Moon. There is however no universal simulant suitable for all applications [40]. That is the reason why, in this work, several preliminary tests were performed to find and use the most suitable simulant for carrying out solar sintering experiments.

Four important aspects of the lunar regolith have been determined:

- Grain size distribution
- Glass content
- Mineral composition
- Grain shape

3.1 Grain size distribution

The grain size distribution influences the overall packing of the bulk powder. Grain-to-grain contacts in the packing are a crucial point for sintering, a process which starts by a neck formation where precisely the grains touch one another, as shown previously in chapter 2. To be relevant for a lunar application, the grain size distribution of the simulant should be in between the range of Apollo samples: a similar compaction of the bulk powder would be then obtained.

A complete grain size distribution analysis of JSC-1A, JSC-2A, DNA, FJS-1 and NU-LHT-3M was carried out by successive sieving. Figure 3.1 shows JSC-1A, FJS-1 and NU-LHT-3M distributions after dry sieving. All simulants, except DNA, have a distribution located in between the Apollo boundaries [67] although the collection of fine particles, $<60\mu\text{m}$, is undervalued using a dry sieving process: charged fine particles do not pass through the sieves by vibrations and gravity. A wet sieving process was not available but a particle size laser diffraction analysis was used for measuring JSC-1A and JSC-2A with a higher accuracy. The as-received DNA simulant has a grain size distribution far from Apollo samples range but a new grain size distribution, close to JSC-1A one, was done by a successive sieving preparation.

In Figure 3.2 are shown the results obtained by particle size laser diffraction. The JSC-1A distribution measured by dry sieving and the curve from the literature [44] are shown for comparison. The distribution given by laser size laser diffraction is more accurate and gives a larger range of particle sizes. The dry sieving gives however a sufficient estimation for controlling if a simulant has a similar granulometry to the actual lunar soil.

Although the grain size distribution of a simulant is a crucial parameter, sieving and ball milling can be easily performed on any simulant thus making the grain size distribution alone not relevant enough to select a simulant.

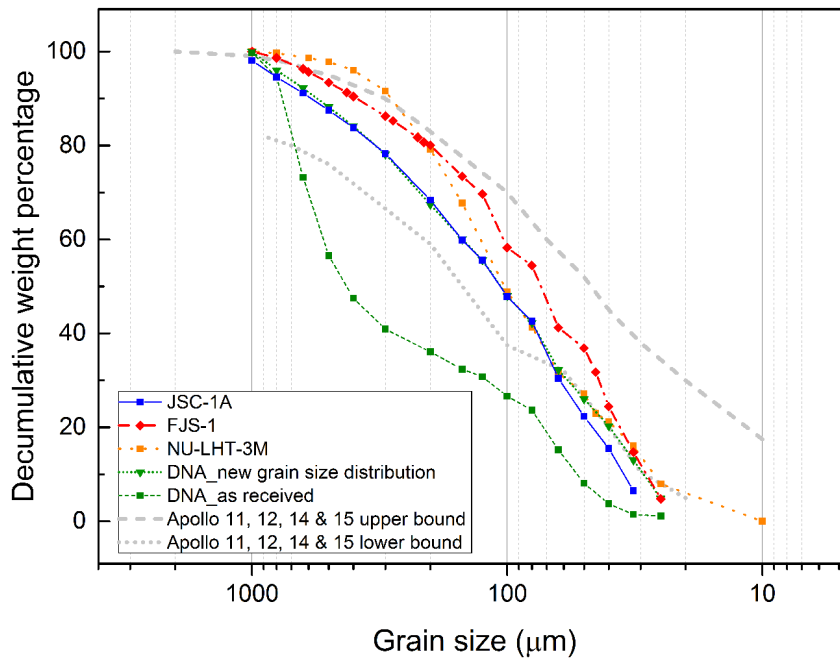


Figure 3.1: Grain size distribution of lunar simulants obtained by a successive sieving process with upper and lower limits of the lunar soil from Apollo returned samples [67].

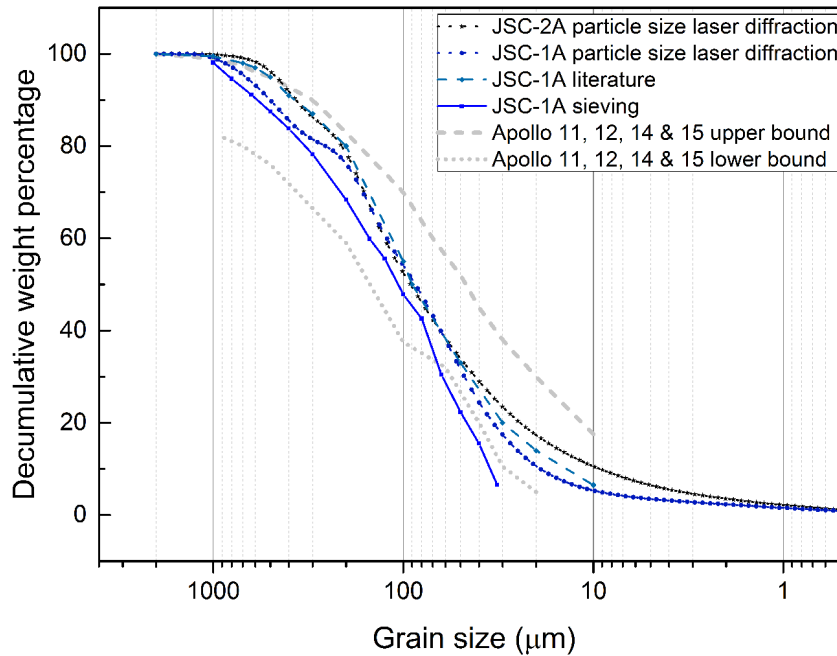


Figure 3.2: Grain size distribution of JSC-1A and JSC-2A obtained by laser diffraction particle size analysers LS 13 320 Beckman Coulter. Data of JSC-1A grain size distribution obtained in the literature [44] and by dry sieving are shown for comparison. Upper and lower limits of the lunar soil from Apollo returned samples come from the Lunar Sourcebook [67].

3.2 Glass content

Another important aspect is the glass content of the lunar simulant. On the Moon, due to micro-meteorite bombardment and space weathering, up to 20% of the soil is glassy [6]. This glass content could have a potential effect on the sintering process according to the chosen sintering temperature. Differential Scanning Calorimetry (DSC) analysis can be performed on lunar regolith simulants to observe if any glass content is part of the material.

DSC is a thermal analysis technique which gives information about the physical transformations occurring in the material while heating it up. Two empty alumina crucibles were first heated at 10 K/min up to 1300°C under argon to obtain a baseline. About 50 mg of lunar simulant was then placed inside one of the two crucibles and the same heating profile was repeated, also with a continuous argon flow. Finally, the baseline was subtracted from the curve obtained with the simulant. In Figure 3.3, the results with JSC-1A and JSC-2A lunar simulants show clearly the behaviour of an amorphous material with three distinguishing features: a vitreous transition, T_g at 620°C, an exothermic change, the crystallisation, T_c at 800°C, and an endothermic phase change, the melting, T_m at 1120°C and 1080°C, respectively.

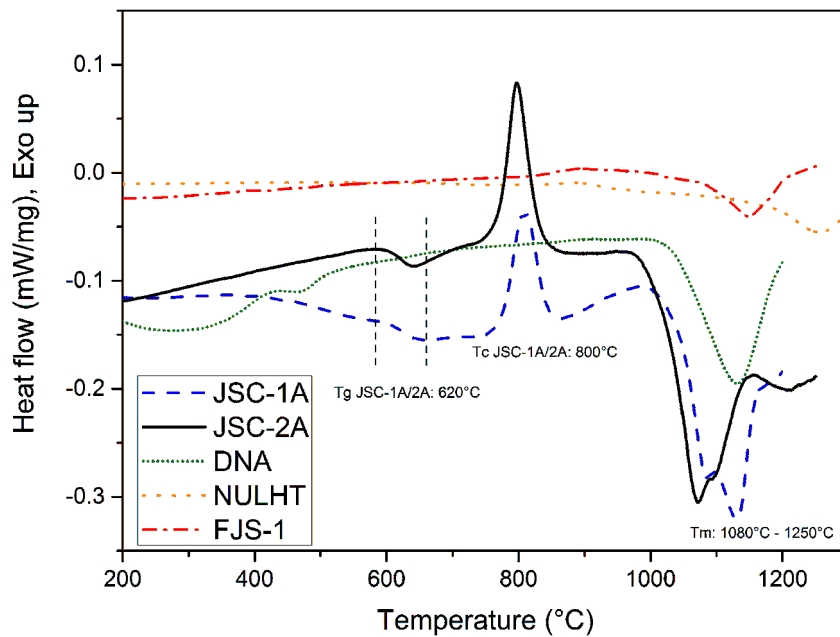


Figure 3.3: DSC curves of as-received lunar simulants. The glass transition, the crystallisation and the melting temperatures are noted T_g , T_c and T_m , respectively. Only JSC-1A and JSC-2A lunar simulants have amorphous grains as shown by their respective glass transitions and crystallisation peaks.

The literature reports a JSC-1A glass content varying from 27 to 49 vol.% [68, 45], without specifying the method used for quantifying it. The measurement of the glass content usually implies the calculation of the enthalpy of crystallisation, fusion and the enthalpy of

fusion of the material crystallised to 100%.

As for FJS-1, NU-LHT-3M and DNA curves, except the melting point at temperatures neighbouring 1150°C, no other discernible feature could be determined. This means that those simulants do not contain any amorphous grains: the simulants are fully crystallised.

It was assessed that the glass content of lunar simulants would impact the sintering process. This hypothesis was supported by two publications [32, 69] referring to another one from 1973 [70] which stipulates that the softening of the glass causes the sintering of particles, and also that the devitrification (crystallisation) reduces the viscous flow thus preventing the densification at a certain density level. However, the crystallisation is a fast process compared to the traditional sintering. The traditional sintering process, described in detail section 3.3.2, is taking about 3 hours at temperatures >1000 °C. Hence, a glassy powder may have recrystallised before even starting sintering. This was confirmed by DSC. JSC-1A and JSC-2A were heated above their crystallisation temperature for 1 hour under vacuum, then, the powder was analysed by DSC, Figure 3.4.

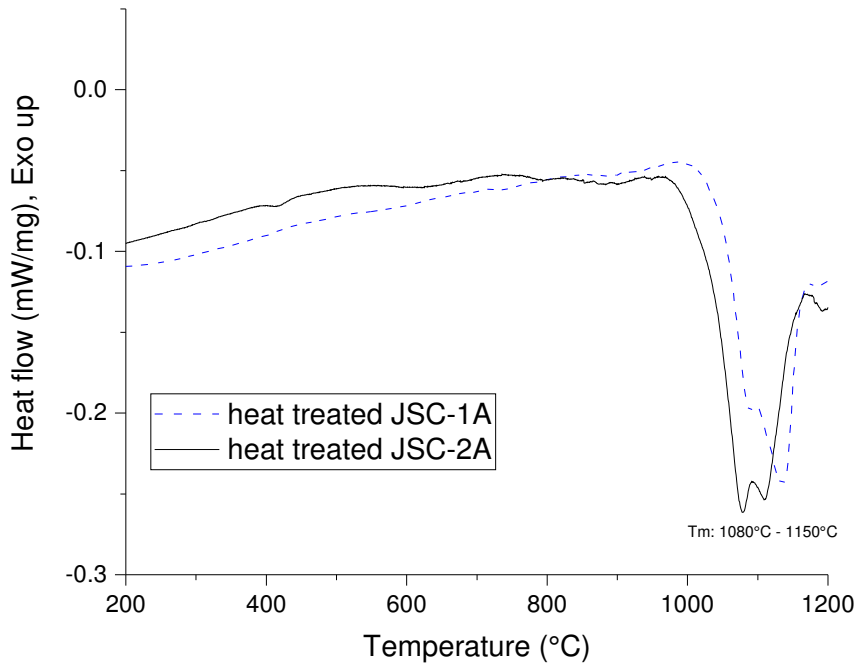


Figure 3.4: DSC curves of JSC-1A and JSC-2A after a 1-hour heat treatment at 900°C. Both lunar simulants do not show anymore an amorphous material feature: they are crystallised.

Both simulants, which originally had glass transition and crystallisation features on their curves, showed only an endothermic peak, characteristic of melting: the powders were therefore fully crystallised. JSC-1A and JSC-2A, fully crystallise before starting sintering in a traditional process. As for sintering below the crystallisation temperature, tests sintering JSC-2A were unsuccessful. At 750°C, 50°C below the crystallisation temperature, for 10 and 24 hours, pressed JSC-2A remained unsintered. The glass content inside the simulant

might be too little to bond all grains together by softening.

The impact of the glass content of a simulant on the solar sintering process may not be understood by performing traditional sintering. The liquid-phase sintering by a concentrated solar beam being a matter of seconds and not hours, the glass content may affect the process although no conclusion can be drawn at this stage.

3.3 Mineral composition

Sintering can also be a matter of chemistry when a LPS process is carried out. A mixture of molten grains could lead to better bonds between the remaining crystallised ones. Hence, the main minerals of the lunar soil should be found in the simulants and it is therefore preferable to use lunar simulants with a close mineral composition to the Apollo samples knowing that a sample could not, in any case, mimic the entire lunar surface.

As shown in the section 1.3, all lunar simulants have a mineral composition close to one another in normative mineralogy. However, they can all have an actual different mineralogical compositions: the ten elements forming the lunar simulant can bond together in various ways thus forming different crystals with their own intrinsic properties. A further characterisation of each simulant was required, at microscopic scale, in order to distinguish precisely the minerals composing the lunar soil simulants.

3.3.1 As-received powder

First, skeletal density of the as-received simulant was calculated using a gas pycnometer. Skeletal density corresponds to the mass of a substance divided by its volume, excluding open and closed (or blind) pores. Results are shown in Table 3.1.

Table 3.1: Skeletal density of lunar soil and simulants

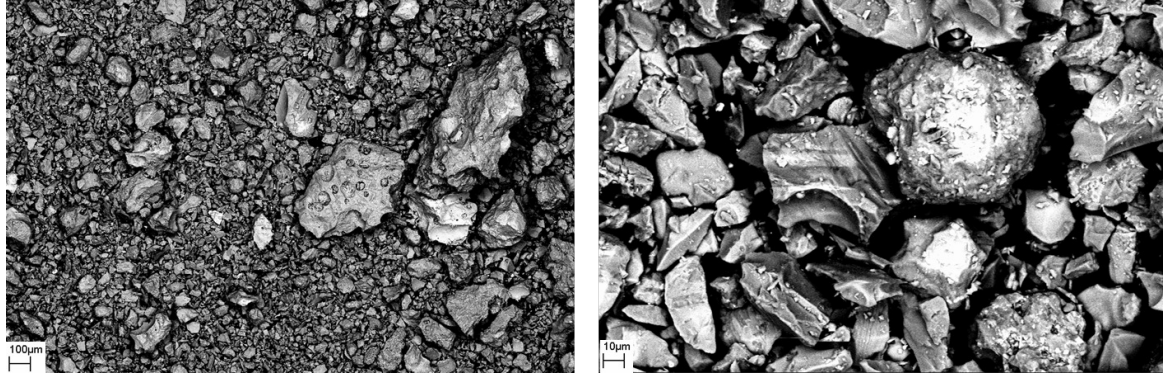
	JSC-1A	JSC-2A	FJS-1	DNA	NU-LHT-3M	Lunar regolith (average) [6]
Skeletal density (g.cm ⁻³)	2.90	2.90	2.94	2.77	2.90	3.1

The skeletal density is an intrinsic property of the material. Even if those materials are supposedly similar, a change in their mineral compositions would directly modify their density. All measured simulants show a skeletal density close to the original lunar soil. Further characterisation was thus required to perform any sorting of the simulants.

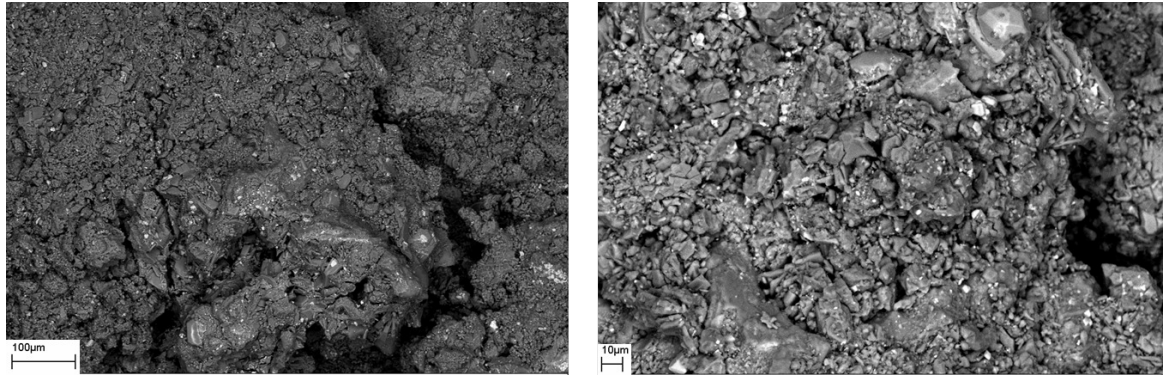
Secondly, Scanning Electron Microscopy (SEM) analysis, combined with Energy-dispersive X-ray spectroscopy (EDX), were performed on each simulant. The SEM apparatus was a Zeiss LEO 1,530 VP with an EDX system by Oxford Instruments.

First observations were made on the as-received JSC-1A and DNA-1 simulants, in a powder state, as shown in Figure 3.5. Information obtained on such pictures are however

very little. The identification of distinct minerals, even with EDX, was complicated due to the low contrast and the surface charging of the particles, the regolith simulants being poorly conductive. The other simulants, JSC-2A, FJS-1 and NU-LHT-3M were therefore not observed by SEM in a powder state.



(a) JSC-1A



(b) DNA-1

Figure 3.5: SEM images of as-received JSC-1A and DNA-1 lunar simulants at different magnifications.

Consequently, minerals analysis of all simulants were carried out on cross-sections of traditionally sintered simulants under vacuum.

3.3.2 Traditional sintering test plan

With a well controlled sintering process, it is possible to assess the impact of differences to lunar regolith on a solar sintering experiment. In this research work, all lunar simulants were first sintered using a traditional approach: the powder was pressed at 255 MPa into a 20 mm diameter die using a manual hydraulic press. Then, the green body was sintered for 3 hours at a temperature slightly below the respective melting point of the simulant in the sintering environment. This temperature was chosen to allow a bonding between the grains without having too much liquid phase involved but also for not having a pure solid-state

sintering, which would take too long for producing samples [32]. Simulant transformations during the process are shown in Figure 3.6.

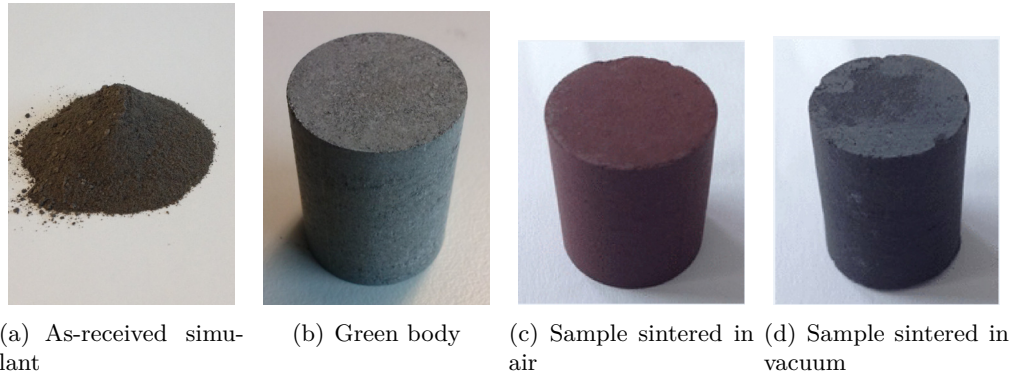


Figure 3.6: Typical transformations for all simulants during the traditional sintering process: About 80 g of raw powder (a) is pressed at 255 MPa in a die to form a green body (b) which is sintered in air (c) or in vacuum (d) for 3 hours. The sintered samples are cylinders, 20 mm diameter wide and with a height ranging from 20 to 30 mm.

From the information given by the DSC, the temperature window for sintering mare simulants was expected to be around 1100°C and around 1200°C for NU-LHT-3M, the highlands simulant, in air and vacuum. The sample size and the atmosphere were however totally different: about 50 mg heated under argon in the DSC whereas the sintering process was performed in air or vacuum with 80 g of lunar soil simulant. The specific sintering temperature was therefore defined with a trial and error approach, the objective being to obtain the denser sample possible without forming any melt. Since the samples were sintered inside an alumina crucible, sintered samples shrank and could be easily removed from the crucible whereas the molten ones bonded to its wall. With this process, it was possible to obtain around 20 mm diameter small cylinders, with a height between 20 and 30 mm, that could be used for compressive tests, following the general outline of the norm Deutsches Institut für Normung (DIN) 51104. The density of the sintered sample was then divided by the powder density to obtain a relative density. Although it would be interesting to obtain all sintered products, in air and in vacuum, with the same relative density, the sintering temperature range for each simulant was small, around 10°C, and the imprecision of the ovens made difficult the realisation of those sintered samples. After preliminary tests, it was therefore decided to fix a relative density in air, about 0.80 and another one in vacuum about 0.90, which will be used as references for the sintering of all simulants. Table 3.2 summarises the sintering temperatures used for each simulant in air and under vacuum.

The relative density of FJS-1 and NU-LHT-3M, respectively 0.75 and 0.76, sintered under vacuum was too low compared to the targeted one of 0.9. Trials to make denser FJS-1A samples were carried out with new sintering parameters. Table 3.3 lists these new parameters and the achieved relative density. As shown in this table, the density of sintered

FJS-1 could not be enhanced even after a 5-hour sintering process. Adjusting the sintering temperature, FJS-1 melted at 1100°C and only a rise of 5°C was possible without much effect on the density of the sintered samples. The density stage reached sintering FJS-1 is due to the compensation of two concurrent effects.

Table 3.2: Sintering temperature of each simulant and sample density after sintering.

Sintering environment		Lunar simulants				
		JSC-1A	JSC-2A	FJS-1	DNA-1	NU-LHT-3M
Air	Sintering temperature (°C)	1125	1130	1125	1100	1200
	Sample density (g.cm ⁻³)	2.25	2.16	2.16	2.48	2.16
	Relative density	0.78	0.74	0.74	0.82	0.74
Vacuum	Sintering temperature (°C)	1100	1090	1090	1070	1200
	Sample density (g.cm ⁻³)	2.54	2.53	2.17	2.27	2.21
	Relative density	0.88	0.87	0.75	0.90	0.76

Table 3.3: New sintering parameters and density of sintered FJS-1. The first set of chosen parameters is shown as a reference. When more than one sample was sintered, the mean value of the density is shown.

Number of samples	Time	Temperature (°C)	Density (g.cm ⁻³)	Relative density
6	3h	1090	2.17	0.75
1	4h	1090	2.13	0.73
1	5h	1090	2.14	0.74
6	3h	1095	2.2	0.76

On one side, longer time and higher temperature help the atom mobility, the reduction of closed pores and the elimination of open ones, but on the other side, they also promote the outgassing of some minerals, thus creating new pores [17]. The trapped gas, by temperature increasing, can also swell the closed pores, reducing the density as it has been shown with mullite LPS with a zirconia-alumina additive [71]. When these two processes are balanced, the sample density stays constant. Since the FJS-1 minerals are different from the ones in JSC-1A/2A, the outgassing, and therefore, the maximal achievable densities cannot be the same. Similar results were expected with NU-LHT-3M, and due to time constraints, new

sintering trials were not performed with this lunar simulant.

The natural next step was to observe the traditionally sintered lunar regolith simulant at the microscopic level. A cross-section of each sintered sample was cut and embedded in a polymer resin to be easily fixed in the SEM. The sintered regolith being poorly conductive, all samples were coated with gold to prevent a surface charging by the electron bombardment.

The first simulant that was observed by SEM was the JSC-1A, in Figure 3.7.

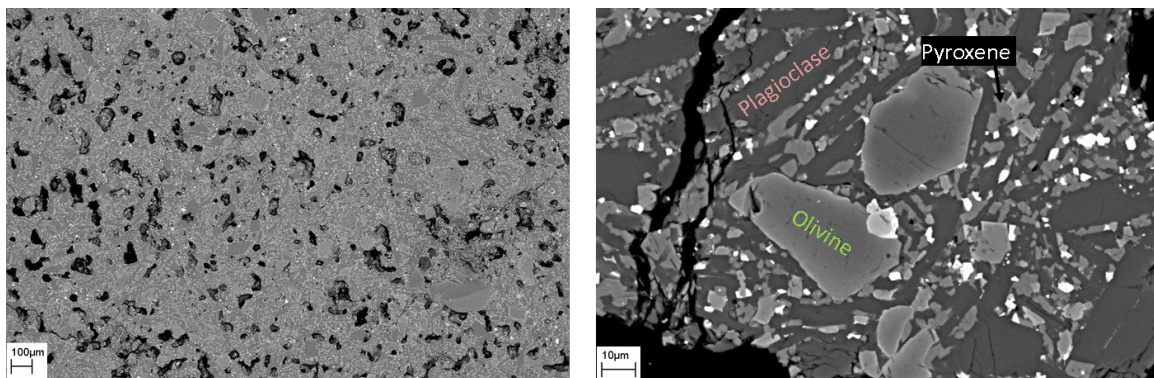


Figure 3.7: SEM images of JSC-1A after sintering in vacuum at 1100°C for 3 hours.

Mineral grains of sintered JSC-1A were wider than 50 µm. All individual grains could be easily distinguished by EDX. Although most of the minerals of JSC-1A were olivine and plagioclase, some pyroxenes were also found. The grains bonded together without any visible melt at the grain boundaries. Since the sample was sintered in 3 hours, a liquid phase should be present between the grains. The layer of melt is most likely too thin, around few nanometres [61], to be seen with the limited resolution of the microscope.

A similar structure was expected sintering JSC-2A lunar simulant, JSC-2A being a replacement of the JSC-1A. Figure 3.8 shows the sintered structure under SEM. Surprisingly, individual crystals could not be distinguished. EDX analysis revealed that only pyroxenes compose the matrix of the material. Those differences regarding the two simulants were unexpected since they are identical according to the material data sheets. The production processes of the simulants being however completely different, the minerals can have very different aspects although the same compounds take part in the simulant. The hypothesis regarding the lack of observable olivine and plagioclase on JSC-2A SEM images comes from the fact that the crystals of those minerals may be nanosized and spread in the pyroxene matrix. A second batch of JSC-2A lunar simulant was however ordered, a year after the first one. Although it was supposed to be the same material as the first batch, the sintering parameters had to be slightly changed to obtain the same end product: 1080°C instead of 1090°C for sintering some samples under vacuum. This unexpected difference, not observed with the other simulants was explained by SEM and EDX, Figure 3.9. The structure of the second batch was closer to JSC-1A lunar simulant, with large plagioclase, >50 µm wide, easily visible by SEM. Large olivine minerals were however still difficult to find. Since

JSC-2A simulant is manufactured by a private company, it was not possible to know if the difference between the two batches came from a change in the raw material being processed by their machine or if the manufacturing process itself was modified.

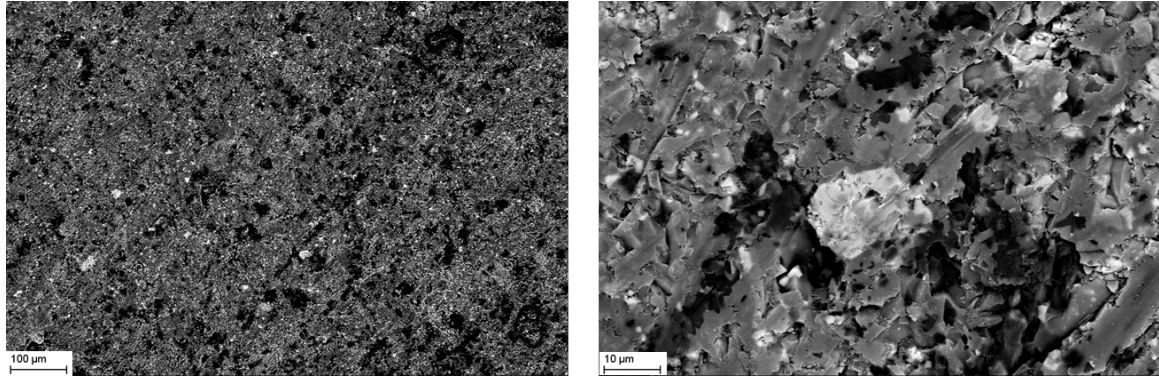


Figure 3.8: SEM images of JSC-2A after sintering in vacuum at 1090°C for 3 hours. Powder taken from a first batch.

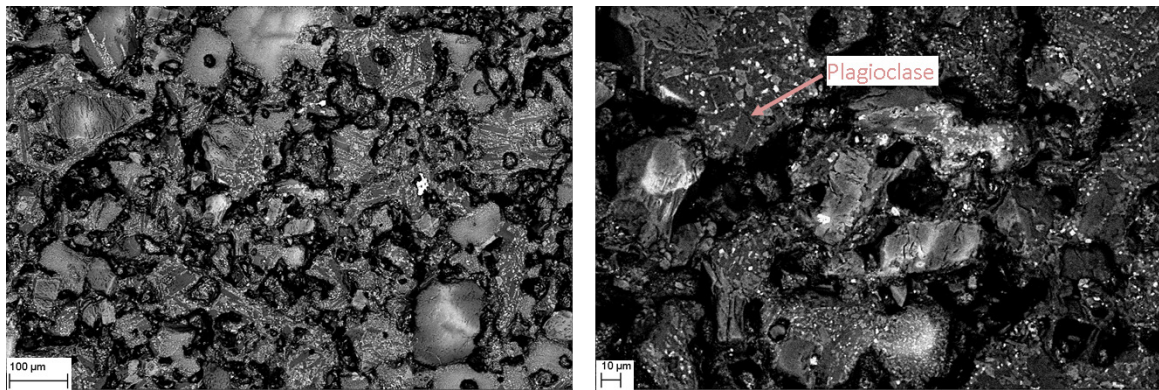


Figure 3.9: SEM images of JSC-2A after sintering in vacuum at 1090°C for 3 hours. Powder taken from a second batch.

Then, SEM and EDX analysis were also performed on a FJS-1 sample. Pictures are shown in Figure 3.10. FJS-1 revealed having crystals of titanomagnetite 50 µm wide in a matrix of pyroxenes. Such large crystals were also observed in JSC-1A lunar simulant. Both, JSC-1A and FJS-1, come from natural eroded rock pieces, also called lithic fragments: the fact that the crystallisation of those simulants took place over a long time in a natural environment could be the reason of the formation of those large crystals around 50 µm wide. Large crystals were however also found in the second batch of JSC-2A artificial lunar simulant.

In NULHT-3M structure, shown in Figure 3.11, no large crystals could be identified, only a matrix of plagioclase and pyroxene. NULHT-3M simulant being processed like JSC-2A, with the controlled recrystallisation of molten oxides, a similar structure to the first JSC-2A batch, with most likely nanocrystals, is observed. The lack of highlands simulants

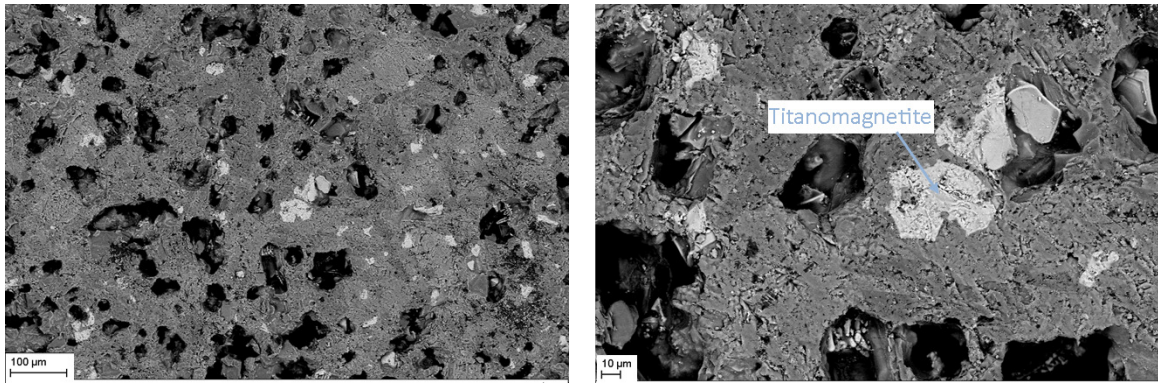


Figure 3.10: SEM images of FJS-1 after sintering in vacuum at 1090°C for 3 hours.

and other SEM images made the observation difficult to interpret.

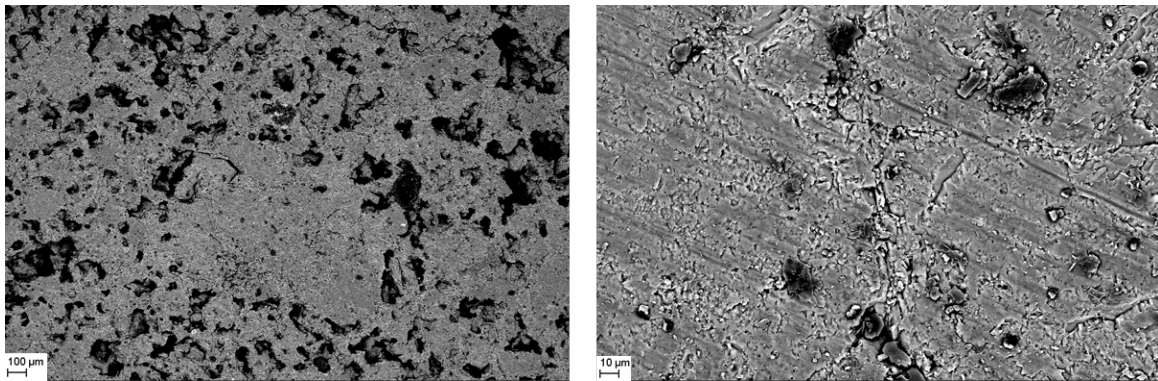


Figure 3.11: SEM images of NULHT after sintering in vacuum at 1200°C for 3 hours.

Finally, DNA-1 lunar simulant, analysed by SEM, Figure 3.12, shows no olivine mineral but a matrix of high-Na plagioclase surrounding pyroxenes crystals. It was the simulant with the highest sodium content although the reported composition [1] does not reveal it. DNA-1 lunar simulant has therefore an opposite plagioclase solid solution to JSC-1A.

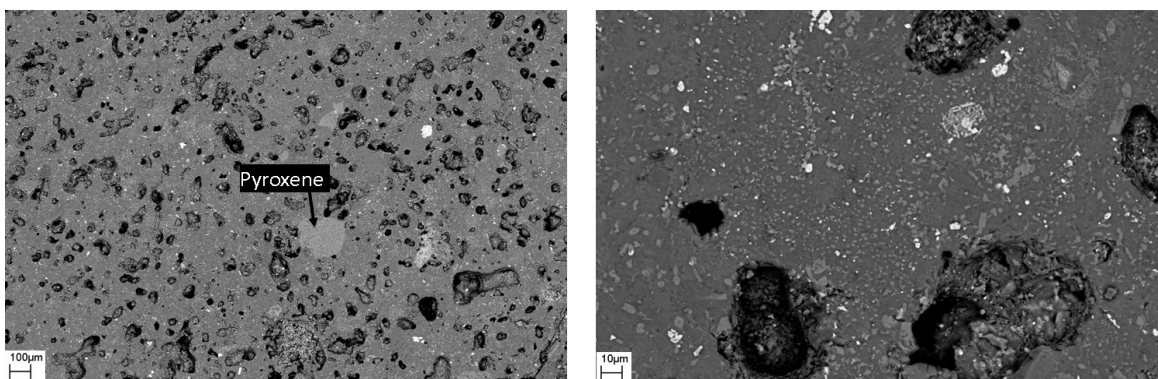


Figure 3.12: SEM images of DNA-1 after sintering in vacuum at 1070°C for 3 hours.

Variations in a feldspar family might not seem important at a first sight, however, two end-members from a same family can have completely different properties. Plagioclase solid solution, for instance, varies from albite $\text{NaAlSi}_3\text{O}_8$ to anorthite $\text{CaAl}_2\text{Si}_2\text{O}_8$. Unlike many other solid solution, plagioclase uses coupled substitution to produce intermediate compositions between the two end-members. The charge balance needs indeed to be kept from one solid solution to another, that is the reason why $\text{Na}^+\text{Si}^{+4}$ is substituted for $\text{Ca}^{+2}\text{Al}^{+3}$ and not only a sodium element can replace a calcium one [72]. For example, the composition of labradorite, which is a Ca-rich intermediary plagioclase mineral, is $(\text{Ca}, \text{Na})(\text{Si}, \text{Al})_4\text{O}_8$. The composition of intermediate solid solutions is however usually presented as a percentage of Anorthite (An) and Albite (Ab), the two end-members. Labradorite is then (70-50% An - 30-50% Ab).

On the Moon, plagioclase minerals are depleted in sodium and only Ca-rich anorthite, bytownite or labradorite could be found in maria and highlands [72, 73]. As for the simulants, the solid solution is different from one to another: Figure 3.13 illustrates the variations in the plagioclase serie, also indicating the plagioclase present in JSC-1A, FJS-1 and DNA-1 compositions.

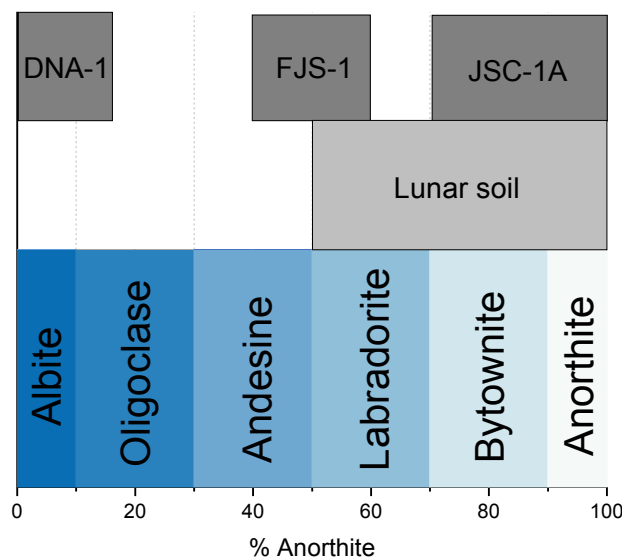


Figure 3.13: Plagioclase minerals in the lunar soil [72, 73], JSC-1A [44], FJS-1[74] and DNA-1. DNA-1 plagioclase composition was measured qualitatively through EDX observations.

The main change from one plagioclase end-member to another is its melting point. Figure 3.14 shows that pure albite melts at 1100°C under atmospheric pressure whereas anorthite needs to reach 1500°C . Plagioclase representing around 50% of the mare and 90% of the highlands, it influences the melting point and, consequently, the sintering temperature of a lunar simulant. Therefore, in order to sinter a simulant at a temperature close to the temperature that will be used to sinter actual lunar soil, it would be more judicious to carry on experiments with JSC-1A and JSC-2A than DNA-1 lunar simulant.

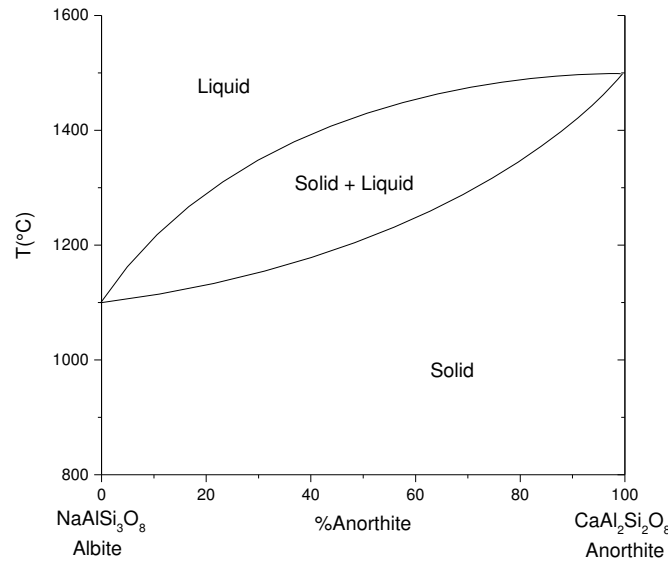


Figure 3.14: Plagioclase temperature-composition diagram, indicating solidus and liquidus temperatures at 1 bar pressure [72].

3.3.3 Ilmenite content variation

An extra simulant could have been interesting to create: a high-Ti mare simulant. This simulant could have replaced the depleted MLS-1, only high-Ti mare simulant ever commercially available in 1970s-80s and considered as the first lunar simulant produced [42]. Ilmenite, FeTiO_3 , is the main mineral containing titanium on the Moon.

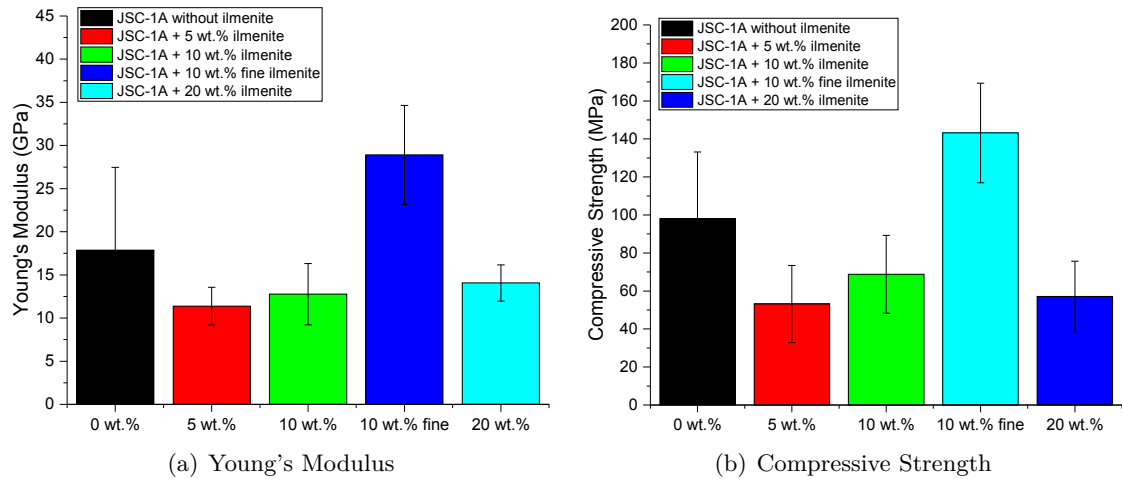


Figure 3.15: Young's Modulus and Compressive Strength of JSC-1A samples sintered in air with different ilmenite coarse contents (indicated by 0, 5, 10, 20 wt. %). The average from 3 samples is shown and the error bar represents the standard deviation. 'fine' indicates the use of the fine ilmenite, with particles $<50 \mu\text{m}$, instead of the coarse, with particles $<300 \mu\text{m}$.

Pure ilmenite with two different grain sizes were available in this project, one coarse

with particles $<300\text{ }\mu\text{m}$ and another, finer, with particles $<50\text{ }\mu\text{m}$. Figure 3.15 shows the Young's Modulus and Compressive Strength of JSC-1A simulant mixed with different coarse ilmenite contents sintered in air. The results were obtained from the stress-strain curve after carrying out the uni-axial compression of the sintered samples. The uni-axial testing machine was a PEZ 1,595 with a piston stroke of 0.5 mm/minute . It is shown that varying the ilmenite content with a grain size $<300\text{ }\mu\text{m}$ from 0 to 20 wt.% doesn't change the overall Young's modulus and compressive strength of the material. However, using 10 wt.% of the fine ilmenite, the sintered material doubled its Young's Modulus and compressive strength. Ilmenite minerals being identical in both case, it has been hypothesised this change in the investigated mechanical properties could be attributed to the higher density of the sintered samples made of JSC-1A + 10 wt.% of fine ilmenite. It was confirmed using a gas pycnometer and a envelope density analyser, Table 3.4.

Table 3.4: Density and porosity of powders, sintered JSC-1A +10wt% ilmenite coarse powder and JSC-1A +10wt% ilmenite fine powder

	Powder density (g.cm^{-3})	Sintered sample density (g.cm^{-3})	Estimated porosity
JSC1A + 10 wt.% coarse ilmenite	3.050	2.552	16.3%
JSC1A + 10 wt.% fine ilmenite	3.050	2.651	13.1%

Although the two original powders have the same densities, the sintered sample with fine ilmenite shows a higher density leading to a porosity of only 13%. These different porosities were responsible for changing the overall mechanical properties of the sintered material. SEM analysis show, in Figure 3.16, that indeed the ilmenite grains do not interact with surrounding minerals during the sintering process.

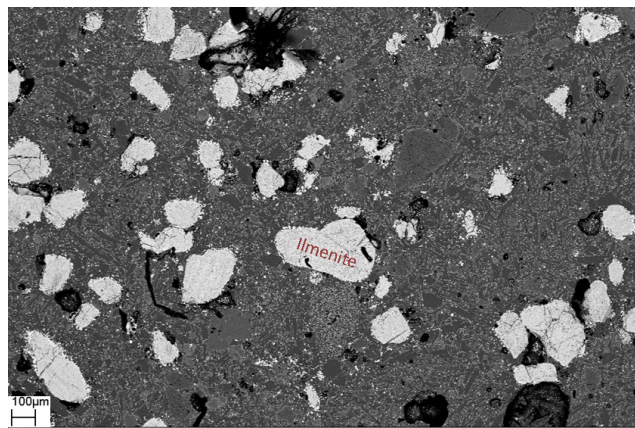


Figure 3.16: Mixture of JSC-1A lunar simulant and 20 wt.% of ilmenite (white grains) sintered under vacuum in a traditional oven at 1100°C for 3 hours.

Similar results were also obtained using DNA-1 simulant, as shown Figure 3.17: the

addition of coarse ilmenite did not change the mechanical properties of the sintered DNA-1 samples.

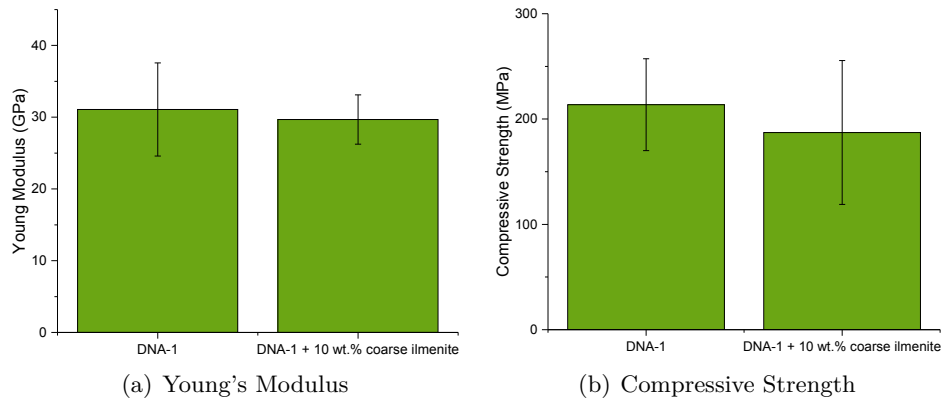


Figure 3.17: Young's Modulus and Compressive Strength of DNA-1 samples sintered in air with 0 and 10 wt.% ilmenite content. The average from 3 samples is shown and the error bars represent the standard deviation of the results.

3.4 Grain shape

On the Moon, the sandy state of the lunar surface comes from the perpetual meteorite bombardment over billions of years. All grains have therefore sharp edges due to a lack of erosion from space weathering [6]. On Earth, the natural erosion prevents the creation of simulants with such grain shape. Sintering of spherical particles has been shown to be less efficient than the sintering of ones with an irregular shape [75]. Hence, in principle, the sintering rate of lunar soil should be faster than any simulant sintered in the same conditions. Consequently, it should be preferable not to use rough simulants with coarse grains, where ball milling would be necessary to obtain the Apollo range of grain size distribution: this additional step would smoothen even more the edges of the grains, making the sintering not relevant enough. However, quantifying the sharpness of the lunar and simulant grains was required for understanding the actual difference. Microscopic images of actual lunar regolith are shown in Figure 3.18.

In order to quantify the shape of the grains, the roundness and sphericity was measured. A table, made by geologists [76] and shown in Figure 3.19, was used as a reference. The different radii needed for the formulas were measured by processing grains pictures with ImageJ computer software [77]. Twelve grains were measured, from pictures found in the literature. Results are shown in Table 3.5. The term “circularity” instead of “sphericity” would be more appropriate since the radius measurements are made on 2D pictures, but the word “sphericity” was also used in the literature for defining 2D objects.

Table 3.5: Roundness and Sphericity of lunar regolith.

	Roundness	Sphericity
Lunar Regolith	0.69	0.52

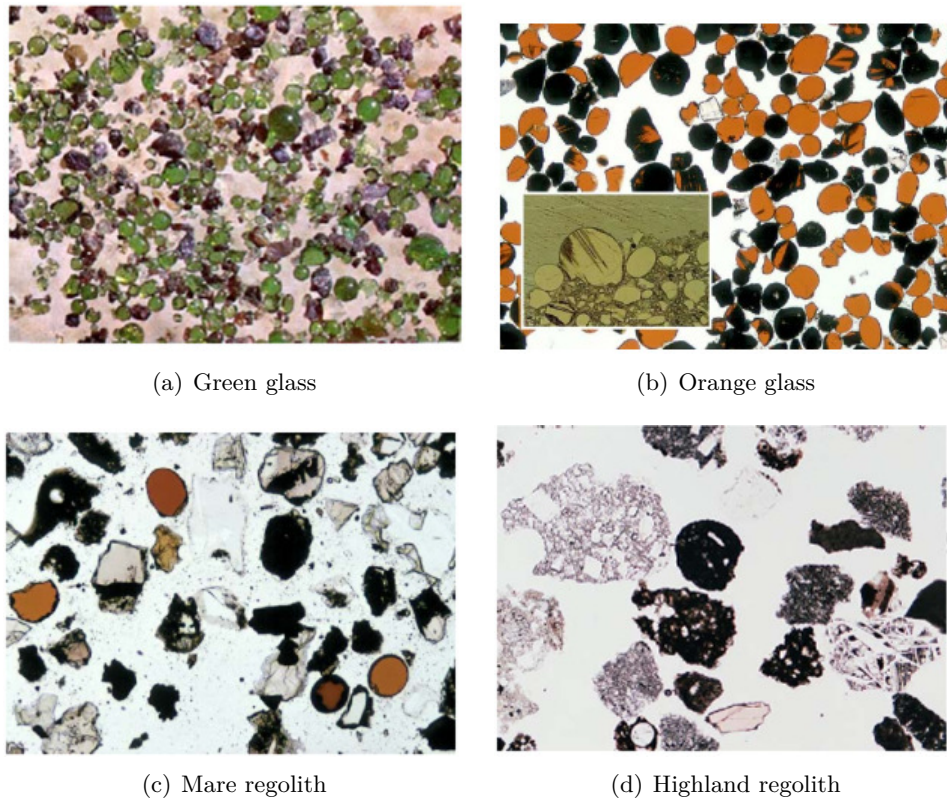


Figure 3.18: Microscopic images of actual lunar soil from Apollo missions. No information about the scale was available but each grain has a size ranging from 20 μm to 250 μm [78].

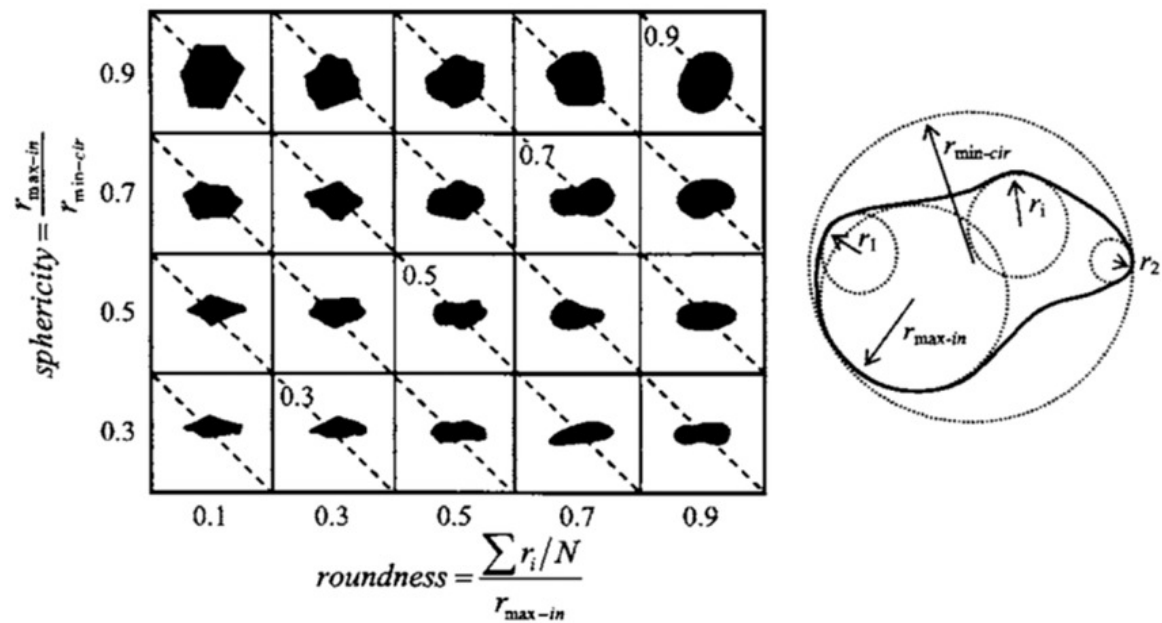


Figure 3.19: Table made by Krumbein et al. [76] classifying grains according to their roundness and sphericity.

As for lunar simulants, shown in Figure 3.20, it was first hypothesised that the ones produced by artificial methods (JSC-2A, NU-LHT-3M) could not have sharp angles due to their manufacturing process. The others, coming from natural volcanic rocks, underwent erosion from Earth weathering. Hence, it seemed impossible to find a simulant with sharp-angular grains like actual lunar regolith. In order to confirm this hypothesis, the roundness and sphericity of twelve grains, bigger than 400 μm , were measured for each simulant, except DNA-1. The Table 3.6 shows the mean value for each measurement. Surprisingly, the simulants seem to have sharper angles than the actual lunar soil. The results show indeed that the simulants have a similar sphericity and a smaller roundness than the lunar soil which is not part of the general belief. This outcome might be due to the difference in grain size, below 250 μm for the measured regolith grains and over 400 μm for the simulants. More microscopic pictures of lunar soil could not be found to cross-check these results.

Table 3.6: Roundness and Sphericity of lunar simulants.

	Roundness	Sphericity
JSC-1A	0.31	0.68
JSC-2A	0.34	0.68
FJS-1	0.39	0.71
NU-LHT	0.33	0.67

However, if a difference in shape between the grains of a simulant and the actual simulant exists, its impact on the sintering process should be negligible compared to the impact of a change in the mineral composition. In order to confirm this hypothesis, since it was not possible to manufacture grains with sharper angles, JSC-1A and JSC-2A grains were milled with a planetary ball miller before being traditionally sintered. Doing so, it was possible to see the effect of rounder grains on the sintering process. After trying several parameters, 3 minutes ball milling at 500 rpm with sixteen 5 mm-grinding balls gave the best results for milling 10 g of lunar regolith simulant: rounder grains with a similar grain size. Pictures of JSC-2A grains before and after milling are shown in Figure 3.21.

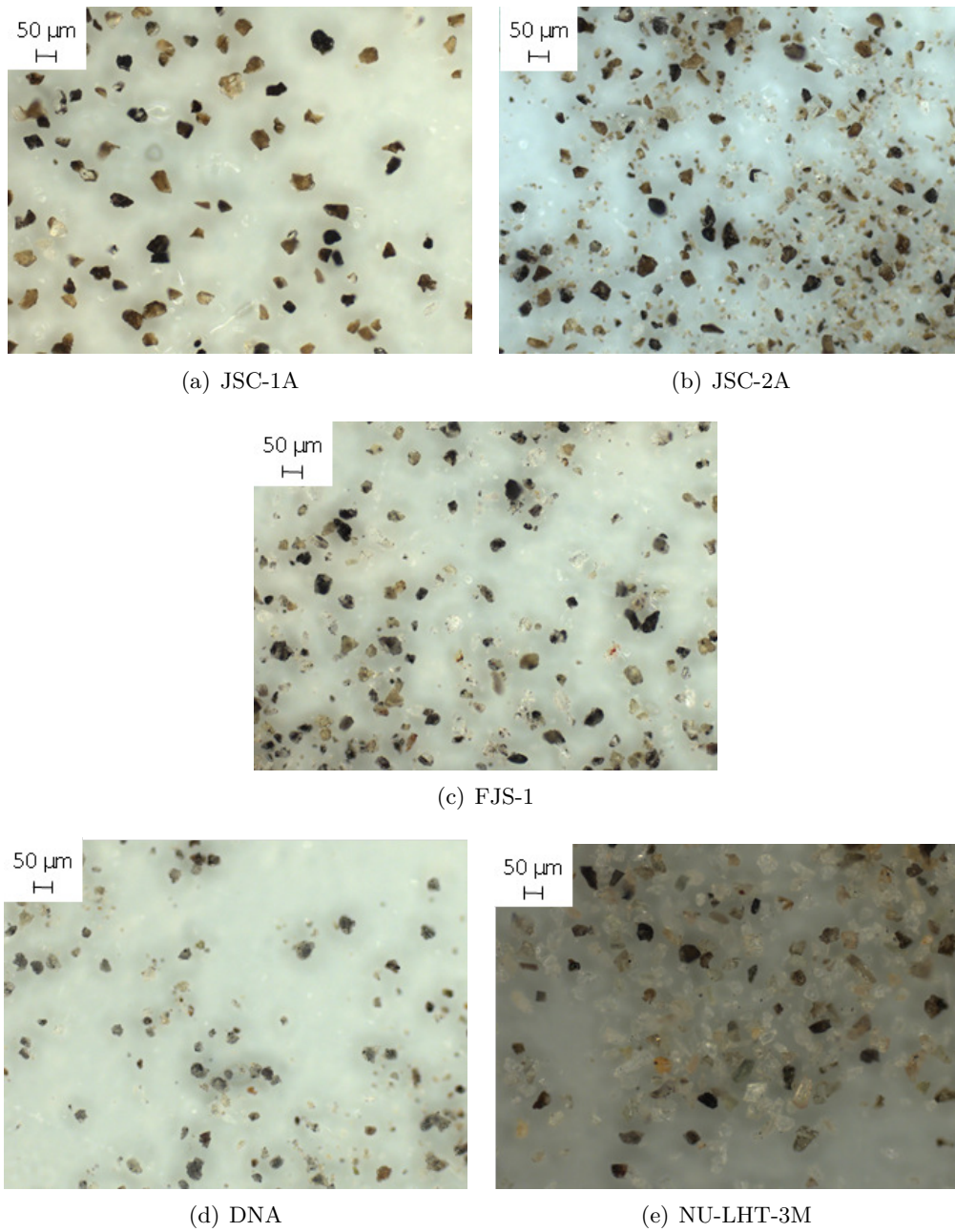


Figure 3.20: Microscopic images of lunar soil simulants.

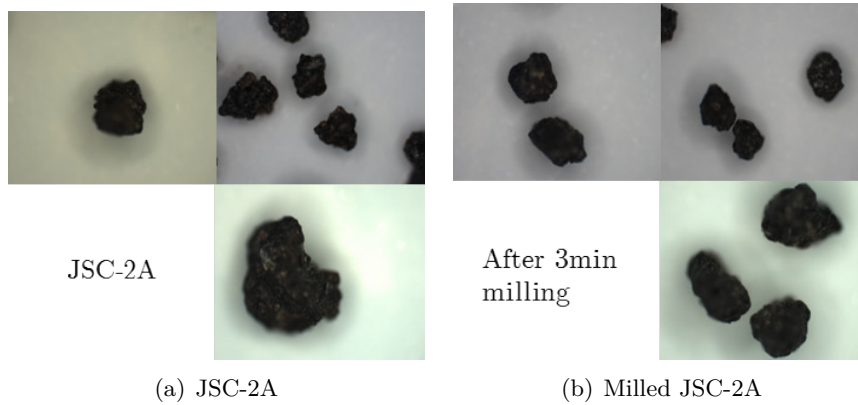


Figure 3.21: Microscopic pictures of grains between 400 μm and 600 μm before (a) and after milling 3 minutes at 500 rpm with sixteen 5 mm-grinding balls (b).

Measuring the roundness and the sphericity of the milled sample, the results, in Table 3.7, expose that the milling increased the roundness but did not affect the sphericity. It was not possible to obtain rounder and more spherical grains.

Table 3.7: Roundness and Sphericity of JSC-2A lunar simulant, before and after milling.

	Roundness	Sphericity
JSC-2A	0.34	0.68
Milled JSC-2A	0.49	0.70

As one could expect, no significant change could be observed at micro-scale, Figure 3.22. The sintering parameters also remained unchanged. The shape difference between lunar regolith and lunar simulants could therefore be neglected for preparing a sintering experiment. More pictures from actual lunar soil would however be required since the measured grains, found in the literature, might not be representative enough of the actual lunar soil.

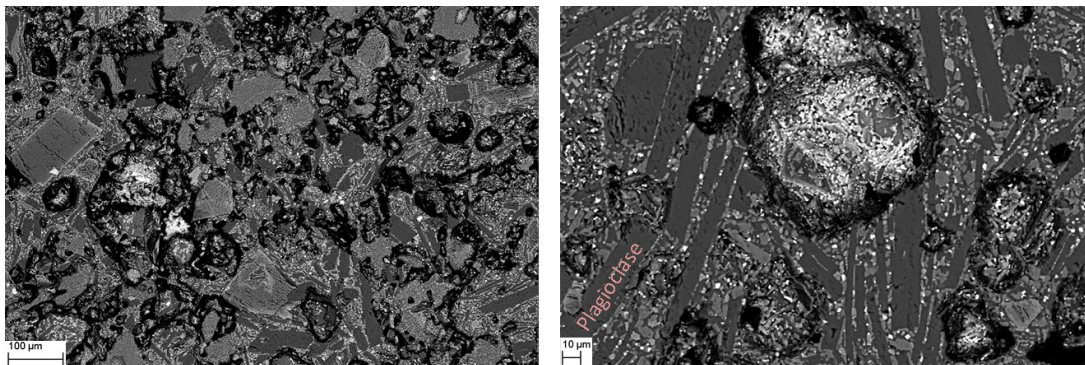


Figure 3.22: SEM images of milled JSC-2A after sintering in vacuum. Powder taken from the second batch.

3.5 Simulant selection

From the analysis of the grain size distribution, the glass content, the mineral composition and the grain shape, it was possible to choose the most suitable simulant for performing solar additive manufacturing of lunar simulant. Although some information could have been lost during the sintering process, some of the minerals being possibly molten, enough data was extracted from the SEM and EDX analysis to get a better idea of which simulant to use, to be as close as the lunar conditions regarding the material aspect while sintering. Table 3.8 summarises the results presented in this section, exhibiting how much a simulant is close to the lunar soil regarding a certain aspect. An extra column was added about the availability in huge quantity of the simulant since large quantities would be required for developing a solar sintering process.

Table 3.8: Table summarising the pros and cons of each lunar simulant.

	Lunar simulants				
	JSC-1A	JSC-2A	FJS-1	DNA-1	NU-LHT-3M
Mineral composition	++	+	+	-	+
Grain shape	++	++	++	+	++
Grain size distribution	++	++	++	+	++
Commerically available	+	++	++	++	++
Legend:	++: close to the lunar soil				
	+: relatively close to the lunar soil				
	-: far from the lunar soil				

All characterised lunar simulants are relatively representative to the actual lunar soil. The most faithful being JSC-1A and the least DNA-1 regarding the aspects that matter for a solar sintering process. This project started when reserves of JSC-1A were not yet depleted, therefore, the first solar sintering tests were performed using JSC-1A. The further development of the technology was however performed using JSC-2A since it was the closer simulant to JSC-1A and available in large quantities. FJS-1 and NU-LHT-3M were not processed due to time and budget constraints.

4 Scope and design of the experimental set-up

4.1 Previous works on solar sintering

Solar sintering was previously performed in Almeria, Spain [79, 80] where is located a solar concentrator similar to the one in DLR-Cologne. The process was targeting the sintering of technical ceramics without any space application. The most successful solar sintering was however so far performed by Kayser M., artist and engineer, who sintered desert sand with a semi-automatic solar 3D printer [81]. Regarding space related solar sintering experiments, NASA tried out few years ago to sinter lunar regolith concentrating as well solar light. Three mains studies were carried out, two focusing sunlight with a Fresnel lens [82, 26, 36] and another one transferring the collected solar light into optical fibres [83]. These studies proved the feasibility of sintering lunar regolith simulant with solar light but did not show any 3D printing capability, limiting the sintering to single dots and lines for dust mitigation purposes as shown in Figures 4.1 and 4.2.



Figure 4.1: Sintered regolith simulant by concentrated solar light into an optical fibre, [83].



Figure 4.2: Fresnel lens combined with a rover and a mirror (left) and regolith testbed with solar sintered material (right) [82].

4.2 Scope of the experiment with respect to the lunar conditions

The complex lunar environment, very different from the Earth one is difficult to mimic at laboratory scale. In the following section are therefore reported the main lunar features not to neglect in order to perform a solar sintering process on the Moon. Not all of those features could be however considered within the project frame, accordingly, in this chapter is later described the actual design of the solar 3D printing experiment.

4.2.1 Vacuum conditions

The effect of the lack of atmosphere was investigated at laboratory scale on lunar regolith test samples. Mechanical tests (compressive strength), X-Ray Diffraction (XRD) and SEM analysis were performed on samples sintered under a pressure of 10^{-5} millibar, considered as vacuum. The first mechanical tests gave an overview of the impact of the environment on the mechanical properties of a sintered product. Figure 4.3 shows the Young's modulus and compressive strength of lunar simulants sintered in a traditional oven in air and under vacuum. Sintering parameters were previously listed section 3.3.2.

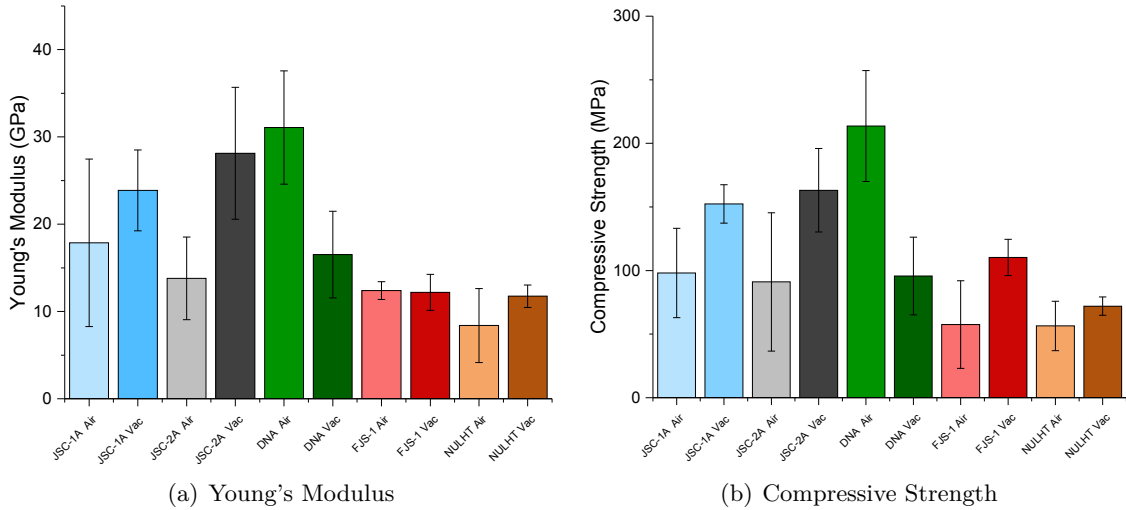


Figure 4.3: Young's Modulus (a) and Compressive Strength (b) of lunar simulant sintered in air and in vacuum (noted "Vac"). The average of 6 samples is shown and the error bar represents the standard deviation.

Under vacuum, the lack of air increased the Young's modulus and compressive strength of JSC-1A, JSC-2A and NU-LHT-3M by around 50%. Only an increase of the compressive strength could be noticed sintering FJS-1 in vacuum and DNA-1 has better Young's modulus and compressive strength in air. These results and differences in mechanical properties between each simulant sintered in air and in vacuum were partly expected due to the density variations, shown previously in Table 3.2, section 3.3.2. On a global trend, shown in Figure 4.4, the denser the sample, the better is the resistance to compressive deformations.

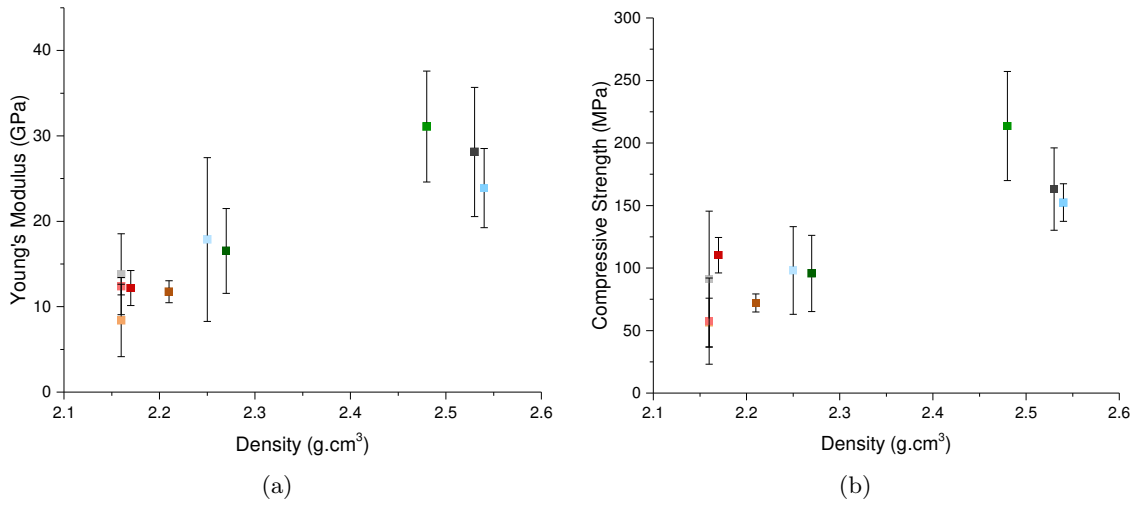


Figure 4.4: Young's Modulus (a) and Compressive Strength (b) of lunar simulant sintered in air and in vacuum related to the samples density.

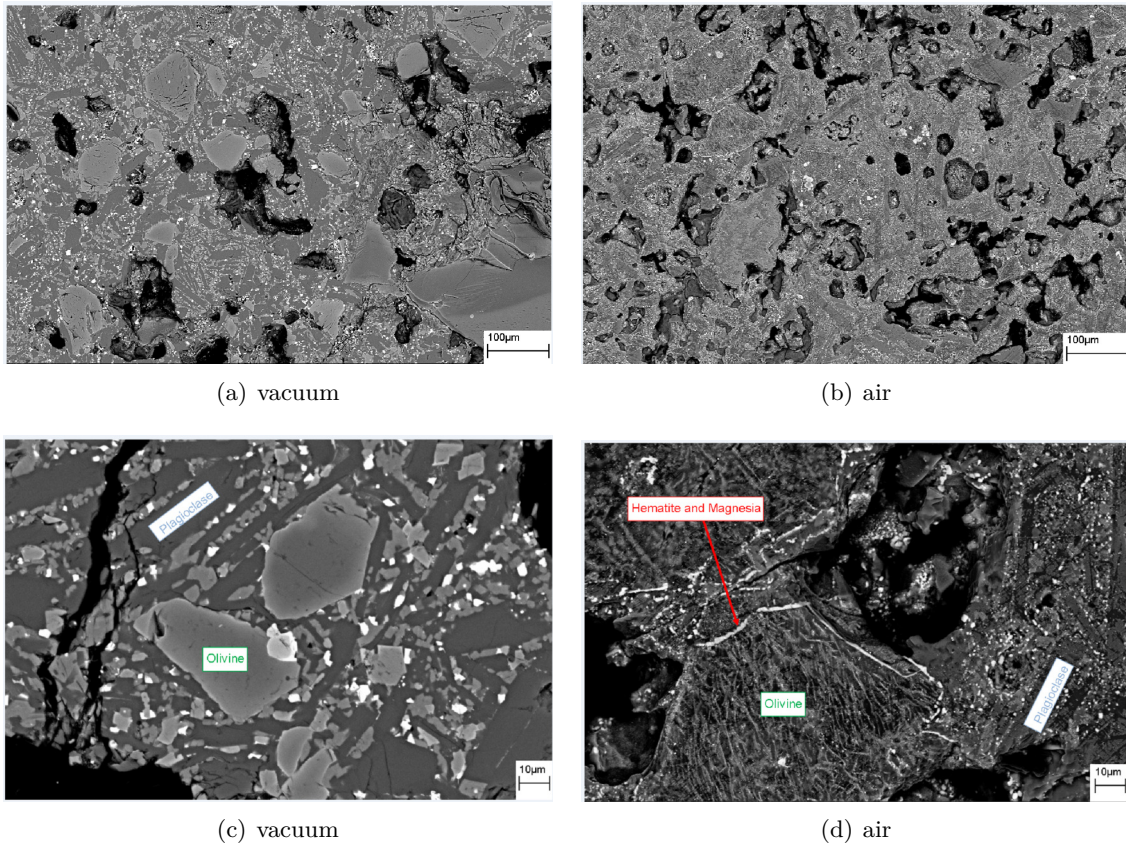


Figure 4.5: SEM images of JSC-1A lunar simulant sintered in air and under vacuum at 1100°C for 3 hours. Hematite and magnesia were formed at the olivine grain boundary after sintering JSC-1A in air. Under vacuum, no phase can be seen at the grain boundaries.

In order to understand why the density of the sintered simulant changes between a

process in two different environments, SEM images of sintered samples were compared. Figure 4.5 shows sintered JSC-1A in air and in vacuum. In Figures 4.5(a) and 4.5(b) can be seen two similar sintered structures with however higher porosity in the sample sintered in air. At higher magnification, in Figure 4.5(d), EDX analysis revealed the formation of hematite (Fe_2O_3) and magnesia (MgO) at the border of an olivine grain with needle-shaped crystals whereas Figure 4.5(c) shows grains without crystallographic transformations and no phase at the grain boundaries between sintered grains. In air, the formation of the observed oxide layer at the grain boundary prevented the grains to sinter directly together. The higher sintering temperature in air resulted in a higher melt fraction which helped the bonding of the grains in the LPS process [84]. The higher temperature caused also more outgassing, explaining the higher porosity of the sample sintered in air.

Although the scale is different, once sintered, it is interesting to notice that JSC-1A looks like lunar rocks as shown by the cross-sections of different rocks in Figure 4.6.

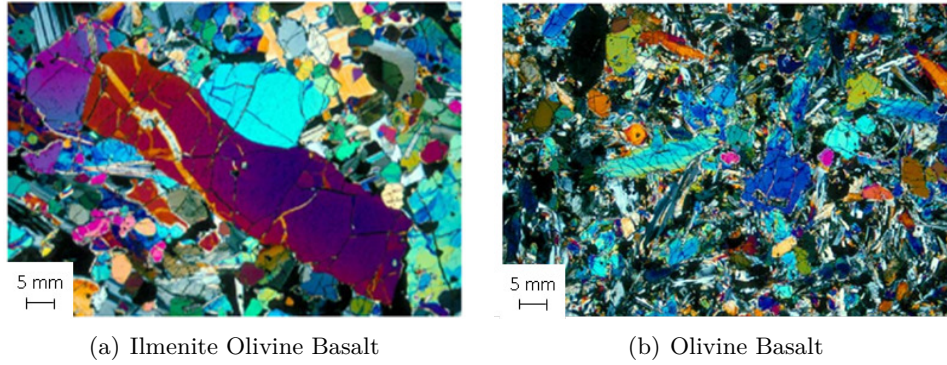
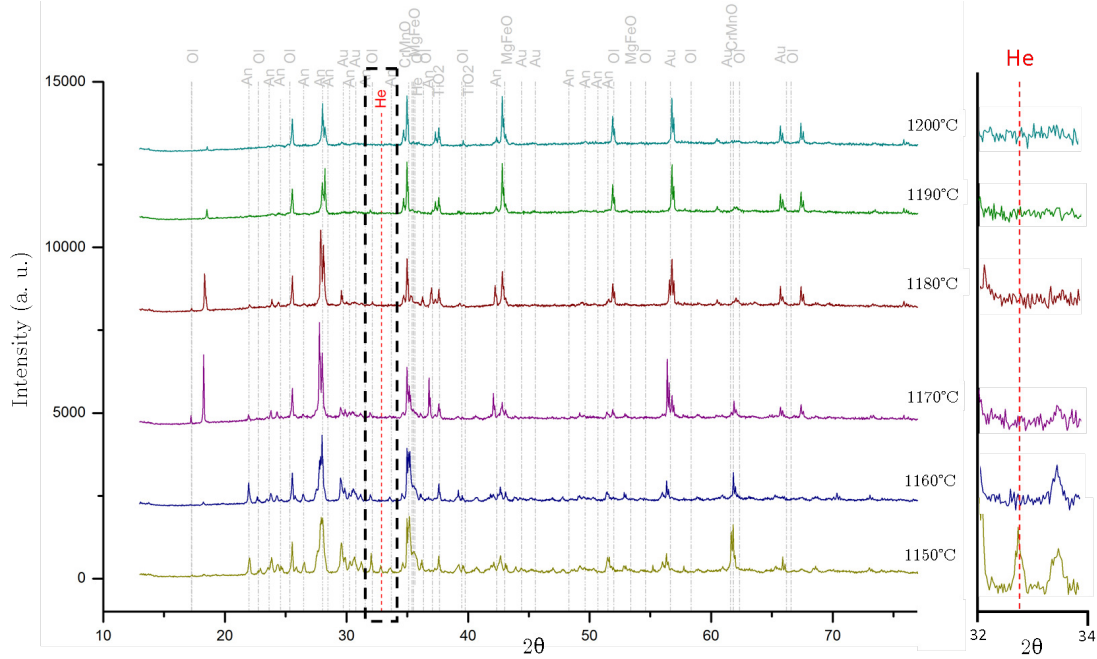


Figure 4.6: Microscopic cross-sections of different lunar rocks [78].

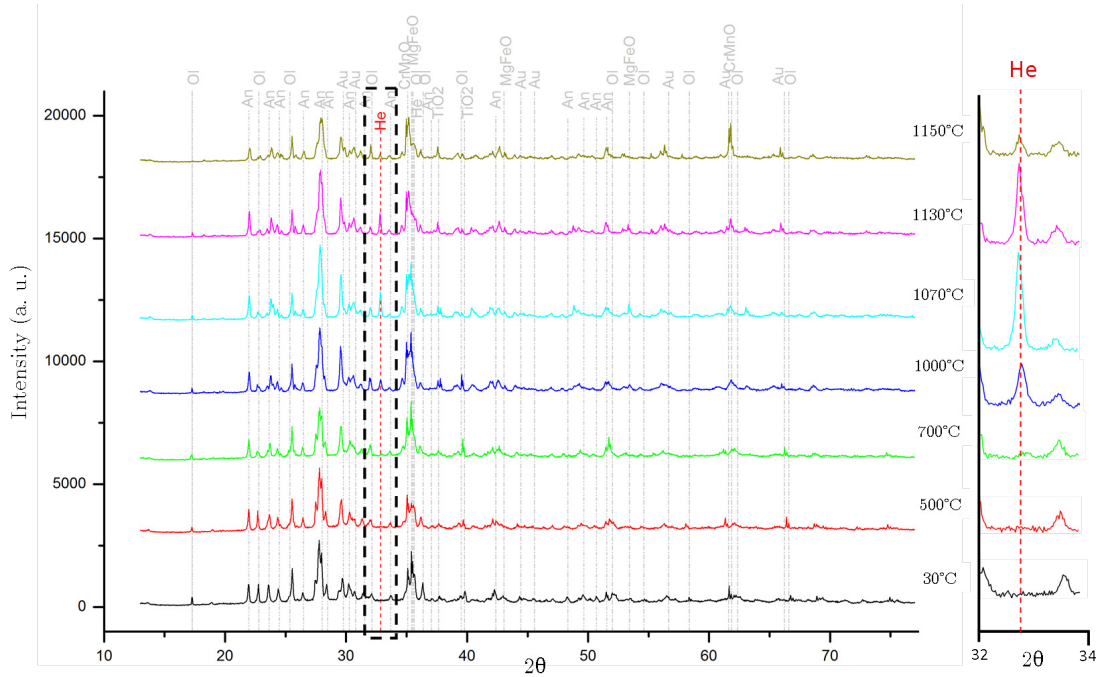
Finally, high-temperature XRD measurements were performed on JSC-1A, in air and in vacuum. A D8 Advance device from Bruker was used, with a AntonPaar HTK1200N heating chamber. The X-Ray source was Cu K- α with a wavelength of 1.5406 \AA . This experiment aimed at watching the evolution of the mineral composition between the room temperature and the melting point of the lunar simulant, heating up the material at 10 K/minute . Figure 4.7 shows the results. In both atmospheres, the minor peak intensity variations and peak shift showed that JSC-1A underwent small mineral transformations until the melting point, here measured around 1150°C . These transformations were difficult to analyse due to the high number of phases in the simulant leading to a lot of overlapping peaks. However, the oxidation of the mineral could be clearly noticed with the formation of hematite, more prominent in air than under vacuum. Hematite did not appear below 700°C due to its crystallisation temperature at 600°C .

More transformations were expected due to the difference in porosity, compressive strength and sample color observed section 3.3.2, between JSC-1A sample sintered in air and in vacuum. Although the overlap of the numerous peaks reduced the visibility of the full picture,

the overall phase changes were still limited thus making a solar sintering process in air relevant enough for proving the concept and rising the Technology Readiness Level (TRL) of the technology up to TRL 4. As JSC-2A lunar simulant is a copy of JSC-1A, even with the differences exhibited chapter 3, similar results were expected and the XRD analysis was not performed with this simulant.



(a) Vacuum: 1150°C - 1200°C



(b) Vacuum: RT - 1150°C

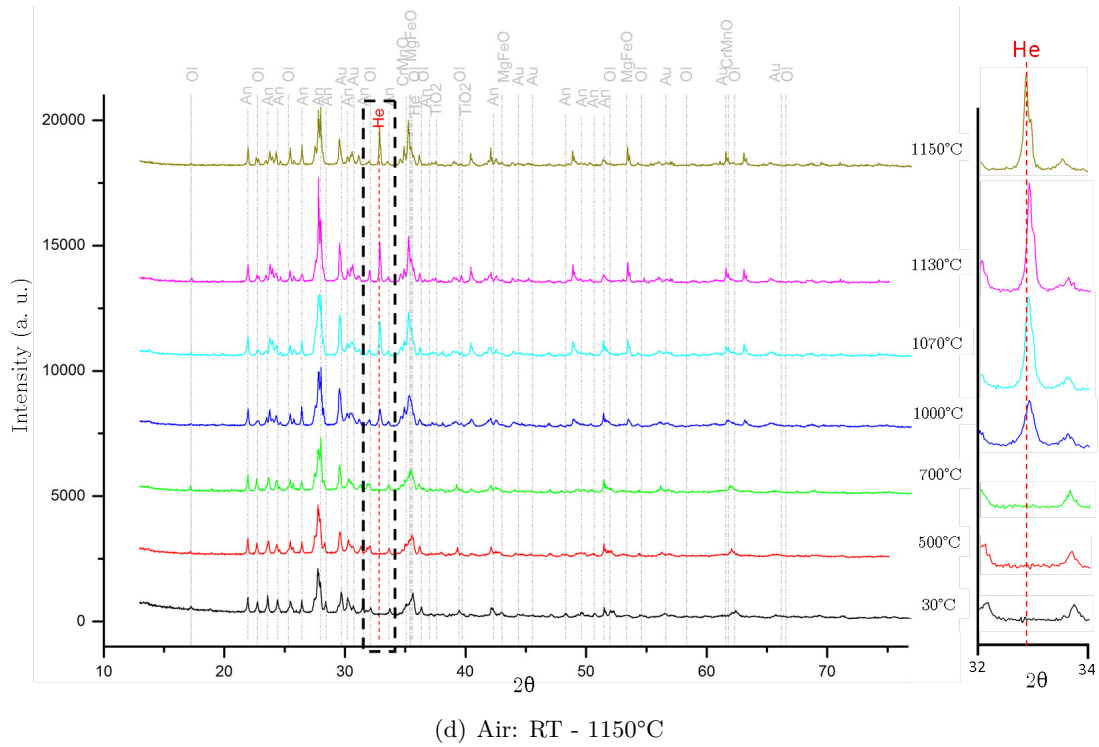
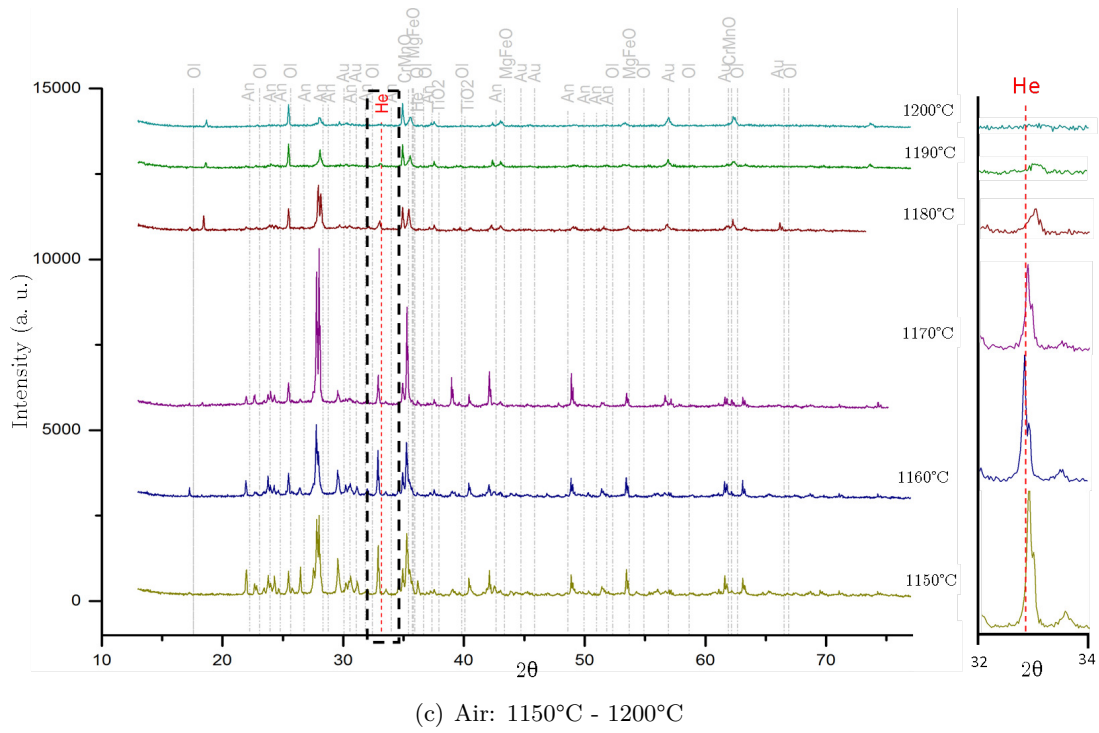


Figure 4.7: Temperature x-ray diffraction analysis of JSC-1A lunar simulant in vacuum (a, b) and in air (c, d). Abbreviations are given to minerals for more clarity. “An”: Anorthite, “Au”: Augite, “Ol”: Olivine, and “He”: Hematite. The main difference between air and vacuum is the hematite formation, more prominent in air. A smaller range, 32°-34°, which includes the main Hematite peak, is shown on the right of each XRD pattern.

The implementation of a vacuum chamber at the solar oven was considered, however, it was not feasible within this project to miniaturise parts of the set-up inside the vacuum chamber. Regolith sintering under vacuum in the solar oven could have been done for only one layer, giving too little information. The limited time at the solar oven was therefore dedicated to the optimisation of solar 3D printing in air.

4.2.2 Variations in mineralogical compositions

As shown previously in section 1.1, the lunar soil mineralogical composition can be split in three main areas: highlands, high-Ti maria and low-Ti Maria. To date, it is unknown where the construction site of a Moon village will be placed but its location tends towards being at the South Pole [85]. In this region, the lunar soil composition is not yet well defined, and therefore it is necessary to study a broad range of simulants, with different mineralogical compositions. Due to the time and budget constraints of the project, the solar sintering of only JSC-1A/2A was carried out and the sintering of other simulants was limited to the tests in traditional ovens.

4.2.3 Electrical charging

Solar winds impart charges to the lunar regolith especially at sunrise and sunset. The literature even reports some continuous flying fine grains over the lunar surface [86, 87]. The charged lunar soil will probably stick to the machine/robot performing the sintering [88]. Understanding the charges are important, transports mechanisms for AM applications could even be possible [89], however, this work focuses on the solar sintering process and the charges that could interfere with the hardware on the Moon were considered out of the scope of this project.

4.2.4 Abrasiveness

The abrasiveness of lunar regolith has been reported by Apollo astronauts to be an issue not to be neglected [90]. Nevertheless, the regolith simulant underwent erosion like all Earth materials, which makes it difficult to understand abrasiveness problems which cannot be encountered while sintering lunar regolith simulant with solar energy. This feature was therefore declared out of the scope of the project.

4.2.5 Light intensity variations

The solar flux density reaching the Moon is about 1000 W.m^{-2} but the solar exposure on the Moon varies according to the location. On Apollo sites, there is a continuous sunlight during approximately 14 days followed by 14 days of darkness. In polar regions, nearby the Shackleton crater, it is possible to find constant shadowed area, not interesting for solar sintering, as well as zones permanently exposed to the Sun. Obviously, the solar exposure time will influence the solar sintering yield. Moreover, the lack of atmosphere insures that

no perturbation, like clouds, could happen in between the sun and the solar concentrator during the sintering process. On Earth, even in good weather conditions, natural sunlight always fluctuates due to some ice crystals forming in the upper layers of the atmosphere, and diffusing the light. If these variations prevent the sintering of lunar regolith, the other available solution in this project was to use artificial sunlight.

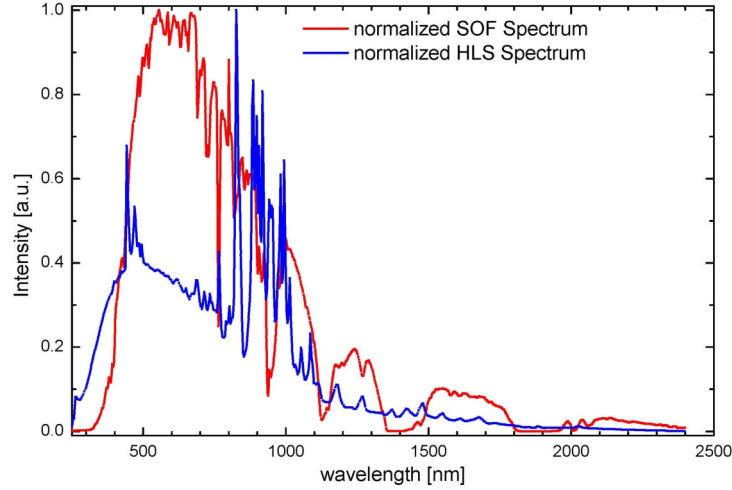


Figure 4.8: Spectra of the sunlight (SOF) and Xenon light (HLS) measured by the Institute of Solar Research of DLR.

Using Xenon lamps, the sintering process would be very close to the lunar conditions with a steady illumination condition during a long time exposure. In addition, Xenon lamps provide a spectrum that is close to the solar spectrum as shown in Figure 4.8.

4.2.6 Temperature variations

Moon temperature varies between -173°C and 100°C according to the location and the Sun position [6]. The machines performing the sintering have to handle such temperature difference and would most likely need some thermal insulator protections. However, this issue was considered out of the scope of this project. The changes in temperature will slightly affect the sintering process but within this project, the solar sintering will only start from powder at room temperature. The thermal fatigue resulting from the temperature fluctuation will also have an effect on the sintered material. This was shown at laboratory scale carrying out thermal cycling experiments. Thermal cycles were carried out on traditionally sintered samples of JSC-1A lunar simulant as presented section 3.3.2, i.e. pressed $\varnothing 20$ mm cylinders sintered at 1100°C for 3 hours. Two independent thermal cycling processes were carried out on two batches of 5 samples: one fluctuating from room temperature (RT) to 150°C , called “Hot cycling” and another fluctuating from -196°C to RT, called “cold cycling”. The samples for the hot cycling stayed each time 2 hours in a oven preheated at 150°C and the samples for the cold cycling stayed 2 hours in liquid nitrogen.

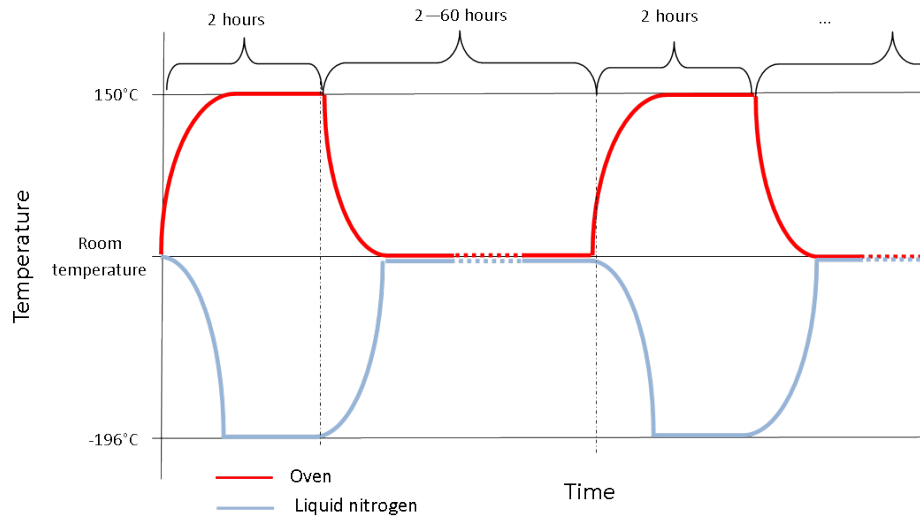


Figure 4.9: Thermal cycling illustration for two hot cycles (red curve) and two cold cycles (blue curve). In total, 26 cycles for both cycling were performed.

Cycles were performed 26 times to simulate two full years on the Moon. Since the samples were manually placed inside the ovens and into the liquid nitrogen, the samples could stay at room temperature from 2 hours to 60 hours (over nights, weekends). Figure 4.9 illustrates the cycles.

Two hours were sufficient for the material to stay at least 1.5 hour at the set temperature, as shown in Figure 4.10, where the sample temperature was measured from room temperature to 150°C with a Pt temperature sensor fixed inside a sample. No solution was found for measuring the ramp from room temperature to -196°C.

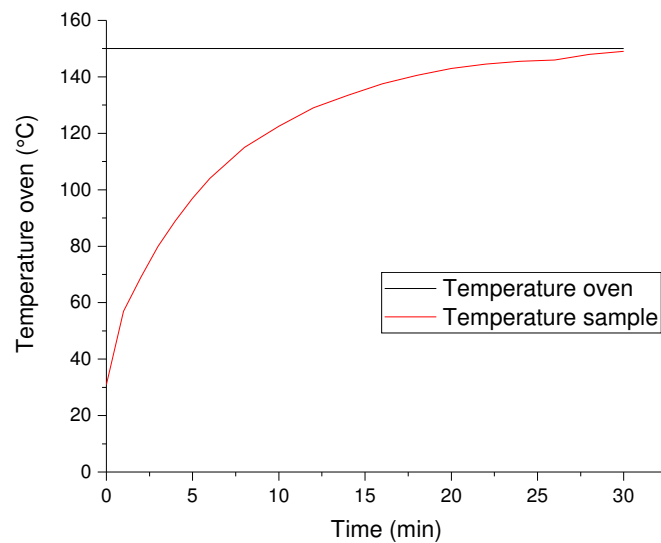


Figure 4.10: Temperature ramp after placing a sample in the oven at 150 °C.

Compressive tests were carried out on all samples which underwent thermal cycling as well as on reference samples which stayed at room temperature. Results are shown in Figure 4.11. Both cycles seem to reduce in average the investigated mechanical properties of the sintered regolith simulant. The compressive strength and Young's modulus of each individual sample were however very scattered as it is shown by the error bar, therefore the results should be interpreted as only a trend.

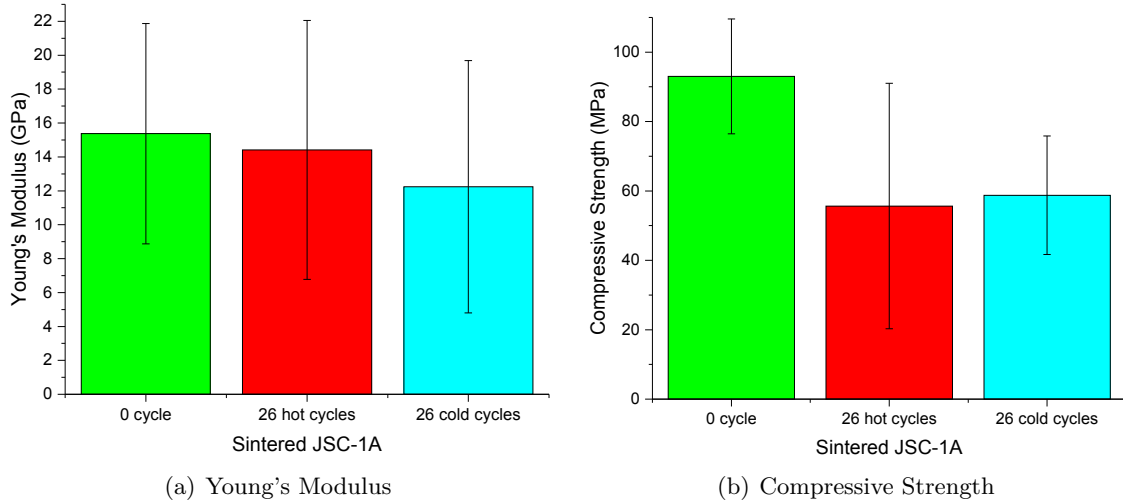


Figure 4.11: Young's Modulus and Compressive Strength of JSC-1A sintered at 1100°C for 3 hours after no thermal cycling, hot thermal cycling and cold thermal cycling.

4.3 Requirements for solar sintering

The scope of the project was now defined: it was relevant to solar sinter JSC-1A/-2A lunar simulant in air using a steady concentrated light source. The experimental set-up could be designed and built at the DLR Solar oven in Cologne, a facility part of the DLR Institute of Solar Research. It is however important to notice that the requirements for a solar sintering experiment are different whether the experiment takes place on the Moon or on Earth.

4.3.1 Requirements for solar sintering on the Moon

On the Moon any device:

- should be able to operate within a range of temperature from -173°C to 100°C [6].
- should operate continuously during at least 14 days to have a maximum yield during day time. If the solar sintering equipment is set up in an area with permanent solar exposure, it should be running on as long as possible.

- should have electronic and mechanical parts functional under vacuum. The lunar soil could interfere with the functioning of the equipment. The space weathering charging continuously the lunar soil, all devices should be able to operate while exposed to electrically charged particles. The system needs to be robust and the mechanical parts hermetic to fine abrasive dust particles.

And the sintering process:

- should be performed on a smooth and flat surface of lunar soil.
- should have an controllable sintering time and light intensity to carry out an adequate sintering of the regolith according to the sun exposure and the soil composition.
- should have an additional piece of equipment able to put regolith on top of the previously sintered layer in order to create 3D structures.

4.3.2 Requirements for solar sintering on Earth

On Earth, due to practical reasons and to create a brick using a solar sintering process within the time frame of the project, several of the requirements for sintering experiments on the Moon were not considered. Regarding the hardware:

- The testbed, containing the lunar regolith simulant, needed to have large enough dimensions to hold a sintered brick of 250 mm x 120 mm wide, defined in the work frame. Additional margins were considered to prevent any effect of the testbed edges on the sintered material. As for the testbed material, it had to sustain high thermal gradient and fatigue.
- None of the devices, with the exception of the testbed, had to bear abrasive materials, electric charges nor high temperature fluctuations.
- The equipment for depositing the powder as well as the 3-axis table were not adapted to work under vacuum.

As for the sintering process:

- The process started at room temperature and in air atmosphere. With the equipment currently available, no solar 3D printing could be performed in a vacuum chamber.
- The regolith, placed in a testbed on top of a 3-axis table, should move under a fixed solar beam.
- To achieve continuous sintering of a brick in the solar furnace, the sunlight should be continuous for about 5 hours without any weather perturbation. If artificial light is used, the light spectrum of the lamps should be close to the solar one.

- It should be possible to turn off the light source or a shutter should be provided in order to stop the concentrated light beam during the deposition of a new layer of powder.

4.4 Design of the experimental set-up and process monitoring

4.4.1 Concentrated light source

Experiments with actual sunlight and Xenon light were carried out at DLR-Cologne solar oven and solar simulator.

The High-Flux Solar Furnace, commonly called solar oven, is composed of an heliostat and a concentrator. The heliostat is a 52 m² flat mirror tracking permanently the sun and reflecting the light on the concentrator. The concentrator consists in 147 mirror facets, focusing the light inside the laboratory. The spot size at the focal point was about Ø40 mm. Figure 4.12 shows a sketch of the actual set-up. A pyrheliometer measures the Direct Normal Irradiance (DNI), the flux density of the sunlight. On a sunny day, with a DNI over 800 W.m⁻², the total power collected can be up to 20 kW with peak flux densities of 4 MW.m⁻² [91].

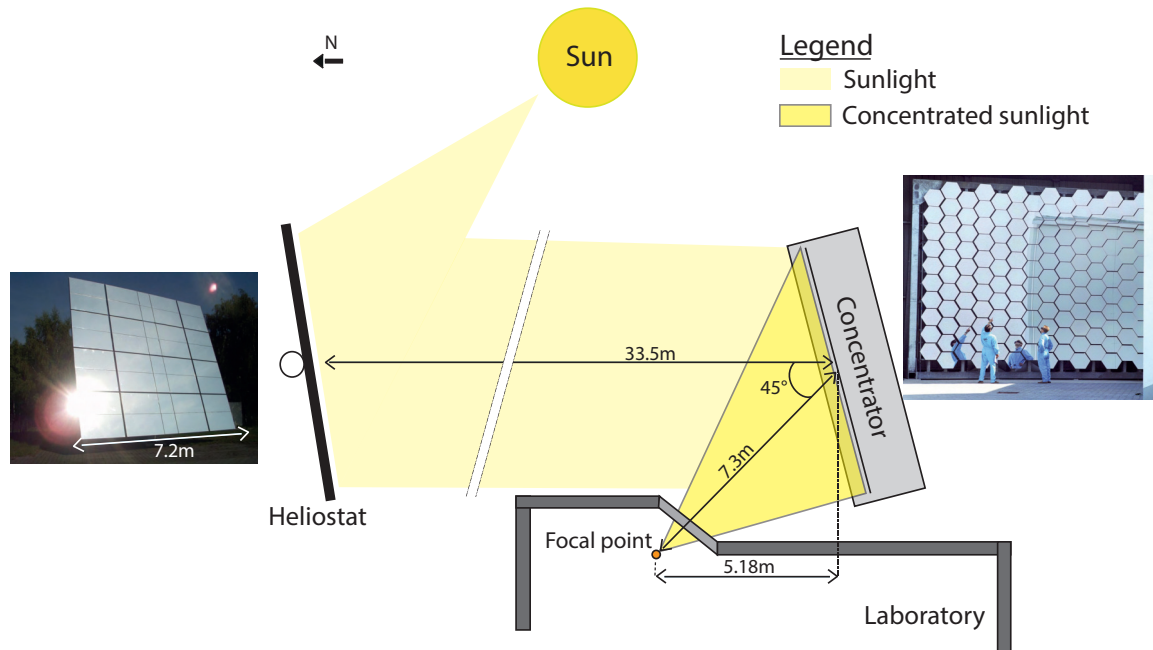


Figure 4.12: Sketch and pictures of the solar oven. The sunlight is reflected on the heliostat and then focused inside the laboratory thanks to the concentrator.

The Xenon High-Flux Solar Simulator [92], or solar simulator, is used for long experiments which require steady light conditions. It consists in ten elliptical reflectors with Xenon short arc lamps as shown in Figure 4.13. They provide all together a power of 21 kW with a flux density of 4.3 MW.m⁻². At the focal point, the spot could be smaller than at the solar oven, down to Ø20 mm.



Figure 4.13: Xenon lamps from the Xenon High-Flux Solar Simulator at DLR-Cologne.

4.4.2 Powder testbed

In this project, a set-up a 270 mm x 200 mm x 30 mm testbed made of 10 mm thick steel has been chosen thus respecting all the requirements mentioned previously. Figure 4.14 shows the aforesaid testbed. For experiments carried out in the solar simulator, the bottom plate of the testbed was replaced to aluminium to save mass. All manufactured objects were sintered in the middle of the testbed to ensure that the edges of the testbed, did not influence the sintering process.

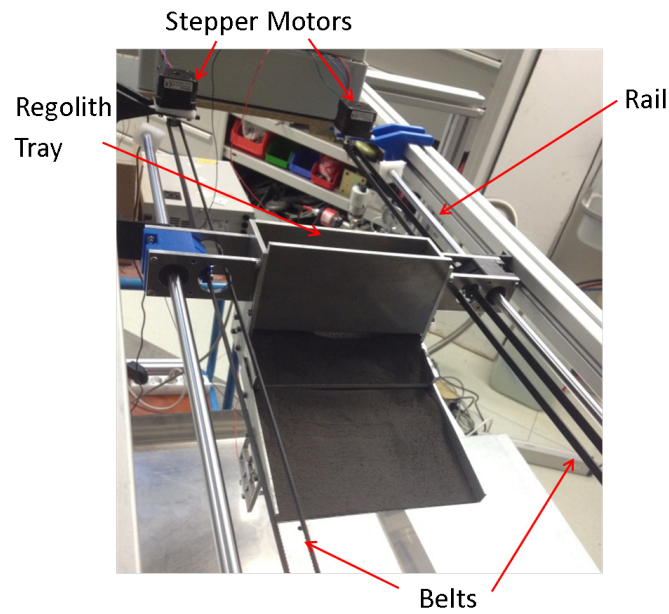


Figure 4.14: Testbed, 270 mm x 200 mm x 30 mm, filled with JSC-1A lunar simulant.

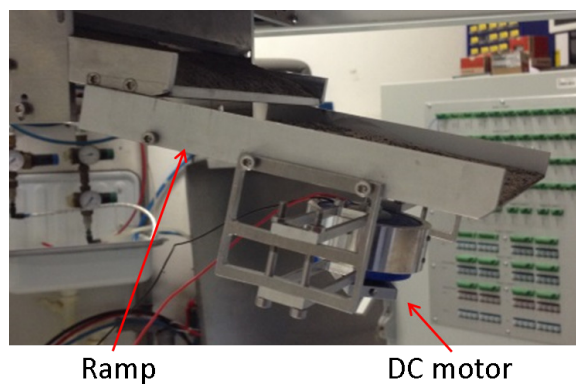
4.4.3 Powder feeder

In order to deposit loose powder on top of the previously sintered layer, an automatic powder feeder was implemented. It consists of a tray full of simulant, of a reclining ramp and a DC-motor rotating with an unbalanced mass. The tray was mounted on a linear stage and pulled by two belts driven using stepper motors. Figure 4.15 shows the device.

The DC-motor rotating with an unbalanced mass created vibrations triggering motion of the simulant towards the slope thus depositing a loose layer on the sintered material once combined with the linear motion of the tray.



(a)



(b)

Figure 4.15: Automatic powder feeder

The powder feeder was fully controlled by an Arduino MEGA controller programmed in C code. The full code can be found Appendix A.1. The two 30V-steppers motors were connected to Big Easy Driver motorshields. The DC motor was connected to a potentiometer to adjust the current and therefore the vibration of the ramp. The solid state relay was used as a programmable switch to turn on and off the DC motor. Figure 4.16 shows a sketch of the electronic components.

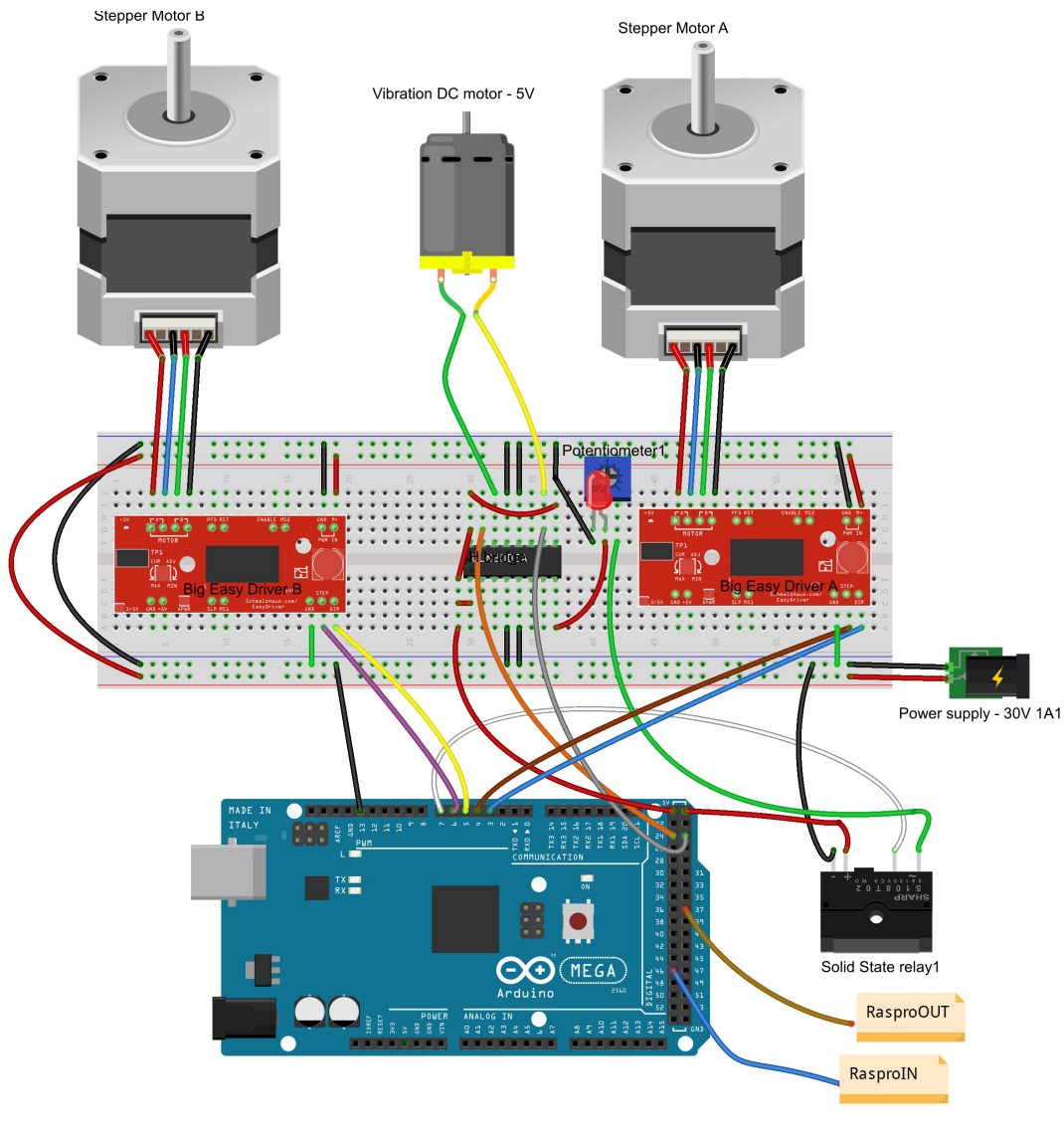
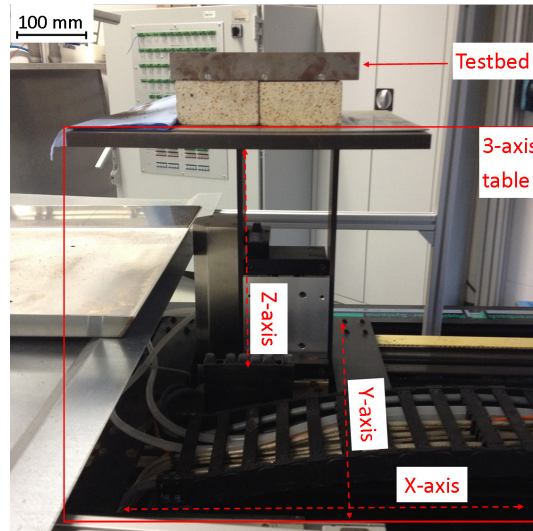


Figure 4.16: Sketch of electronic components used to automate the powder feeder

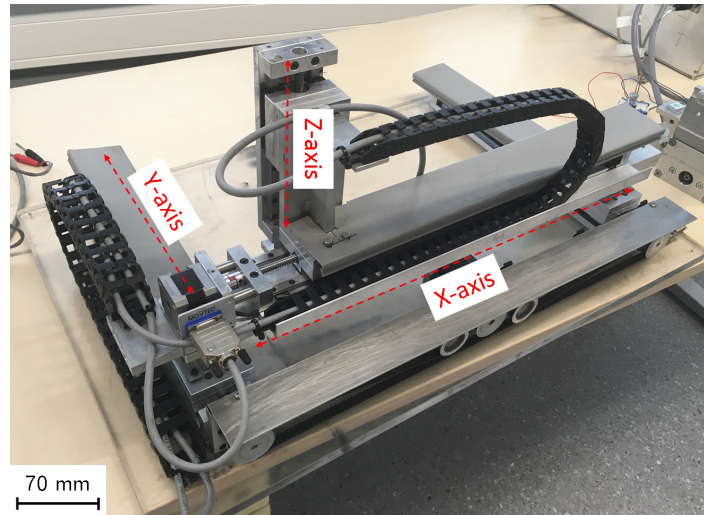
The system allowed the deposition of homogeneous layers of lunar regolith simulant. The thickness of the layers was adjusted varying the slope, the voltage of the DC-motor and the speed of the tray.

4.4.4 3-axis tables

Solar 3D-printing required the motion in all spacial dimensions of the solar beam or the testbed. At laboratory scale, it was easier to deal with a precise displacement of the testbed, that is the reason why, it was mounted on a 3-axis table. Two different 3-axis tables were used in this project. One, pre-assembled in the solar oven, Figure 4.17(a), could not be fully automated but was used for preliminary tests at the solar oven.



(a)



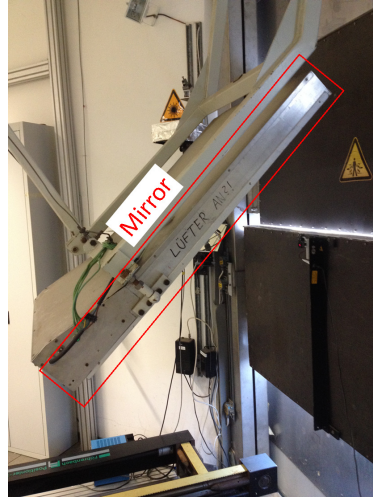
(b)

Figure 4.17: Testbed mounted on the 3-axis table in the solar oven (a) and the 3-axis table used in the solar simulator (b).

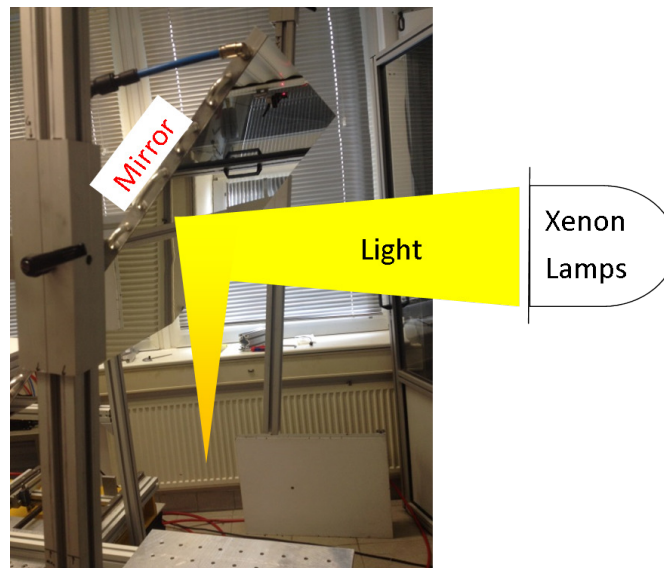
The other one, Figure 4.17(b), was a smaller off-the-shelf 3-axis table that could register positions and send/receive digital signals for being synchronised with the other devices of the set-up. A control unit connected to it was able to run G-codes, basic language for 3D-printers, piece of an example code is shown in the Appendix A.2.

4.4.5 Cooled mirrors:

An air-cooled mirror, Figure 4.18(a), was needed at the solar oven to change the direction of the solar beam from horizontal to vertical. In the solar simulator, the beam was more concentrated on the mirror and a water-cooled mirror, Figure 4.18(b), was required to reflect the concentrated solar energy from the Xenon lamps to the testbed below.



(a) Air-cooled mirror



(b) Water-cooled mirror

Figure 4.18: Mirrors reflecting the concentrated sunlight (a) and Xenon light (b).

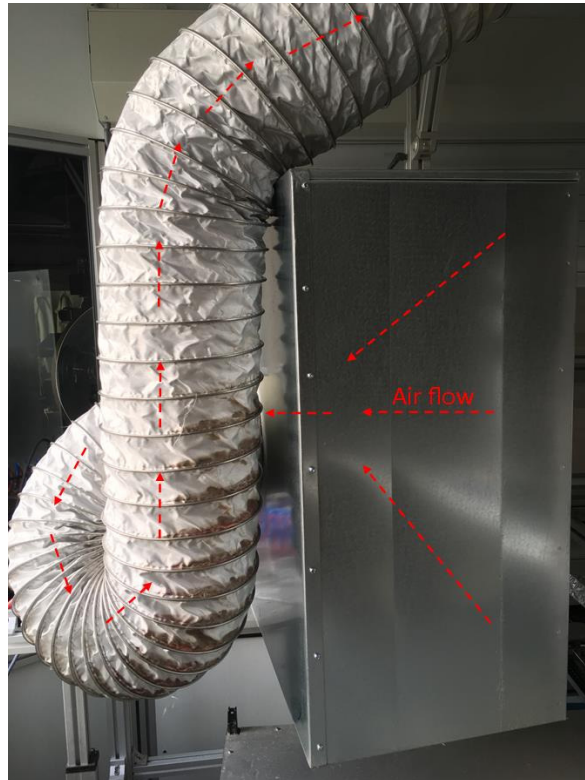
The two lamps were focused at two different places on the mirror since too focused beams resulted in the melting of the mirror. Using more Xenon lamps was not recommended by the solar simulator operators for the same reasons. An air blower (not shown on the picture), was mounted on the side of the mirror during sintering to blow away small particles which could fly up, stick to the mirror and reduce its reflectivity.

4.4.6 Extractor hood:

For long sintering processes in the solar simulator, a device for mitigating the dust deposition on the machines was required. An extractor hood was installed to suck up most of the small particles blown away by an air flow created by fans, placed on the side of the mirror (not yet installed on pictures). This extractor reduced the overall dust deposition in the room.



(a) Front view

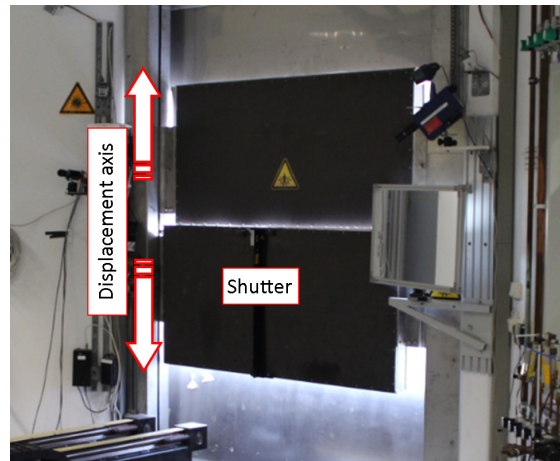


(b) Side view

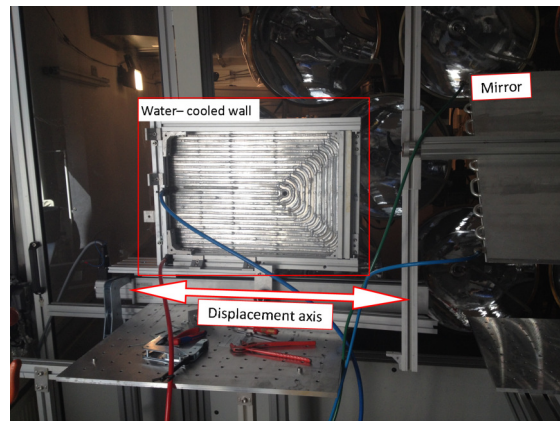
Figure 4.19: Extractor hood in the solar simulator.

4.4.7 Light Shutter

Two different systems were used in the solar oven and the solar simulator. The solar oven has an integrated shutter, remotely controlled, used for adjusting the incoming light intensity. This shutter allowed fast opening and closure but could not be controlled nor programmed by an exterior system. As for the solar simulator, the Xenon lamps could not be switched on and off like regular light bulbs. Immediately after each ignition, while the electrodes are being heated, erosion occurs on their surfaces. The eroded tungsten settles on the inside of the bulbs which causes the blackening of the lamp and reduces its lifetime. A water-cooled wall was therefore implemented since no equipment was available for obstructing the concentrated light. This water-cooled wall was mounted on a rail that could be programmed and synchronised with the other devices. The only drawback was the lower speed of opening and closing compared to the shutter of the solar oven. Around 5 seconds were necessary for fully blocking the light or letting it shine on the regolith simulant. Both pieces of equipment are shown in Figure 4.20.



(a)



(b)

Figure 4.20: Solar oven shutter (a) and solar simulator water-cooled wall (b).

4.4.8 Process monitoring

Monitoring of the sintering process was performed with an Infra-red (IR) camera, a pyrometer and also mainly by naked eyes, based on the experience accumulated over the several test campaigns.

The pyrometer was only available at the solar oven and could give the temperature over time at the single spot. The IR camera was available in both, solar oven and simulator, and could provide a mapping of the temperature in its field of vision. Figure 4.21 shows the mentioned equipment. The during- and post-process observations were however the most used monitoring tool to control the sintering quality of the solar sintered parts. The process parameters could not change during the process and a trial and error approach was therefore targeted.

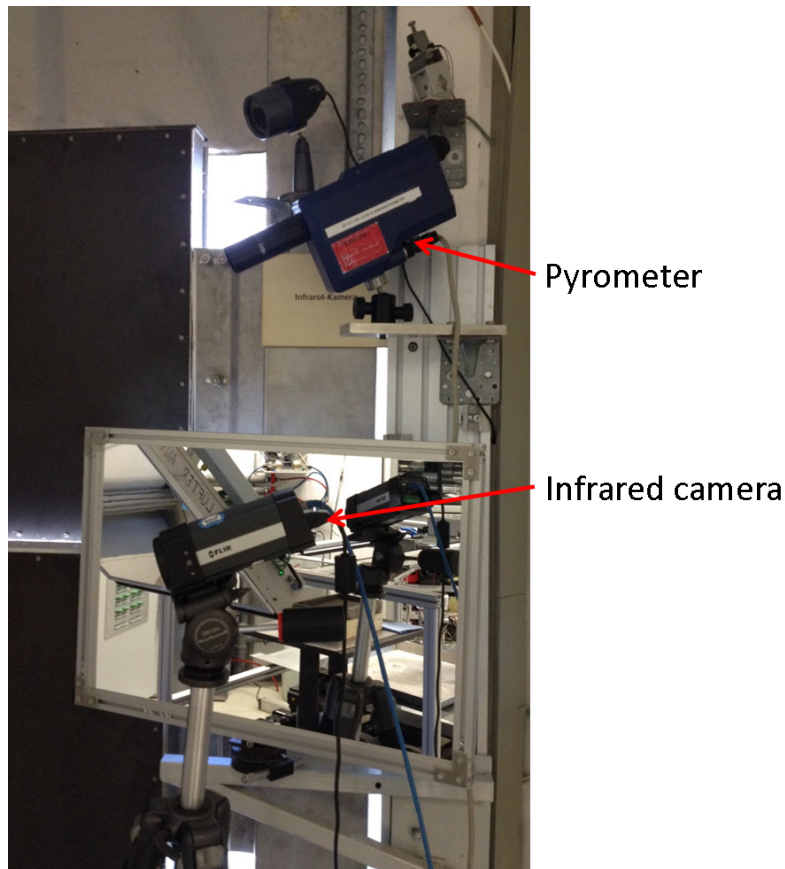


Figure 4.21: Pyrometer and infra-red camera at the solar oven

4.4.9 Complete set-up

Figure 4.22 shows the CAD model of the current set-up in the solar oven. Figure 4.23 exhibits the same set-up during operational solar sintering.

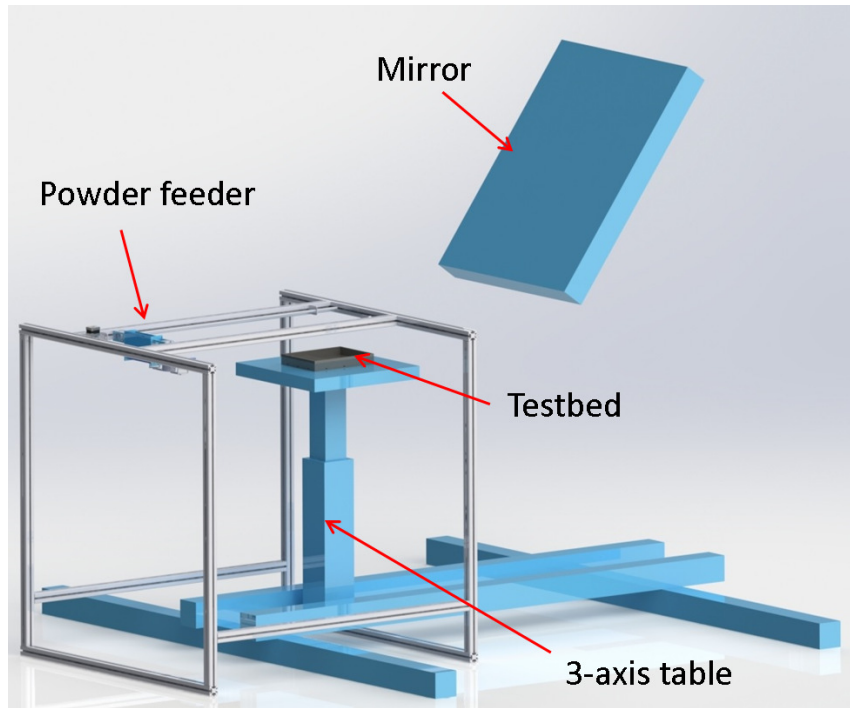
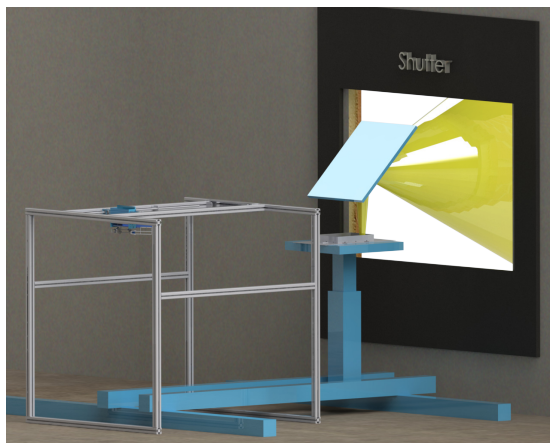


Figure 4.22: CAD drawing of the set-up



(a) Inside view



(b) Outside view

Figure 4.23: Solar oven in operation. The yellow cone represents the concentrated solar light.

Figure 4.24 shows the actual set-up in the solar oven and Figure 4.25 the one in the solar simulator.

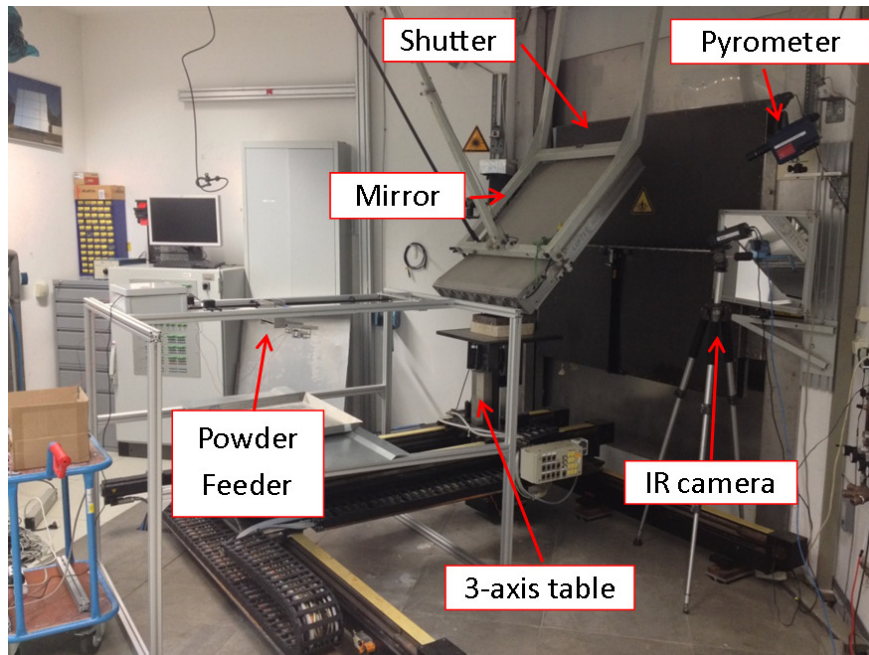


Figure 4.24: Complete device set up in the solar oven.

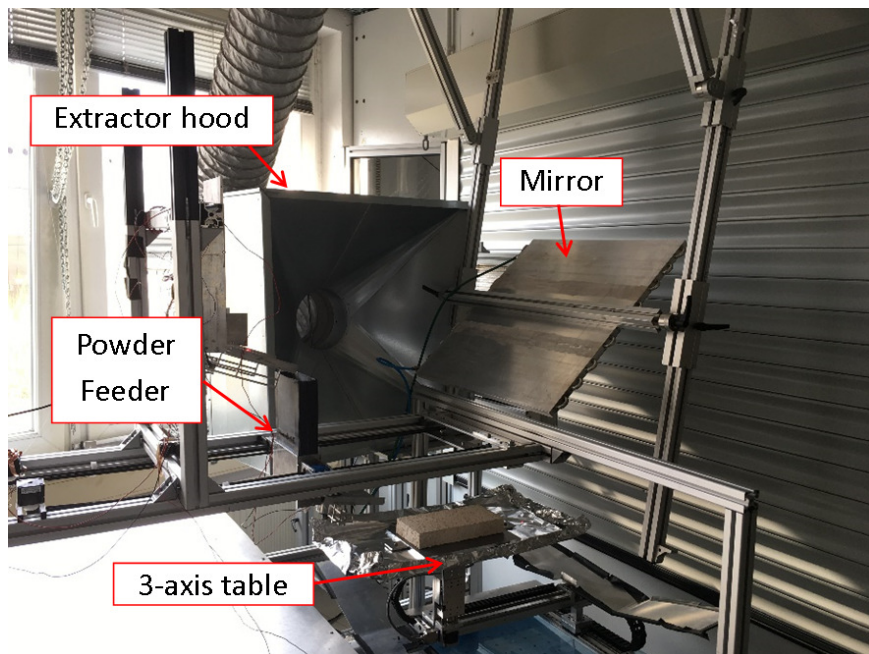


Figure 4.25: Complete device set up in the solar simulator. The Xenon lamps are behind the metallic jalousie and the water-cooled wall cannot be seen on the picture.

5 Solar additive manufacturing experiments

5.1 Sintering strategy

5.1.1 Sets of parameters allowing 3D objects manufacturing

Several parameters can influence a sintering process. For solar sintering, there is a correlation between scanning speed and the power of the concentrated light. In principle, since the heat conductivity of lunar regolith is extremely low, a same sintered material can be obtained with a low scanning speed and a relatively low power as with a high scanning speed and a high power of concentrated sunlight. In this project, at the solar oven, a solar irradiance of 800 W.m^{-2} provided a sharp beam and enough energy to sinter lunar regolith opening less than 20% of the shutter. No measurement of the actual flux density could be performed. At the solar simulator, two Xenon lamps were used to sinter the regolith without damaging the water-cooled mirror thus providing a power density at the focal point around 1200 kW.m^{-2} , as shown in Figure 5.1. The sintering was performed at the focal point to get the best resolution possible on planar sintering, with a 20 mm diameter spot. The main parameter to find with trial and error was therefore the scanning speed to get an acceptable sintering over 1D, 2D and 3D.

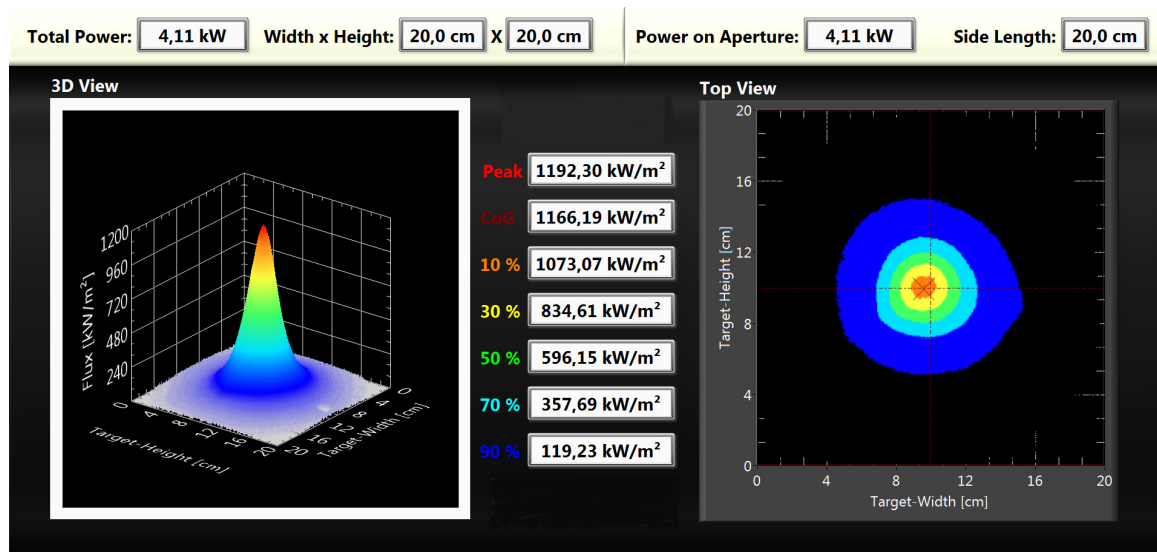


Figure 5.1: Modelled concentrated solar beam from the measured energy provided by two Xenon lamps.

5.1.2 Sintering a line - 1D printing

The first step was to sinter a line, 20 mm wide due to the 20 mm diameter spot from the solar beam at the solar simulator. The beam diameter was about 40 mm at the solar oven. This line had to be flat enough to be able to bond to the adjacent ones in order to form a planar surface, and solid enough not to break due to the thermal stresses generated during the process. The power from the Xenon lamps and the distance from the mirror to the test bed (focal distance) being fixed, only the scanning speed could be adjusted to obtain the best quality of sintering. After testing, 48 mm.s^{-1} seemed to be the most suitable scanning speed for sintering JSC-1A and JSC-2A lunar simulants. Higher speed, over 50 mm.s^{-1} , led to a loose sintered line and a slower speed, under 42 mm.s^{-1} , produced curved line with molten regolith on the edges as shown in Figure 5.2. The same sintered part, Figure 5.3, is shown from a top view with a scale.

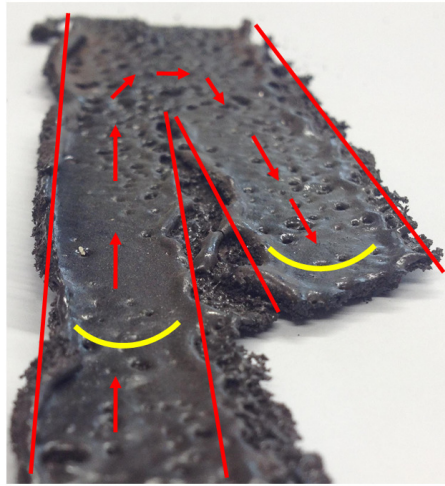


Figure 5.2: Two lines sintered continuously and differentiated by red lines. The arrows show the path of the solar beam. The yellow curves enhance the curvature of each layer.

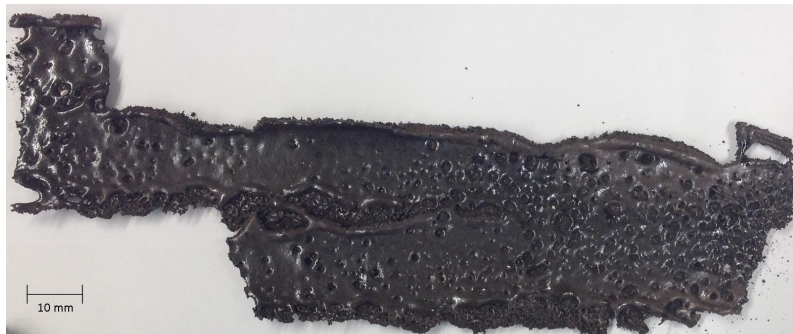


Figure 5.3: Typical sintered regolith part after a too slow sweeping of the concentrated solar beam over the surface.

5.1.3 Sintering a layer - 2D printing

Once a line was sintered without curvature, another parameter had to be fixed to sinter a full layer: the distance between the lines. Some overlaps were indeed required to connect the lines in a 2D plane. With the same strategy as for setting the scanning speed, a trial and error approach was the easiest way to find the right distance between the lines. Solar sintering JSC-1A and JSC-2A, with an interline space over 20 mm, the lines were not connected together and with an interline space smaller than 10 mm, molten regolith formed at the overlap between the first and the second sintered lines, which affected the planarity of the sintered surface. At the solar simulator, the optimal interline distance was found to be 14 mm, meaning that an overlap band of 6 mm width was sintered twice to ensure the cohesion between the two adjacent lines. Figure 5.4 shows an acceptable sintered layer in comparison with Figure 5.5, which shows a typical example of a surface where too much overlapping occurred during the 2D sintering.

At the solar oven 2D layers could also be sintered but the surface was rough and wavy due to the inhomogeneous sintering. The part was indeed partially molten and partially unsintered due to the light intensity variations coming from the Earth atmospheric fluctuation. The unevenness of the 2D planes prevented the next layer of lunar regolith simulant to bond in order to create 3D parts.

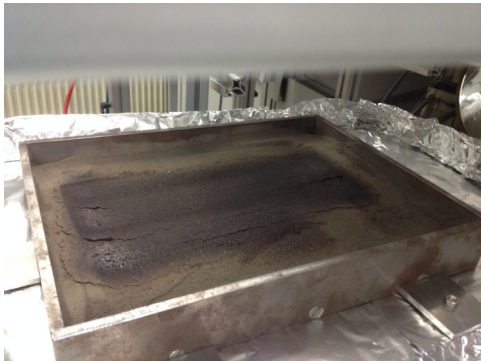


Figure 5.4: Acceptable planar sintering of JSC-2A lunar regolith simulant. Dimensions of the testbed: 270 mm x 200 mm.



Figure 5.5: Typical sintered plane of JSC-2A lunar regolith simulant where sintered lines are too close to each other. Dimensions of the testbed: 270 mm x 200 mm.

5.1.4 Sintering a brick - 3D printing

The last step was to connect sintered 2D planes together to obtain 3D printed building elements. This step, only performed at the solar simulator, required to have the cooled wall, the 3-axis table and the powder feeder perfectly synchronised in order to be as efficient as possible for sintering and feeding without burning the hardware with the concentrated Xenon light. Figure 5.6 shows the algorithms used for synchronising the different pieces of equipment, all having a dedicated software for functioning.

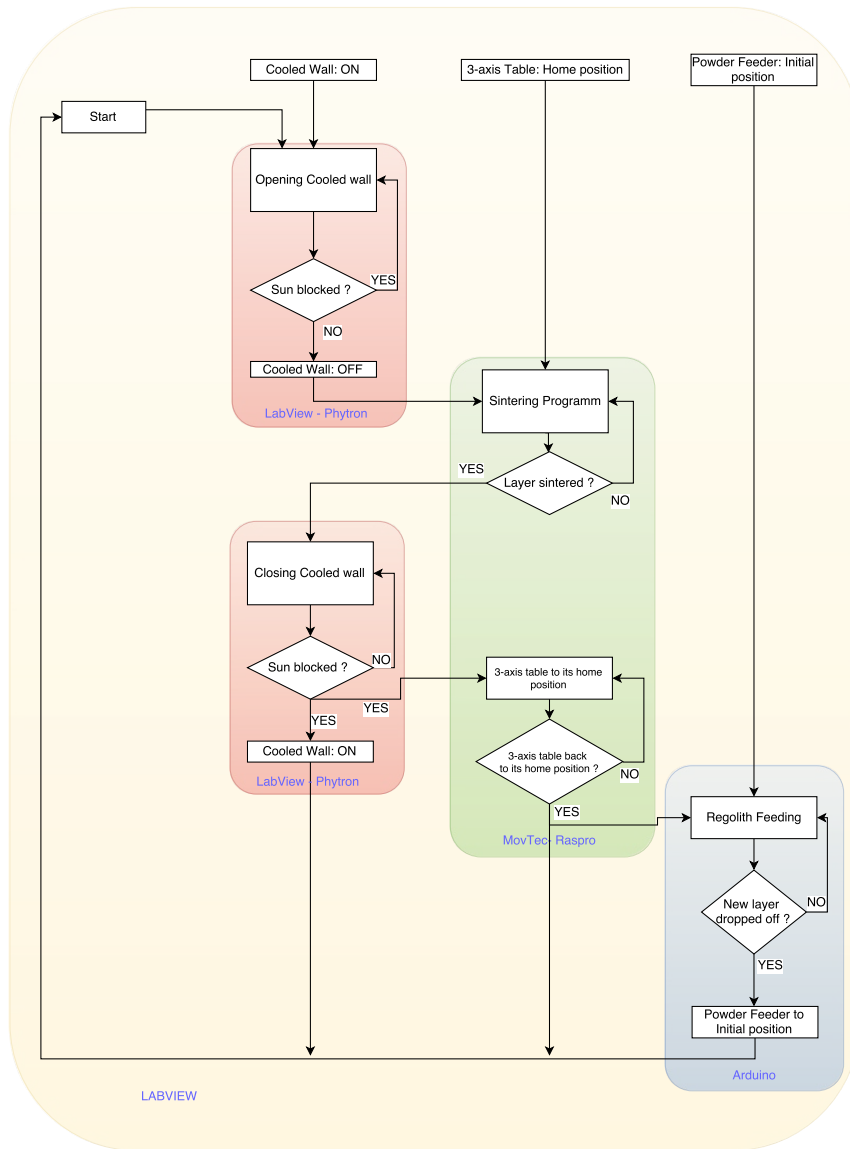


Figure 5.6: Algorithm for 3D printing building elements at the DLR solar simulator.

Regarding the sintering itself, although, when no substrate material was used, the first sintered layer was around 1 mm thick, the following layers were thinner, around 0.1 mm, since each layer had to bond with the previous sintered one. Parameters to deposit the suitable quantity of lunar regolith simulant were directly linked to the powder feeder system. With the current set-up, the angle of the slope was fixed to 103° , Figure 5.7, and the voltage of the vibration motor to 7.5 V. It represented the deposition of 15 ± 2 g of lunar regolith simulant spread over the testbed surface, 200 x 280 mm. During the tests, when more than 20 g was poured, on top of the previous sintered layer, high delamination could be observed between the sintered layers. When less than 8 g of regolith simulant was poured, molten regolith formed on the sintered surface.

Stops longer than 30 seconds, within a layer or between layers had to be avoided in order

to successfully 3D-print objects. All attempts to reheat the top sintered layer in order to restart the process after a stop were unsuccessful. Each time, the delamination of the new sintered layer could be observed. Section 7.5 explains in detail this phenomenon.

Table 5.1 summarises the parameters used to produce a 3D printed object from JSC-2A lunar regolith simulant and concentrated Xenon light. The available quantity of JSC-1A lunar simulant was too little to manufacture 3D objects. Pictures of 3D printed objects produced with these parameters can be seen in section 5.2.

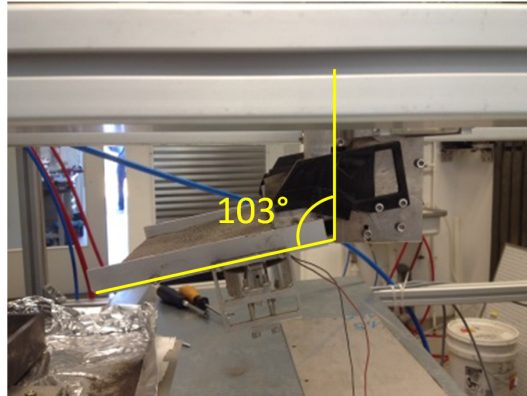


Figure 5.7: The slope angle of the powder feeder was fixed to 103° .

Table 5.1: Recap chart of sintering parameters of JSC-2A.

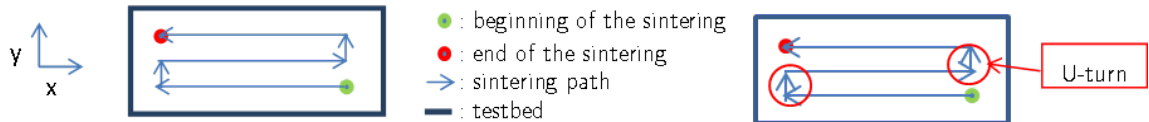
	Parameters	Value
Xenon lamps	Flux density	1200 kW.m^{-2}
	\varnothing spot focal point	20 mm
Powder Feeder	Voltage vibration motor	7.5 V
	Slope angle	103°
Sintering 1D	Scanning speed	48 mm/s
Sintering 2D	Inter-layer distance	14 mm
Sintering 3D	Layer thickness	0.1 mm
	Maximum stop duration	30 sec

5.2 Solar sintering campaigns

All relevant tests performed over the different campaigns at the DLR solar simulator are listed below. The tests were numbered to be easily referenced.

5.2.1 First experiments

Test 1



Parameters

- Distance between lines: 20 mm
- Scanning speed: 50 mm/s
- Pause between positions: 200 ms
- Substrate: Loose regolith
- Material: As-received JSC-2A lunar regolith simulant

This manufactured part was the first 3D printing trial. The part showed an homogeneous 2D sintering, Figure 5.8. After 30 minutes, the part, shown in Figure 5.9 could carry its own weight but was easily breakable.

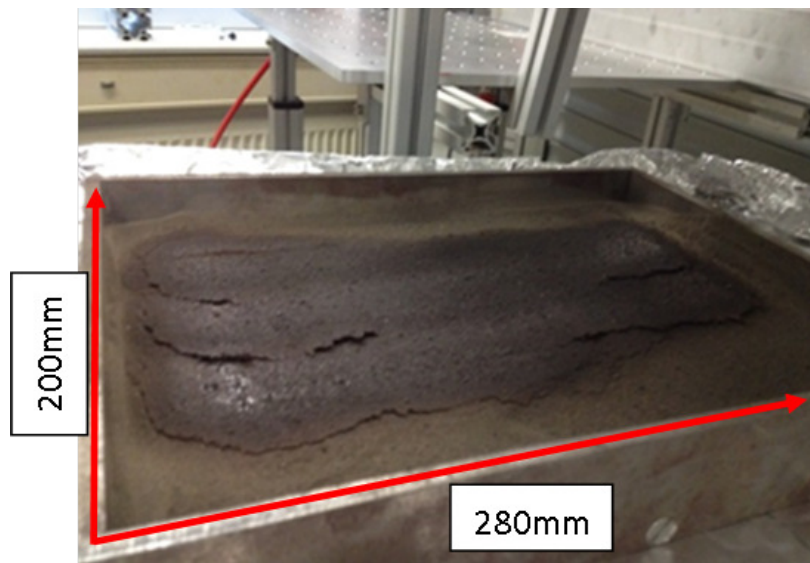


Figure 5.8: First sintered layers using Test 1 parameters.

It could be observed that the edges were rolling up in the direction of the sintering. It was hypothesised that this behaviour was due to a thermal gradient during heating. The 200 ms pause between the registered positions, forming the sintering path, were responsible for the extra heat and light melting visible at the U-turns. At this step, the hardware was responsible for these pauses and they could not be avoided.

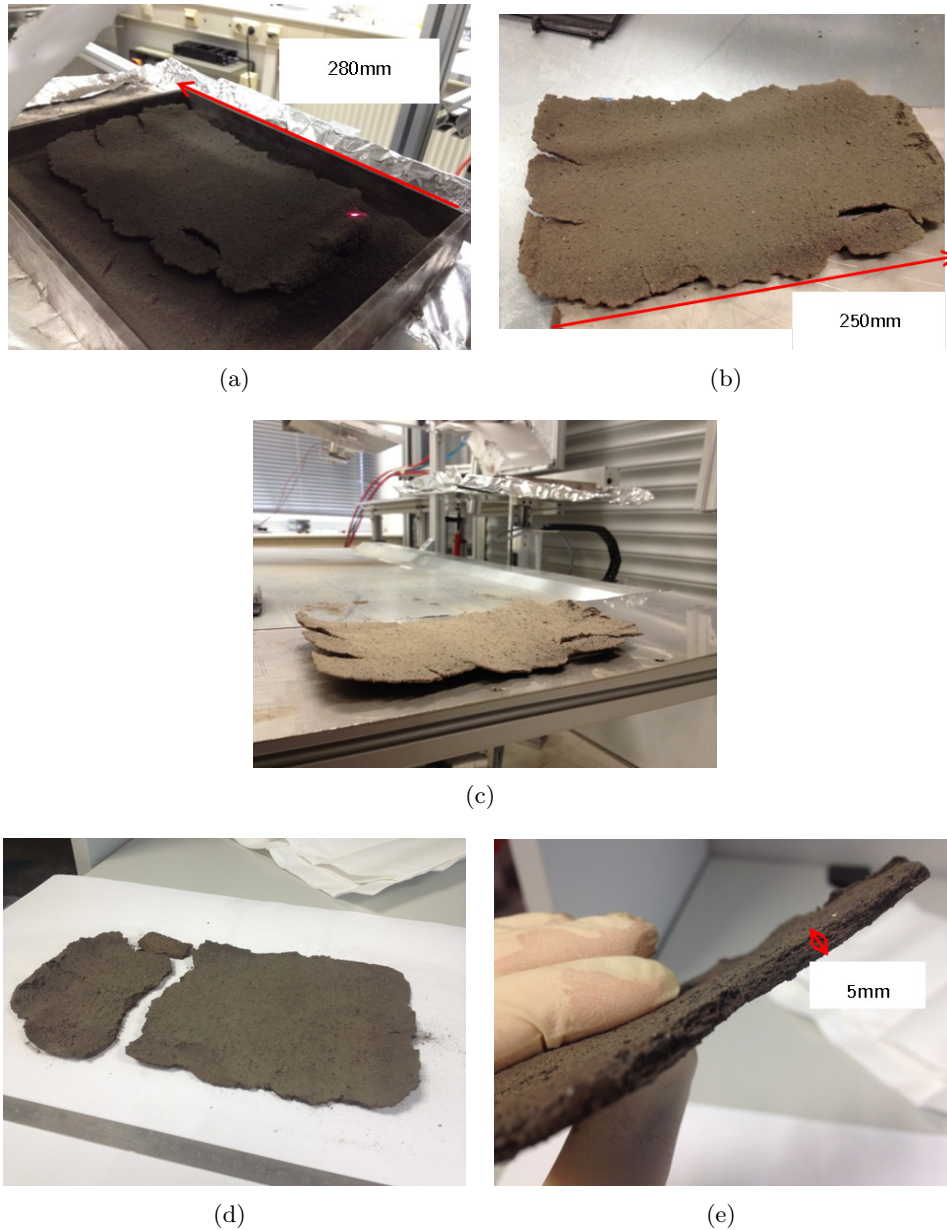
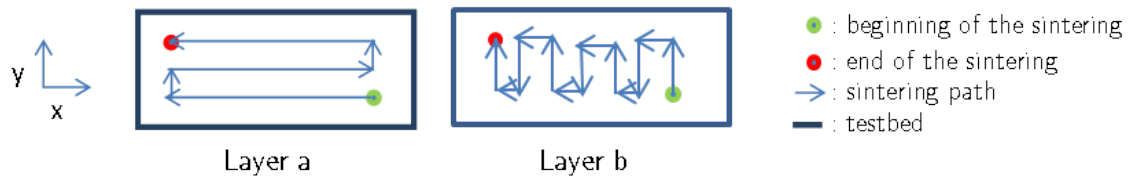


Figure 5.9: Sintered object after a 30-minute process using Test 1 parameters. Different view angles (a-e).

Test 2



Parameters

- Sintering path: Layer a / Layer b, alternately
- Distance between lines: 15 mm
- Scanning speed: 50 mm/s
- Pause between positions: 200 ms
- Substrate: Loose regolith
- Material: As-received JSC-2A lunar regolith simulant

The second test targeted a new sintering path. The beam was now sweeping the surface of a layer over the length and the next layer was sintered along the width of the part. With these parameters a stronger sintering was obtained: the printed part did not break during manipulation and was not as breakable as the one obtained from Test 1. However, Figure 5.10 shows that all the edges rolled up leading to a wavy profile of the brick. Trials to stop and restart the process on a previously sintered layer resulted in a lack of bonding between the layers and in the production of independent layers with poorer and poorer quality as shown in Figure 5.11 and 5.12. Delamination, shown in Figure 5.13, is explained in detail in section 7.4.

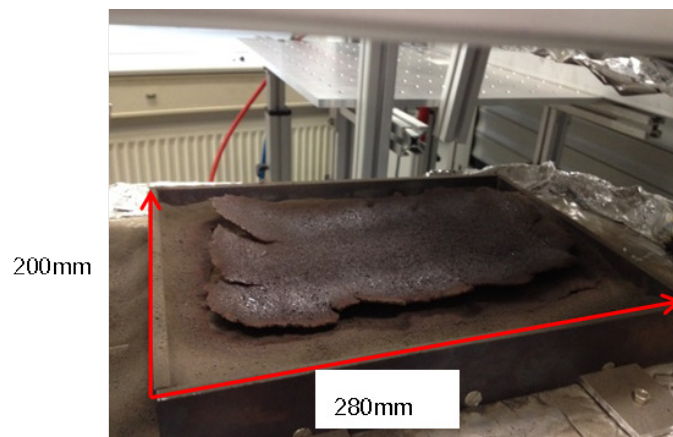


Figure 5.10: Sintered object after a 30-minute process using Test 2 parameters.

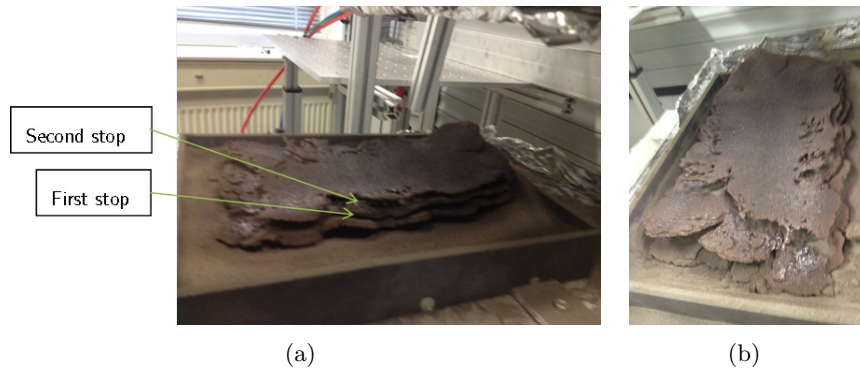


Figure 5.11: Stops of several minutes in the process led to the formation of independent objects on top of the previous sintered one: no bonds between the parts were formed. Different view angles (a, b).

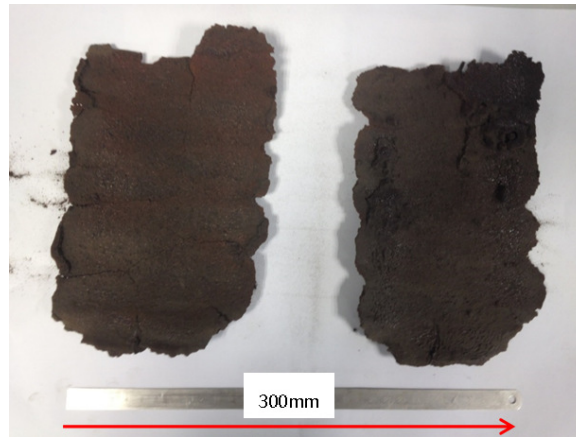


Figure 5.12: Bottom and middle sintered parts.

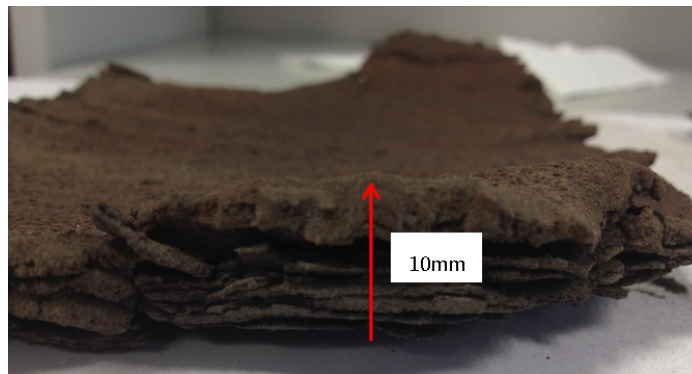
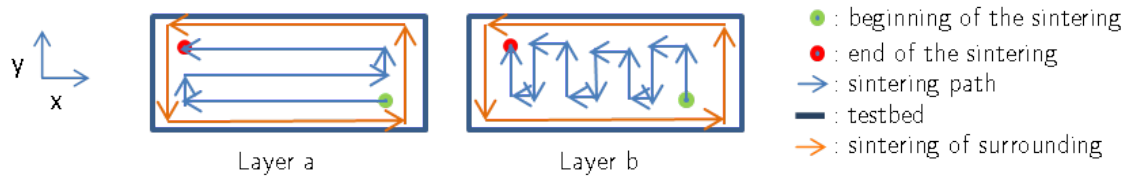


Figure 5.13: Delamination of successive groups of layers at the edges. These groups of layers, around 0.5 mm thick, are constituted of 5 sintered layers. More details about delamination are given in section 7.4.

Test 3Parameters

- Sintering path: Layer a /Layer b, alternately and sintering/melting of the surrounding area
- Distance between lines: 15 mm
- Scanning speed: 48 mm/s
- Scanning speed of the surrounding: 38 mm/s
- Pause between positions: 200 ms
- Substrate: Loose regolith
- Material: As-received JSC-2A lunar regolith simulant

This third test aimed at reducing the warping of the sintered part which prevented the AM of thicker bricks. The idea was to sinter/melt first the contour of the testbed to create an area with high liquid phase content around the brick. This liquid phase would play a role of interface between the brick and the poorly sintered warped edges. Once the sintering process complete, curved edges should be cut out in order to get a flat brick. This idea worked partially: a molten contour played a role of interface, however the brick was still not perfectly flat. This was the first relatively thick and solid manufactured brick with a thickness between 15 and 20 mm. Figure 5.14 shows the sintered part in the testbed at the end of the sintering process. The part removed from the testbed is presented in Figure 5.15.

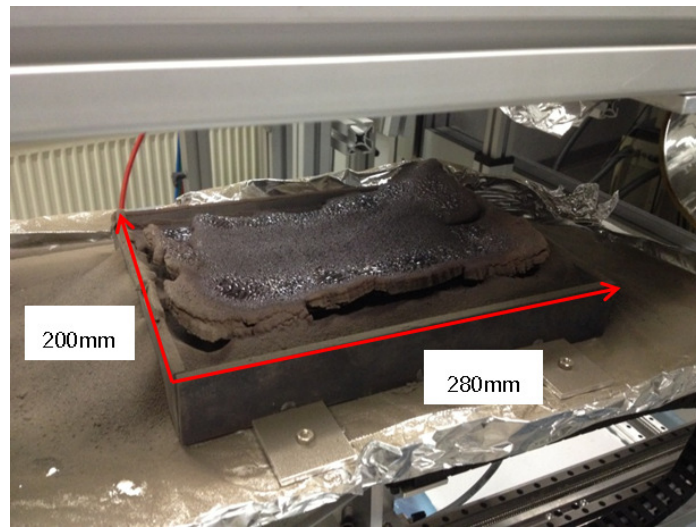
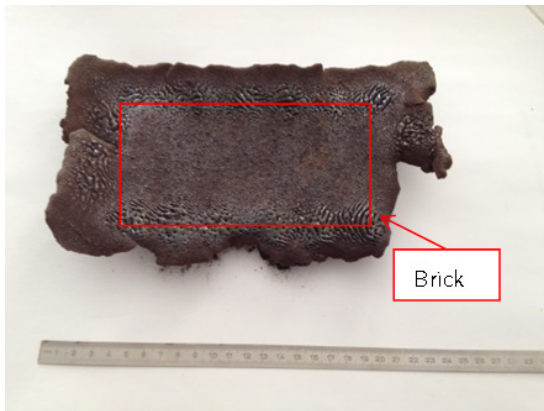


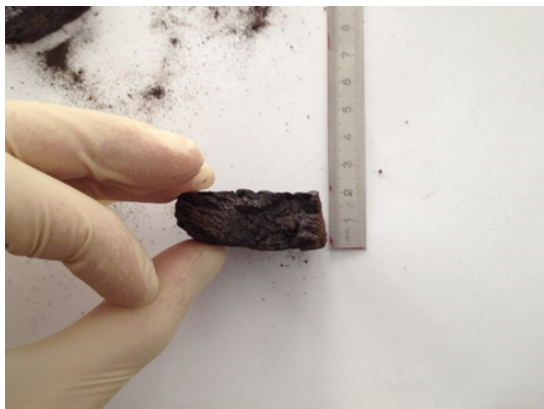
Figure 5.14: Sintered object after a process of 3 hours and 45 minutes using Test 3 parameters



(a)



(b)



(c)



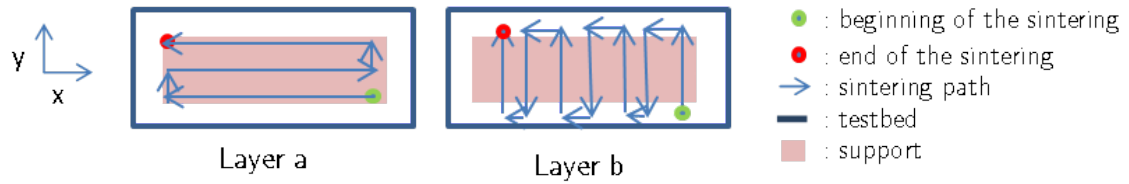
(d)

Figure 5.15: Brick obtained using Test 3 parameters. Different view angles (a-d).

5.2.2 Sintering on a solid substrate

Test 4

From Test 4 onwards, a solid substrate was used for each sintering experiment, the objective being to sinter high quality parts. The use of a solid substrate is discussed further, in section 7.1.



Parameters

- Sintering path: Layer a / Layer b, alternately
- Distance between lines: 14 mm
- Scanning speed: 48 mm/s
- Pause between positions: 200 ms
- Substrate: Porous ceramic brick
- Material: JSC-2A regolith simulant with particles smaller than 100 μm

Test 4 repeated the main features of Test 2 sintering path. The sintering speed was slightly reduced and a porous brick was used as substrate. JSC-2A lunar simulant was sieved and only particles $<100 \mu\text{m}$ were sintered.



Figure 5.16: Brick obtained using Test 4 parameters. The picture was taken right after the end of the process.

The first layers were strongly bonded to the substrate, thus making the 3D-printed brick really flat as shown in Figure 5.16. One side was detached from the substrate due to a small programming mistake leading to a bad overlapping between layers sintered along x and y axis. After 4h30, the process had to be stopped during 7 minutes to refill the powder feeder. The reheating phase partially worked: only the part which was perfectly flat bonded with the sintered layer after the stop. The part which did not bond well to the brick was removed, Figure 5.17.

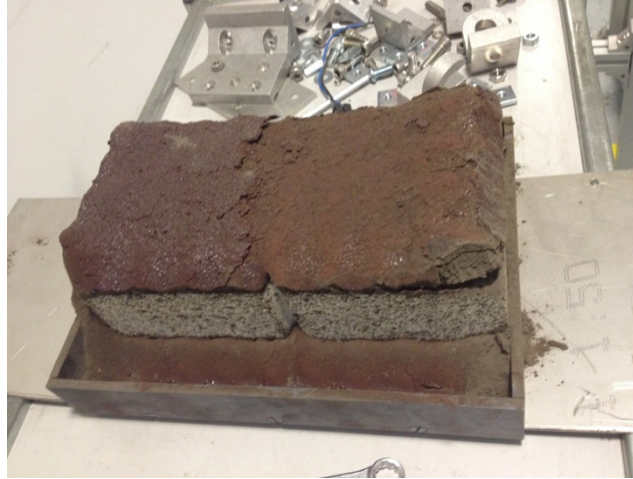


Figure 5.17: Brick obtained using Test 4 parameters on its substrate.

This new layer was totally removed in Figure 5.18. There was also weakly sintered regolith at the edges which could be easily removed.

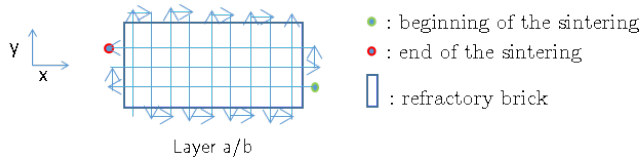


Figure 5.18: Brick obtained using Test 4 parameters. The substrate and the top layer, created after the 7-minute stop, were removed.

The sintering of sieved regolith was not performed again due to the long sieving process for collecting enough material and the assessed low impact of the smaller grain size on the warping issues, the main focus of these first sintering trials.

Test 5

From Test 5 onwards, the control unit of the 3-axis table was changed in order to have more control of the motions. The pauses between positions, non-intentional in the Tests 1 to 4, were now voluntary added in order to reproduce the processes tried with the former control unit. The scanning strategy, presented in a different sketch below, was unchanged, alternating a layer along the length and one along the width.

Parameters

- Sintering path: Layer a / Layer b, alternately
- Distance between lines: 14 mm
- Scanning speed: 48 mm/s
- Pause between positions: 200 ms
- Substrate: Porous ceramic brick
- Material: As-received JSC-2A regolith simulant

Test 5 aimed at reproducing Test 4 results. The only difference was the use of a slightly smaller substrate and the lunar regolith simulant was not sieved but used as-received.

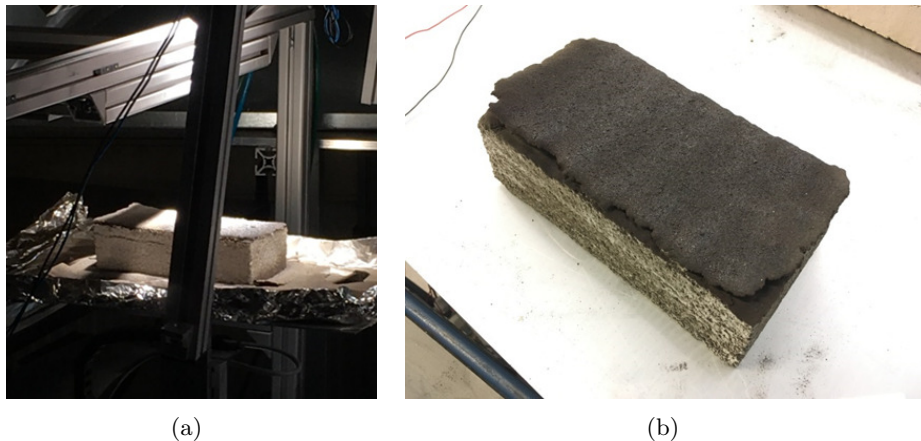
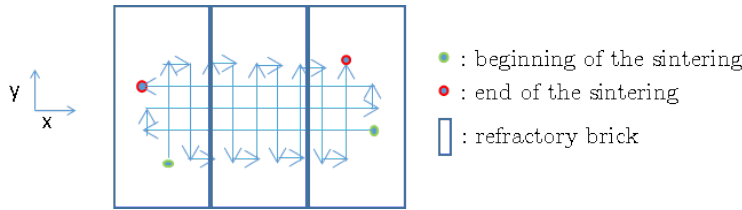


Figure 5.19: During the sintering process (a) and after a 40-minute process (b).

The sintering process was stopped after 40 minutes due to the bending of the brick which prevented the formation of a strong thick sintered part over a longer time. The substrate surprisingly did not play its role as for Test 4.

Test 6Parameters

- Sintering path: Layer a / Layer b, alternately
- Distance between lines: 14 mm
- Scanning speed: 48 mm/s
- Pause between positions: 200 ms
- Substrate: 3 porous ceramic bricks
- Material: As-received JSC-2A regolith simulant

The objective of Test 6 was to reproduce again the part obtained in Test 4. The part was sintered over the 3 porous ceramic bricks thus limiting the bending of the part.

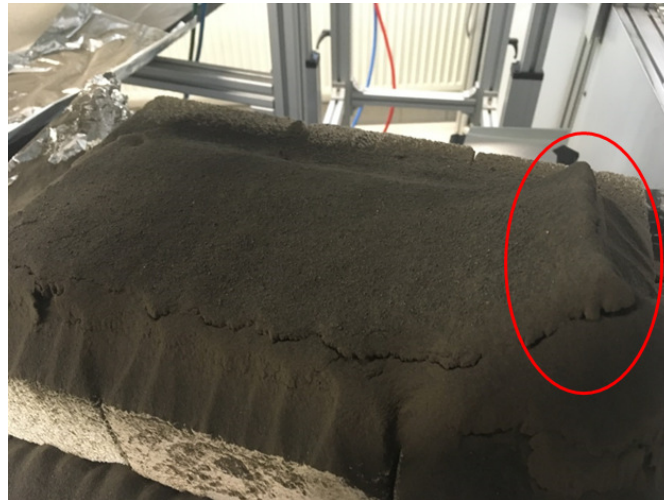


Figure 5.20: Solar sintered part after a 5-hour process and Test 6 parameters.

A formation of a hill was observed due to the feeding (circled in red in Figure 5.20): when the powder feeder reached the end of its displacement, it dropped down some extra powder which, over time, created a hill.

The sintered part was 290 mm long and 160 mm wide. The bricks on the sides could be easily removed due to a slight bending. The substrate in the middle was strongly sintered to the part and had to be cut with a saw. Some pictures and post-processing steps are shown Figure 5.21.

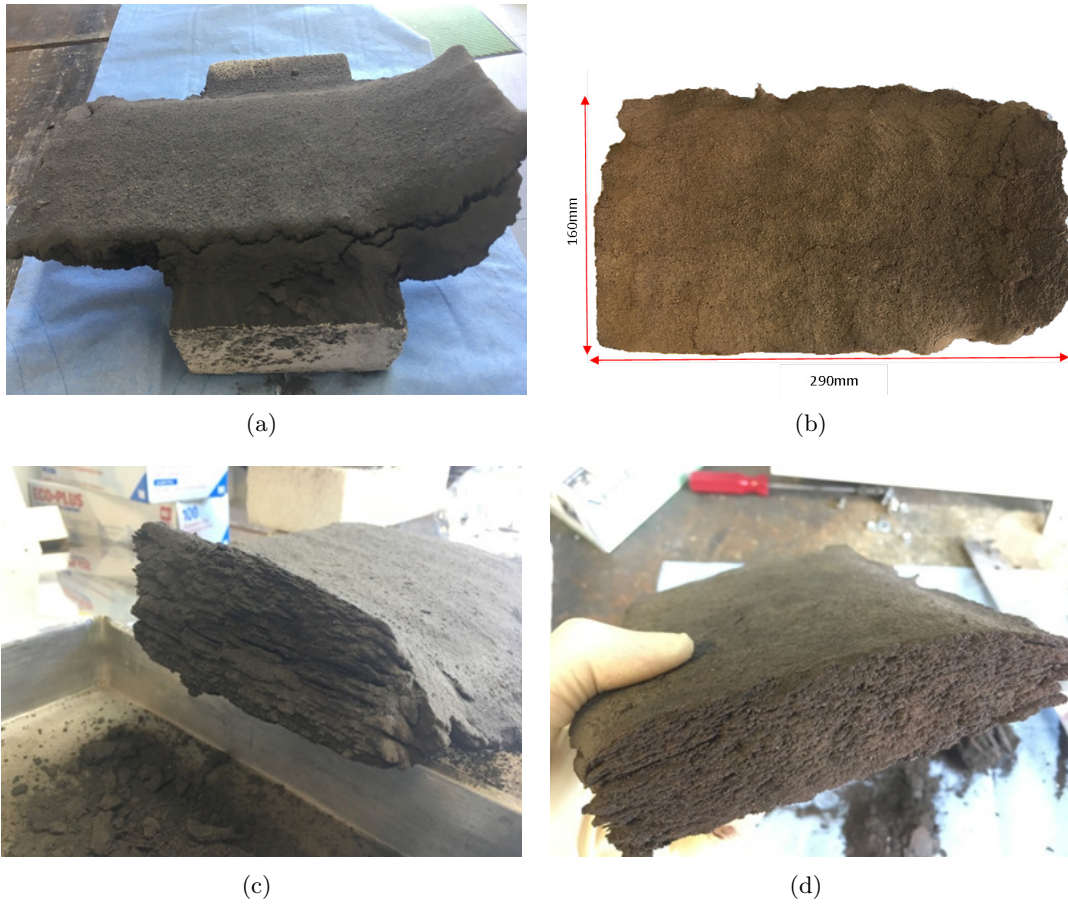


Figure 5.21: Test 6 sintered part once the side porous ceramic bricks were removed: side view (a) and top view (b). The sintered hill was then removed by manual polishing as well. Here are the pictures, before (c) and after (d) polishing.

The thickness of the sintered part fluctuated between 30 mm and 40 mm due to the bending. After polishing the sides to remove the loose regolith, the final part was a brick-shape part, 225 mm long and 125 mm wide, as shown Figure 5.22.

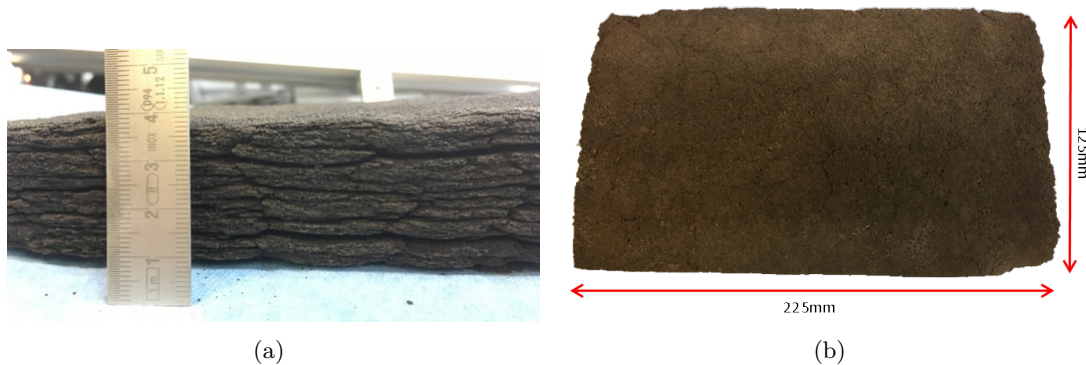
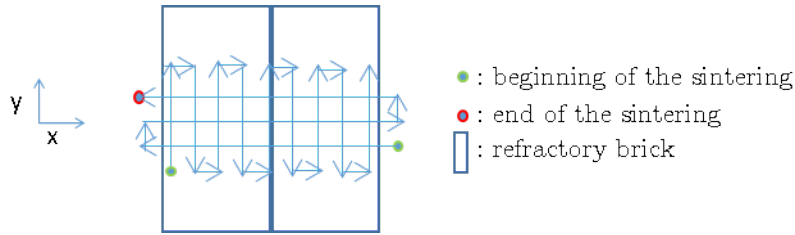


Figure 5.22: Side view (a) and top view (b) of the sintered part after polishing the edges to remove the loosely sintered powder.

Test 7Parameters

- Sintering path: Layer a / Layer b, alternately
- Distance between lines: 14 mm
- Scanning speed: 48 mm/s
- Pause between positions: 200 ms
- Substrate: 2 porous ceramic bricks
- Material: As-received JSC-2A regolith simulant

The same parameters Test 6 were used. The only change was the substrate: only two bricks were used to prevent the formation of a hill. Figure 5.23 shows the configuration of the substrate.

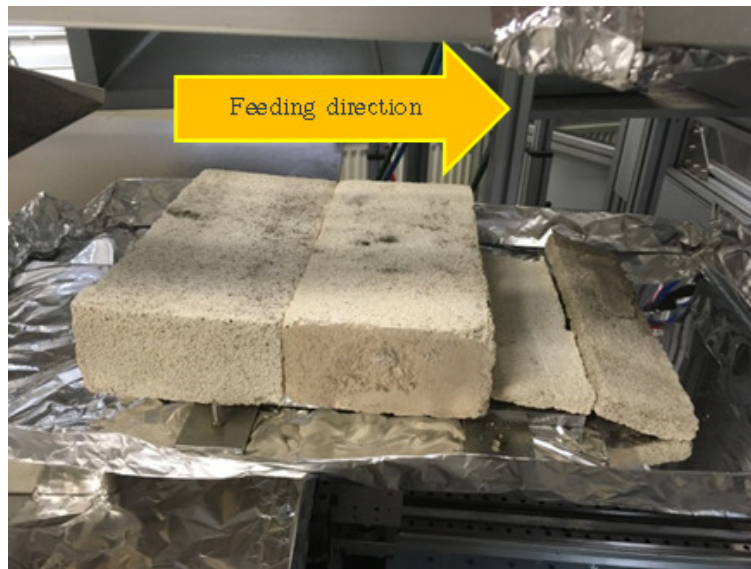


Figure 5.23: Substrate configuration for Test 7.

The process was however stopped after 30 minutes due to the warping of the edges as shown Figure 5.24.

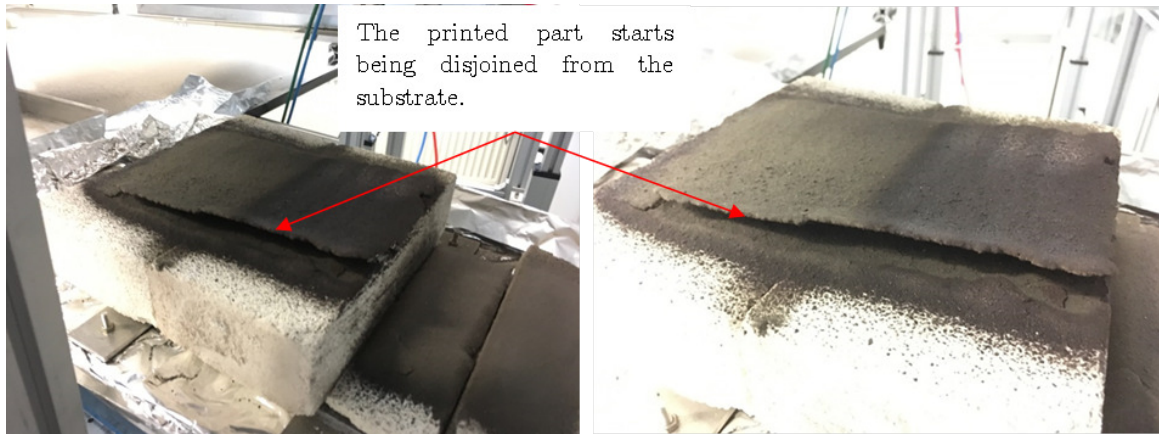
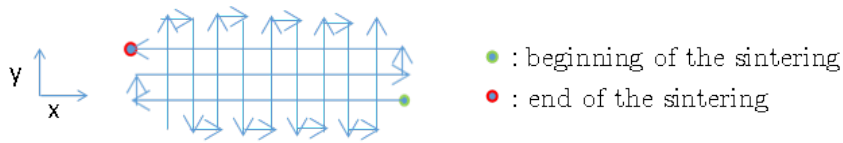


Figure 5.24: Part 3D printed after 30 minutes. A gap between the part and the substrate can easily be noticed.

Test 6 and Test 7 should, in principle, have produced similar parts. The process was however not yet reliably reproducible: although a larger substrate surface delayed the fracture of the substrate, the porous ceramic brick broke at a rather random time. A new substrate, more robust had to be found. Details about the substrates tried out in this work are part of the section 7.1.

Test 8Parameters

- Sintering path: Layer a / Layer b, alternately
- Distance between lines: 14 mm
- Scanning speed: 48 mm/s
- Pause between positions: 200 ms
- Substrate: Loose regolith
- Material: As-received JSC-2A regolith simulant

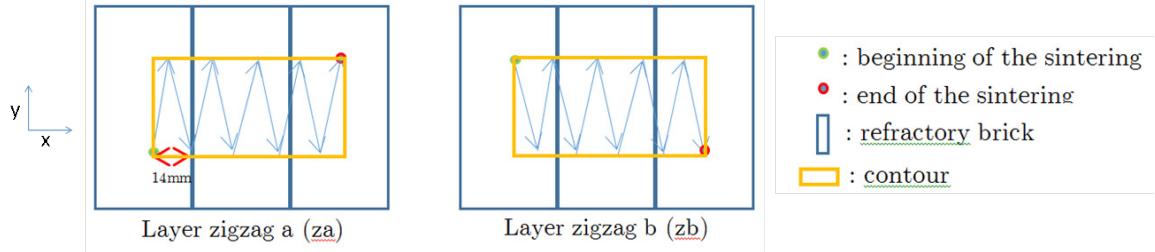
The same sintering parameters as for Test 6 and 7 were used for Test 8. The difference was again the substrate since this part was printed directly on loose regolith simulant. After a 2-hour sintering process, a wavy profiled brick was formed as shown in Figure 5.25, proving the need of starting the sintering on a solid substrate where the regolith could bond to.



Figure 5.25: Solar sintered part after a 2-hour process and Test 8 parameters: side (a) and top (b) views.

5.2.3 Zig-zag sintering path

Test 9



Parameters

- Sintering path: Layer za / Layer zb, alternately
- Distance between lines: 14 mm
- Contour speed: 30 mm/s
- Scanning speed: 48 mm/s
- Pause between positions: 200 ms
- Substrate: 3 porous ceramic bricks
- Material: As-received JSC-2A regolith simulant

For Test 9, a different path was tried. The part was sintered over the 3 porous ceramic bricks thus limiting the bending of the part like for Test 6. A contour path was first sintered at slow speed (30 mm/s) then the inside was sintered normally in a zig-zag path at (48 mm/s). The time for sintering each layer in Test 9 was about 40 sec whereas it was around 60 sec for the Test 1 to 8.

After 2h30 was obtained the part Figure 5.26. The part was similar to the ones obtained by sintering using layer a and b paths thus showing that different sintering strategy could work.

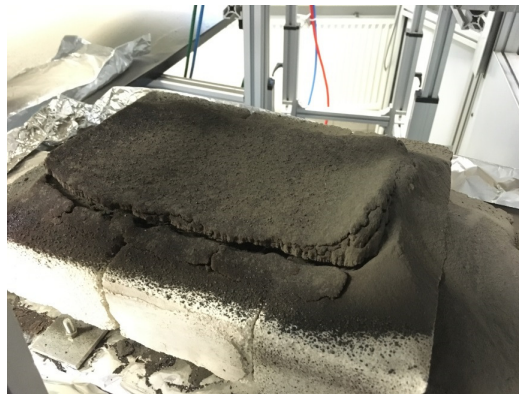
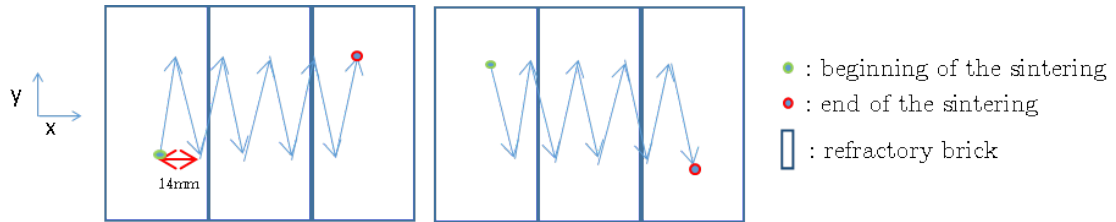
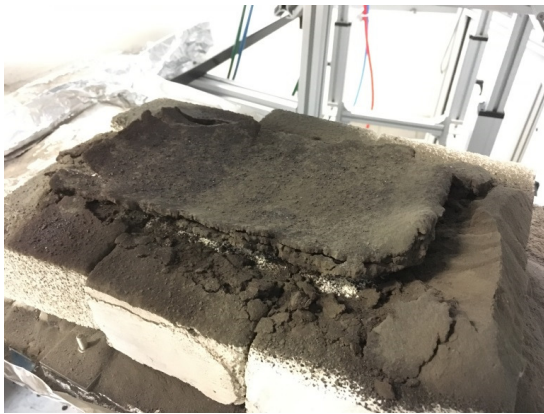


Figure 5.26: Solar sintered part using a zig-zag path for 2h30 and Test 9 parameters.

Test 10Parameters

- Sintering path: Layer za / Layer zb, alternately
- Distance between lines: 14 mm
- Scanning speed: 48 mm/s
- Substrate: 3 porous ceramic bricks
- Material: As-received JSC-2A regolith simulant

Test 10 was identical to Test 9 but without warming up the contour and with no small stops between the positions. After 2h30 was obtained the part shown in Figure 5.27. This part was much more bent at the edges than the one produced in Test 9. Providing extra heat to the contour seemed to have balanced out the faster cooling occurring on the side by convection.



(a)

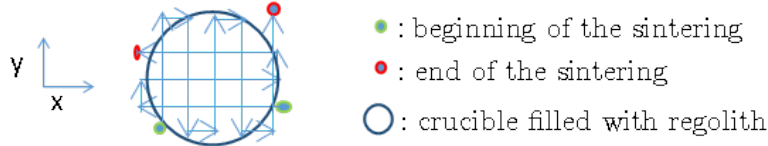


(b)

Figure 5.27: Solar sintered part using a zig-zag path for 2h30 and Test 10 parameters: side (a) and top (b) views.

5.2.4 Sintering on melt

Test 11



Parameters

- Sintering path: Layer a / Layer b, alternately
- Distance between lines: 14 mm
- Scanning speed: 48 mm/s
- Substrate: Molten regolith
- Material: As-received JSC-2A regolith simulant

Test 11 was designed in order to see if molten regolith could be used as a substrate for sintering regolith on top. Since two Xenon lamps provide too little energy to melt quickly the regolith, the test was done at small scale, using an alumina crucible, 100 mm diameter wide, filled with lunar regolith simulant, as shown in Figure 5.28.



Figure 5.28: Crucible filled with lunar regolith simulant before (a) and during (b) melting.

The centre of the crucible was irradiated by the two Xenon lamps for two minutes, thus creating a melting pool in the middle of the crucible around 60 mm wide. The sintering process then started directly on top of the molten regolith. The part is exhibited in Figures 5.29 and 5.30.



Figure 5.29: Sintered regolith with Test 11 parameters at the end of the process.

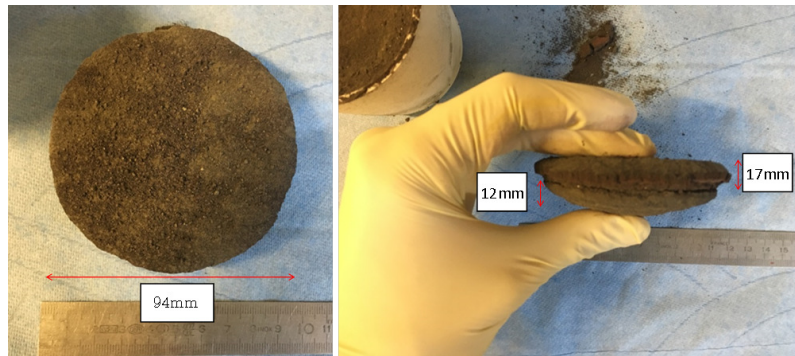
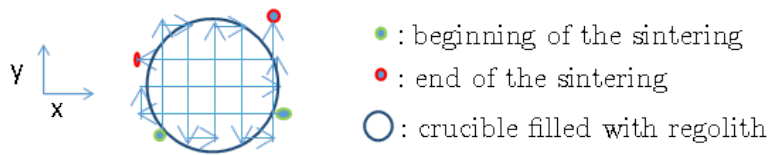


Figure 5.30: Part sintered with Test 11 parameters: Top view and side view. The melt has a clear visible demarcation to the sintered part.

The sintered part was flat and slightly connected to the molten regolith. However, both parts could be detached from one another. The part was flat and did not bend as the previous ones due to the round shape and relatively small size of the part. The mechanical strength seemed also to be much better.

Test 12Parameters

- Sintering path: Layer a / Layer b, alternately
- Distance between lines: 14 mm
- Scanning speed:
 - 4 layers out of 5: 48 mm/s
 - 1 layers out of 5: 60 mm/s
- Substrate: Molten regolith
- Material: As-received JSC-2A regolith simulant

Test 12 was designed in order to check an hypothesis expressed in section 7.4 that one layer out of five melts due to the accumulation of heat in successive sintered layers. The same parameter as Test 11 were used except that the sintering speed was changed from 48 mm/s to 60 mm/s one layer out of five. After 2 hours 45, the part Figure 5.31 was sintered. The molten part could be again easily detached as shown in Figures 5.32 and 5.33.

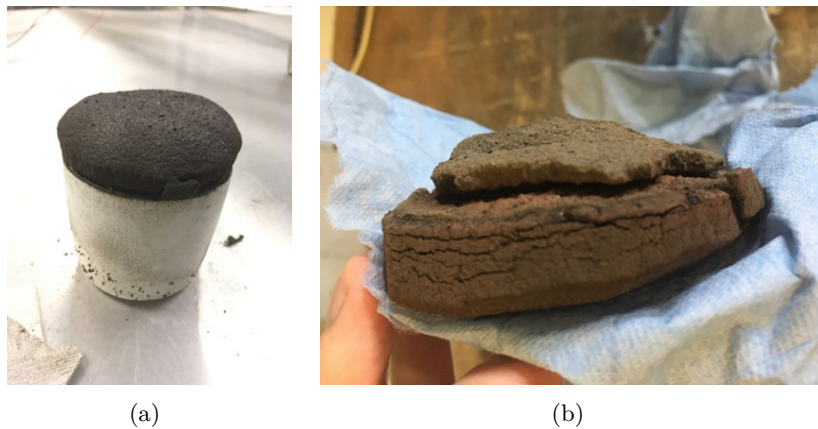


Figure 5.31: Part sintered with Test 12 parameters: over the crucible (a) and flipped (b).



Figure 5.32: The molten part was detached from the sintered one (a). The top side, which was in contact with the sintered regolith simulant, showed a tiny amounts of sintered grains connected to it, proving the poor bonding between melt and sintered regolith (b).

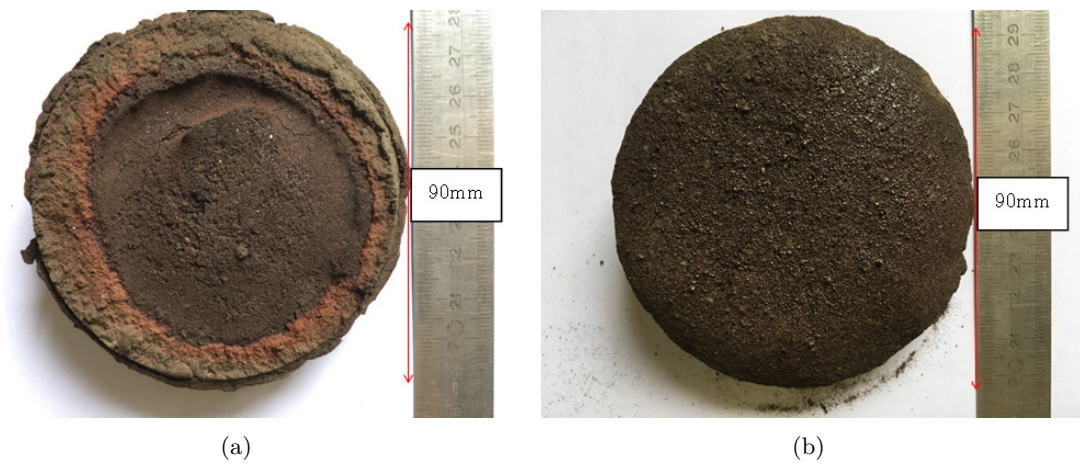
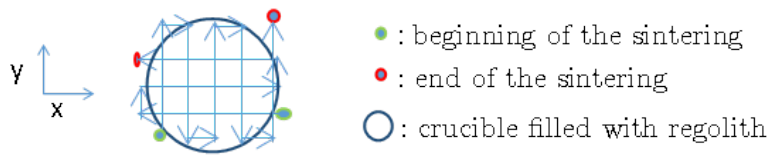


Figure 5.33: Part sintered with Test 12 parameters: bottom side in contact with the molten regolith simulant (a) and top side (b).

Test 13



Parameters

- Sintering path: Layer a / Layer b, alternately
- Distance between lines: 14 mm
- Scanning speed:
 - 4 layers out of 5: 48 mm/s
 - 1 layers out of 5: 60 mm/s
- Substrate: Loose regolith
- Material: As-received JSC-2A regolith simulant

Test 13 takes the same parameters as Test 12. This test was carried out in order to show the low impact of the molten regolith substrate on the sintered part with Test 11 and 12. After 1h45, a similar part was obtained, shown in Figures 5.34 and 5.35, as flat as the ones with the molten regolith used as substrate.

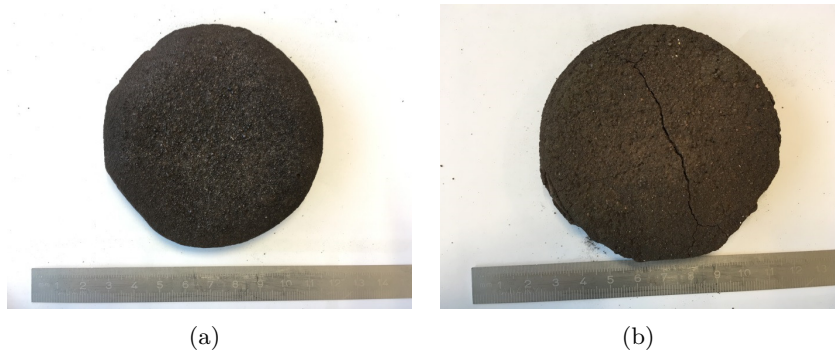


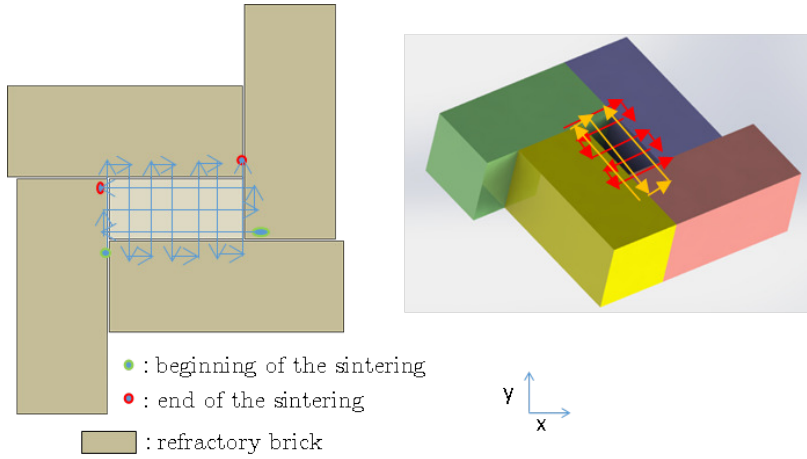
Figure 5.34: Part sintered with Test 13 parameters: top side (a) and bottom side (b).



Figure 5.35: Part sintered with Test 13 parameters:, side view

5.2.5 Convection shielding

Test 14



Parameters

- Sintering path: Layer a / Layer b, alternately
- Distance between lines: 14 mm
- Scanning speed: 48 mm/s
- Substrate: Porous ceramic bricks
- Material: JSC-2A regolith simulant

The idea in Test 14 was to use porous ceramic bricks not only as a substrate but also as a mould in order to see if the quality of the parts would increase in this configuration. The sides of the mould would reduce the cooling rate of the part. Due to time constraints, a small brick-shape part was targeted. After 3h30 and a slight polishing, the part shown Figures 5.36 and 5.37 was obtained:

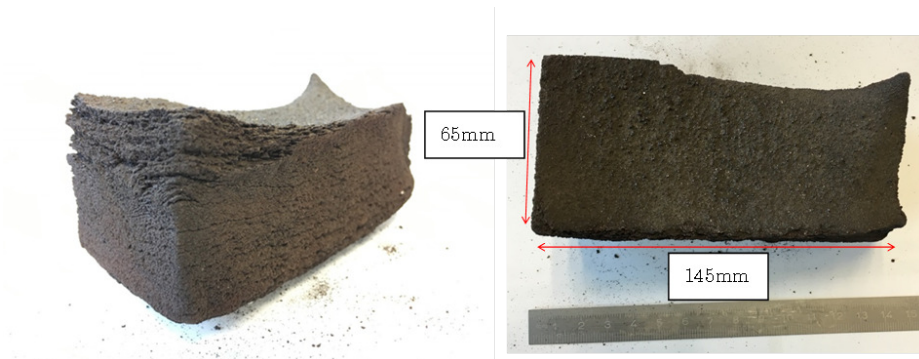


Figure 5.36: Part sintered with Test 14 parameters collected out the mould made of porous ceramic bricks.

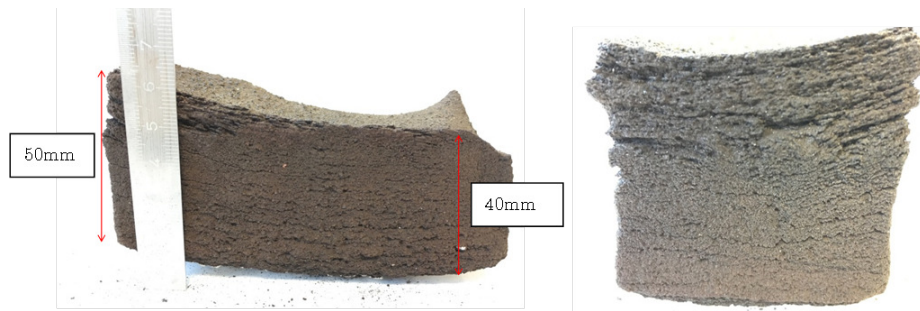


Figure 5.37: Part sintered with Test 14 parameters collected out the mould made of porous ceramic bricks.

The part seemed to be denser than the previous sintered large ones. The part was slightly bent due to the substrate fracture and the irregularities at the top were due to the amount of powder accumulating on the sides of the porous ceramic bricks falling down the hole after few hours of process thus creating irregularities in the powder deposition.

Obtaining this denser part was first correlated to the porous ceramic bricks surrounding the part and providing extra heat. However, the scanning path and the regolith deposition overlapping the surrounding porous ceramic bricks, especially on one side, the regolith deposited on top of the bricks also got sintered. The most densely sintered part collected on top of the bricks was kept (see Figures 5.38 and 5.39) and appeared to also be stronger than previous sintered large parts, just as the targeted sintered part collected in the mould. The smaller thickness was due to the irregularities in the regolith deposition on the sides since no part was expected to be sintered in this area. Figure 5.40 summarises the process and results of Test 14.

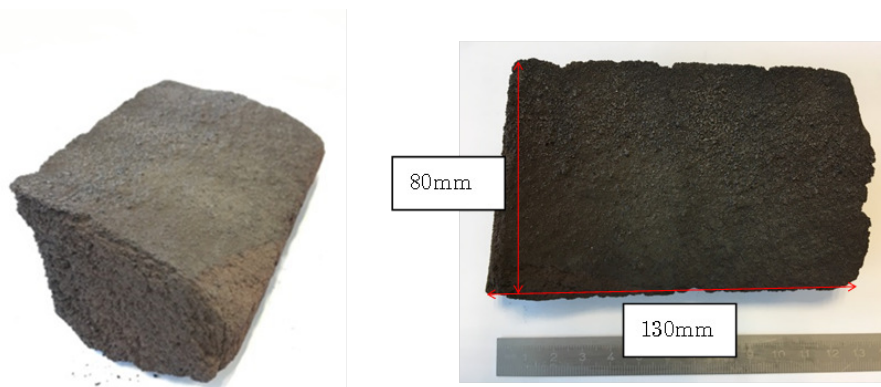


Figure 5.38: Part sintered with Test 14 parameters and collected on top of the porous ceramic bricks.

The fact that the targeted part, sintered in the mould, and the part sintered on the side of the mould appear to have better mechanical properties than the large parts sintered in previous tests (Tests 4, 6, 9 in sections 5.2.2 and 5.2.3), is believed to be a result of the faster sintering of each layer. Each layer was indeed sintered in about 20 seconds for Test

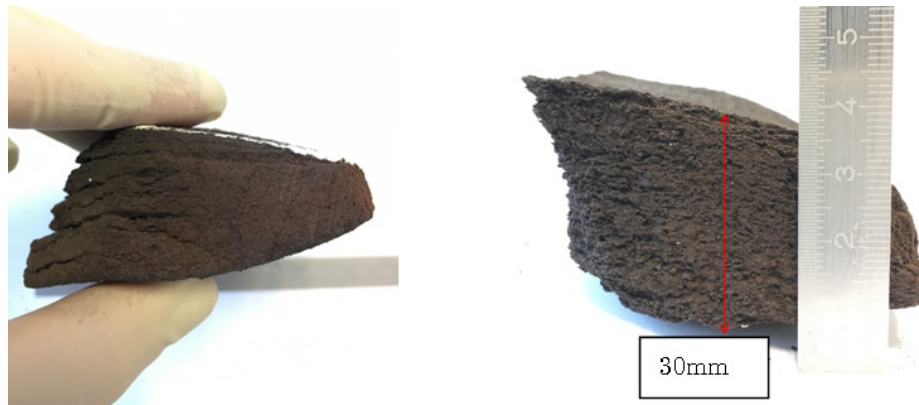


Figure 5.39: Part sintered with Test 14 parameters and collected on top of the porous ceramic bricks. Other views.

14 whereas in previous tests, for larger parts, each layer was sintered in about 60 seconds thus giving each layer three times longer cooling time before next layer than for parts in Test 14. If sintering on warmer layers increased significantly the bonding between the layers and the strength of the part, then the temperature of the layer before sintering the next one would be a key parameter to solar 3D print objects with high strength. This hypothesis was investigated in detail in section 7.4.

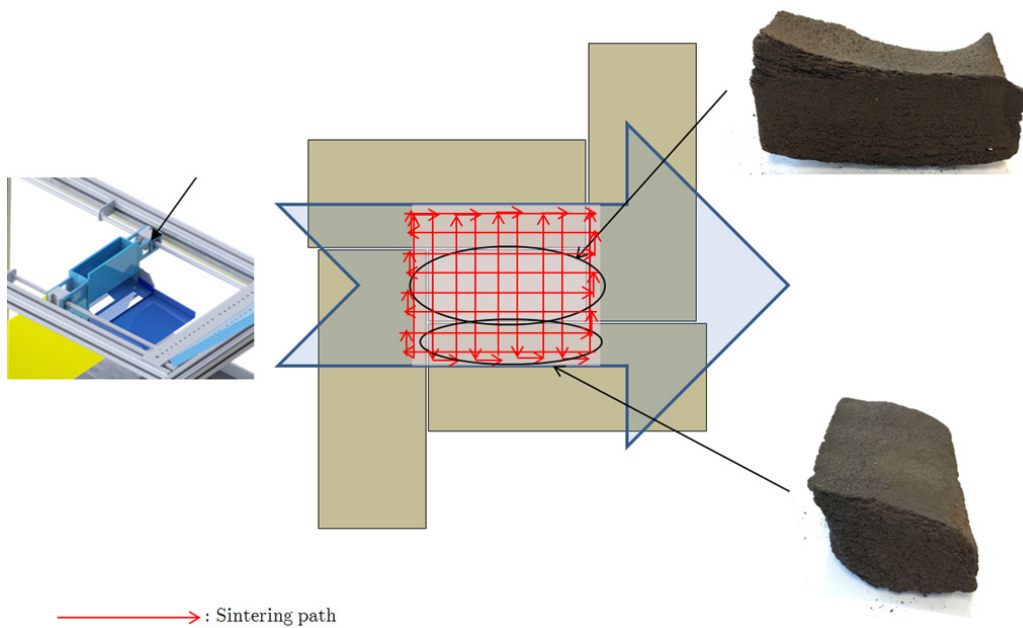
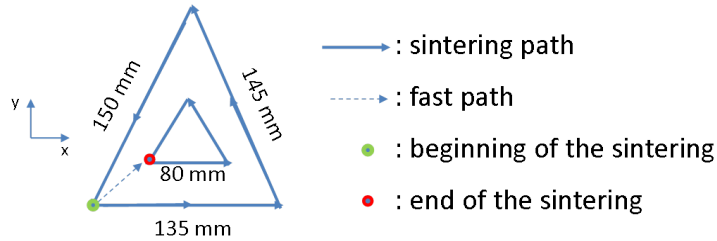


Figure 5.40: Location of the sintered regolith parts collected in the mould and on top of the surrounding porous ceramic bricks.

5.2.6 Complex shape sintering

Test 15



Parameters

- Sintering path: Customised triangle path
- Distance between lines: 14 mm
- Scanning speed: 48 mm/s
- Substrate: Loose regolith
- Material: As-received JSC-2A regolith simulant

Test 15 looked into the capability of sintering shapes more complex than a brick with the current set-up. The sintering path was programmed manually with the help of the drawing shown above. Results of the sintered part are shown on the following Figure 5.41. Some polishing was carried out to remove the loosely sintered powder in the middle of the part and on the edges. Since no solid substrate was used, the bending of the part was quite significant. Although the manufacturing of a triangle-shape part was successful, manual programming could only be carried out for parts with a constant 2D cross-section and not for complex 3D geometries where a software is required.



Figure 5.41: 3D printed triangle: (top left) before polishing, (bottom left) side view, (Right) top view.

5.2.7 Summary of 3D printing experiments

Fifteen relevant tests were carried out to understand the solar sintering mechanisms of the lunar regolith over a line, a plane and a volume, sintering layer-by-layer JSC-2A lunar simulant. All tests have shown the ease with which it was possible to bond lines together to sinter an homogeneous plane. Traditional back-and-forth path, zig-zag path, or customised path for sintering the section of a triangle were all successful. No difference in the quality of the 2D-sintered planes was visible to the naked eye and a traditional back-and-forth path was chosen for most of the tests. The main requirements for a successful 2D printing were a constant light intensity, here provided by two Xenon lamps, a suitable speed of the 3-axis table and a well-defined shift between the sintered lines.






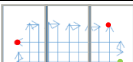



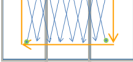
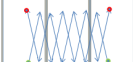
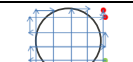
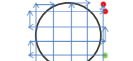
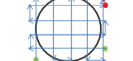
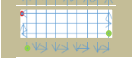
As the 3D-printed parts were growing up layer-by-layer, a significant deformation of the sides of the parts could be observed. This effect was due to the thermal gradients within the sintered parts and prevented the completion of 3D-printed parts thicker than 20 mm. Sintering back and forth along the length and the width alternately was distributing the heat more evenly and the preheating of the layer contour was performed to balance out the convection cooling over the layer. However, the warping problem was partially solved using a porous ceramic brick as a substrate for the first layer. Trials to use molten regolith as a substrate were unsuccessful. Other substrates were also tested as described in section 7.1.

The interlayer bonding seemed to be stronger for the smallest sintered parts. Since the sintering strategy was the same for the small and large parts, only the substrate temperature could have played a role in the bonding quality between two layers. Trials changing the speed every other five layers were performed but no change could be seen at macroscale. Solar sintering simulations, in chapter 6, and the analysis of the sintered part in chapter 7 will help understanding further the involved sintering mechanisms during a solar additive manufacturing process.

Although the 3D-printed parts do not seem to have yet the strength of concrete, several brick-shape building elements, up to 50 mm thick, were successfully manufactured by the designed solar additive manufacturing apparatus. A triangle-shape part was also 3D-printed. These 3D-printed elements have shown the reliability of the developed solar sintering process.

Table 5.2 sums up the tested parameters.

Table 5.2: Recap table of performed solar sintering tests.

Test No.	Sintering path	Distance between the lines (mm)	Scanning Speed (mm/s) + Contour Speed (mm/s)	Substrate	Material
1		20	50	Loose Regolith	As-received JSC-2A
2		15	50	Loose Regolith	As-received JSC-2A
3		15	48 + 38	Loose Regolith	As-received JSC-2A
4		14	48	Porous ceramic brick	JSC-2A <100 μm
5		14	48	Porous ceramic brick	As-received JSC-2A
6		14	48	3 porous ceramic bricks	As-received JSC-2A
7		14	48	2 porous ceramic bricks	As-received JSC-2A
8		14	48	Loose Regolith	As-received JSC-2A
9		14	48 + 30	3 porous ceramic bricks	As-received JSC-2A
10		14	48	3 porous ceramic bricks	As-received JSC-2A
11		14	48	Molten regolith	As-received JSC-2A
12		14	48 (4/5) and 60 (1/5)	Molten regolith	As-received JSC-2A
13		14	48 (4/5) and 60 (1/5)	Molten regolith	As-received JSC-2A
14		14	48	Porous ceramic brick	As-received JSC-2A
15		14	48	Loose Regolith	As-received JSC-2A

Legend:

● : beginning of the sintering

→ : sintering path

— : testbed

■ : brick

● : end of the sintering

→ : contour path

— : porous ceramic

○ : crucible

6 Solar sintering modelling

Improving the current solar additive manufacturing process requires a better understanding of the heat diffusion and distribution inside the 3D printed building element. With the hypothesis formulated during the test campaigns, at macroscale, the temperature fluctuation along the length and the width of the 3D printed part should be reduced to a minimum for preventing thermal stresses weakening the sintered part and warping its edges. No assessment of the maximum temperature gradient allowed was however possible. At the microscale, the diffusion processes between a sintered layer and the newly deposited powder being irradiated need also to be investigated in order to have a clearer idea of the sintering mechanisms involved during solar irradiation.

Data obtained from the IR camera (e.g. Figure 6.1) were not sufficient for having a global picture of the heat transfers happening within the solar 3D printed part. The IR pictures gave only a rough idea of the heat distribution on the surface and showed to be inaccurate with a mobile heat source. However, the provided information could be used as an input for a finite element method (FEM) analysis. FEM is a common engineering technique for handling physics problems, hardly solvable analytically. The method consists in solving algebraic equations for finding the unknowns at a discrete number of points. The mesh size and computer calculation capability are the two main factors limiting the accuracy of this method. COMSOL MultiPhysics software was used to simulate the heat transfer during a solar 3D printing process. This tool provided extensive functions for modelling complex heat transfers in porous media, but was more limited concerning the AM. Compromises and suitable definition of the boundary conditions were therefore required for modelling the solar AM process.

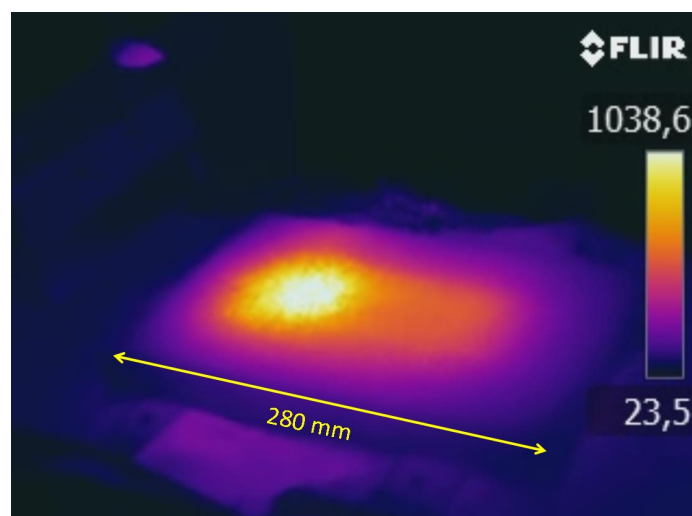


Figure 6.1: Typical experimental IR picture during a solar 3D printing process. Picture taken while monitoring Test 8. The scale represents the temperature gradient in °C.

6.1 Model definition

6.1.1 Solar Heat flux

First, the heat flux distribution of the March 2016 solar simulator campaign, shown in Figure 6.2(a), was used for the model. The idea was to redistribute the 4.11 kW in a Gaussian profile in order to obtain the same heat flux distribution over the surface of the printed part. After normalisation of the two-dimensional Gaussian function, the heat flux can be defined by:

$$Q_{solar}(x, y) = \frac{2 \cdot P_{solar}}{\pi \cdot r_{spot}^2} \cdot e^{\left(\frac{-2(\sqrt{(x-x_0)^2 + (y-y_0)^2})^2}{r_{spot}^2} \right)} \quad (2)$$

where

Q_{solar} : Heat flux provided by two xenon lamps

P_{solar} : Total power from the two xenon lamps

x_0, y_0 : Centre coordinates of the Gaussian

r_{spot} : Radius of the solar beam

The radius of the solar beam remained unknown for fully defining the heat flux function. Using the heat flux distribution of March 2016 campaign, a fit was found considering the radius of the solar beam as $r_{spot} = 47$ mm. The fit heat flux is shown Figure 6.2(b).

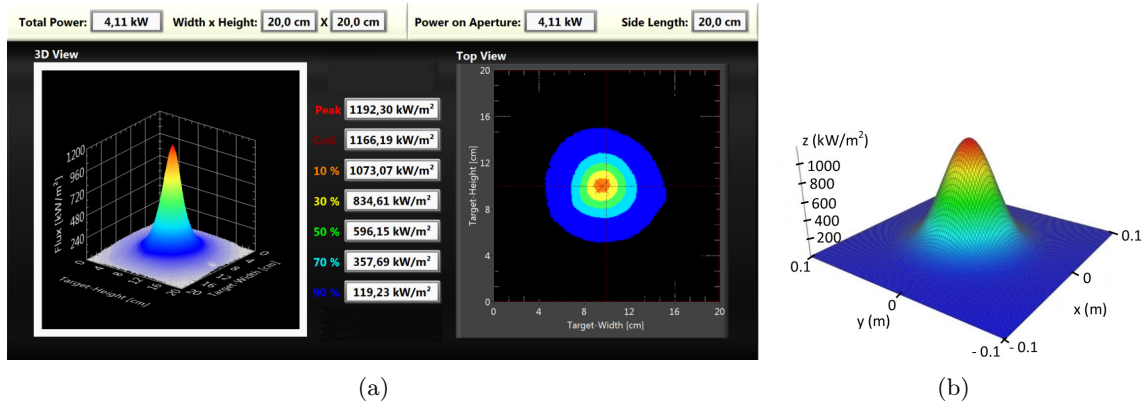


Figure 6.2: Flux density provided by two xenon lamps calibrated for the March 2016 campaign (a) and the fit flux used for the modelling (b).

6.1.2 Geometry

Two objects were designed for representing two important periods of the process. The first design, Figure 6.3, was a thin part but as wide as a brick, 200 mm x 100 mm large

and 4 mm thick. This designed object was used for modelling the very beginning of the process, showing the low penetration of the heat inside the loose regolith powder. An extra-fine mesh, with tetrahedral elements smaller than 3 mm, was used on this small volume. Simulation using this designed part is referred in the next pages as 'Model 1'.

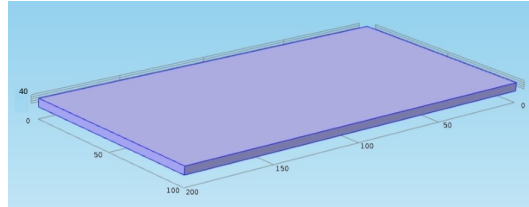


Figure 6.3: Model 1 used for heat transfer simulation. In blue is a 200 mm x 100 mm x 4 mm part made of only loose regolith.

The second designed object, Figure 6.4, was a targeted brick, 200 mm x 100 mm large and 20 mm thick. The objective was to observe the heat transfer in depth during the sintering process. Unlike the first model, a layer was being sintered on top of previously sintered lunar regolith and not on loose material. The thickness was limited to 20 mm not to increase unreasonably the computation time. The brick was placed on top of a 300 mm x 200 mm ceramic substrate, 40 mm thick, for modelling the porous substrate filled with regolith powder. A thin mesh, with elements smaller than 6 mm, was used for the brick and a coarser one, with elements about 20 mm, for the ceramic plate since a low interest was given to the heat diffusion in this element. The boundary between the brick and the ceramic plate was however finely meshed. Simulation using these designed parts is referred in the next pages as 'Model 2'.

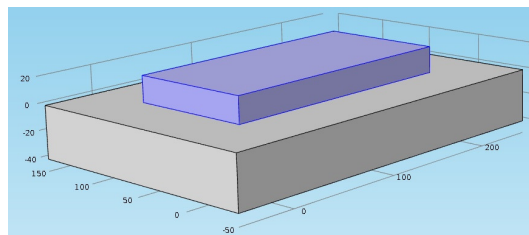


Figure 6.4: Model 2 used for heat transfer simulation. In blue is the sintered brick and below is the porous support filled with loose regolith.

6.1.3 Boundary conditions

A convective cooling was defined to simulate the ambient convection. Convection flux from ambient are often assessed between 10 and 20 $\text{W.m}^{-2}.\text{K}^{-1}$. It was assessed that the air flux created by the extractor hood and the fans, used for preventing the dust to stick on the mirror, would induce an air flow resulting in the formation of a light forced convection

flux. Therefore, the upper limit was used and the convection flux assessed at $20 \text{ W.m}^{-2}.\text{K}^{-1}$. The heat removal by convection is described by:

$$Q_{conv} = hA_{surf}(T_{surf} - T_{amb}) \quad (3)$$

where

Q_{conv} : Convective heat loss [W]

h : Heat transfer coefficient [$\text{W.m}^{-2}.\text{K}^{-1}$]

A_{surf} : Area of the surface [m^2]

T_{surf} : Temperature of surface i [K]

T_{amb} : Temperature of the surrounding atmosphere [K]

All surfaces were chosen as susceptible to the convective heat flux except the bottom one of the brick, in contact with the ceramic substrate.

On the Moon, no significant convective heat loss will occur during a solar sintering process. A simulation without a convective heat flux as part of the boundary conditions can be found in the Appendix C.3.

A surface diffusion condition was also defined. The top surface was indeed not completely black and some of the incoming energy could not be absorbed thus leading to a radiative flux going outward which needed to be taken into account. This flux, also called radiosity, is defined by the following equation:

$$Q_{rad} = \sigma A_{surf} \varepsilon_{surf} (T_{surf}^4 - T_{amb}^4) \quad (4)$$

where

Q_{rad} : the thermal energy leaving the surface [W]

σ : Stefan-Boltzmann constant [$\text{J.s.m}^{-4}.\text{K}^{-4}$]

A_{surf} : Area of the surface [m^2]

ε_{surf} : Emissivity of the surface

T_{surf} : Temperature of the surface [K]

T_{amb} : Temperature of the surrounding atmosphere [K]

In our model, the emissivity ε was equal to the absorptivity $\alpha = 0.82$ [93]. The temperature of the air T_{amb} was 20°C and since the concentrated solar beam only shined on the top surface, the top area, $200 \text{ mm} \times 100 \text{ mm}$, was selected for defining A_{surf} . The

Stefan-Boltzmann constant is equal to $\sigma = 5.670373 \times 10^{-8} J.s.m^{-4}.K^{-4}$.

6.1.4 Simulation architecture

In both simulations, the modelled beam was moving back and forth along the length and the width of the brick, at 48 mm.s^{-1} , following predefined functions to simulate the alternating sintering paths used during the campaigns. A faster contour sweeping was also added in some of the simulations. Between each layer, a pause of 10 seconds was set to simulate the deposition time of a new layer.

Both models had different time lengths and time steps. At the end of the simulation, temperature was read at interesting places.

Lunar regolith and its simulants were not common materials that could be found in the material databases of the simulation software: the material had to be added manually. Two different materials were considered; both having their intrinsic thermophysical properties: the loose regolith and the sintered regolith, used in Model 1 and 2, respectively.

The heat transfer equation solved by COMSOL software is then driven by the first law of thermodynamics referring to the energy conservation. Using Fourier's law of heat conduction, the heat equation can be written:

$$\rho Cp \frac{\partial T}{\partial t} = \nabla \cdot (k \nabla T) + Q \quad (5)$$

where

ρ : density [g.cm^{-3}]

Cp : Specific heat capacity of the material [$\text{J.kg}^{-1}.K^{-1}$]

k : Thermal conductivity of the material [$\text{W.m}^{-1}.K^{-1}$]

T : Temperature [K]

Q : inner heat-generation rate per unit of volume [W.m^{-3}]

with the boundary conditions:

$$(k \nabla T) = Q_{solar} - Q_{rad} - Q_{conv} \quad (6)$$

6.1.5 Model limitation

The material addition on top of the original defined brick could not be successfully modelled and was therefore not defined in this analysis. The time of pause between the sintering of two layers was kept identical to the actual process although an extra cooling exists, provided by the deposition of a $100 \text{ }\mu\text{m}$ thick layer of regolith simulant. The thermal mass change, from the addition of the new layers, could be indeed neglected for the purpose

of the simulation. A more advanced model, for modelling the whole process over several hours, was not possible due to the limited time frame and computer calculation capability.

6.2 Model 1 - Loose regolith

The specific heat capacity, the thermal conductivity and the density of the material were required for defining the material. JSC-2A lunar simulant skeletal density was 2.9 g.cm^{-3} , but the bulk density of uncompacted simulant was about 1.3 g.cm^{-3} thus defining the density of the model. As for the thermal conductivity and the specific heat capacity, their variations in temperature were too high to use a constant. Tests and measurements of these thermophysical properties were carried out only from room temperature to 150°C on already sintered regolith (see Section 6.3), and a model was therefore required for high temperature and loose regolith. Schreiner et al. presented in a paper [94] all published measurements and existing models for the thermal conductivity and specific heat capacity of lunar soil and some simulants. A model from Colozza A. [95] was chosen for the specific heat capacity and defined by the equation:

$$C_{p_{loose}} = -1848.5 + 1047.41 \times \log(T) \quad (7)$$

where

$C_{p_{loose}}$: Specific heat capacity of loose lunar regolith [$\text{J.kg}^{-1}.\text{K}^{-1}$]

T : Temperature of loose lunar regolith [K]

This model was fitting data from the Apollo programs and measurements performed on lunar simulants [96, 97]. Figure 6.5 shows the used model.

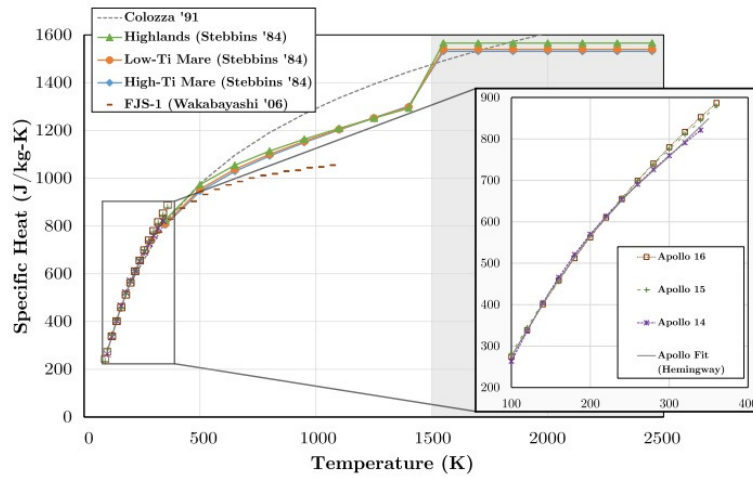


Figure 6.5: Specific heat capacity of lunar regolith.[94, 95]

Thermal conductivity was modelled differently: a piece-wise fit [94] was chosen. This fit used data taken from a basalt-like material, and was defined by the equations (8) and (9):

For $T < 1500\text{K}$,

$$k_{loose} = 0.001561 + 5.426 \times 10^{-11} \times T^3 \quad (8)$$

For $T > 1500\text{K}$,

$$k_{loose} = \exp\left(-9.332 + \frac{1.409 \times 10^4}{T}\right) \quad (9)$$

where

k_{loose} : Thermal conductivity of loose regolith [$\text{W.m}^{-1}.\text{K}^{-1}$]

T : Temperature of loose lunar regolith [K]

The 1500 K mark was supposed to correspond to the melting temperature of the material. Although this temperature is lower for our simulants, about 1400 K, no better fit could be found. Figure 6.6 shows the above modelling with data from actual lunar regolith and FJS-1 lunar simulant [97] for comparison. The continuous fit was not used in the following simulation.

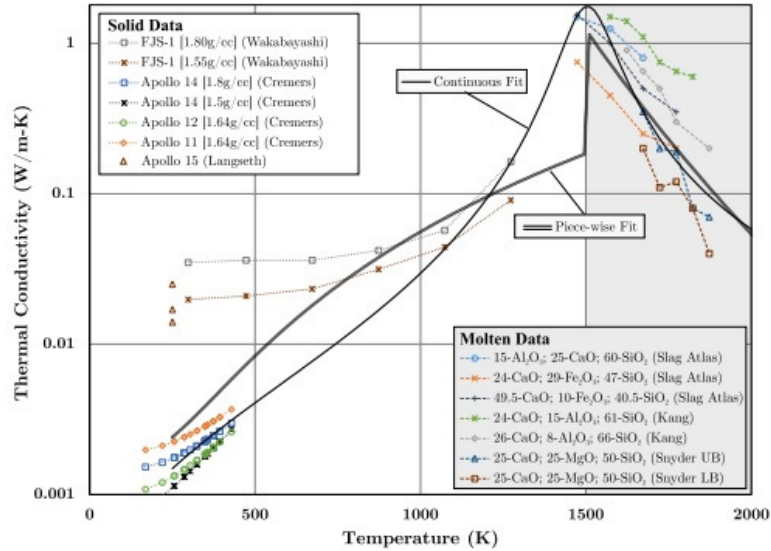


Figure 6.6: Thermal conductivity of lunar regolith. [94]

In case of phase transformation, the latent heat was defined to 450 J.g^{-1} and the melting range from 1400 K to 1700 K [94]. Density of the melt was set to 2.9 g.cm^{-3} .

Once the material property was defined for the loose lunar regolith model, the volume was divided in tetrahedrons smaller than 3 mm, defining the mesh. The time step was reduced to 0.1s and the simulation ran over 1000s. Temperatures variation were read at three interesting points: at the surface, at 0.5, and at 1 mm below the surface. The three points were taken in the centre of the brick. Figure 6.7 shows the selected points.

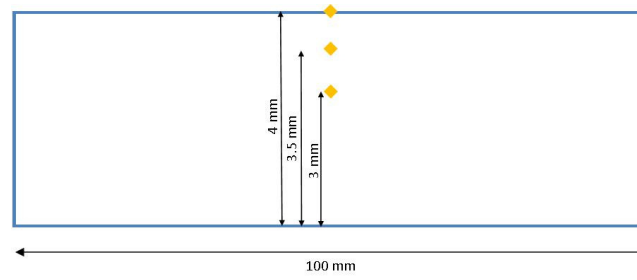


Figure 6.7: Cross-section in the middle of the model brick. The three yellow points are the locations of the read temperatures. The sketch is not to scale for more readability.

Temperature profiles of these three points are shown Figure 6.8. The peaks maximum corresponds to the moment where the solar beam passes over the centre of the brick. In 17 minutes, 19 layers are therefore represented. The model overvalues the temperature as 1300°C would result in the melting of all regolith constituents, however it shows clearly the low heat penetration on loose regolith powder: at 1 mm under the surface, the heat does not even reach 1000°C, which is also most likely overvalued. This model also highlights the high temperature gradient, with $\Delta T \approx 1200^\circ\text{C}$ between the time the beam passes over the centre and the end of the feeding pause. This temperature gradient created thermal stresses in the structure and the implied quenching of the freshly formed glass did not provide structural strength to the brick.

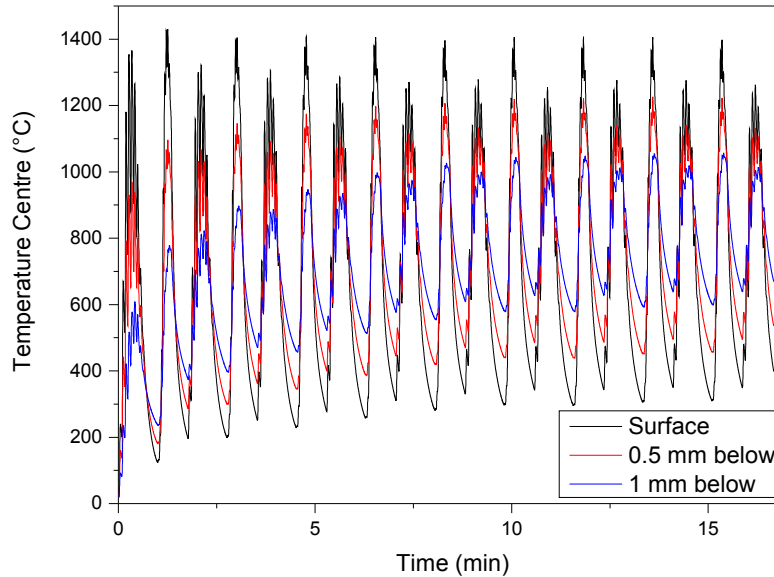


Figure 6.8: Simulated temperature profile at the centre of the model, at the surface, at 0.5, and 1 mm below the surface.

This model is however, in principle, only valid for the first layer as the thermophysical properties of the lunar regolith change when the regolith becomes sintered. For long run simulations, Model 2 is more appropriate.

6.3 Model 2 - Sintered regolith

Thermophysical properties had to be re-defined for Model 2, taking into account that the lunar regolith simulant is now sintered. The measured envelope density of sintered material was about 1.7 g.cm^{-3} and the same value was used for the model. Regarding the specific heat capacity and the thermal conductivity, measurements were made by DSC at the Institute of Materials Research at DLR-Cologne, within an ESA-GSP project, on lunar simulant sintered by various ways. The samples were produced at the Institute of Materials Physics in Space. Measured specific heat capacities are shown Figure 6.9.

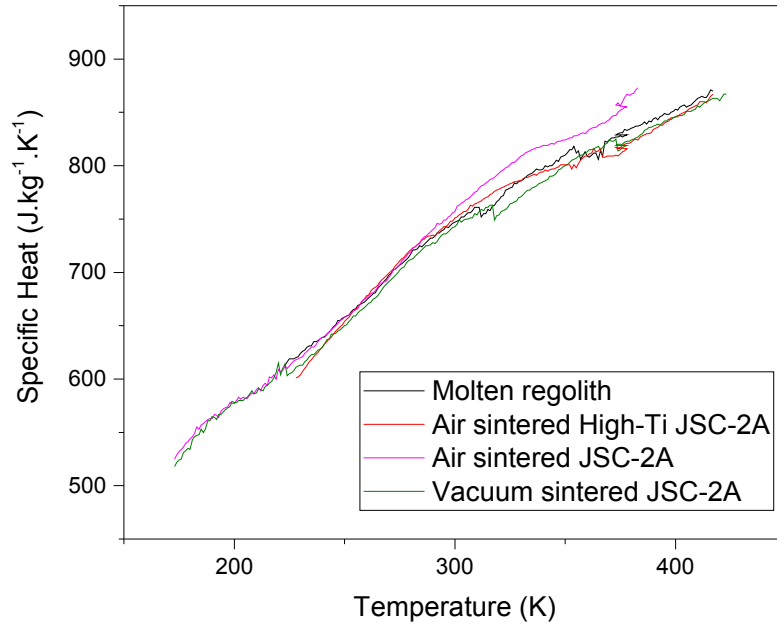


Figure 6.9: Measured specific heat capacity of JSC-2A lunar simulant sintered by several means.

Similar specific heat capacities can be noticed whether the regolith was molten or sintered, sintered in air or in vacuum, and even changing the composition of the simulant adding ilmenite mineral to the simulant in order to increase its titanium content. These results were closed to the specific heat capacity measured during the Apollo program, shown previously Figure 6.5. Therefore, the specific heat capacity was defined with the same equation (7) and $C_{p_{sintered}} = C_{p_{loose}}$.

Measurement of the thermal conductivity was possible combining the specific heat capacity, the density, and the thermal diffusivity, also measured at the Institute of Materials Research by laser flash analysis (LFA). Results of the measurements are shown Figure 6.10. Unlike the specific heat capacity, the variations in thermal conductivity were minor over temperature for each different sample.

It was assessed that the thermal conductivity should increase up to $1.1 \text{ W.m}^{-1}.\text{K}^{-1}$, which is the maximum reached before melting according to the model presented above, Figure 6.6.

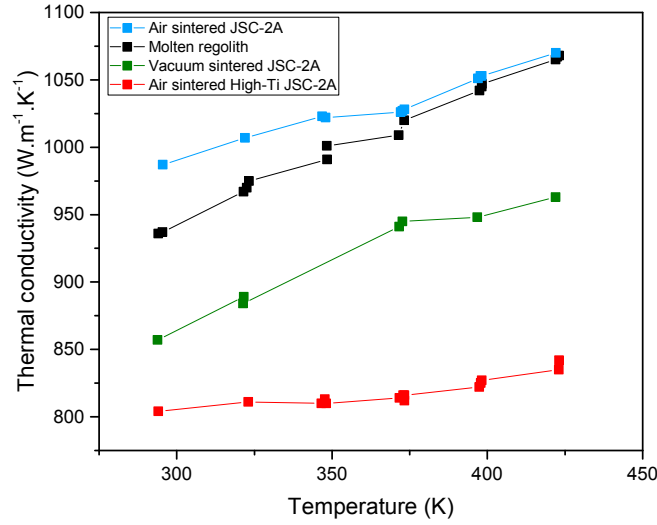


Figure 6.10: Measured thermal conductivity of JSC-2A lunar simulant sintered by several means.

Therefore, due to the low variations in temperature and in order to save computation capability, the thermal conductivity was set to the constant value $k_{sintered} = 1.1 \text{ W.m}^{-1}.\text{K}^{-1}$.

The temperature measurements were performed along the thickness at the bottom, at the middle, 20 mm from the bottom and the top, and at the top of the brick, the measurement from the top being directly comparable to the IR camera data. Across the surface three interesting locations for these temperatures reading were defined: in the centre of the brick, on a side, at the middle of the length and on another side, at the middle of the width. Figure 6.11 shows the model and the places where the temperatures were read.

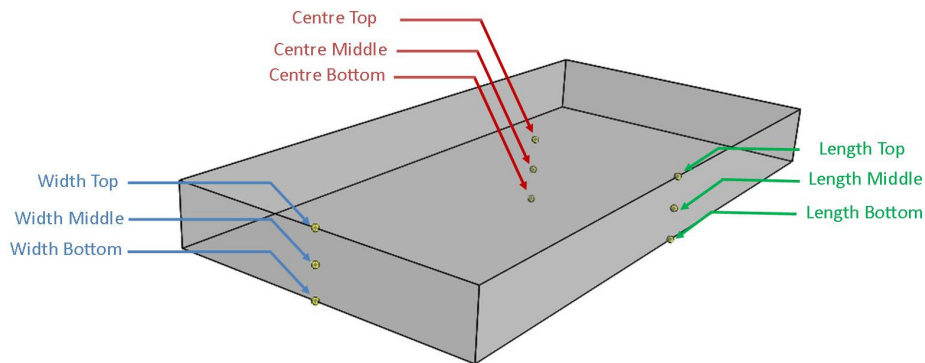


Figure 6.11: Locations of the read temperature on the studied brick. The naming is used afterwards in this work.

Results from the simulation at the centre of the brick are shown Figure 6.12. The maximal temperature was between 1150°C and 1200°C and in harmony with the targeted

temperature since this range would allow a partial melting of the regolith constituents. Although the centre of the brick should be the hottest place of the surface, a temperature gradient about $\Delta T \approx 500^\circ\text{C}$ remained between the sintering point and the end of the pause required for depositing a new layer. This ΔT was also observed with the IR camera. Looking at the temperature inside the sintered brick, the middle point experienced only little fluctuation, increasing slowly between 600°C and 800°C . This temperature was however not sufficient for further sintering of the already solar sintered regolith. A similar trend, 100°C lower, could be observed at the bottom of the brick, in contact with the porous ceramic plate filled with regolith. It could be noticed that after 20 minutes, the surface could reach lower temperatures than the middle of the brick and after 80 minutes, lower temperature than the very bottom. As for the cooling, after a 2-hour process, as one could expect, the surface cooled down faster than the bottom due to the air convection. The simulation had a similar profile as the data taken from the IR camera considering the imprecision range of both, the camera and the simulation.

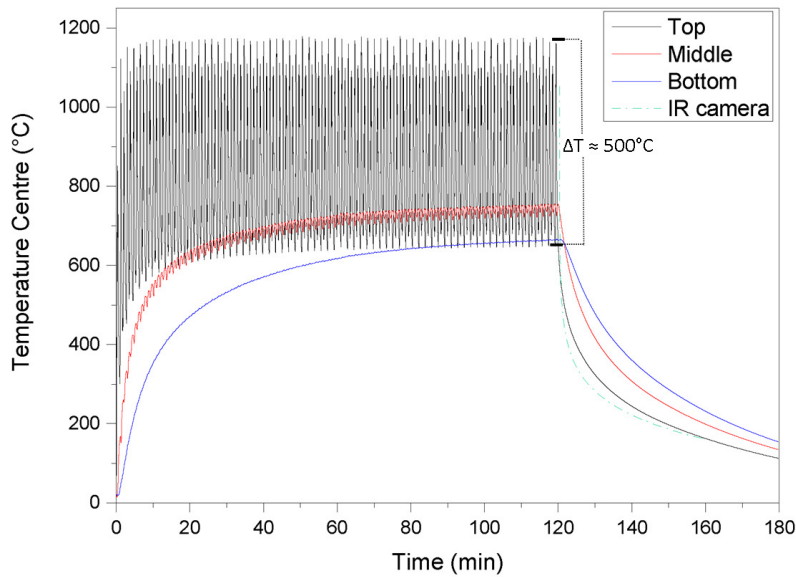


Figure 6.12: Simulated temperature evolution at the centre of the brick over a 2-hour sintering process and 1-hour cooling. The cooling measured by the infra-red camera was added for comparison.

From the solar sintering experiments, it was noticed that the smaller sintered parts had better mechanical properties than the large ones. One hypothesis was that the shorter time for sintering one layer led to less cooling time and therefore a better bonding between the layers. A small Model 2 was designed with a width of 50 mm and a length of 100 mm, the other parameters remaining unchanged. Results of the simulations are shown Figure 6.13.

First, one can see that the maximal temperature is now higher, reaching 1250°C at the peaks when the concentrated solar beam passed over the referenced surface point. This increase of temperature was linked to the reduced ΔT , lowered down to 400°C sintering a

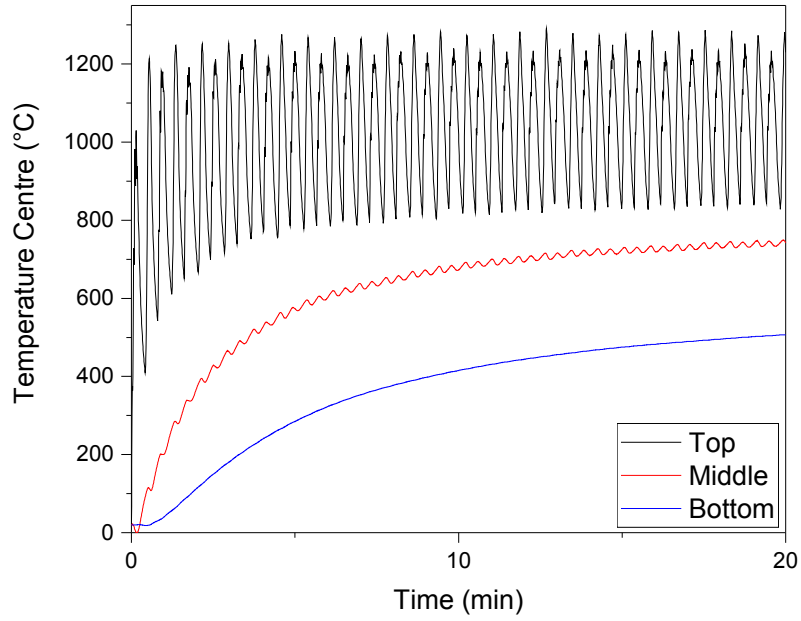


Figure 6.13: Simulated temperature evolution at the centre of a small brick over a 20 minute sintering process.

smaller brick. The layers had now less times for cooling down by air convection.

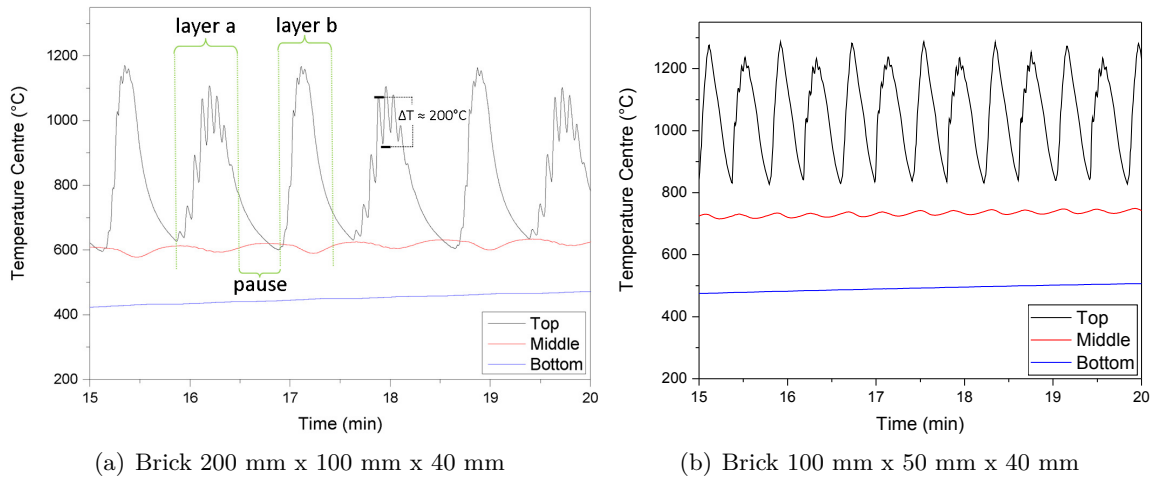


Figure 6.14: Temperature variation over 5 minutes for the standard size brick (a) and the smaller one (b).

On a closer scale, in Figure 6.14(a), it can be observed that, even during the sintering of one layer, ΔT variations could reach 200°C. This phenomenon, happening only every other layer, was due to the length of the brick, long enough for the centre to cool down while the concentrated solar beam was passing over the sides. 3D-printing a smaller element showed, in Figure 6.14(b), no quick temperature variations within the sintering of a layer thus reducing again the thermal stresses in the sintered material.

Another challenge was to reduce the thermal stresses over the sintering area. On the side, the air convection increased the cooling rate thus leading to inhomogeneous temperatures over the surface and bending of the parts from the different shrinkages and sintering density within a single layer. The temperature gradient can be seen in Figure 6.15.

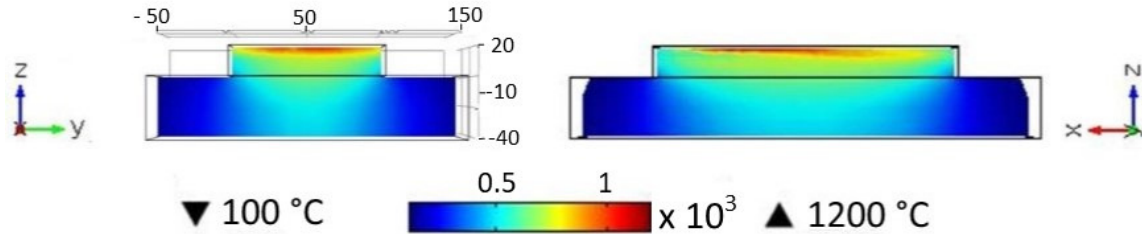


Figure 6.15: Temperature profile along the width and the length of the brick at 80 min 45 sec.

One way of reducing the planar thermal stresses was tried during the sintering campaigns. The idea was to preheat first the contour of the brick, moving the solar beam at 60 mm.s^{-1} for balancing out the convection cooling. Effects of this sintering strategy are shown Figure 6.16. A smaller peak, increasing the temperature up to about 800°C , can be seen ahead of the peak showing the sintering. Comparing the peaks at the sintering time, with and without preheating, the preheating seemed to have increased the maximal reached temperature of about 50°C at the middle of the width. Effects at the middle of the length are however very discreet. Although a 50°C difference could already affect a lot the sintering efficiency on the sides, more time should be allocated to have perfectly similar peaks at the three defined points and to homogenise the temperature over the brick surface.

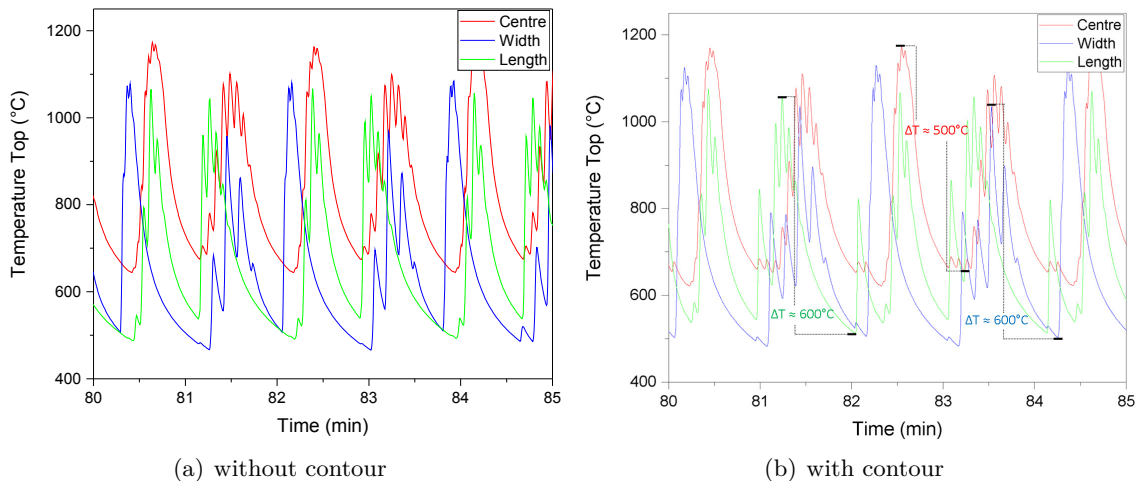


Figure 6.16: Surface temperatures for the brick 3D-printed without (a) and with a pre-heated contour (b).

The only difference should be the unavoidable phase shift between the peaks. A reduction of the temperature variations should also be aimed in order to have a similar and limited temperature gradient between the sintering time and the end of the pause. Currently, at the surface, $\Delta T_{centre} \approx 500^\circ C$, as mentioned above, while $\Delta T_{width} \approx \Delta T_{length} \approx 600^\circ C$.

Summarising, the simulations performed on Model 2 confirmed the assessments made during the sintering campaigns. The modelling helped obtaining the magnitude of the temperature variations at some specific points, difficult to measure with an experiment. It was shown that sintering at small scale, representative of a faster sintering with a higher solar flux density, reduces the overall thermal gradient and quick temperature changes at the surface. From the experiments, this reduction of the temperature fluctuation limits the thermal stresses and improves the investigated mechanical properties. As for homogenising the temperature between the centre and the sides, more reactive to convective cooling, the preheating of the contour seemed to have a low but positive effect. A slower contour preheating could have had a higher positive effect but it would also increase the time between two layers thus not being beneficial for improving the overall mechanical strength of the part.

All other simulations carried out in this work can be found in Appendix C. In particular, it includes a simulation without atmospheric cooling to simulate the same solar sintering process in a lunar environment.

7 Analysis and discussions on solar sintered lunar soil

7.1 Evaluation of the thermally induced deformations of the samples and the internal stresses in the material

Thermally induced deformations of the 3D printed product seemed to be a significant issue of the solar sintering process. Figure 7.1 shows an overview of occurrences of this problem, when sintering lunar regolith layer-by-layer. The warping was created by a different cooling rate between the middle of the sintered product (trapped heat, slow cooling) and the edges of the sintered products (air convection, fast cooling).

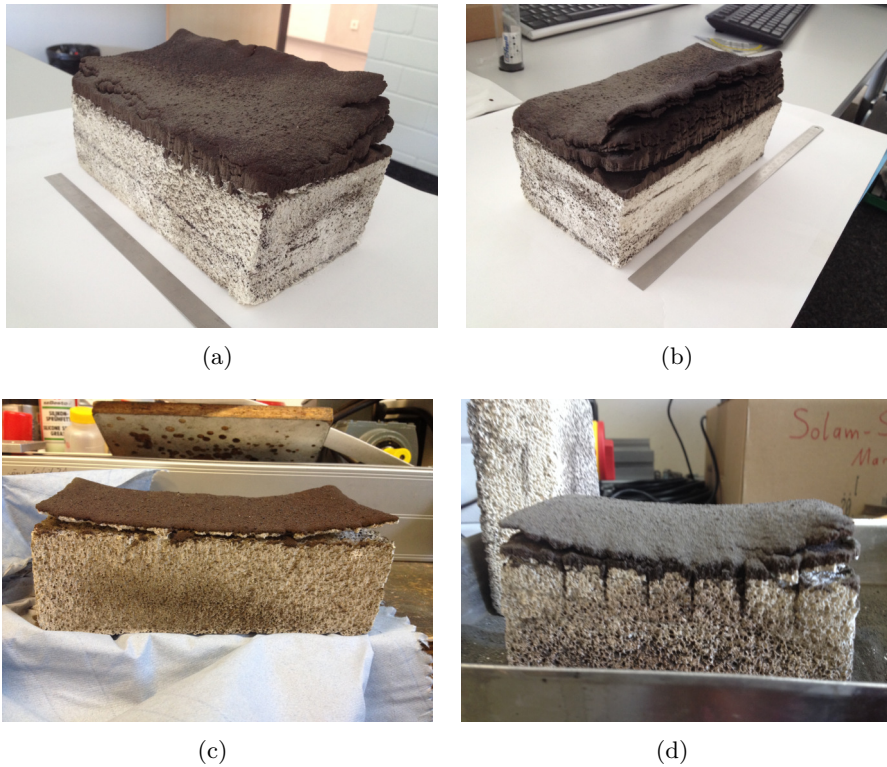


Figure 7.1: Thermally induced bending of the samples on their porous substrates after solar sintering JSC-2A using Test 4 parameters.

Solutions to solve this problem exist. Although the design of the experiment was targeting the sintering on a raw lunar regolith substrate, first tests have shown that a solid support could prevent the thermal stresses within the 3D-printed brick to deform the structure during the process. The most efficient solution would have been a substrate heated at high temperature with a porous surface. The porous surface would have allowed a good bonding of the regolith to the substrate and the heat provided by the substrate would have reduced the cooling rate as well as the thermal stresses in the sintered part from the bottom. Having a disposable substrate for each individual brick would however not be suitable for a lunar application but was the chosen trade-off in order to be able to 3D print and characterise

larger parts. In addition, the sweeping speed on the edges of the sintered part was reduced thus providing more heat in these areas. The extra heat could compensate the faster cool down on the edges of the sintered part. Another concentrated solar beam, defocused, could have also provided a constant heat to the sintered part, reducing the overall cooling. This latter option could however not be implemented in DLR solar oven nor solar simulator.

Regarding the support structures themselves, not all materials were suitable for bonding with the first layers of sintered lunar regolith. Several substrates, placed inside the testbed, were therefore tested: a porous ceramic brick, a fibrous ceramic, an aluminium coated plate with high temperature resistance glue and a ceramic foam.

The porous ceramic brick, Figure 7.2 was commonly used as a refractory element.

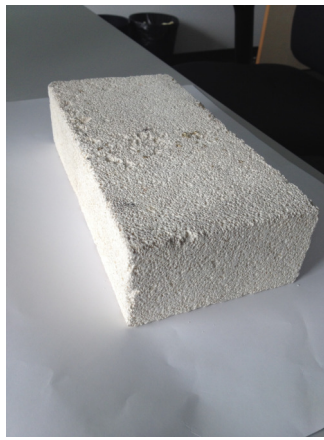


Figure 7.2: Porous ceramic brick.

The first layers of lunar regolith simulant nicely bonded to the porous ceramic substrate, as shown Figure 7.3(b). Preliminary tests led to the manufacturing of a flat brick Figure 7.3(a) as described in section 5.2.2.



Figure 7.3: Brick solar sintered on a porous ceramic substrate using Test 4 parameters (a). The regolith bonded with the porous ceramic substrate (b).

Lot of trials at the solar simulator campaign were unsuccessful with this substrate: when

too much thermal stresses occurred, the porous structure broke and did not play its role as substrate as shown Figure 7.4.



Figure 7.4: (a) Thermal stresses breaking the porous ceramic substrate. (b) Sintered part in contact with the substrate.

Fibrous ceramic, WHIPOX®, Figure 7.5, was a material developed in DLR which could also sustain high temperature [98]. Similar results were expected with this substrate, however, no bonds were formed between the substrate and the sintered part. As for the aluminium plate coated with a mixture of glue and regolith simulant, in Figure 7.6, the thermal stresses were too high and the glue debonded from the aluminium plate after a few sintered layers.

Those two substrates were therefore not suitable as support material in a solar sintering process.



Figure 7.5: Fibrous ceramic substrate.



Figure 7.6: Aluminium plate coated with high temperature resistance glue mixed and dried with one layer of JSC-2A lunar regolith simulant. Image 90°rotated.

The last tested support structures were two porous ceramics, Figure 7.7, commonly used for molten metal filtration purposes. One was alumina base and the other one zirconia base. Those supports had pores large enough so the first layers could sinter inside the porous structure thus providing a mechanical interlock. The regolith was also slightly bonding to the zirconia base one making it the best substrate.

Since these ceramic filters were only found for the last sintering campaign, the parts sintered with this substrate were only used as demonstrators, Figure 7.8, as part of the EU-H2020 project RegoLight [99]. The manufacturing of these parts was performed partly using the hardware from a project partner.

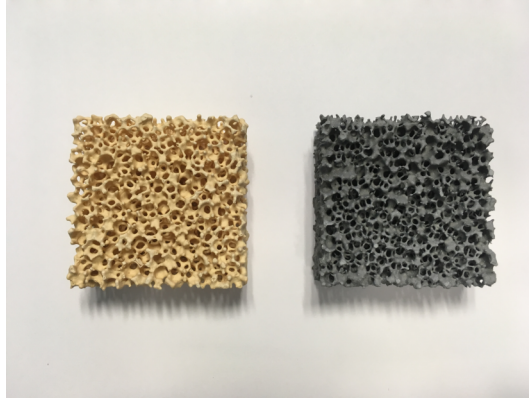


Figure 7.7: Zirconia base (left) and alumina base (right) ceramic filters.

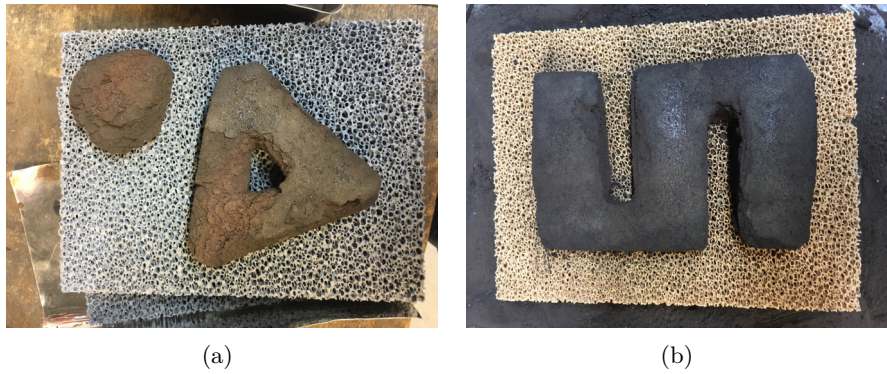


Figure 7.8: 3D printed triangle and half sphere (a), and S-shape parts (b).

7.2 Impact evaluation of the different contributors to the analogue lunar environment on the consolidation mechanisms

7.2.1 Xenon Lamps

The use of Xenon lamps was a solution to get a constant concentrated sunlight over several hours since monitoring the sunshine and automatically adjusting the sintering parameters was not possible within the scope of the project. Xenon lamps have a light spectrum close to the sunlight as shown before in section 4.2. The differences in the spectra had most likely an effect on the sintering parameters (time, temperature) but were negligible compare to the impact of other contributors of the analogue environment such as the lunar regolith simulant.

7.2.2 Lunar regolith simulant

Lunar regolith simulant was the crucial part of the analogue environment. As it was already mentioned in chapter 3 with traditional sintering, a change in the plagioclase serie, in the grain size distribution or in the glass content leads to different sintering parameters. The plagioclase members having melting points ranging from 1100°C to 1500°C, the sintering temperature of the regolith changes according to the plagioclase member in its composition. The grain size distribution plays a role on the grains arrangement, the packing, which is directly connected to the sintering efficiency since sintering is a matter of grain-to-grain contacts. The influence of the glass phase on the sintering parameters was not yet clear but it is believed that it affected the bonding of the grains, the interface crystallised grain/amorphous grain being different from the interface between two crystallised grains.

Although JSC-1A/2A, the chosen simulants in this study, were the best available simulants regarding their fidelity to some Apollo samples brought back and analysed on Earth, it was clear that the sintering speed and the solar energy required for 3D printing should be adjusted on the lunar surface according to the lunar soil composition in-situ. It was however believed that the values obtained for each process parameter in this project gave a representative order of magnitude of what would be suitable to use on the Moon.

7.2.3 Environment

The effect of the environment, sintering in air and in vacuum, was already shown in section 4.2 with traditional sintering. The vacuum environment reduced the sintering temperature and limited the iron oxidation (hematite formation). Vacuum enhanced as well the mechanical properties of JSC-1A, JSC-2A, FJS-1 and NULHT, the most representative lunar simulants in terms of mineral compositions. Compressive strength and Young's modulus of DNA simulant were reduced after sintering under vacuum, its sintering mechanisms being different to the ones for other simulants.

In this project, the solar 3D printing was performed in air. From the colour of the sample, less reddish hematite (Fe_2O_3) seemed to have formed during the solar sintering process than for the traditional sintering but the environment played certainly an active role on the final sintered material. The main impact working under 1 bar atmosphere was the positive effect of the air to protect the hardware from dust ejection. During the sintering process, some small fine particles were ejected out the testbed, some others flew away, following a flow of hot air. Over time, those two particle displacements lead to cover the mirror, reducing its reflectivity and increasing the risk of breaking it. This problem was overcome setting up a stream of pulsed air on one side of the mirror which pushed away the particles on their way to the mirror surface. Under vacuum, no air flow will displace particles up to the mirror but the outgassing will be more prominent and the spattered particles may also cover the mirror surface after a long sintering time. Ways to mechanically clean the mirror or setting up the mirror to a safe distance over the lunar soil would be required on the Moon to perform 3D printing over a long period of time in vacuum. Regarding the material structure, some gas will be trapped in the melt thus forming some large closed pores. Sintered regolith under vacuum will have most likely a foamy structure. Figure 7.9 gives an insight into what should look like solar sintered regolith under vacuum: JSC-1A was traditionally sintered at 1125°C for three hours under vacuum. The high melt fraction combined with the outgas caused the simulant, originally in the small crucible to come out into the second larger crucible, used for safety measures. Once the oven returns back to room temperature, the large crucible was taken out and broken, showing the foamy structure on the picture.

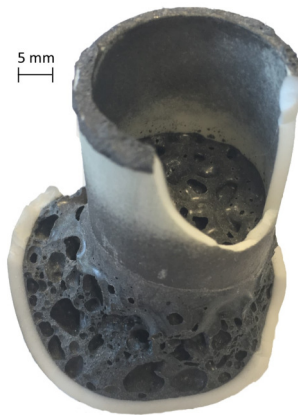


Figure 7.9: JSC-1A traditionally sintered under vacuum at 1125°C for three hours. The high out gassing level, trapped in the melt, led to a foamy structure.

A positive aspect of vacuum should be however noticed. Without the convection, the layers will cool down more homogeneously, reducing the thermal stresses. Warping of the sides of the 3D printed part should not happen under vacuum. The fact that the layers will also cool down slower than in air will increase the interlayer bonding as explained in detail further in this chapter.

7.3 Mechanical characterisation of solar sintered samples

Four bricks, parts of the deliverables were not analysed and were delivered to ESA and DLR. Details of the deliverables can be found in Appendix B.

Two solar 3D printed bricks underwent an uni-axial compression testing, one produced after Test 3 and another one after Test 14 (see section 5.2 for more details about the manufacturing parameters). The first brick was a large one with a size about 200 mm x 120 mm x 20 mm whereas the second one was a thick brick with dimensions around 145 mm x 65 mm x 40 mm. As mentioned previously, the second brick gave a feeling to be mechanically more robust due to the shorter sintering time of each layer thus leading to stronger interlayer bonds.

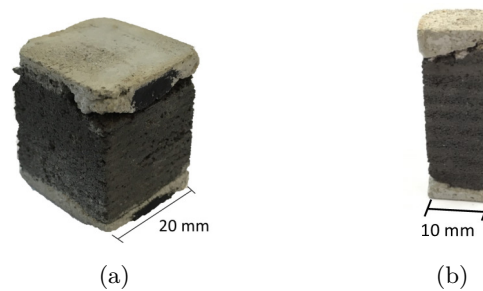


Figure 7.10: Cut solar sintered samples after being coated. (a) Sample cut from a brick, 200 mm x 120 mm x 20 mm, solar sintered on a loose regolith (Test 3). (b) Sample cut from a brick, 45 mm x 65 mm x 40 mm, solar sintered on a porous ceramic substrate surrounded by extra ceramic bricks preventing convection cooling from the sides (Test 14).

The bricks needed to be cut in parallelepiped rectangles, following the main guidelines of the norm DIN 51104. The objective of the cutting step was to get a maximum of samples, therefore, two different sizes of samples were chosen for both bricks. The large brick (Test 3) was cut using a diamond-wire saw into cubes, 20-mm wide and about 20-mm high. No cut in the height direction was performed, leading to small variations in height. Smaller samples were not possible due to the too poor sintering quality. As for the thicker brick, sintered with Test 14 parameters, it was cut into samples with dimensions 10 mm x 10 mm wide and around 20-mm high. Twelve samples of each brick were therefore produced. The cut was performed perpendicular to the layering. The sample surfaces were rough and the layered structure prevented any polishing, consequently, before the compressive tests, a thick mortar coating of 3-4 mm was added on top and bottom of each sample in order to have flat surfaces in contact with the machine. Mortar was chosen due to its higher mechanical properties in comparison to the solar sintered samples. Both samples before and after being coated are shown in Figure 7.10. During the testing phase, the samples were placed between the pressing jaws of the uni-axial compression machine. The piston stroke was 1 mm/minute. A laser recorded the precise position of the jaws in order to measure the sample's deformation. Each sample was pressed until failure. Typical failure is shown in Figure 7.11.

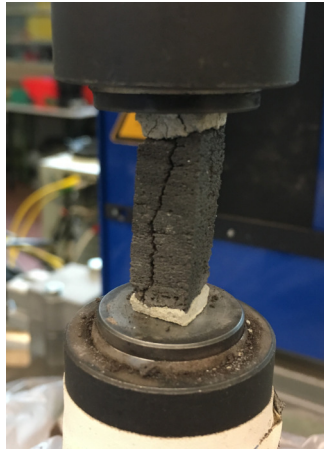


Figure 7.11: Solar sintered sample broken after undergoing a compressive stress by an uniaxial testing machine PEZ 1595.

Results, in Figure 7.12, show the average Young's Modulus and Compressive strength of the 12 samples for both bricks. Both of them had a strength similar to gypsum but they were however subject to more elastic deformation due to their porous structure (E modulus of gypsum around 1 GPa). Although the thicker brick (Test 14) had a Young's modulus 0.1 GPa higher than the wider one (Test 3), the difference was not as significant as expected. This surprisingly low Young's modulus and compressive strength was associated to the relatively small size of samples. Some defects being of a mm-size, they affected drastically the quality of a sample 10 mm x 10 mm x 20 mm. Choosing a bigger sample size would have been more judicious to get the actual strength of the solar sintered regolith with Test 14 parameters. The limited number of solar sintered bricks prevented the possibility to carry out a new compression test campaign on bigger samples. The measured values gave however the lower limit of the mechanical properties of solar sintered parts.

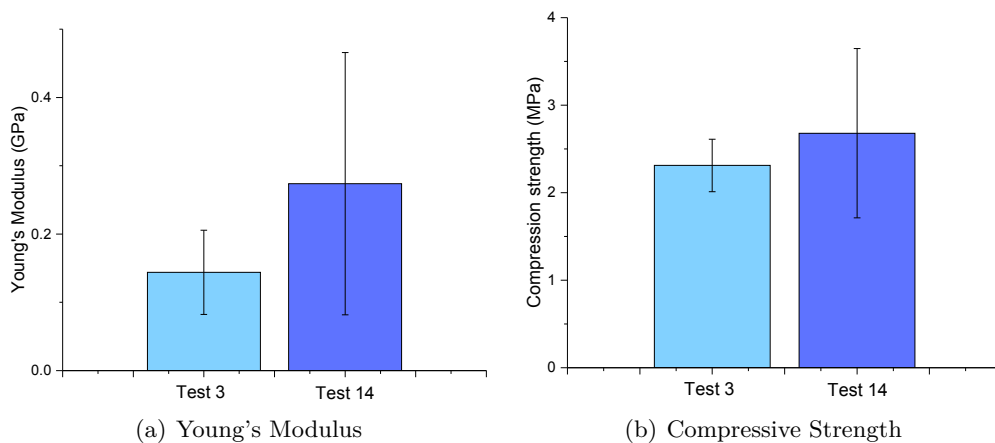


Figure 7.12: Young's Modulus and Compressive Strength of solar 3D printed regolith. The error bar represents the standard deviation.

7.4 Compactness and homogeneity of the consolidated material on a line, a layer, a volume

7.4.1 Melt fraction between sintered layers

Parameters, optimised for the set-up during the test campaigns at the solar oven and solar simulator were presented in the section 5.1. Those parameters allowed the consolidation of the material on a line, a layer and a volume.

From the 30 mm thick brick, obtained after Test 4 (see section 5.2.2), the estimated thickness of each sintered layer was 0.1 mm. A cross section of a piece of another large brick, manufactured with Test 3 parameters, is shown Figure 7.13(a).

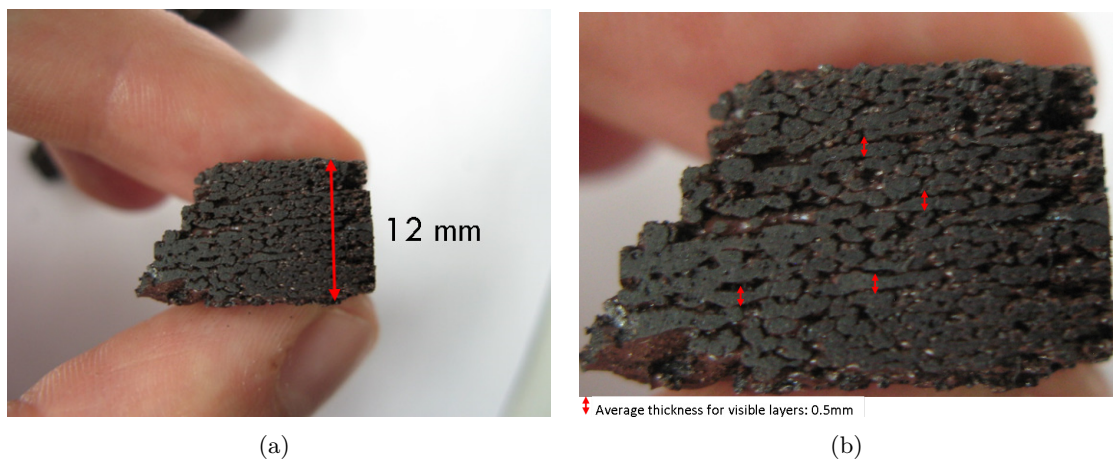


Figure 7.13: Cross section of solar sintered regolith simulant.

With a closer look at the sample, Figure 7.13(b), visible layers approximately 0.5 mm thick (i.e. corresponding to 5 sintered layers) could be observed. The irregular length and distribution of these visible layers was thought to come from the fact that some regolith grains could be up to 1 mm in diameter, creating defects in the consolidated material structure during sintering.

At this point, the first hypothesis to explain the visible laminated structure of the sintered material was that a temperature gradient existed between the sintered layers. Sintering occurred at a temperature very close to the melting point of the regolith and some constituents could even have already been molten. Moreover, the thermal conductivity of lunar regolith simulants being low, heat accumulated over the successive sintered layers: the sintered $n+1$ surface onto which the layer $n+2$ of regolith simulant was deposited was hotter than the sintered n surface onto which the layer $n+1$ of loose simulant was deposited. As a result, there was a point where the melting point was reached and all the regolith simulant constituents melted instead of having an LPS process.

It was assessed that this point was reached after five layers. Then, the next regolith simulant layer, which was at room temperature when deposited, would quickly cool and solidify the molten layer, leading to poor bonding between the grains. This phenomenon

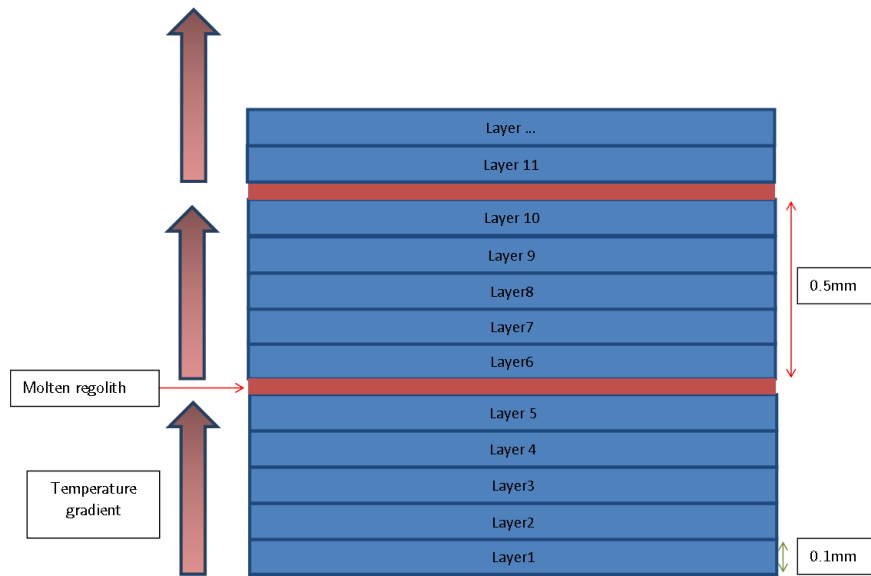


Figure 7.14: Cross section of solar sintered regolith simulant. Model describing the first hypothesis.

seemed to repeat itself all over the solar sintering process. Figure 7.14 illustrates the above hypothesis. This hypothesis was partially confirmed looking at the surface where delamination of the sintered material was observed. As shown in Figure 7.15, all the delaminated surfaces feature molten (and resolidified) regolith. The performed heat transfer simulation was however not accurate enough at the layer level to observe potential temperature change or melt formation.

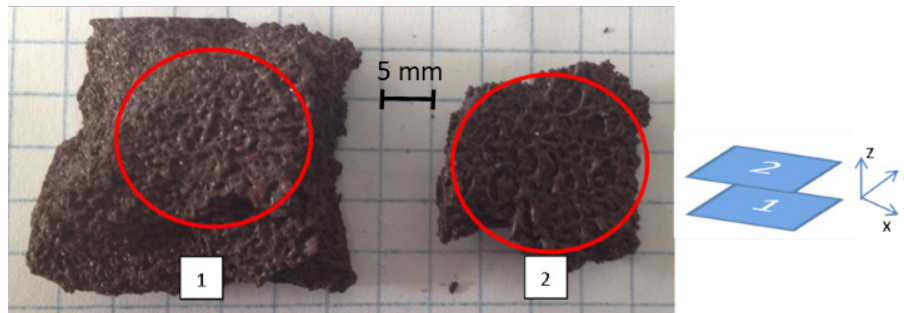


Figure 7.15: Top view of a sintered part split along the XY plane. Molten areas are circled in red.

No more information about the recurrence could be seen by naked eyes. A closer look was required before drawing any conclusion. Figure 7.16 shows the optical microscopic images of samples sintered with Test 11 and Test 13 parameters, two cylinders 100-mm diameter wide. The change of parameter between these two tests was the scanning speed: one layer out of five was sintered faster for the part manufactured with Test 13 parameters. All layers were sintered at the same scanning speed for Test 11.

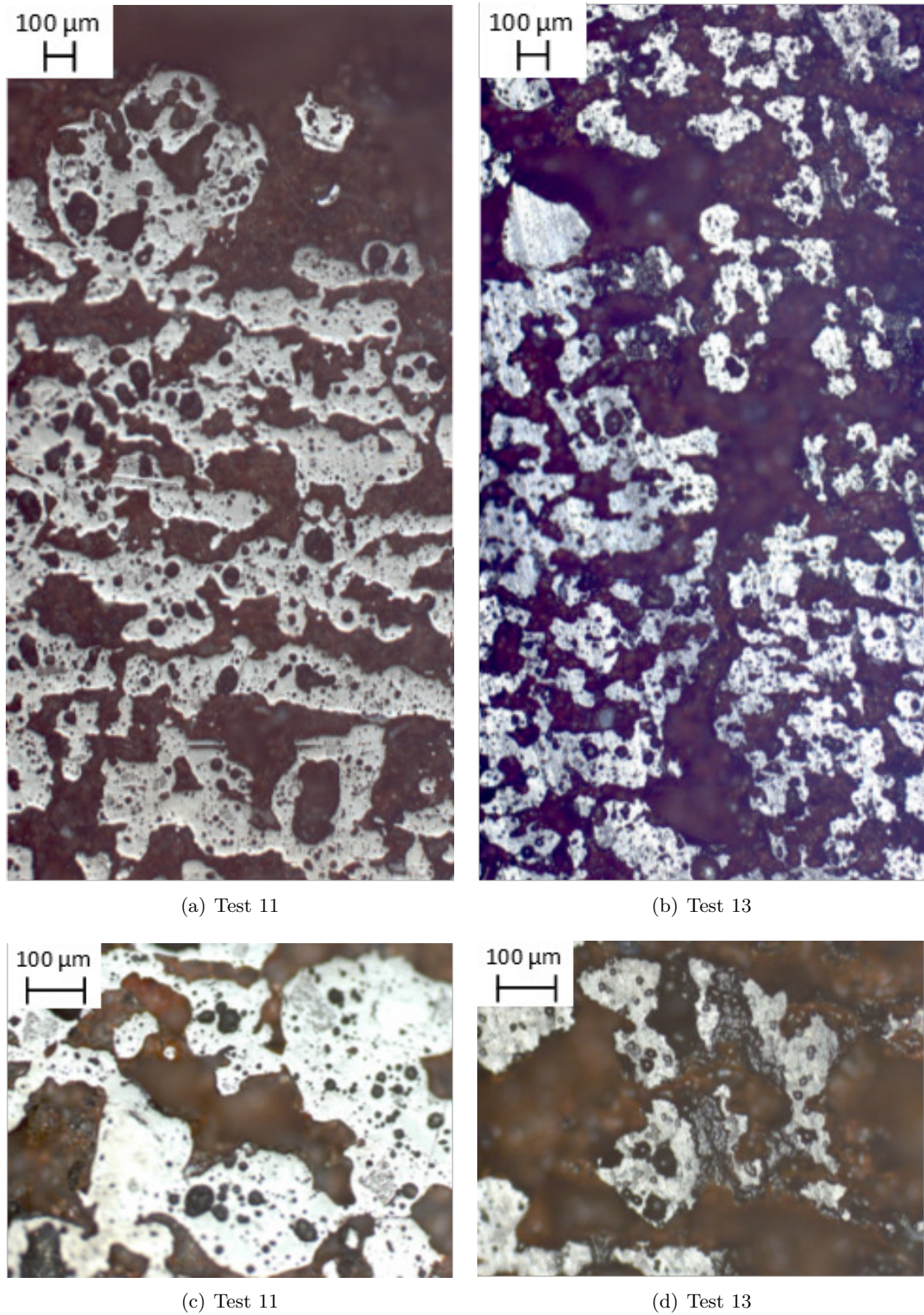


Figure 7.16: Optical microscopic pictures of a cross-section of solar sintered JSC-2A lunar regolith simulant with a constant scanning speed set at 48 mm/s (Test 11, (a), (c)) and with every other 5 layers sintered faster, at 60 mm/s (Test 13, (b), (d)).

The microscopic views of these two samples show discontinuous layers, about 200 μm thick, with numerous open and closed pores. The process difference between these two samples could not be noticed but some information might have been lost during the polishing step. The use of tomography was therefore relevant to get more details about the structure.

Tomography was carried out on several solar sintered parts using a phoenix Computed Tomography System. The objective was to have a close look of the layer size and arrangement, and to observe the open and closed pores. Pieces from 5 to 8 mm-large of regolith sintered with different parameters were used in order to keep a high resolution with a voxelsize about 6 μm^3 .

First was investigated the previously mechanically tested sample: the large brick manufactured with Test 14 parameters, when bricks were used around the sintering area to reduce the heat loss by convection. Figure 7.17 shows a tomographic cross-section of the sample.

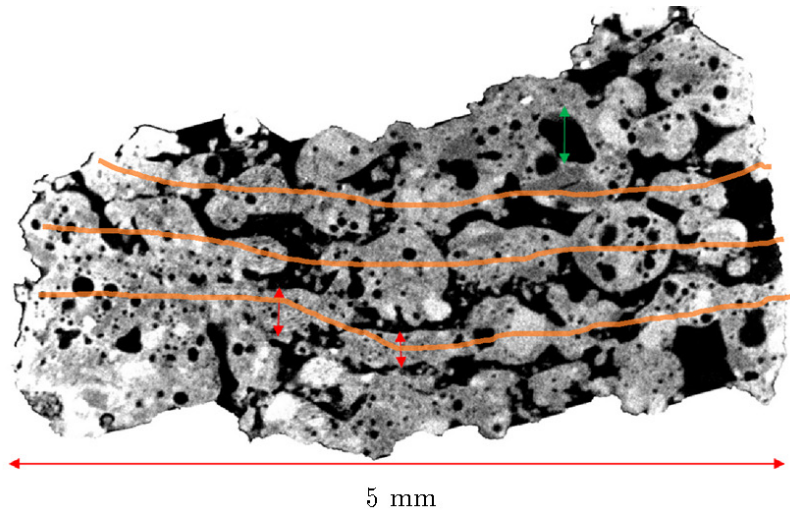


Figure 7.17: Tomography of a regolith sample solar sintered with bricks surrounding the sintering area (Test 14). In orange is shown the trend of visible layers. The red arrows represent the smallest visible layer thickness, 200 μm , and the green arrow the biggest closed porosity, 500 μm .

Previous assessments of a layer thickness was about 100 μm . This value was calculated using the final thickness of the part, the sintering time and the scanning speed. Therefore, seeing trends of 200 μm thick layers was first confusing considering that it was also observed here above that around five layers bond to form 500 μm thicker layers, visible by naked eye after polishing. Recalculation using the data from several bricks manufactured during different campaigns reassured that the thickness of a deposited layer was ranging between 90 μm and 110 μm , thus confirming the original calculation and the stability of the deposition process over the campaigns. The variations of ± 10 μm could be neglected due to the grain size, ranging from 10 μm to 1 mm according to the lunar soil grain size distribution. The thickness layer being confirmed, the layer trends, never thinner than 200 μm , suggested

that deposited grains were always sintering with their neighbours in contact and with the previously sintered layer.

Regarding the porosity, the numerous closed pores, up to 500 μm big, revealed the significant melting and outgassing occurring during the sintering process. This outgassing played also a role in the formation of the open porosity, preventing all layers to bond together. Other processes were involved in the formation of the open porosity: the spherical shape of some of the fused grains reminded the mm-size droplets of molten regolith staying on the surface due to the high surface tension of the material during the test campaigns with the real concentrated sunlight. The non-wetting property of the molten regolith was therefore considered as the main responsible factor for the weak and irregular bonding between the layers, thus leading to a significant open porosity. Section 7.5 details this phenomenon.

Similar observations were made using samples sintered with similar parameters to Test 14, Figure 7.18. The scanning speed change, one layer out of five, in the sample sintered with Test 12 and Test 13 parameters, did not show any difference compared to the samples sintered at constant scanning speed.

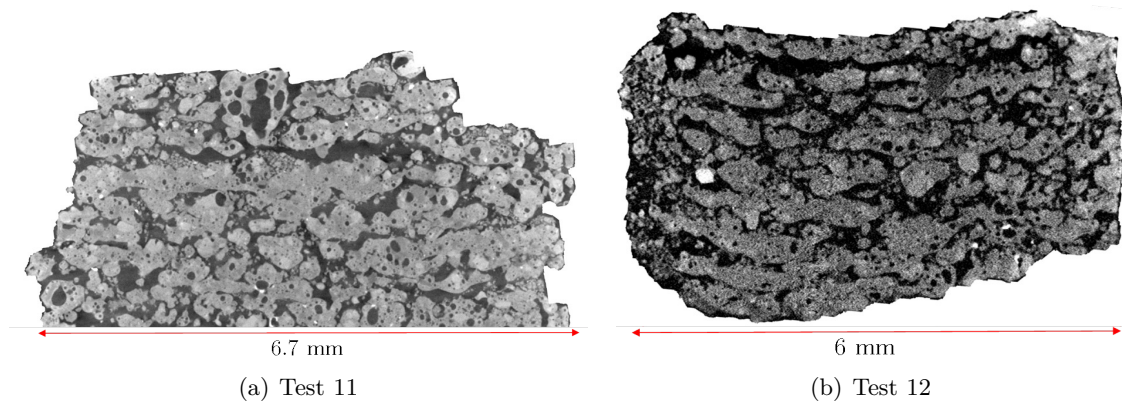


Figure 7.18: Tomography of solar sintered JSC-2A lunar regolith simulant with a constant scanning speed set at 48 mm/s (Test 11, (a)) and with every other 5 layers sintered faster, at 60 mm/s (Test 12, (b)).

Sample sintered with Test 10 parameters which used a different sintering path, Figure 7.19(a), did not show either a structure different from the previous tests. Figure 7.19(b) shows the melt used as substrate for Test 11. Some closed pores were visible in the melt due to the outgassing of the minerals. It was interesting to see the non-mixing of the melt with the grains underneath showing again the non-wettability of the melt to regolith grains.

As for the sample with Test 3 parameters, which was showing thick layers of 500 μm Figure 7.13(b), the tomography, Figure 7.20, revealed that the polishing might have simply highlighted the thick fused layers. The average thickness of fused layers was more about 300 μm . These thicker fused layers, compared to the other samples were most likely due to the fact that the sample was taken next to the molten contour. The model shown in

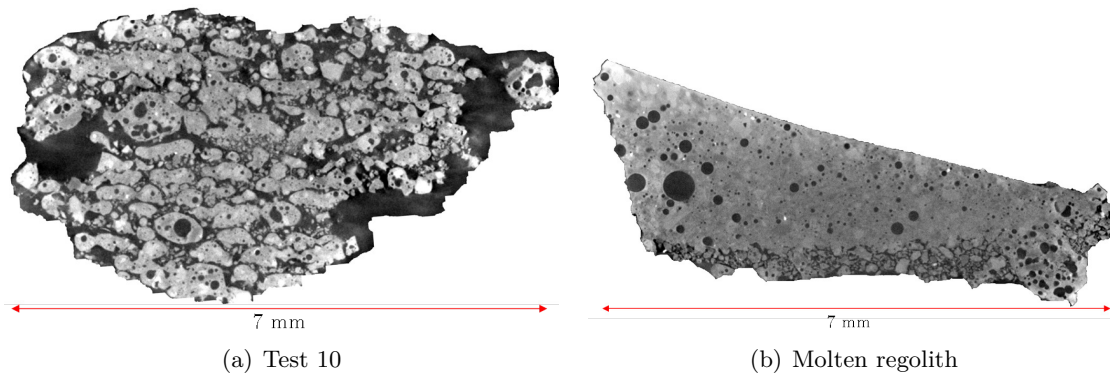


Figure 7.19: Tomography of a solar sintered JSC-2A with a zig-zag path (Test 10, (a)) and a piece of molten regolith used as a substrate (Test 11, (b)).

Figure 7.14 might therefore be true at different scales according to the sintering parameters and the piece of samples: the recurrence of 5 layers not being observed for all samples by tomography.

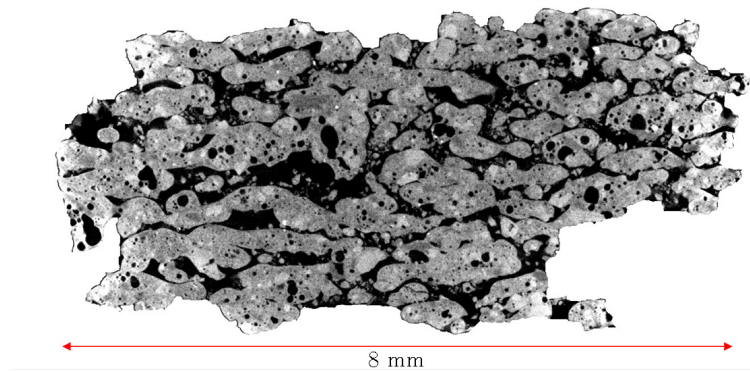


Figure 7.20: Tomography of a solar sintered JSC-2A at 48 mm/s with a contour sintered at 38 mm/s (Test 3).

Envelope density analysis on different samples did not show any trend. The density ranged from 1.5 to 1.7 g.cm⁻³ thus confirming the tomography images: all the samples have a similar structure but the bonds between the layers should be stronger on the samples 3D-printed with the shortest cooling times between the layers, like for the small parts manufactured with the parameters from Test 11 to 14.

7.4.2 Sintered grain interfaces

Another aspect of the solar sintering process that needed to be understood was to see if some new phases were formed at the interface between two sintered layers or grains. In section 4.2.1, new phases of hematite and magnetite were observed after sintering JSC-1A lunar regolith simulant in a traditional oven. In order to see if similar phases could have

formed and prevented the layers to sinter together, SEM measurements were carried out on a cross section of a sample cut from the part sintered with Test 11 parameters. Since the solar sintered part could not stand the 15 kN applied by the embedding machine, the cut sample was simply placed into a mixture of urethane resin and an hardener. The mixture, originally liquid, could nicely embed the sample. After a couple of days, the sample was hard and could be polished and sputtered with platinum on its surface. A conductive tape was used for conducting the electrons to the ground of the SEM. Figure 7.21 shows the embedded sample. The corner of the tape was used as a landmark for orienting the SEM images.

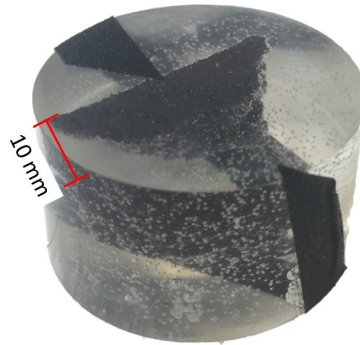


Figure 7.21: Cut solar 3D printed sample, 30 mm x 10 mm, embedded in hardened urethane resin for SEM observation.

The sample was observed by SEM in secondary electron detection mode, Figure 7.22, to see the topology of the surface. Similar observation as on the tomography images could be made, with closed pores that could reach 500 μm and the high density of open pores making the layers discontinuous. Back-scattered electrons images were more interesting to look at potential new phases.

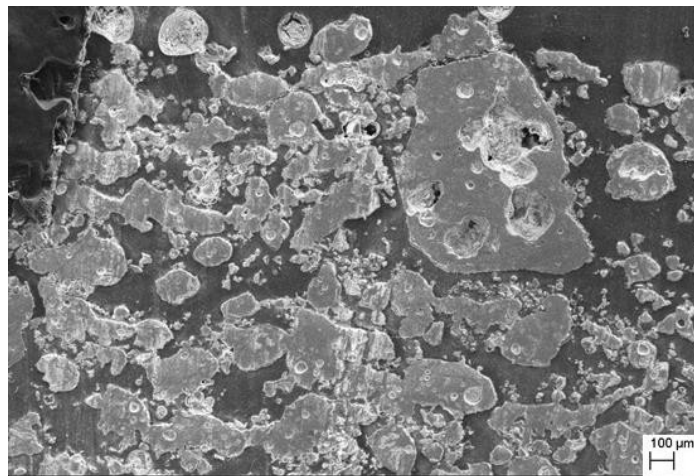


Figure 7.22: Secondary electron image of the cross section of JSC-2A solar sintered on top of molten regolith at 48 mm/s (Test 11). The conductive tape is visible in the top left corner.

Figure 7.23 shows ten back-scattered electron images merged together. This combination allowed the observation of the sample over the whole thickness. It was however difficult to find a sure spot where two different layers sintered together could be identified.

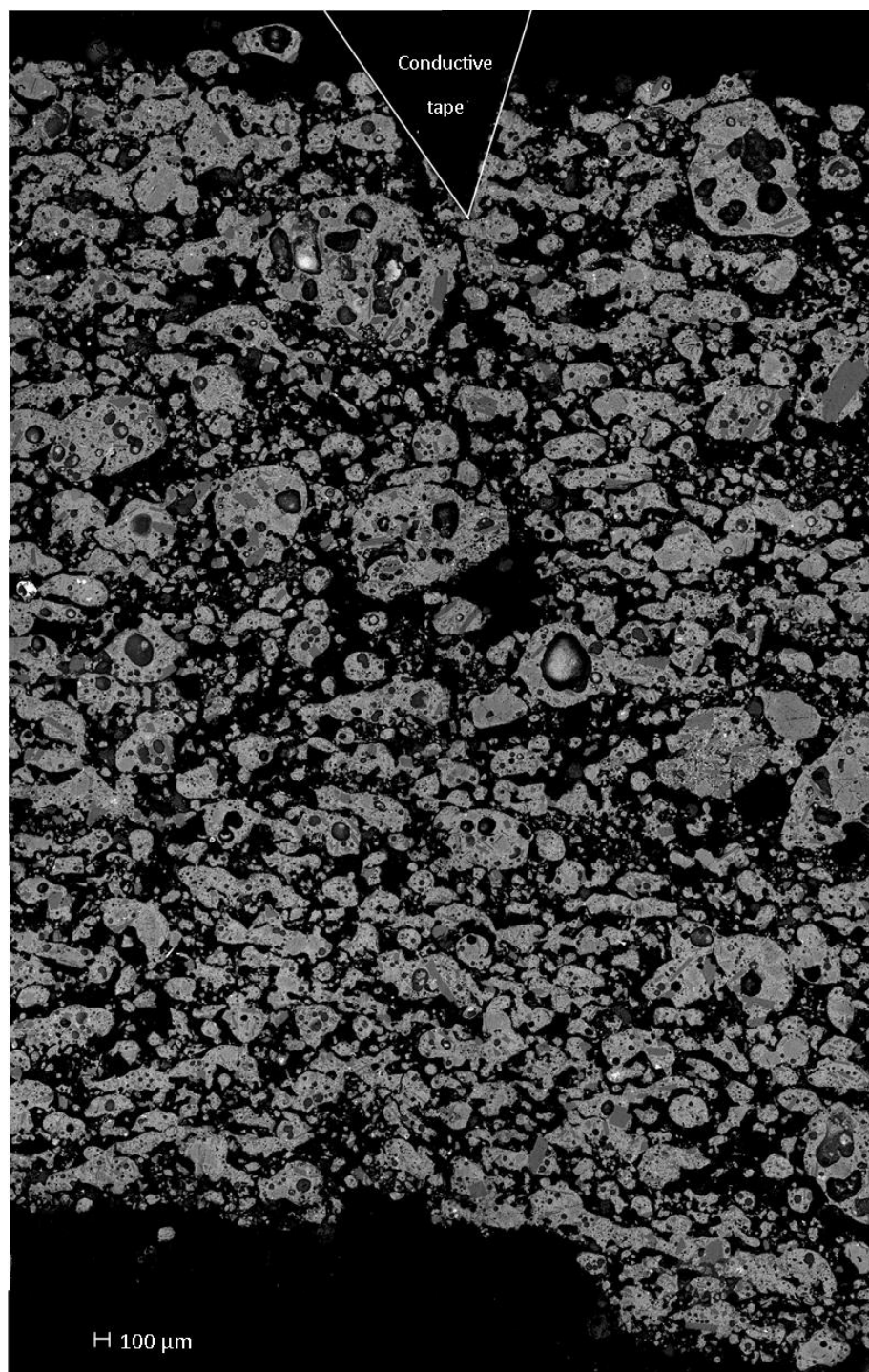


Figure 7.23: Joined back-scattered electron images of the cross section of JSC-2A solar sintered on top of molten regolith at 48 mm/s (Test 11). Each layer was sintered in about 20 seconds. The conductive tape is visible in the middle top.

The higher magnification image, Figure 7.24 where two layers could possibly have bonded, did not show any interface but only large plagioclase grains embedded in a molten matrix. These large grains, not melting due to their high melting point, about 1500°C, might have blocked the viscous melt to flow into pores.

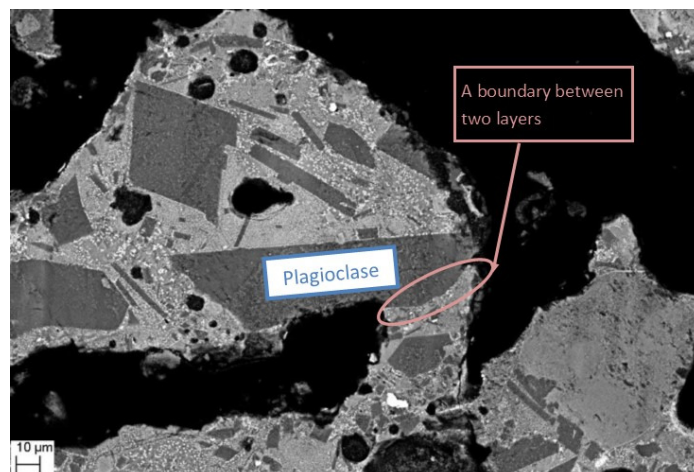


Figure 7.24: Back-scattered electron images of the cross section of JSC-2A solar sintered on top of molten regolith at 48 mm/s (Test 11). Each layer was sintered in about 20 seconds. Higher magnification.

7.5 Regolith sintering mechanisms

From the solar sintering experiments and the characterisation of the sintered parts, several hypotheses were stated regarding the mechanisms playing a role in the grain-to-grain (1D and 2D) and the grain-to-surface (3D) bonding. This section aims therefore at giving a clear picture of the solar sintering process of lunar regolith.

7.5.1 Planar mechanisms

Going back to the 2D sintering, with the right amount of heat and the right overlap between the lines, a sintered plane was easily homogeneous. The as-deposited lunar regolith simulant grains simply sintered when the concentrated solar beam passed over them. No boundary nor interface could be noticed. Understanding why the sintered lines bonded nicely into a plane was crucial for explaining the issues happening going from 2D to 3D printing.

Solar sintering required LPS. Within the few seconds where the concentrated solar beam shined on the regolith, solid state sintering could not bond the grains together [100]. Some elements of the lunar regolith needed therefore to melt and play the role of a binder. From the SEM pictures shown previously, only plagioclase minerals could be identified, meaning that the olivine and pyroxenes, other important constituents of lunar soil, were either not part of the as-received simulant, or were present in too small crystals to be visible by SEM, or were molten during the solar sintering process. A significant glass content was also present in the as-received simulant.

Olivine and pyroxene minerals were clearly visible in sintered JSC-1A SEM pictures and since JSC-2A lunar simulant was supposed to mimic JSC-1A according to the material data sheet, it was guessed that olivine and pyroxene minerals were present in the simulant, in the form of nano-meter size crystals. Olivine, pyroxene and glass should have therefore represented about 70% of the simulant constituents. During the solar LPS process, these three constituents partially melted, mainly the smallest grains, and spread around the bigger grains and the plagioclase grains remaining at powder state. If olivine, pyroxene and glass would have completely melted under the temporary solar radiation exposure, the melt fraction would have been higher and the viscosity lower. A balling process, common in laser AM [100], could have created molten spheres. Connected molten spheres forming the experimentally observed molten channel could have then formed on the surface of the substrate and prevent the 3D printing process. During cooling, all molten elements recrystallised as the cooling rate was not high enough to create a pure ceramic glass [101].

When one line was sintered and a second one had to be sintered next to it, an overlap was required. Fixed to 14 mm during the test campaigns, this overlap remelted the solidified melt fraction used for bonding the first sintered line. Doing so, the melt of the second line mixed with the melt of the first one thus leading to a uniform layer formed by the two merged lines. This process could be repeated over the surface, line by line, to form the desired layer.

7.5.2 Volume mechanisms

Bonding the sintered layers together has shown to be more challenging, weak bondings and delamination playing a role in most of solar sintered parts over the different test campaigns at the solar simulator. From the observation of the successful and unsuccessful solar sintered parts throughout the solar oven and simulator campaigns, four possible cases, Figure 7.25, were distinguished according to the amount of heat transferred to the as-deposited regolith and to the layer of already sintered regolith.

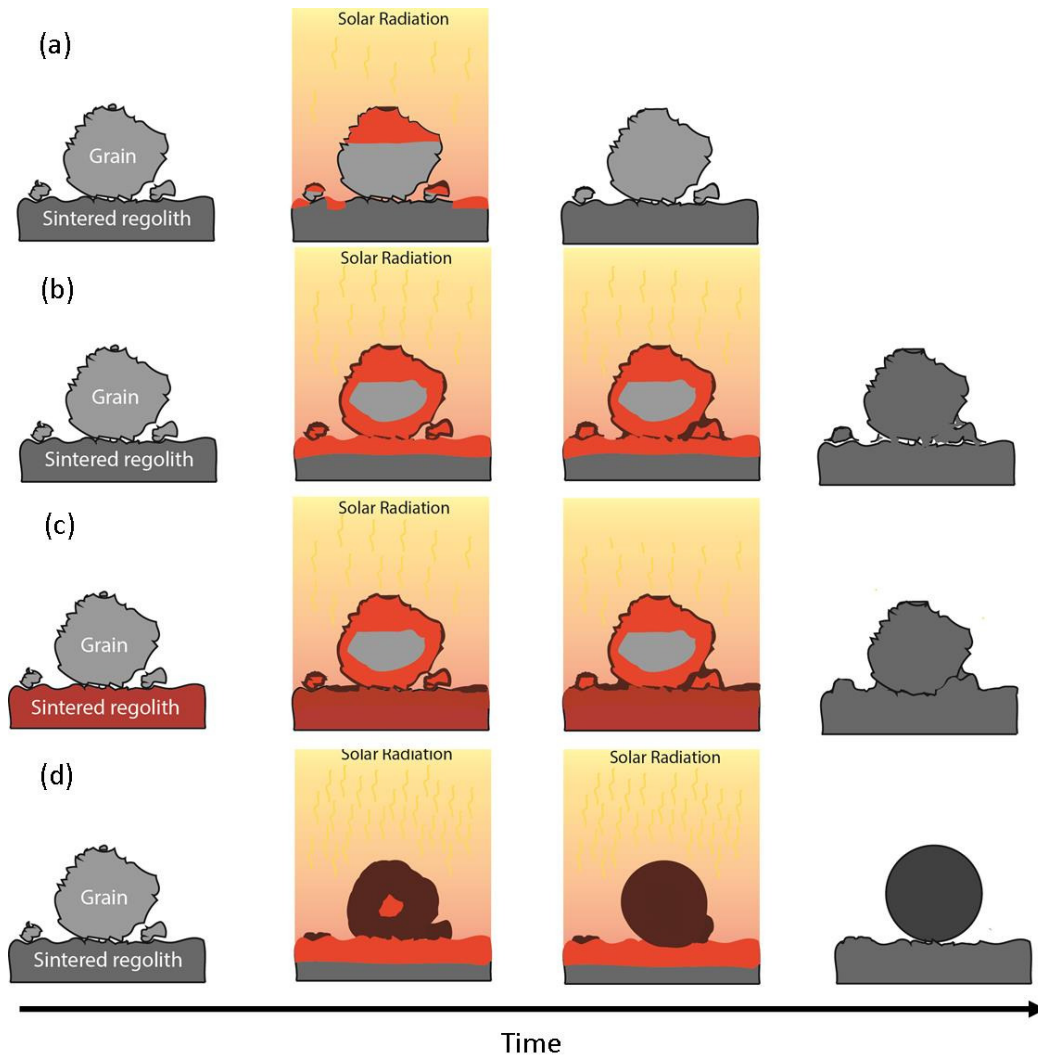


Figure 7.25: Different scenarios of grain-to-surface bonding according to the delivered solar flux density: not enough heat is distributed (a), sufficient heat is distributed without (b) and with a hot substrate (c), and too much heat is distributed (d). Time line from as-deposited powder to end product. The temperature gradient goes from grey to red to brown (melt).

The first case, Figure 7.25(a) is simple: not enough heat is distributed to the material due to a too fast sweeping of the concentrated beam or a too low solar flux density. When this happens, only the surface of the grains are slightly heated. The tiniest grains could melt

but the heat reaching the substrate between the grains would be fully absorbed and not reflected. No solar sintering can happen this way, the grains remain practically unchanged after cooling.

In the second case, Figure 7.25(b), a sufficient heat is provided to the as-deposited lunar simulant to bond perfectly over a plane. The sintered regolith is at a temperature about 600°C as it was the case sintering the large bricks, 200 mm x 100 mm wide, at the solar simulator and in the Model 2 presented in section 6.3. In this case, the heat passing between the grains diffuses inside the substrate and is reflected on the grains thus allowing grains of all sizes and shape to have at least a bit of melt on their surface to merge with their direct neighbours. The heat is however not sufficient for partially remelting the surface of the already sintered layer and a poor interlayer bonding is then formed.

The third case, Figure 7.25(c), is similar to the second one, the same heat is provided but the sintered regolith is this time at a higher temperature, about 800°C. It would be the case when sintering a small part like in Tests 11-14, or for the smaller brick, 100 mm x 50 mm wide, simulated in section 6.3. This 200°C change compared to the second case is sufficient for partially remelting the substrate when the concentrated solar beam passes over. The melt of the grains and the substrate can merge and create bonds. This case should be targeted for every solar sintering process of lunar regolith.

Finally, the last case, Figure 7.25(d), involves an overheating of the as-deposited regolith, from a too slow sweeping or a too high solar flux density. The substrate can be considered at about 600°C. Comparing Model 1 and Model 2 in section 6, it was possible to see that the same amount of heat would increase the temperature of lunar regolith as a powder much faster than for the sintered one, due to the heat conductivity difference. Hence, if too much heat is distributed to the layer, the grains completely melt whereas the sintered regolith just absorbs and reflects the heat. The absorbed heat might not be sufficient for partially melting the surface and, as mentioned above for the mechanisms involved over a plane, the melt minimises its surface tension, creating a sphere. Cooling down, this sphere has almost no contact with the sintered regolith, the non-wetting property of the molten lunar regolith, detailed further, preventing any cohesion.

An extra case, where the substrate melt with the molten grains was voluntarily not detailed. This scenario would lead to molten regolith flows, far from the current sintering process targeted on the Moon in this work. The use of molten regolith for lunar application would require to investigate the crystallisation processes, and the sensitivity of the glassy material to lunar temperature fluctuations would need to be understood further.

7.5.3 Melt/sintered regolith interaction

Understanding the non-wetting behaviour of the molten regolith towards porous sintered regolith is the key to significantly enhance the solar sintering process. Non-wetting issues are not so uncommon with other materials: the most classic example is the non-wetting of the lead or tin in contact with a Printed Circuit Boards (PCB) while soldering. Nevertheless,

reasons causing this non-wetting behaviour can be numerous.

Our case of molten regolith in contact with sintered regolith is ruled by molten ceramic/ceramic interactions, poorly studied in the literature. Interactions between molten metals and ceramics/metals have however been extensively treated over the last decades as it is an interesting topic for brazing and soldering activities in electronic industries [102, 103]. Driven by thermodynamics, the issues raised by the wetting of molten metal on ceramic could be similar for our melt/sintered regolith interactions. When a droplet of liquid is in contact with a flat solid, the droplet changes its shape until the total surface and interfacial energies have reached a minimum [104, 105]. Three interfacial energies are present in the system: γ_{SL} , γ_{SG} and γ_{LG} , respectively the interfacial energies of solid/liquid, solid/gas and liquid/gas. The shape of the droplet is then driven by the Young-Dupré equation [106]:

$$\gamma_{SG} - \gamma_{SL} = \gamma_{LG} * \cos(\theta) \quad (10)$$

where θ is the wetting angle as shown Figure 7.26.

If the wetting is targeted, the droplet needs to spread over the surface, meaning the θ angle has to be minimum. This result can be achieved if the γ_{SG} is high or if the γ_{LG} is low. When the γ_{LG} or γ_{SL} are high, the droplet will form a ball to minimise its surface area with the surrounding gas (air in this work) or the surface [58, 104].

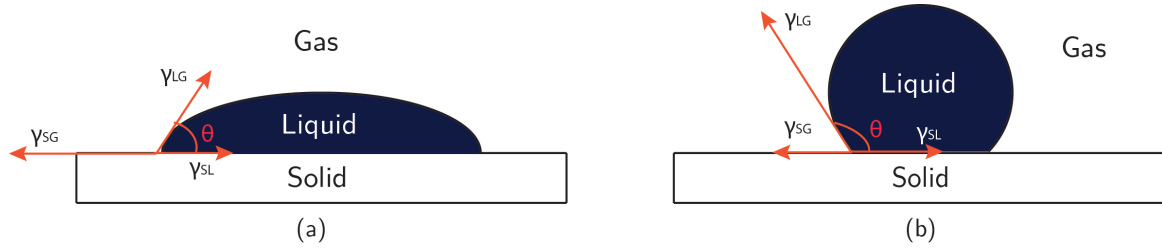


Figure 7.26: Contact angle of wetting (a) and non-wetting (b) of the solid surface by a drop a liquid.

The point where the droplet is considered as wetting the surface depends on the definition [104]. Mostly, the wetting is reached if $\theta < 90^\circ$, and non-wetting if $\theta > 90^\circ$ [106]. The adhesion work is then ruled by the Dupré equation:

$$W_{ad} = \gamma_{SG} + \gamma_{LG} - \gamma_{SL} \quad (11)$$

where

W_{ad} : Adhesion work [J]

γ : Interfacial energies [J]

During the solar sintering campaigns, the slightly molten grains were generally poorly wetting the sintered material if its temperature was too low. It resulted a solar sintered part

with low mechanical properties, shown by a Young's modulus of 0.15 GPa and a compressive strength of 2.5 MPa. Smaller sintered sample had however a higher substrate temperature during the deposition and sintering of the layers and higher compressive strength. These higher mechanical properties can be explained by a change in the wetting properties: a higher temperature of the substrate reduces γ_{SL} and a higher melt temperature reduces γ_{LG} [107], thus increasing the area covered by the melt. Doing so, the sintering goes from the previously exposed case (b), Figure 7.25(b), to the case (c), Figure 7.25(c). The end-product has a better sturdiness, not quantifiable in this work due to the limited amount of solar sintered samples that could be used for standard destructive tests.

Other parameters can influence how the liquid spreads over the surface. The roughness of the sintered regolith could favour the spreading of the melt over the surface [108] or be detrimental [109]. Surfactants could also theoretically be added to lower the interfacial energy γ_{SL} and increase the wetting. This later solution is however not suitable for lunar application if the surfactant cannot be extracted from the lunar regolith.

Spreading of the melt fraction is however not sufficient for insuring a strong bonding of the layers once the material cools down. The interfacial energies are linked to the intermolecular bonds within the material and at the boundary. Wetting is happening when the adhesive forces overcome the intermolecular cohesion forces of the melt. Once the liquid is spread, chemical wetting or physical wetting hold the melt and the substrate together. In case of chemical wetting a reaction occurs between the melt and the substrate. With metals, an intermetallic layer is usually formed at the boundary, and bonds with the droplet and the substrate. For instance, in classic soldering of tin over a copper substrate, Cu_3Sn and Cu_6Sn_5 phases are formed at the boundary and insure the cohesiveness and electrical conduction between the tin and the copper [110]. In the case of lunar soil solar sintering, the plurality of the compounds in the regolith prevents any strong chemical affinity for producing such “intermineral” layer. Figure 7.27 shows as-received grains of JSC-2A lunar simulant and solar sintered grains of JSC-2A.

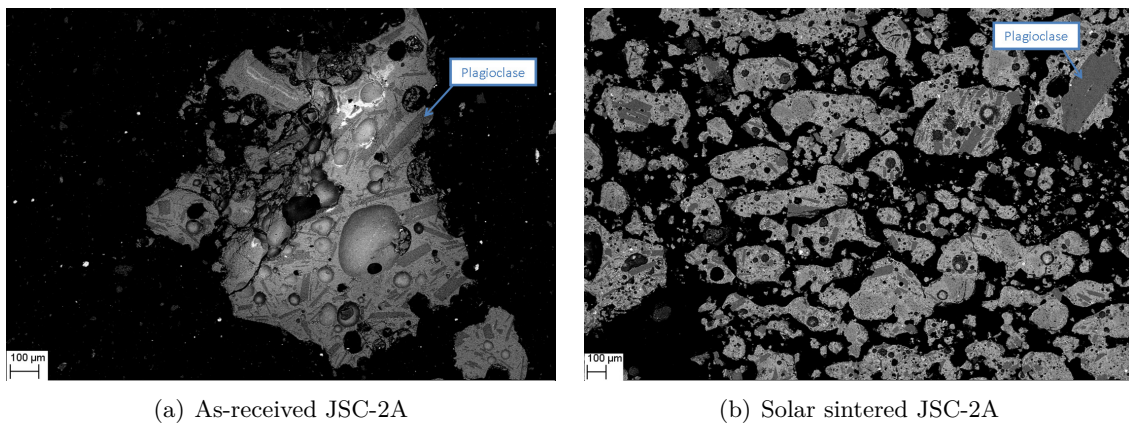


Figure 7.27: Back-scattered images of as-received (a) and solar sintered JSC-2A (b).

No difference can be noticed, there is no interfacial layer at the hardly distinguishable grain boundaries in the solar sintered regolith sample, only Van der Waals forces are therefore contributing to the adhesion of the molten regolith on the surface. London interactions and polar bonds hold the layers together. These forces are weak compared to the ionic and covalent bonds of a crystallised ceramic. Increasing the melt fraction of the substrate and the deposited powder to a correct level during a lunar soil solar sintering process may lead to the mix of the melt and the recrystallisation into minerals with strong bonds. Capillarity forces may also help the melt to get inside the open porosity thus enhancing the bonding.

8 Outlook and Applications

8.1 Solar 3D printing of sand

Markus Kayser developed back in 2011 a solar 3D printer solely working with concentrated sunlight and desert sand [81]. On the promotion video for his project, he presented some nice complex shape 3D-printed parts. At the DLR solar oven, the set-up for solar 3D printing lunar regolith was used with sand for a day in order to see the easiness to 3D print sand compared to the lunar regolith. Higher temperatures were required to sinter sand and the solar oven had to be used since two Xenon lamps would have sintered the material too slowly. Nevada sand was used for the experiment. It was a low grade sand which was rich in aluminium and silicon oxides with lot of small stones, few mm size. The sand was placed in a steel testbed and the powder feeder. The testbed was then moved manually under the concentrated solar beam, at about 10 mm/s, as in Figure 8.1(a). The shutter being fully open, the temperature was estimated to 1800°C - 2000°C. The feeding rate was voluntary excessive as the aim of the activity was more to observe the sintering behaviour of the sand than manufacturing 3D printed objects, as shown Figure 8.1(b).

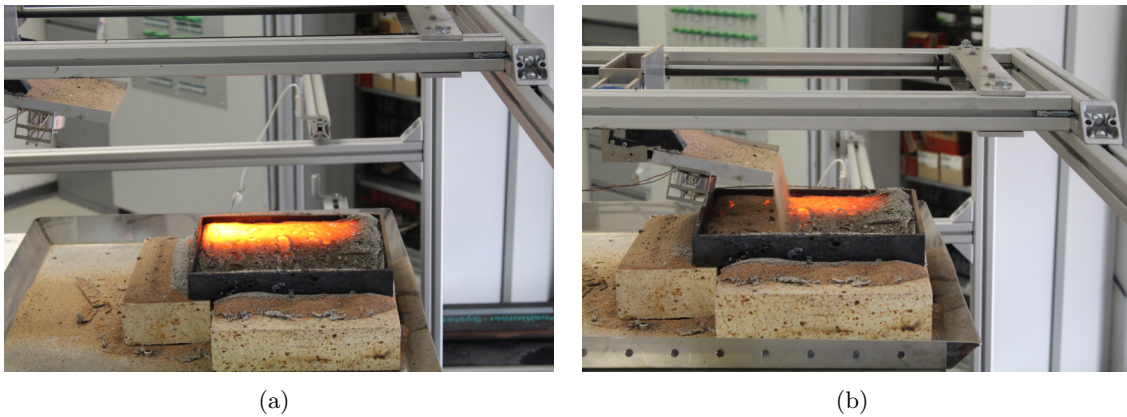


Figure 8.1: Solar sintering of one layer of sand moving the tray at 10 mm/s under the concentrated solar beam (a) and deposition of a layer about 2 - 3 mm-thick (b).

After about 30 layers, a solid block of sintered sand, Figure 8.2(a), could be removed from the testbed. The surface was smooth and glassy, the molten sand forming a matrix and embedding the bigger grains. By hand, more strength had to be applied to break a side of the block and see how the material was sintered in depth than for any solar sintered part. Figure 8.2(b) shows a cross-section of the solar sintered block of Nevada sand. Layers were clearly visible, their thickness varying between 2 and 3 mm.



Figure 8.2: Solar sintered block of sand (a) and a cross-section of the same part (b).

Although the aim of this experiment was not to tune the sintering parameters to do solar additive manufacturing, a solid brick was obtained in about one hour at the solar oven without having any previous experience of sand sintering. The heat penetrating through several millimetres, instead of micrometers for regolith, the 3D printing process was faster. Also, the melt, which bonded with surrounding grains, helped in the bonding of the material thus making the solar sintering of sand a LPS process with a high melt content much easier to handle than lunar regolith sintering where an excess of melt needed to be prevented as explained in section 7.5.

8.2 Recommendation on process enhancement.

Further developments of the solar sintering technology need to be carried out on Earth for a better understanding of the process and its limitation.

8.2.1 Strength enhancement

One of the sintered material's weaknesses was its low mechanical strength, exhibited after the compressive strength measurements. A possible solution to enhance the mechanical properties, would be to sinter the brick faster in order to reduce the cooling time between the sintering of two layers. With the set-up used in this project, it was not possible to provide more energy for sintering faster due to the fragility of the water-cooled mirror. Therefore, the design of a new set-up should take into account the weakness of a mirror, placing the Xenon lamps vertically not to use any reflection optics. Figure 8.3 shows the set-up in this configuration.



Figure 8.3: CAD drawing of the modified set-up, not using a mirror.

Another way of improving the mechanical strength of the material would be to press the deposited layers of lunar regolith thus increasing the grain-to-grain contacts and therefore the mechanical properties over one layer of lunar regolith. The pressing should however not cool down the deposited lunar regolith to prevent a loose bonding between the layers.

8.2.2 Sintering area

The low resolution of solar sintering, around 20 mm over the x- and y- directions, combined with the relatively small sintering area, around 270 mm x 200 mm, reduced the fidelity of the process in relation to a lunar application. The current deposition and sintering of the lunar regolith simulant was indeed prone at the boundaries to the Earth gravity angle of repose of the soil, thus affecting the sintering process to an extent that might not be negligible. The sintering of larger parts, using a larger testbed, would therefore be more relevant for sintering lunar soil keeping in mind a direct lunar application since the boundaries impact on the process would then be smaller.

8.2.3 Substrate

Substrates made of sintered or molten regolith were not satisfactory due to the lack of chemical and physical bonds with the sintered parts. In this work, different substrates were tested, the most promising one being a porous technical ceramic, usually used as filters in smelting plant. Hence, further research works needed to be performed to produce a substrate material using in-situ resources or to prevent the warping of the parts during the sintering process.

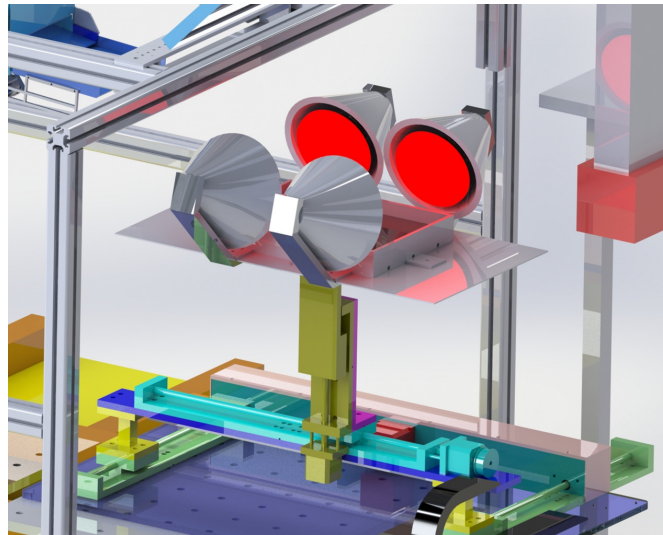


Figure 8.4: CAD drawing of the modified set-up, using infra-red lamps for keeping the sintered part at high temperature.

A steady heat source on the side of the testbed, using for instance infra-red lamps, could reduce the thermal stresses in the part thus reducing the deformations during cooling. Figure 8.4 shows the possible upgrade to the current set-up.

8.2.4 Layer deposition system

In this project, vibrations and gravity were used to deposit a new layer of regolith on top of a freshly sintered one. On the Moon, with the reduced gravity, better solutions could be found for depositing thin, homogeneous, compacted and smooth layers of lunar regolith. A sweeper, already used in conventional commercial powder base 3D printers, could be a solution for spreading regolith on top of a sintered layer.

8.2.5 Equipment robustness and dust mitigation

Hardware and electronic parts of the set-up worked in extremely dusty conditions during the solar sintering campaigns. Several fans and an extractor hood were used to remove the dust from key pieces of hardware like the mirror. However, the 3-axis table, yet cleaned everyday, showed a clear deterioration over time. The axial screws were not protected, originally for safety issues, since folded plastic protections would have caught fire in case of direct contact with the concentrated sunlight. The accumulation of dust in the bearing led to wrong displacements of the 3-axis table preventing sintering processes longer than 5 hours. During the last campaign, problems started occurring after only 3-hour processes. The electronic, even covered with dust, did not show any trouble. After each campaign, the room where the sintering took place had to be meticulously cleaned due to the dust deposited in every nook and cranny. The next set-up should take more into account the dusty working environment, closing the space around the feeder and the testbed and protecting all bearing from micro-metric dust particles.

8.2.6 Vacuum environment

Solar sintering of lunar regolith needed to be performed under vacuum. The outgassing and the slight melting of the regolith, observed during the sintering process in air, will most likely have a more prominent effect under vacuum and needed to be understood beforehand.

8.2.7 Close-loop sintering

Currently, the set-up was optimised with a steady light source, the Xenon lamps, and only one lunar soil simulant, JSC-2A. For preparing a lunar application, the flux density of concentrated solar light should be controlled in a way that it could stay steady even with light fluctuation due to Earth atmospheric changes. A shutter could be more or less open to reduce or increase the incoming focused light. In a more advanced version of the set-up, the mirrors of the concentrator could defocus and refocus the light, according to the direct normal irradiance (DNI), in order to keep a constant flux density at the sintering point.

As for material variations, it was challenging to monitor the sintering process and adjust in-situ the sintering parameters. So far, the parts were sintered with a trial and error approach, using mainly the operator experience to adjust the sintering parameters before starting a new trial. Research work should be allocated to the development of a piece of

equipment, maybe using IR cameras, capable of monitoring the sintering quality by image processing and able of changing the sintering parameters automatically in order to adapt constantly the process to the material being sintered.

8.3 Recommendation on potential process adaptation for lunar application.

With a solar sintering approach, this study has shown that it is not required to sieve nor to sort the lunar regolith for manufacturing parts layer-by-layer. The regolith can therefore be picked by a rover equipped with a tool similar to a dustpan. The right thickness of regolith, around 100 μm , should then be spread and compacted homogeneously over the surface to sinter. Big rocks, with a size >10 mm, scattered across the lunar surface should however be removed from the sintering area. If the regolith is first used for oxygen production in another process, the waste, a metal-rich regolith, should be collected and integrated to the construction process.

However, some adjustments need to be foreseen in order to use the solar sintering technology on the lunar surface.

8.3.1 Mobile concentrated solar beam

The current laboratory set-up used a 3-axis table to move a testbed with lunar regolith under a fixed concentrated sunbeam. On the Moon, the concentrated sunbeam will have to move over the lunar soil in order to go from the 3D-printing of bricks to the additive manufacturing of continuous structures, around an inflatable dome for instance. Different technologies were tested in the last 10 years, using a mirror and a Fresnel lens [82] or concentrating sunlight into fibre optics [83]. The TRL of these processes is still however very low and they can only be used for dust mitigation purposes. A rover could carry around the mirror and lenses, or the fibre optics.

8.3.2 Shielding

Radiations coming from outer space charge any device on the lunar surface. These charges could disrupt the proper functioning of the machine and fine particles of lunar regolith could stick to the rover and optical elements surfaces thus reducing the lifetime of the apparatus. The set-up should also be able to undergo temperature fluctuations, from -153°C to 123°C , during lunar nights and days. An appropriate shielding is therefore required on the Moon to reduce the thermal cycling and the charging of the set-up.

8.4 Radiation shielding

One use of solar sintered regolith would be for protecting the astronauts from Galactic Cosmic Rays (GCR) and Solar Particle Events (SPE). GCR are chronic highly ionising

radiations coming from outer space with an intensity varying from 1 to 2.5 particles.cm⁻².s⁻¹ [111, 112]. SPE are high energy protons delivered by the Sun. These events are punctual and mostly unpredictable although they are related to the peak solar activity in an about 11-year cycle [112, 113]. SPE can eject up to 10¹¹ particles.cm⁻². GCR and SPE particles can both have energies reaching 1 GeV.

Protecting the crew from GCR and SPE is required in any mission planning [114]. GCR are not a concern for short-term Apollo-like missions but could exhibit a career limiting radiation dose to the astronauts in case of long-duration mission. No career limit exposure currently exists for space flight but a maximum one exists for Low Earth Orbit (LEO). This career limit dose corresponds to a 3% lifetime excess fatal cancer risk [112, 115]. The most sensitive parts of the body to radiation are the so-called Blood Forming Organs (BFO): their annual limit dose equivalent is 500 mSv, not exceeding 250 mSv in a month¹.

Precise measurements of the radiations levels on the lunar surface are required for assessing the thickness of sintered regolith required for protecting the astronauts for their entire mission. Apollo astronauts performed some radiation measurements on the lunar surface but were able to detect only low energy protons thus making the measurements not sufficiently accurate. More recently, computer models and laboratory experiments were carried out using 290 - 400 MeV.nucleon⁻¹ ¹⁰B ions [116, 55] or 1 GeV.nucleon⁻¹ ⁵⁶Fe, both mimicking GCR radiations. Around the Moon, the Radiation Dose Monitor (RADOM) on-board the Chandrayaan-1 lunar probe, measured radiations levels of 0.227 mGy⁻¹ 100 km above the surface and 0.257 mGy.day⁻¹ 200 km above the surface. The increasing was due to the reduction of the lunar shadow effect [113]. As for the Cosmic Ray Telescope for the Effects of Radiation (CRaTER), on-board the LRO, 0.220 - 0.270 mGy.day⁻¹ were measured 50 km above the surface [113, 117]. For SPE, only computer modellings exist: with a strong SPE, without any protection, BFO could be exposed to a 900 mSv dose [113] thus showing the necessity of radiation shielding.

Shielding efficiency is related to the thickness and the material used for protection. Water and polyethylene are the best choice for shielding the crew from neutrons, but these materials could also freeze or create dangerous corrosion in the habitat walls [112]. Different materials can be used for radiation protection: as shown Figure 8.5, aluminium and regolith provide both a fair dose reduction. These results are in agreement with other existing models and previous works [113, 118, 55, 112, 119].

Figure 8.6 shows in details the effective dose decreasing as the shield thickness increases. In concrete terms, a 15 cm thick wall of sintered lunar regolith covering the habitat, with a density of 1.7 g.cm⁻³, would reduce the 900 mSV absorbed by the BFO down to 150 mSv [113]. For long time exposure and in order to be protected from the primary and secondary radiations [118], 120 g.cm⁻² of regolith has to be used as shield [112]. It represents about

¹The conversion Sievert/Gray is dependent on the type of radiation. In our case, it can be fairly assessed that 1 millisievert (mSv) corresponds to the equivalent dose produced by exposure to 1 milligray (mGy) of radiation.

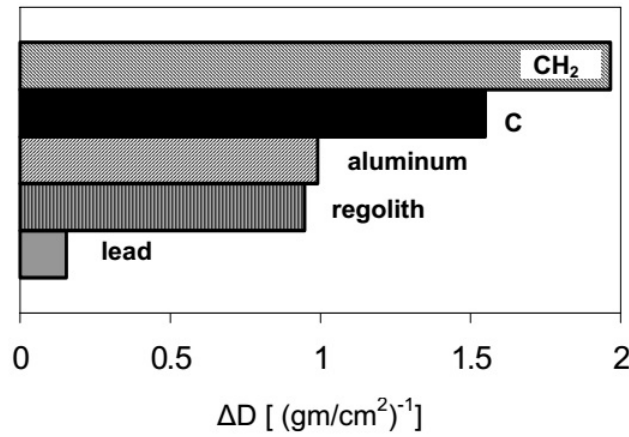


Figure 8.5: Average percent dose reduction per unit areal density ($g \cdot cm^{-2}$) for lunar regolith compared to polyethylene, graphite, aluminium and lead [116].

70 cm thick wall of sintered lunar regolith around the habitat. For comparison, the Apollo module shields were about $10 g \cdot cm^{-2}$ and the ISS, orbiting within the Earth magnetic field, has a shielding about $10s g \cdot cm^{-2}$ [120].

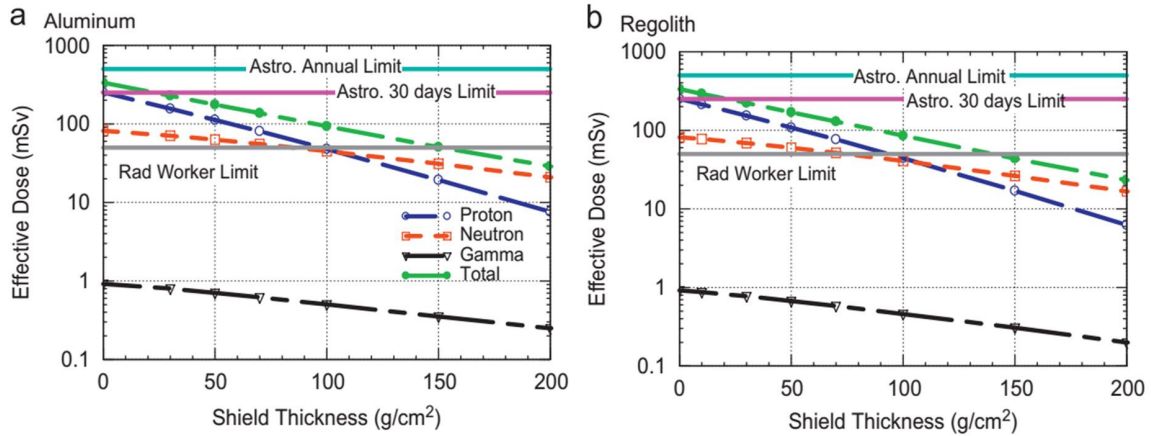


Figure 8.6: Dose estimate inside the lunar shelter as function of aluminum and regolith shield thickness, assuming center seeking incidence of source protons. The rad worker limit represents the maximum dose an exposed worker can receive in nuclear research facilities and nuclear power plants in any single year. It is defined by the International Atomic Agency [112].

Regarding the protection against strong SPE, architectural strategies have been designed for protecting the crew during theses temporary events [121, 122].

8.5 Martian application

After the Moon, the closest planetary body men could land on would be Mars. A solar sintering technology could be also an approach for building shelters and roads on the Martian surface. The solar irradiance, ranging between 800 and 1200 W.m⁻² on a sunny day on Earth, could not be higher than 590 W.m⁻² on Mars at the zenith [123, 124]. This lower irradiance, due to the larger distance of the planet from the Sun, would result in scaling up the lunar set-up. The clouds, the Martian weathering, the iron-rich soil, the CO₂ atmosphere, will change the sintering parameters. However, the solar sintering layer-by-layer of Martian soil is feasible.

Experiments could be carried out at laboratory scale using NASA Martian simulant JSC-Mars-1A made of Hawaii volcanic soil.

8.6 Cost estimate

A precise assessment of the cost for the solar sintering technology is currently difficult to write. No heavy payloads have landed on the Moon since the end of the Apollo program, 45 years ago. Nowadays, the technology used at all stages of the mission from the launcher to the landing has considerably changed. However, going through the existing literature, a rough estimation can be given. It is important to notice that when it comes to cost, a very little number of scientific papers can be found and mainly press articles can be used as references. The following calculation does not include any over cost, which could however represents over 50% of the original budget [125].

The solar sintering technology is not yet ready to be tried out on the lunar surface. Further research development is needed for having an approved payload. The payload would contain the required optics and mechanical parts for the solar sintering device plus two small rovers that could carry around the regolith for the layer deposition and also for removing stones, too big to be sintered. Finally, although the sintering technology should work unaided, the payload includes also the required communication system for controlling the sintering device and the rovers from Earth. The cost for developing this technology, currently TRL 4, to TRL 9 is estimated to €1 billion. The total weight of the payload should be around 10 ton.

A suitable launcher for such payload is required. Only one launcher has been so far able to launch heavy payloads to the Moon: the NASA Saturn V rocket. This rocket can carry 10 tons from Earth surface to the Low Lunar Orbit (LLO). Such trip would cost €3.6 billion converting the cost of an Apollo launch to today's currency value [126]. Of course, this rocket will not fly anymore and a new Space Launcher System (SLS) is in development at National Aeronautics and Space Administration (NASA) for future launches to the Moon and Mars. The cost for this new rocket is still unknown but SLS deputy project manager Jody Singer reported that the price per launch should be closed to €500 million [127]. Solar sintering technology has however no purpose in LLO.

The development of a lander, able to transfer hardware from LLO to the lunar surface several times, is also necessary for this technology and future pieces of equipment taking part in the lunar base settlement. Another SLS would be required for placing the lander into LLO. The cost for a lander during the Apollo missions was €1.5 billion [126]. Since Apollo landers could only go to and from the lunar surface once, a similar price is assessed today for placing a lander in LLO that is able to go back and forth the lunar surface several times with the technologies, which have been developed over the last 50 years.

With the use of the chosen payload, rocket and lander mentioned above, the total cost for having solar sintering technology on the Moon would be:

Cost calculation:

$$\begin{aligned} & \text{payload} + 2 \times \text{SLS} + 1 \text{ reusable lander} \\ &= \text{€1 billion} + 2 \times \text{€0.5 billion} + \text{€1.5 billion} \\ &= \text{€3.5 billion} \end{aligned}$$

The previous calculation does not take into account any use of rockets designed by the private sector. Companies like SpaceX, Blue Origin, Boeing and Airbus will be however part of the next trip to the Moon. Using a detailed study of a return to the lunar surface by the private sector [128], it can be assessed that the landing of the payload defined above would roughly cost €3.85 billion (payload cost included). This cost does not include the adjustments required to the Falcon Heavy rocket, the Dragon module nor the development of a Centaur-like upper stage.

It remains to be calculated how much brick-size building blocks can be produced on the lunar surface. It is clear that it is unlikely that actual individual building blocks will be produced on the Moon. 3D printing of continuous structure, around an inflatable habitat is most likely to happen. Yet, the building block is a good representation of the technology capability. The current set-up can produce a brick, 200 x 100 x 100 mm, in about 6 hours. With the optimisation of the technology, it is assessed that the production time per brick could be reduced to 30 minutes. For a lunar base located at the lunar pole, the solar energy is permanent, thus extending the solar sintering capability to 24 hours, seven days a week, for sintering bricks. 336 bricks can therefore be created every week. Due to some defects or technical potential issues, it is assumed that 300 bricks could be used for construction. Current inflatable habitats have a volume about 15 m³ [129], which is too small for a spherical habitat on the lunar surface, where gravity puts a constraint on the use of all accessible volume. A cylindrical habitat, suitable for being connected to the International Space Station (ISS), would require more shielding than a similar volume in a spherical habitat: the ratio surface/volume needs to be reduced to a minimum. For a crew-size of one or two astronauts, about 30 m³ habitat is enough [130], 15 m³ needs for this reason to be covered by sintered regolith: half of a spherical habitat could be buried into the lunar soil so that only half of it has to be shielded by solar sintered regolith. Studies about radiation shielding [112, 115, 122, 55, 114, 131, 118, 113, 116, 121, 119] do not specify the exact thickness of regolith required for protecting the crew. Hence, the following scenarios are deliberately

pessimistic, the kevlar and aluminium shielding of the inflatable habitat is not taken into account. Concepts of bigger habitats, not treated in this report, also exist for long-term missions with sizes up to 2000 m^3 for different mission scenarios [130, 132].

8.6.1 First scenario - Thick shell

In section 8.4, it was shown that a 70-cm thick layer of sintered lunar regolith around the habitat is sufficient to completely protect the crew against GCR. Here, with a more advanced sintering technology, the sintered regolith should have a density about 2.5 g.cm^{-3} . With high error margins, it is therefore possible to assess that a 100-cm thick layer of sintered regolith is enough for shielding the habitat from space radiations and meteoroids, 38 m^3 of bricks are required, as shown in Figure 8.7.

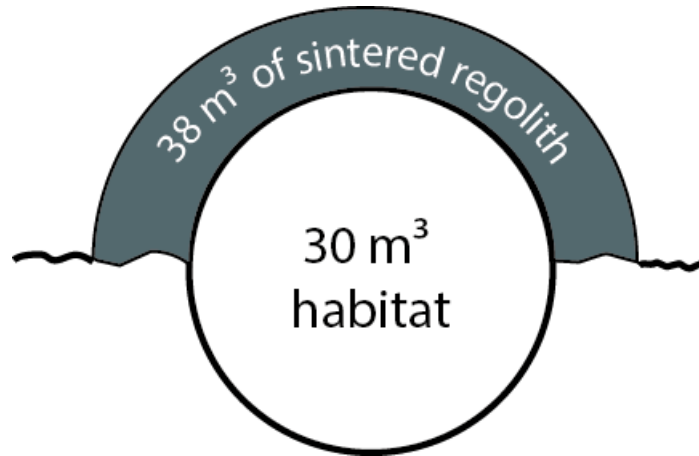


Figure 8.7: Scenario 1

With the volume of the brick defined above, 19,000 bricks would be needed for covering the habitat, that being 64 weeks, or about 1 year and 3 months per habitat if one brick can be produced every half an hour. Although this construction time can seem too long to be interesting for a lunar base settlement. The launch of a solar sintering technology could be carried out several years before explorers step on the lunar surface again. 19,000 bricks represent a saved weight from Earth of 95,000 kg. If sending the equipment on the lunar surface cost €3.5 billion, the price/kg is about €37,000/kg, much cheaper than sending a 95,000 kg payload, which will take at least 10 SLS rockets (9 with 10-ton payload + 1 reusable lander) for a cost of €6.5 billion or €68,000/kg.

Obviously, if the solar sintering equipment is able to work continuously over 4 years, which should be the objective with €1 billion development, the price/kg could even be reduced to €10,000/kg, which is the current price to send cargo to the ISS.

8.6.2 Second scenario - Thin shells

Another solution would be not to sinter 1-meter thick wall around the habitat but to create two thinner shells with loose lunar regolith in between. Two 10-cm thick shells spaced by a 2-meter thick gap filled with loose lunar regolith, with a density about 1.3 g.cm^{-3} , would provide a shield of 310 g.cm^{-2} . Figure 8.8 shows the design. With this strategy, the inner shell would only need about 2 m^3 of lunar regolith and the outer shell about 11 m^3 of solar sintered regolith. The total 13 m^3 represents 6,500 bricks or 22 weeks of continuous sintering. One habitat could be therefore protected in less than 6 months, leaving some extra time to the solar sintering equipment for other habitats or for building roads or launch pads, both often left out of lunar base development plans.

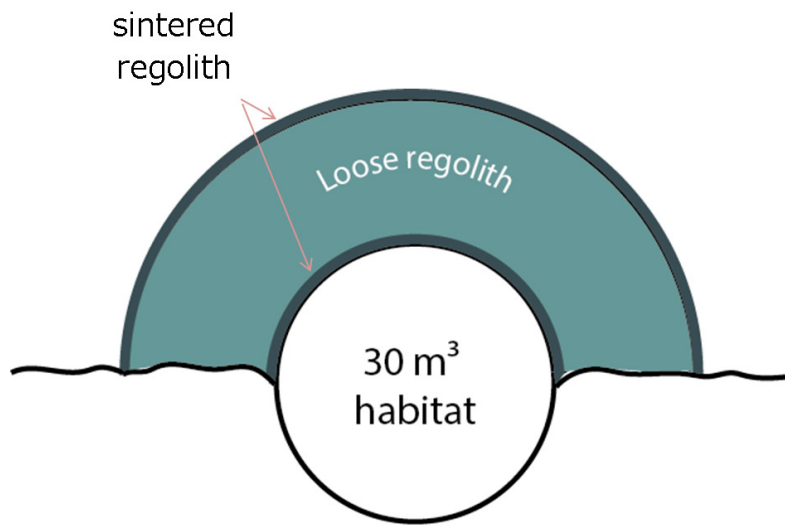


Figure 8.8: Scenario 2

To sum up about the cost of the equipment, it is clear that the technology should be sufficiently developed to have a reliable and robust machine on the Moon. The mechanical parts and optics should be able to work continuously in a dusty environment for several years. Modelled on the experience of the Curiosity rover, still running in 2017 whereas it was planned to be working for only 2 years after landing in 2012 on the Martian surface, it is difficult to assess the lifetime of the machine on the lunar surface. The solar sintering technology could always be used for shielding any new habitat landing on the Moon thus making this technology hardly obsolete. The cost/kg of shielding material is therefore strongly connected to the longevity of the machine, and to the manufacturing speed of bricks or continuous layers. Any long-term mission should anyway be preceded by a cheaper mission, with a cost $< \text{€}100$ million. The landing of a small rover that could sinter 10 to 30 bricks would be indeed an interesting prove of concept that could trigger the construction of a Moon village.

Conclusion

In this project, the experiments carried out with glass beads mixtures and the characterisation of five different commercial lunar simulants gave important results to efficiently sinter lunar regolith:

- The preponderance of the particles surface area over the green body packing was highlighted for increasing the sintering rate.
- The effect of plagioclase and ilmenite minerals were investigated. The low melting temperature of albite affected clearly the sintering temperature of the DNA simulant. Ilmenite did not prevent nor enhance the sintering of JSC-1A. No difference in parameters should be therefore expected between a sintering process of High-Ti maria and Low-Ti maria soils.
- JSC-1A proved to be the simulant closest to the lunar soil regarding the mineral composition and the glass content.
- The grain shape of all simulants was very similar to the actual lunar soil and only a low impact on the sintering was expected.
- The sintering environment mattered: hematite formation, observed by XRD and EDX, was prominent after a traditional sintering process performed in air. The formed interboundary layer of hematite and similar oxides prevented the regolith grains to sinter together and a higher temperature, with a higher fraction of melt, was therefore required for sintering in air compared to the same process under vacuum. Although increasing the temperature usually helps the atomic mobility and the densification of the sintered material, the outgassing coming from the oxygen-rich minerals, balanced out the densification creating new pores.

These results were used in the development of the first solar 3D-printer solely working with sunlight. After several test campaigns:

- The demonstration of solar 3D printing of lunar regolith was successful. Depositing and sintering layers of 100 μm of JSC-2A lunar simulant, it was possible to build up 3D printed parts. This achievement required the sweeping at 48 mm.s^{-1} of the deposited layer with a light flux density of 1.2 MW.m^{-2} focused on a $\varnothing 20$ mm spot.
- The concentrated light was provided by two Xenon lamps since the natural atmospheric fluctuation prevented the use of sunlight: a constant solar energy over the process was required to keep the lunar regolith at the sintering temperature.
- A fast sintering of a layer, under 30 seconds, exhibited an enhancement of the interlayer bonds, limiting the cooling and reducing the thermal stresses inside the material.

- Computer simulations confirmed the existing temperature gradient responsible for internal stresses over the surface, and along the thickness of the solar 3D printed parts.
- Compression testing revealed that the solar sintered material had a compressive strength and a Young's modulus close to gypsum, thus letting space for an improvement of the process, a material concrete-like being achievable traditionally sintering the same material.
- The microscopic cross-sections and tomography showed discontinuities in the partially molten layers. Open and closed pores, up to 500 μm large, combined with the weak interlayer bonding, were responsible for the low mechanical properties of the solar sintered samples.
- On the Moon, a robust device for carrying out solar sintering, able to work continuously several years, would reduce significantly the cost for all dust mitigation, pavement and shielding operations.

References

- [1] G. Cesaretti, E. Dini, X. De Kestelier, V. Colla, and L. Pambaguian. Building components for an outpost on the lunar soil by means of a novel 3D printing technology. *Acta Astronautica*, 93:430–450, 2014.
- [2] B. Khoshnevis, A. Carlson, N. Leach, and M. Thangavelu. Contour crafting simulation plan for lunar settlement infrastructure buildup. *Earth and Space*, 10:9780784412190–155, 2012.
- [3] V. Krishna Balla, L. B. Roberson, G. W. O’Connor, S. Trigwell, S. Bose, and A. Bandyopadhyay. First demonstration on direct laser fabrication of lunar regolith parts. *Rapid Prototyping Journal*, 18(6):451–457, 2012.
- [4] M. Fateri and A. Gebhardt. Process parameters development of selective laser melting of lunar regolith for on-site manufacturing applications. *International Journal of Applied Ceramic Technology*, 12(1):46–52, 2015.
- [5] V. Srivastava, S. Lim, and M. Anand. Microwave processing of lunar soil for supporting longer-term surface exploration on the moon. *Space Policy*, 37:92–96, 2016.
- [6] G. Heiken, D. Vaniman, and B. M. French, editors. *Lunar sourcebook: A user’s guide to the Moon*. CUP Archive, New-York, 1991.
- [7] P. G. Lucey, D. T. Blewett, and B. L. Jolliff. Lunar iron and titanium abundance algorithms based on final processing of Clementine ultraviolet-visible images. *Journal of Geophysical Research: Planets (1991–2012)*, 105(E8):20297–20305, 2000.
- [8] S. E. Basu, A. and Riegsecker. Reliability of calculating average soil composition of apollo landing sites. In *New Views of the Moon: Integrated Remotely Sensed, Geophysical, and Sample Datasets*, volume 1, page 20, 1998.
- [9] Significant lunar minerals - official NASA ISRU webpage. <https://isru.msfc.nasa.gov/>.
- [10] K. A. Lee, L. Oryshchyn, A. Paz, M. Reddington, and T. M. Simon. The ROxygen project: Outpost-scale lunar oxygen production system development at johnson space center. *Journal of Aerospace Engineering*, 26(1):67–73, 2012.
- [11] B. Keller, D. Clark, and J. Kirkland. Field test results of the PILOT hydrogen reduction reactor. In *AIAA SPACE 2009 Conference & Exposition*, page 6475, 2009.
- [12] D. Linne, J. Kleinhenz, and U. Hegde. Evaluation of heat recuperation in a concentric hydrogen reduction reactor. In *50th AIAA Aerospace Sciences Meeting including the New Horizons Forum and Aerospace Exposition*, page 636, 2012.
- [13] L. A. Taylor and W. D. Carrier. Oxygen production on the moon: an overview and evaluation. *Resources of near earth space*, page 69, 1993.

- [14] Y. Zhao and F. Shadman. Production of oxygen from lunar ilmenite. *Nasa Technical Report*, 1990.
- [15] W. Seboldt, S. Lingner, S. Hoernes, W. Grimmeisen, R. Lekies, R. Herkelmann, D. M. Burt, J. Lewis, et al. Lunar oxygen extraction using fluorine. *Resources of Near Earth Space, U. Arizona Press, Tucson, AZ*, pages 129–148, 1993.
- [16] M. Sauerborn et al. *Pyrolyse von Metalloxiden und Silikaten unter Vakuum mit konzentrierter Solarstrahlung*. PhD thesis, Universitäts-und Landesbibliothek Bonn, 2005.
- [17] C. Senior. Lunar oxygen production by pyrolysis. In *Space Programs and Technologies Conference*, page 1663, 1993.
- [18] E. J. Faierson, K. V. Logan, B. K. Stewart, and M. P. Hunt. Demonstration of concept for fabrication of lunar physical assets utilizing lunar regolith simulant and a geothermite reaction. *Acta Astronautica*, 67(1):38–45, 2010.
- [19] H. Benaroya and L. Bernold. Engineering of lunar bases. *Acta Astronautica*, 62(4):277–299, 2008.
- [20] F. Ruess, J. Schaenzlin, and H. Benaroya. Structural design of a lunar habitat. *Journal of Aerospace Engineering*, 19(3):133–157, 2006.
- [21] T. Rousek, K. Eriksson, and O. Doule. Sinterhab. *Acta Astronautica*, 74:98–111, 2012.
- [22] M. D. Hogue, R. P. Mueller, L. Sibille, P. E. Hintze, and D. J. Rasky. Regolith-derived heat shield for planetary body entry and descent system with in-situ fabrication. In *Proceedings of the ASCE Earth & Space Conference*, pages 526–536, 2012.
- [23] R. P. Mueller, L. Sibille, P. E. Hintze, T. C. Lippitt, J. G. Mantovani, M. W. Nugent, and I. I. Townsend. Additive construction using basalt regolith fines. In *Earth and Space 2014*, pages 394–403. St. Louis, 2014.
- [24] D. Tucker, E. Ethridge, and H. Toutanji. Production of glass fibers for reinforcing lunar concrete. In *44th AIAA aerospace sciences meeting and exhibit*, pages 9–12, 2006.
- [25] A. Delgado and E. Shafirovich. Towards better combustion of lunar regolith with magnesium. *Combustion and Flame*, 160(9):1876–1882, 2013.
- [26] P. E. Hintze, J. Curran, and T. Back. Lunar surface stabilization via sintering or the use of heat cured polymers. In *47th AIAA Aerospace Science Meeting*, pages 1009–1015, 2009.
- [27] T. S. Lee, J. Lee, and K. Y. Ann. Manufacture of polymeric concrete on the moon. *Acta Astronautica*, 114:60–64, 2015.

-
- [28] C. Montes, K. Broussard, M. Gongre, N. Simicevic, J. Mejia, J. Tham, and G. Al-louche, E.and Davis. Evaluation of lunar regolith geopolymer binder as a radioactive shielding material for space exploration applications. *Advances in Space Research*, 2015.
- [29] R. N. Grugel. Integrity of sulfur concrete subjected to simulated lunar temperature cycles. *Advances in Space Research*, 50(9):1294–1299, 2012.
- [30] S. Wilhelm and M. Curbach. Manufacturing of lunar concrete by steam. In *Earth and Space 2014*, pages 274–282.
- [31] B. L. Cooper. Sintering of lunar and simulant glass. In *Space Technology and Applications International Forum-STAIF*, pages 186–194, 2008.
- [32] B. J. Pletka. Processing of lunar basalt materials. *Resources of Near Earth Space, University of Arizona Press*, pages 325–350, 1993.
- [33] L. A. Taylor and T. T. Meek. Microwave sintering of lunar soil: properties, theory, and practice. *Journal of Aerospace Engineering*, 18(3):188–196, 2005.
- [34] T. Gualtieri and A. Bandyopadhyay. Compressive deformation of porous lunar regolith. *Materials Letters*, 143:276–278, 2015.
- [35] P. E. Hintze and S. Quintana. Building a lunar or martian launch pad with in situ materials: Recent laboratory and field studies. *Journal of Aerospace Engineering*, 26(1):134–142, 2012.
- [36] P. E. Hintze. Building a vertical take off and landing pad using in situ materials. *Proceedings of Space Manufacturing*, 14:2010, 2010.
- [37] A. Goulas, R. A. Harris, and R. J. Friel. Additive manufacturing of physical assets by using ceramic multicomponent extra-terrestrial materials. *Additive Manufacturing*, 10:36–42, 2016.
- [38] B. Khoshnevis, J. Zhang, M. Fateri, and Z. Xiao. Ceramics 3D printing by selective inhibition sintering. In *Solid Free Form Symposium (SFF)*, 2014.
- [39] A. E. Jakus, K. D. Koube, N. R. Geisendorfer, and R. N. Shah. Robust and elastic lunar and martian structures from 3D-printed regolith inks. *Scientific Reports*, 7, 2017.
- [40] L. A. Taylor and Y. Liu. Important considerations for lunar soil simulants. *Proceeding of the Earth and Space*, 2010.
- [41] M. Weinstein and S. Wilson. Apparatus and method for producing a lunar agglutinate simulant, December 17 2013. US Patent 8,610,024.

- [42] D. S. McKay, J. L. Carter, W. W. Boles, C. C. Allen, and J. H. Allton. JSC-1: A new lunar soil simulant. *Engineering, construction, and operations in space IV*, 2:857–866, 1994.
- [43] H. Arslan, S. Batiste, and S. Sture. Engineering properties of lunar soil simulant JSC-1A. *Journal of Aerospace Engineering*, 23(1):70–83, 2009.
- [44] D. Rickman, C. McLemore, and J. Fikes. Characterization summary of JSC-1A bulk lunar mare regolith simulant. *National Aeronautics and Space Administration, Washington, DC*, 2007.
- [45] C. Schrader, D. Rickman, C. McLemore, J. Fikes, S. Wilson, D. Stoesser, A. Butcher, and P. Botha. Extant and extinct lunar regolith simulants: modal analyses of NU-LHT-1M and-2m, OB-1, JSC-1, JSC-1A and -1AF, FJS-1, and MLS-1. In *Planetary Mining and Science Symposium, Montreal*, 2008.
- [46] E. Garboczi. Three dimensional shape analysis of JSC-1A simulated lunar regolith particles. *Powder Technology*, 207(1):96–103, 2011.
- [47] J. N. Mpagazehe, K. W. Street, I. R. Delgado, and C. F. Higgs. An experimental study of lunar dust erosive wear potential using the JSC-1AF lunar dust simulant. *Wear*, 316(1):79–91, 2014.
- [48] C. S. Ray, S. T. Reis, S. Sen, and J. S. O’Dell. JSC-1A lunar soil simulant: Characterization, glass formation, and selected glass properties. *Journal of Non-Crystalline Solids*, 356(44):2369–2374, 2010.
- [49] K. A. Alshibli and A. Hasan. Strength properties of JSC-1A lunar regolith simulant. *Journal of geotechnical and geoenvironmental engineering*, 135(5):673–679, 2009.
- [50] S. M. Allan, B. J. Merritt, B. F. Griffin, and P. E. Hintze. High temperature microwave dielectric properties of JSC-1AC lunar simulant. *Journal of Aerospace Engineering*, 26:874–881, 2013.
- [51] S. Batiste and S. Sture. Minnesota lunar regolith MLS-1. In *Lunar Regolith Simulant Materials Workshop, Marshall Institute, Huntsville, AL*, 2005.
- [52] S. Sen, C. S. Ray, and R. G. Reddy. Processing of lunar soil simulant for space exploration applications. *Materials Science and Engineering: A*, 413:592–597, 2005.
- [53] D. Stoesser, D. Rickman, and S. Wilson. Preliminary geological findings on the BP-1 simulant. *NASA Technical Report*, 2010.
- [54] Y. Zheng, S. Wang, C. Li, Z. Ouyang, J. Feng, J. Liu, and Y. Zou. The development of CAS-1 lunar soil simulant. In *International Lunar Conference*, 2005.

-
- [55] J. Miller, L. Taylor, C. Zeitlin, L. Heilbronn, S. Guetersloh, M. DiGiuseppe, Y. Iwata, and T. Murakami. Lunar soil as shielding against space radiation. *Radiation Measurements*, 44(2):163–167, 2009.
- [56] J. Richard, L. Sigurdson, and M. Battler. OB-1 lunar highlands physical simulant evolution and production. In *2007 Lunar and dust regolith simulant workshop*, 2007.
- [57] L. C. De Jonghe and M. N. Rahaman. *Sintering of Ceramics*, volume 2. Academic Press, San Diego, 2003.
- [58] C. B. Carter and M. G. Norton. Sintering and grain growth. In *Ceramic Materials*, pages 439–456. Springer, New-York, 2013.
- [59] C. B. Carter and M. G. Norton. *Ceramic materials: science and engineering*. Springer Science & Business Media, 2007.
- [60] E. Rabinovich. Preparation of glass by sintering. *Journal of Materials Science*, 20(12):4259–4297, 1985.
- [61] M. N. Rahaman. *Ceramic Processing and Sintering 2nd Edition*. CRC Press, 2003.
- [62] H. M. Jaeger, S. R. Nagel, and R. P. Behringer. Granular solids, liquids, and gases. *Reviews of modern physics*, 68(4):1259, 1996.
- [63] S.-J. L. Kang. *Sintering: densification, grain growth and microstructure*. Butterworth-Heinemann, Oxford, 2004.
- [64] M. Rahaman and M. N. Rahaman. *Ceramic processing*. CRC press, Boca Raton, 2006.
- [65] S. Frank-Richter. *Disordered Binary Granular Packings in Three Dimensions*. PhD thesis, Universität Düsseldorf, 2014.
- [66] W. Kingery, D. R. Uhlmann, and H. K. Bowen. *Introduction to ceramics*. New York: John Wiley & Sons Inc, New York, 1976.
- [67] W. D. Carrier, G. R. Olhoeft, and W. Mendell. *Physical properties of the lunar surface*. Cambridge University Press, Cambridge, Cambridge, 1991.
- [68] E. Hill, M. J. Mellin, B. Deane, Y. Liu, and L. A. Taylor. Apollo sample 70051 and high-and low-ti lunar soil simulants MLS-1A and JSC-1A: Implications for future lunar exploration. *Journal of Geophysical Research: Planets (1991–2012)*, 112(E2), 2007.
- [69] U. Hegde, R. Balasubramaniam, S. Gokoglu, K. Rogers, M. Reddington, and L. Oryshchyn. Hydrogen reduction of lunar regolith simulants for oxygen production. In *49th AIAA Aerospace Sciences Meeting including the New Horizons Forum and Aerospace Exposition*, page 608, 2011.

- [70] C. H. Simonds. Sintering and hot pressing of fra mauro composition glass and the lithification of lunar breccias. *American Journal of Science*, 273:428–439, 1973.
- [71] R. M. German, P. Suri, and S. J. Park. Review: liquid phase sintering. *Journal of materials science*, 44(1):1–39, 2009.
- [72] V. Badescu, C. Schwandt, J. A. Hamilton, D. J. Fray, and I. A. Crawford. *Moon: Prospective Energy and Material Resources*. Springer Science & Business Media, Berlin, 2012.
- [73] D. A. Crown and C. M. Pieters. Spectral properties of plagioclase and pyroxene mixtures and the interpretation of lunar soil spectra. *Icarus*, 72(3):492–506, 1987.
- [74] C. M. Schrader, D. L. Rickman, C. A. McLemore, and J. C. Fikes. Lunar regolith simulant user’s guide. *NASA Technical Report*, 2010.
- [75] I. B. Cutler and R. E. Henrichsen. Effect of particle shape on the kinetics of sintering of glass. *Journal of the American Ceramic Society*, 51(10):604–604, 1968.
- [76] W. Krumbein and L. Sloss. Properties of sedimentary rocks. *Stratigraphy and Sedimentation*, pages 106–113, 1963.
- [77] C. A. Schneider, W. S. Rasband, and K. W. Eliceiri. NIH image to ImageJ: 25 years of image analysis. *Nature methods*, 9(7):671–675, 2012.
- [78] L. Sibille, P. Carpenter, R. Schlagheck, and R. A. French. Lunar regolith simulant materials: recommendations for standardization, production, and usage. *National Aeronautics and Space Administration: Marshall Space Flight Center*, 2006.
- [79] R. Román, I. Cañadas, J. Rodríguez, M. Hernández, and M. González. Solar sintering of alumina ceramics: Microstructural development. *Solar Energy*, 82(10):893–902, 2008.
- [80] F. A. C. Oliveira, N. Shohoji, J. C. Fernandes, and L. G. Rosa. Solar sintering of cordierite-based ceramics at low temperatures. *Solar energy*, 78(3):351–361, 2005.
- [81] M. Kayser. Solar sinter project. *Markus Kayser*, 2011.
- [82] E. Cardiff and B. Hall. A dust mitigation vehicle utilizing direct solar heating. In *Joint Annual Meeting of Lunar Exploration Analysis Group-International Conf. on Exploration and Utilization of the Moon-Space Resources Roundtable*, 2008.
- [83] T. Nakamura and B. Smith. Solar thermal system for lunar ISRU applications: development and field operation at mauna kea, hi. In *49th AIAA Aerospace Sciences Meeting including the New Horizons Forum and Aerospace Exposition*, page 433, 2011.

-
- [84] A. Meurisse, J. C. Beltzung, M. Kolbe, A. Cowley, and M. Sperl. Influence of mineral composition on sintering lunar regolith. *Journal of Aerospace Engineering*, 30(4):04017014, 2017.
- [85] D. De Rosa, B. Bussey, J. T. Cahill, T. Lutz, I. A. Crawford, T. Hackwill, S. van Gasselt, G. Neukum, L. Witte, A. McGovern, et al. Characterisation of potential landing sites for the european space agency’s lunar lander project. *Planetary and Space Science*, 74(1):224–246, 2012.
- [86] E. Grün, M. Horanyi, and Z. Sternovsky. The lunar dust environment. *Planetary and Space Science*, 59(14):1672–1680, 2011.
- [87] M. Horányi, J. Szalay, S. Kempf, J. Schmidt, E. Grün, R. Srama, and Z. Sternovsky. A permanent, asymmetric dust cloud around the moon. *Nature*, 522(7556):324–326, 2015.
- [88] T. L. Jackson, W. M. Farrell, and M. I. Zimmerman. Rover wheel charging on the lunar surface. *Advances in Space Research*, 55(6):1710–1720, 2015.
- [89] M. Adachi, H. Moroka, H. Kawamoto, S. Wakabayashi, and T. Hoshino. Particle-size sorting system of lunar regolith using electrostatic traveling wave. *Journal of Electrostatics*, 89:69–76, 2017.
- [90] C. A. Bühler. Experimental investigation of lunar dust impact wear. *Wear*, 342:244–251, 2015.
- [91] A. Neumann and U. Groer. Experimenting with concentrated sunlight using the DLR solar furnace. *Solar Energy*, 58(4-6):181–190, 1996.
- [92] I. Alxneit and G. Dibowski. R12. 5 solar simulator evaluation report. *Project SFERA.*, August, 2011.
- [93] J. R. Gaier, S. Ellis, and N. Hanks. Thermal optical properties of lunar dust simulants. *Journal of Thermophysics and Heat Transfer*, 26(4):573–580, 2012.
- [94] S. S. Schreiner, J. A. Dominguez, L. Sibille, and J. A. Hoffman. Thermophysical property models for lunar regolith. *Advances in space research*, 57(5):1209–1222, 2016.
- [95] A. J. Colozza. Analysis of lunar regolith thermal energy storage. Technical report, Sverdrup Technology, Inc., Brook Park, OH (United States), 1991.
- [96] J. Stebbins, I. Carmichael, and L. Moret. Heat capacities and entropies of silicate liquids and glasses. *Contributions to mineralogy and petrology*, 86(2):131–148, 1984.
- [97] S. Wakabayashi and K. Matsumoto. Development of slope mobility testbed using simulated lunar soil. *JAXA Research and Development Memorandum*, 2006.

- [98] H. Schneider, J. Goring, B. Kanka, and M. Schmücker. WHIPOX: Ein neuer Oxidfaser/Oxidmatrix-Leichtbauwerkstoff für Hochtemperaturanwendungen. *Keramische Zeitschrift*, 53(9):788–791, 2001.
- [99] M. Sperl, D. Urbina, B. Imhof, P. Weiss, and C. Preisinger. EU-H2020 RegoLight project, 2016. www.regolight.eu/.
- [100] N. K. Tolochko, S. E. Mozzharov, I. A. Yadroitsev, T. Laoui, L. Froyen, V. I. Titov, and M. B. Ignatiev. Balling processes during selective laser treatment of powders. *Rapid Prototyping Journal*, 10(2):78–87, 2004.
- [101] S. Pauly, L. Löber, R. Petters, M. Stoica, S. Scudino, U. Kühn, and J. Eckert. Processing metallic glasses by selective laser melting. *Materials Today*, 16(1):37–41, 2013.
- [102] J. Lu, S. C. Busch, and D. F. Baldwin. Solder wetting in a wafer-level flip chip assembly. *IEEE Transactions on Electronics Packaging Manufacturing*, 24(3):154–159, 2001.
- [103] M. Wu, L. Chang, L. Zhang, X. He, and X. Qu. Wetting mechanism of AgCuTi on heterogeneous surface of diamond/cu composites. *Surface and Coatings Technology*, 2017.
- [104] A. M. Hadian. *Joining of silicon nitride-to-silicon nitride and to molybdenum for high-temperature applications*. PhD thesis, 1996.
- [105] R. Do Nascimento, A. Martinelli, and A. Buschinelli. Recent advances in metal-ceramic brazing. *Cerâmica*, 49(312):178–198, 2003.
- [106] A. Tomsia. Ceramic/metal joining for structures and materials. *Le Journal de Physique IV*, 3(C7):C7–1317, 1993.
- [107] R. Asthana, A. Kumar, and N. B. Dahotre. *Materials processing and manufacturing science*. Butterworth-Heinemann, 2006.
- [108] M. Wu, L. Chang, L. Zhang, X. He, and X. Qu. Effects of roughness on the wettability of high temperature wetting system. *Surface and Coatings Technology*, 287:145–152, 2016.
- [109] K. Kubiak, M. Wilson, T. Mathia, and P. Carval. Wettability versus roughness of engineering surfaces. *Wear*, 271(3):523–528, 2011.
- [110] J. Parent, D. Chung, and I. Bernstein. Effects of intermetallic formation at the interface between copper and lead-tin solder. *Journal of materials science*, 23(7):2564–2572, 1988.
- [111] M. Shea and D. Smart. A summary of major solar proton events. *Solar Physics*, 127(2):297–320, 1990.

-
- [112] T. T. Pham and M. S. El-Genk. Dose estimates in a lunar shelter with regolith shielding. *Acta Astronautica*, 64(7):697–713, 2009.
- [113] G. Reitz, T. Berger, and D. Matthiae. Radiation exposure in the moon environment. *Planetary and Space Science*, 74(1):78–83, 2012.
- [114] G. Horneck, R. Facius, M. Reichert, P. Rettberg, W. Seboldt, D. Manzey, B. Comet, A. Mailliet, H. Preiss, L. Schauer, et al. HUMEX, a study on the survivability and adaptation of humans to long-duration exploratory missions, part i: lunar missions. *Advances in space Research*, 31(11):2389–2401, 2003.
- [115] F. A. Cucinotta, M.-H. Y. Kim, and L. J. Chappell. Evaluating shielding approaches to reduce space radiation cancer risks. *NASA Technical Memorandum*, 217361, 2012.
- [116] J. Miller, L. Taylor, M. DiGiuseppe, L. Heilbronn, G. Sanders, C. Zeitlin, et al. Radiation shielding properties of lunar regolith and regolith simulant. *LPI Contributions*, 1415:2028, 2008.
- [117] H. E. Spence, A. Case, M. Golightly, T. Heine, B. Larsen, J. Blake, P. Caranza, W. Crain, J. George, M. Lalic, et al. CRaTER: The cosmic ray telescope for the effects of radiation experiment on the lunar reconnaissance orbiter mission. *Space Science Reviews*, 150(1):243–284, 2010.
- [118] C. Zeitlin, S. B. Guetersloh, L. H. Heilbronn, and J. Miller. Measurements of materials shielding properties with 1GeV/nuc 56 Fe. *Nuclear Instruments and Methods in Physics Research Section B: Beam Interactions with Materials and Atoms*, 252(2):308–318, 2006.
- [119] F. F. Badavi, D. O. Adams, and J. W. Wilson. Validity of the aluminum equivalent approximation in space radiation shielding. In *40th International Conference on Environmental Systems*, page 6184, 2009.
- [120] N. R. Council et al. *Managing space radiation risk in the new era of space exploration*. National Academies Press, Washington, DC, 2008.
- [121] O. Bannova and L. Bell. Radiation shielding design strategies for lunar minimal functionality habitability element. *Acta Astronautica*, 67(9):1103–1109, 2010.
- [122] L. Bell and O. Bannova. Lunar habitat micrometeoroid and radiation shielding: Options, applications, and assessments. *Journal of Aerospace Engineering*, 24(1):72–78, 2010.
- [123] J. Appelbaum and D. J. Flood. Solar radiation on mars. *Solar Energy*, 45(6):353–363, 1990.

- [124] A. Spiga and F. Forget. Fast and accurate estimation of solar irradiance on martian slopes. *Geophysical Research Letters*, 35(15), 2008.
- [125] V. Sbathier, J. Weppler, and A. Bander. Costs of an international lunar base. *Center for Strategic and International Studies*, 24, 2009.
- [126] W. Productions. How much would it cost to live on the moon?, 2016. <https://www.youtube.com/watch?v=7ouiTMXuDAQ>.
- [127] M. Wall. Nasa’s huge new rocket may cost \$500 million per launch, 2012. <https://www.space.com/17556-giant-nasa-rocket-space-launch-cost.html>.
- [128] J. R. French, S. A. Stern, M. Vozoff, T. McCallum, and C. Deiterich. Architecture for lunar return using existing assets. *Journal of Spacecraft and Rockets*, 2013.
- [129] L. David. Bigelow aerospace’s inflatable habitat ready for space station trip, 2015. <https://www.space.com/28855-inflatable-space-station-habitat-bigelow.html>.
- [130] A. Vogler. Modular inflatable space habitats. In *First European Workshop on Inflatable Space Structures*, ESA/ESTEC, 2002.
- [131] R. Tripathi, J. Wilson, and R. Joshi. Risk assessment and shielding design for long-term exposure to ionizing space radiation. *SAE Technical Paper*, 2006.
- [132] M. Roberts. Inflatable habitation for the lunar base. In *Lunar Bases and Space Activities of the 21st Century*, page 249, 1992.

Appendix

A Computer Programs of the Solar 3D printer

A.1 Arduino Program

Arduino Program which was controlling the powder feeder

```
1  /*
2  Master Code for controlling powder dispenser in a solar 3D printing system.
3
4  Board: Arduino Mega
5
6  Author: A. Meurisse, 2016
7  */
8
9  const int stepperDistanceOrigin = 0; //Origin position of the feeding system
10 const int stepperDistanceBeginVib = 100; //Step number for starting the
    vibration motor
11 const int stepperDistanceEndVib = 32000; //Step number for stopping the
    vibration motor
12
13 const int RasproIN = 46; //Pin definition of the INPUT signal from the 3-axis
    table controller running the G-Code
14 const int RasproOUT = 37; //Pin definition of the OUTPUT signal to the cooling
    wall.
15 const int vibPin = 7; //Pin controlling the relay used for powering the DC-
    motor vibrating the system
16 const int motor_Vib[] = {24, 25}; //Definition of the H-bridge pins for the
    vibration motor
17 const int DirA = 3; //Pin controlling direction of rotation of the Stepper
    Motor A
18 const int StepA = 4; //Pin controlling the step level of the Stepper Motor A
19 const int DirB = 5; //Pin controlling direction of rotation of the Stepper
    Motor B
20 const int StepB = 6; //Pin controlling the step level of the Stepper Motor B
21
22 int distance; //Creation of the step counter, named "distance"
23 int counter = 0; //Initialisation of the signal counter
24
25 boolean over = false; //Initialisation boolean "over"
26 boolean rotation = false; //Initialisation boolean "rotation"
27
28 void setup() //Definition INPUTs and OUTPUTs
29 {
30     pinMode(RasproIN, INPUT);
31
32     pinMode(RasproOUT, OUTPUT);
33     pinMode(vibPin, OUTPUT);
34     pinMode(DirA, OUTPUT);
```

```
35 pinMode(StepA, OUTPUT);
36 pinMode(DirB, OUTPUT);
37 pinMode(StepB, OUTPUT);
38 int i; //H-Bridge
39 for (i = 0; i < 2; i++) {
40     pinMode(motor_Vib[i], OUTPUT);
41 }
42
43 //Initialisation first logic levels
44 digitalWrite(RasproOUT, HIGH);
45 digitalWrite(vibPin, LOW);
46 digitalWrite(DirA, LOW); //Stepper Motors A and B rotate in opposite
    directions
47 digitalWrite(StepA, LOW);
48 digitalWrite(DirB, HIGH); //Stepper Motors A and B rotate in opposite
    directions
49 digitalWrite(StepB, LOW);
50
51 distance = 0; //Initialization of the step counter
52 }
53
54 void loop()
55 {
56     if (digitalRead(RasproIN) == LOW) //If a signal is received from the 3-axis
        table
57     {
58         int ii = 0; //While loop for preventing the feeder to start because of a
            noisy signal
59         bool noise = false;
60         while (ii < 500) {
61             ii++;
62             if (digitalRead(RasproIN) == HIGH)
63                 noise = true;
64         }
65         if (!noise) {
66             counter++; //Increment counter
67             over = !over; //Change boolean level
68             delay(2000);
69         }
70     }
71     if (counter % 2 == 1 && over == true) //If the signal counter is an odd
        number and the layer is not yet deposited
72     {
73         for (int i = 0; i < 2; i++)
74         {
75             if (distance < stepperDistanceEndVib) //If the end is not reached
76             {
77                 while (distance < stepperDistanceBeginVib) // While the distance is
                    inferior to the point where vibrations should start,
```

```
78                                     //the feeder simply moves
forward
79     {
80         digitalWrite(StepA, HIGH);
81         digitalWrite(StepB, HIGH);
82         delayMicroseconds(50); // Delay set between two steps, the smaller,
the faster moves the feeder
83         digitalWrite(StepA, LOW);
84         digitalWrite(StepB, LOW);
85         delayMicroseconds(50);
86         distance++;
87     }
88
89     while ((distance >= stepperDistanceBeginVib && distance <=
stepperDistanceEndVib)) // While the distance is inferior to the endpoint,
90
91         //the feeder simply moves forward with vibration: Deposition
of the regolith simulant
92     {
93         digitalWrite(vibPin, HIGH); // Beginning of the vibrations
94         if (rotation == true) // Alternating rotation direction of the
vibration DC-motor for homogenizing the feeding
95         {
96             drive_forward();
97         }
98         else
99         {
100             drive_backward();
101         }
102
103         digitalWrite(StepA, HIGH);
104         digitalWrite(StepB, HIGH);
105         delayMicroseconds(50);
106         digitalWrite(StepA, LOW);
107         digitalWrite(StepB, LOW);
108         delayMicroseconds(50);
109         distance++;
110     }
111     else { //The endpoint is reached, the feeder moves to the original
position
112         motor_stop(); //The vibration motor stops (H-bridge level)
113         digitalWrite(vibPin, LOW); //The vibration motor stops (Relay level)
114         rotation = !rotation; //The rotation boolean changes state for the
next layer
115         delay(1000); //1 second Pause
116         digitalWrite(DirA, HIGH); //Change of rotation direction of both
stepper motors to move backward
117         digitalWrite(DirB, LOW);
```

```
118     while (distance > stepperDistanceOrigin) //The feeder moves backward
      until the original position
119     {
120         digitalWrite(StepA, HIGH);
121         digitalWrite(StepB, HIGH);
122         delayMicroseconds(40);
123         digitalWrite(StepA, LOW);
124         digitalWrite(StepB, LOW);
125         delayMicroseconds(40);
126         distance--;
127     }
128     digitalWrite(DirA, LOW); //Change of rotation direction of both
      stepper motors to move forward
129     digitalWrite(DirB, HIGH);
130 }
131 }
132 over = !over; // The layer is deposited
133 digitalWrite(RasproOUT, LOW); //Signal sent for opening the cooling wall,
      the sintering can start
134 delay(350);
135 digitalWrite(RasproOUT, HIGH);
136 }
137 else if (counter % 2 == 0 && over == true) // If the counter is an even
      number, the Arduino Mega should send a signal for closing the coolign wall
      , the feeding will start soon.
138 {
139     delay(2000);
140     digitalWrite(RasproOUT, LOW);
141     delay(350);
142     digitalWrite(RasproOUT, HIGH);
143     over = false;
144     delay(6000);
145 }
146 }
147 // -----H-Bridge-----
148 //Define the rotation diections of the vibration motor
149
150 void drive_forward() {
151     digitalWrite(motor_Vib[0], HIGH);
152     digitalWrite(motor_Vib[1], LOW);
153 }
154 void drive_backward() {
155     digitalWrite(motor_Vib[0], LOW);
156     digitalWrite(motor_Vib[1], HIGH);
157 }
158 void motor_stop() {
159     digitalWrite(motor_Vib[0], LOW);
160     digitalWrite(motor_Vib[1], LOW);
161 }
```

A.2 G-code

Example piece of G-code used for manufacturing a brick. The G-code was running on a control unit with an interpolation controller. The Layer A and B repeat themselves alternatively over hundreds of layers.

```
1 (Sample Brick Additive manufacturing program, author: A. Meurisse)
2 (Layer A)
3 G90 (absolute mode) F70 (speed 70 mm/s)
4 G0X0Y150 (Feeding position, in principle no Z position is needed)
5 G4P8000(wait 8 sec for feeding)
6 M44P3(set output 3, send signal to the data acquisition (DAQ) device running
   with the LabView program)
7 G4P10(wait 10 ms for sending the signal to the cooled wall_OPENING)
8 M45P3(reset output 3, send signal to the DAQ)
9 G91 (relative mode)
10 G1Z-0.1(lower z by 0.1)
11 G90
12 G0X155Y95 (start Point Layer A)
13 G91(relative mode)
14 G1X+230 (First line) F48 (speed 48 mm/s)
15 G1Y14 (14 mm shift)
16 G1X-230 (Second line)
17 G1Y14 (14 mm shift)
18 G1X+230 (etc...)
19 G1Y14
20 G1X-230
21 G1Y14
22 G1X+230
23 G1Y14
24 G1X-230
25 G1Y14
26 G1X+230
27 G1Y14
28 G1X-230
29 G1Y14
30 G1X+230
31 M44P3(set output 3)
32 G4P10(wait 10 ms for sending the signal to the cooled wall_CLOSURE)
33 M45P3(reset output 3)
34 G1Y+30 F70 (beam away from the sintering area during closure)
35 G1X-230
36 (Layer A finished)
37 G90 (absolute mode)
38 G0X0Y150 (Feeding position, in principle no Z position is needed)
39 G4P8000(wait 8 sec for feeding)
40 M44P3(set output 3)
41 G4P10(wait 10 ms for sending the signal to the cooled wall_OPENING)
42 M45P3(reset output 3)
43 G91 (relative mode)
```

```
44 G1Z-0.1(lower z by 0.1)
45 G90 (absolute mode)
46 G0X155Y90 (startPoint Layer B)
47 G91 F48
48 G1Y130
49 G1X+14
50 G1Y-130
51 G1X+14
52 G1Y130
53 G1X+14
54 G1Y-130
55 G1X+14
56 G1Y130
57 G1X+14
58 G1Y-130
59 G1X+14
60 G1Y130
61 G1X+14
62 G1Y-130
63 G1X+14
64 G1Y130
65 G1X+14
66 G1Y-130
67 G1X+14
68 G1Y130
69 G1X+14
70 G1Y-130
71 G1X+14
72 G1Y130
73 G1X+14
74 G1Y-130
75 G1X+14
76 G1Y130
77 G1X+14
78 G1Y-130
79 G1X+14
80 G1Y+130
81 M44P3(set output 3)
82 G4P10(wait 10 ms for sending the signal to the cooled wall_CLOSURE)
83 M45P3(reset output 3)
84 G1Y+40 F70 (beam away from the sintering area during closure)
85 G1X-230
86 (Layer B finished)
87 G90 (absolute mode)
88 G0X0Y150 (Feeding position, in principle no Z position is needed)
89 G4P8000(wait 8 sec for feeding)
90 M44P3(set output 3)
91 G4P10(wait 10 ms for sending the signal to the cooled wall_OPENING)
92 M45P3(reset output 3)
```

```
93 G91 (relativ mode)
94 G1Z-0.1(lower z by 0.1)
95 G90
96 G0X155Y95 (startPoint Layer A)
```


B Deliverables

Within this project, four bricks had to be delivered to ESA-ESTEC, ESA-EAC and DLR. Pictures and dimensions of these bricks are shown below.

Brick 1

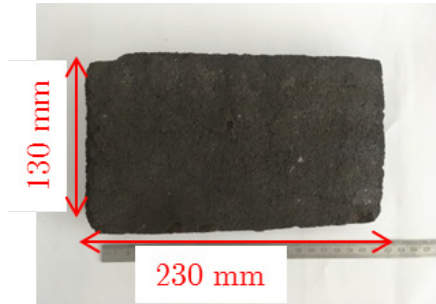


Figure B.1: First brick, top view



Figure B.2: First brick, side view

Brick 2

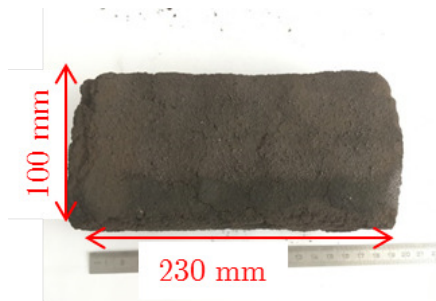


Figure B.3: Second brick, top view

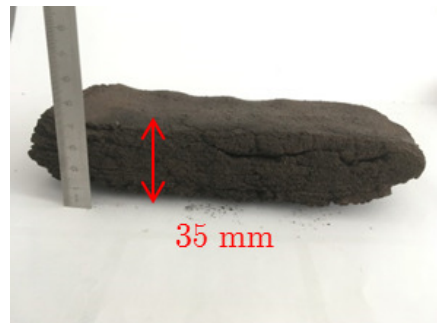


Figure B.4: Second brick, side view

Brick 3

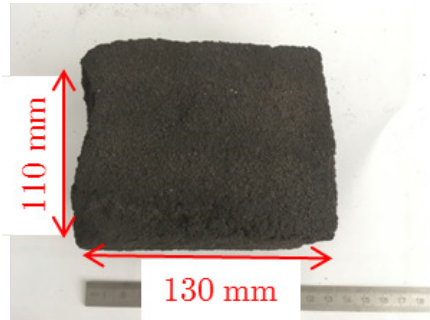


Figure B.5: Third brick, top view



Figure B.6: Third brick, side view

Brick 4

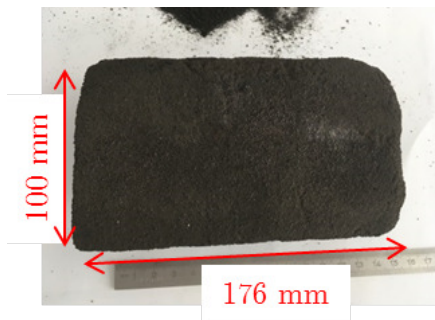


Figure B.7: Fourth brick, top view

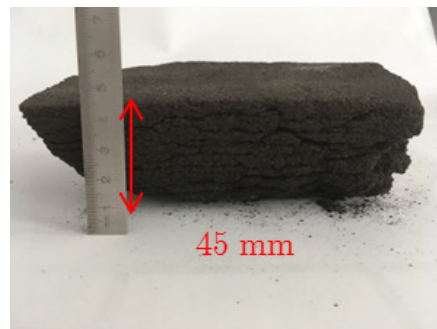


Figure B.8: Fourth brick, side view

C Other solar sintering simulations

All following heat transfer simulations use the Model 2 which defines the material as sintered regolith.

C.1 Sintering without preheating contour

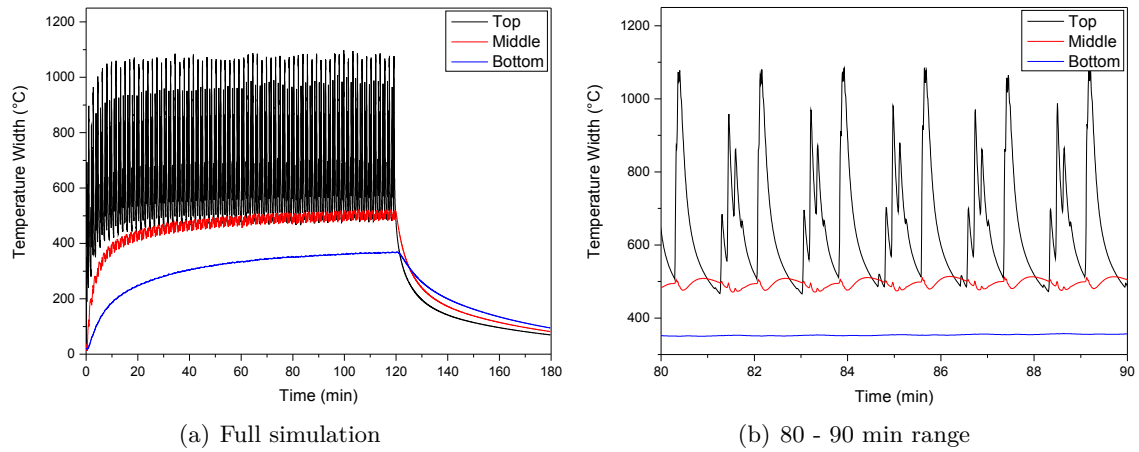


Figure C.1: Simulated temperature evolution at the middle of the width of the brick over a 2-hour sintering process and 1-hour cooling. Full simulation (a) and shorter time range (b).

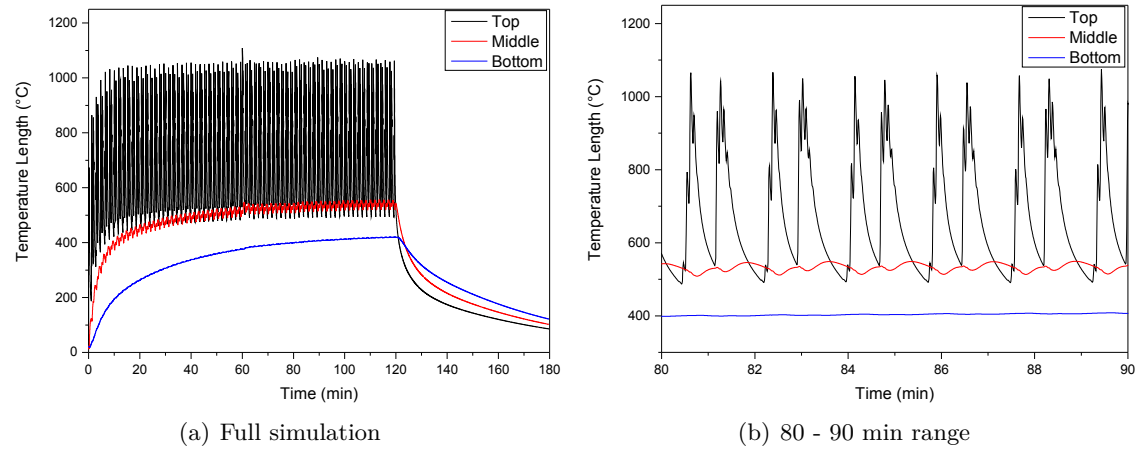


Figure C.2: Simulated temperature evolution at the middle of the length of the brick over a 2-hour sintering process and 1-hour cooling. Full simulation (a) and shorter time range (b).

C.2 Sintering with preheating contour

The artefact at 60 min comes from the division of the simulation into two individuals ones.

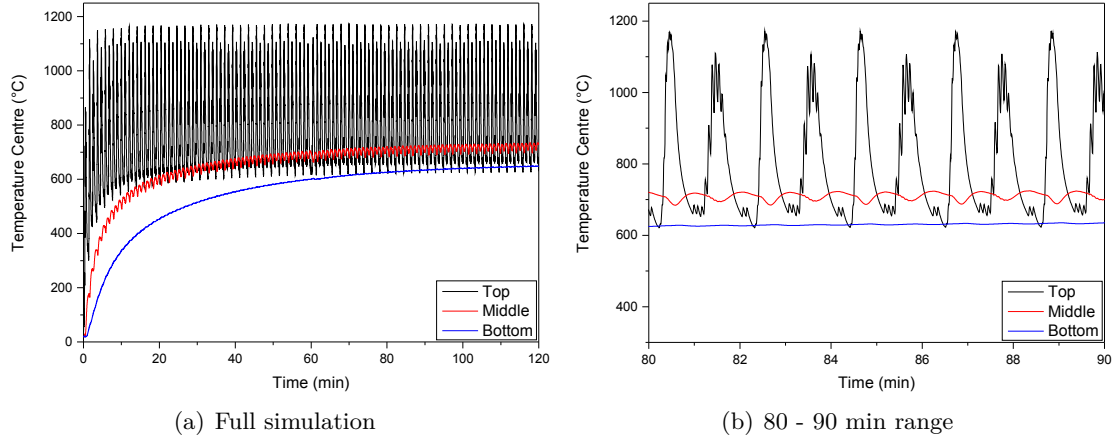


Figure C.3: Simulated temperature evolution at the centre of the brick over a 2-hour sintering process with a contour preheating before sintering. Full simulation (a) and shorter time range (b).

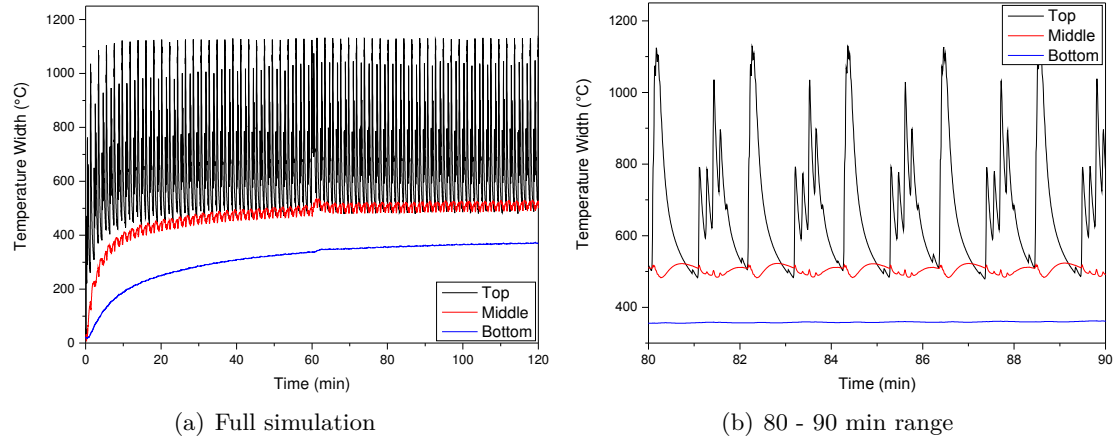


Figure C.4: Simulated temperature evolution at the middle of the width of the brick over a 2-hour sintering process with a contour preheating before sintering. Full simulation (a) and shorter time range (b).

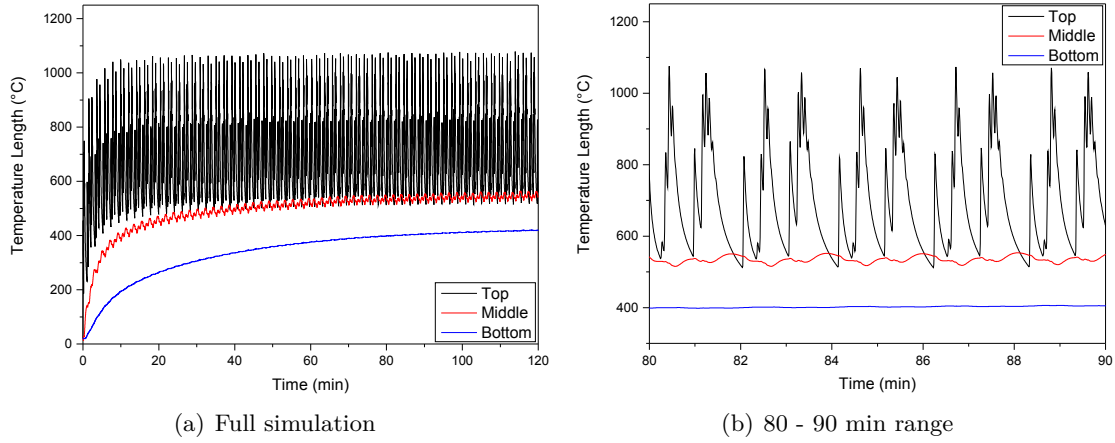


Figure C.5: Simulated temperature evolution at the middle of the length of the brick over a 2-hour sintering process with a contour preheating before sintering. Full simulation (a) and shorter time range (b).

C.3 Sintering in lunar conditions

The two main features of the lunar environment are the reduced gravity and the lack of atmosphere. The gravity should not influence the heat transfer in sintered lunar regolith but the vacuum environment will result in a lack of heat removal by convection. Setting the convection heat to zero, the following simulation was obtained:

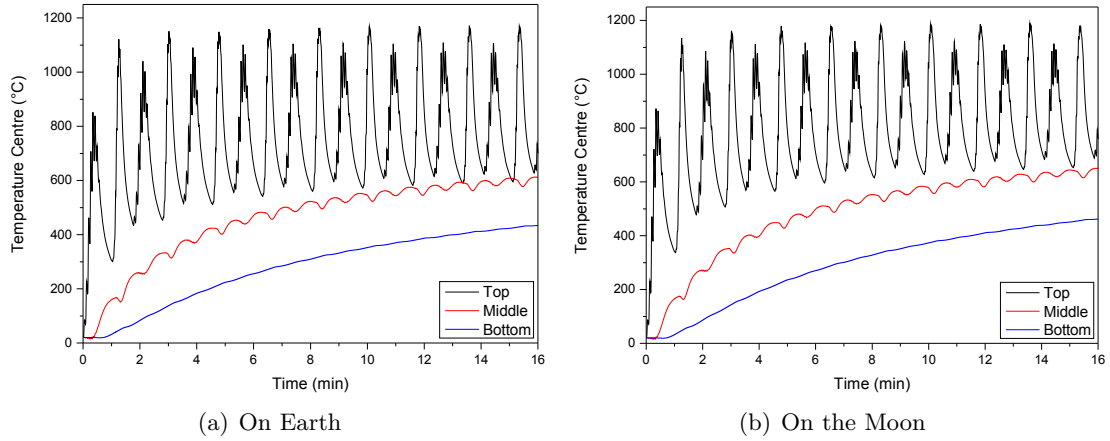


Figure C.6: Simulated temperature evolution at the centre of the brick over a 16-minute sintering process without a contour preheating before sintering. Results on Earth, with air convection (a) and on the Moon, without air convection (b).

As shown in Figure C.6, after 15 minutes sintering, some changes due to the lack of convection can be observed. On the surface (Top), the maximal reached temperature is about 10°C higher on the Moon, about 1180°C. A more prominent difference is observable

during the cooling phase: on Earth the temperature drops down to 600°C when it stays over 650°C on the Moon. The smaller ΔT on the Moon should be beneficial to the sintering quality, reducing the thermal gradients. The reduction of thermal gradients in the brick can also be seen in Figure C.7 where the decrease in temperature on the sides of the brick was less significant between the sintering of two layers on the Moon.

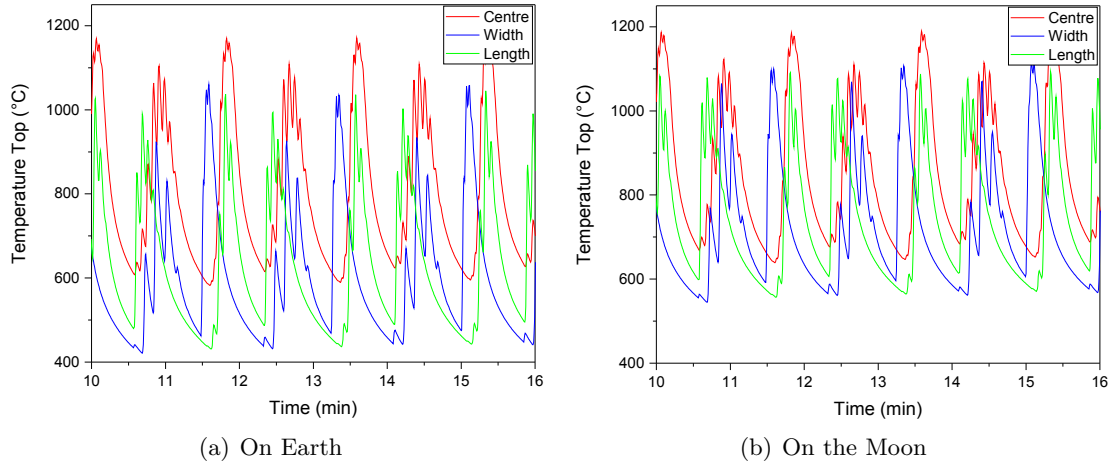


Figure C.7: Simulated temperature evolution at the top of the brick over a 16-minute sintering process without a contour preheating before sintering. Results on Earth, with air convection (a) and on the Moon, without air convection (b).

It is however important to keep in mind that the outgassing of the sintered material, not taken into account in this model, will play a significant role under vacuum and affect the heat transfer and sintering quality of the lunar regolith.

Curriculum vitae

Alexandre Meurisse

Ph.D Candidate, M. Eng. Materials, B. Eng. Materials
M. Sc. Nanofilms



Education:

2015 - present Ph.D Candidate at the Institute for Materials Physics in Space at the German Aerospace Centre (DLR)
Graduation in January 2018 from RWTH Aachen University, Germany.

Title: Solar 3D printing of lunar regolith

Supervisor: Prof. Dr. Matthias Sperl

meurisse.alexandre@gmail.com

Date of birth:

November 26th 1991

Nationality:

French

2011 - 2014

Double Master's degree:

2013-2014: M.Sc. at the National University of Science and Technology MISiS in Moscow, Russia.

Title: Multicomponent nanostructured coatings and Nanofilms.

Supervisor: Philipp V. Kiryukhantsev-Korneev

2011-2012: M. Eng. at the European School of Materials Science and Engineering (EEIGM) in Nancy, France.
Bachelor obtained in June 2012.

Language skills:

-French: Native
-English: Fluent
-Spanish: Fluent
-Russian: Fair
-German: Basics

2009 -2011

Classes préparatoires aux grandes écoles PCSI-PSI at Jacques de Vaucanson high school in Tours, France.

Additional Education and Awards

- 2nd place at the French Engineering competition "Trophées des ingénieurs du future 2016" in three categories: "Research", "International" and "Public's choice".
- DELE B2 del Instituto Cervantes in 2014 certifying my Spanish skills
- Cambridge English First (FCE) in 2012 certifying my English skills

Scientific Publications:

<p><u>A. Meurisse</u>; J. C. Beltzung; M. Kolbe; A. Cowley; and M. Sperl</p>	<p>Influence of Mineral Composition on Sintering Lunar Regolith</p>	<p><i>Journal of Aerospace Engineering</i>, Volume 30 Issue 4 - July 2017</p>
--	---	---

Poster and Oral presentations:

- Granular Matter in low gravity, Erlangen, Germany, 2015: Poster presentation: “Solar sintering of regolith”
- International Symposium on Moon 2020-2030, Noordwijk, Netherlands, 2015, Poster presentation: “Lunar environment influence on sintered regolith”
- European Lunar Symposium, Amsterdam, Netherlands, 2016, Oral presentation: “Solar 3D Printing of Lunar Regolith”
- Space Engineering and Technology Final Presentation Days, Noordwijk, Netherlands, 2017, Oral presentation: “3D printing of a model building block for a lunar base outershell”

Contributions

- International Astronautical Congress, Adelaide, Australia, 2017, Oral presentation: “Robotic prototypes for the solar sintering of regolith on the lunar surface developed within the RegoLight project”
- International Astronautical Congress, Adelaide, Australia, 2017, Oral presentation: “Advancing solar sintering for building a base on the moon”
- Lunar Exploration Analysis Group, USA, 2015, Oral presentation: “SPACESHIP EAC – Fostering activities relevant to Lunar Exploration and ISRU”

Other Publications:

Could 3-D Printers Create Shelters for Future Lunar Settlers?, 2016, *Earth & Space Science News*

<https://eos.org/articles/could-3-d-printers-create-shelters-for-future-lunar-settlers>

Printing bricks from Moondust using the Sun’s heat, 2017, *ESA web page*

http://www.esa.int/Our_Activities/Space_Engineering_Technology/Printing_bricks_from_moondust_using_the_Sun_s_heat